Local structure of dilute nitrides and effects of post-growth treatments

Gianluca Ciatto

UNIVERSITE GRENOBLE I - JOSEPH FOURIER

Thèse
pour obtenir le titre de

DOCTEUR de l'UNIVERSITE JOSEPH FOURIER
(Arrêtés ministériels du 5 juillet 1984 et du 30 mars 1992)

Spécialité Physique

preséntée et soutenue publiquement par

Gianluca CIATTO

Structure locale des nitrures d'éléments III-V $GaAs_{1-y}N_y$ et $In_xGa_{1-x}As_{1-y}N_y$ et effets des traitements post-croissance

Date de soutenance: 19 Mars 2004

Composition du Jury:

H. Mariette	Présidente
M. Sauvage	Rapporteur
J. C. Harmand	Rapporteur
F. Boscherini	Examinateur
M. G. Proietti	Examinateur
S. Mobilio	Directeur de thèse

Thèse préparée au sein du laboratoire: Gilda CRG - European Synchrotron Radiation Facility- BP 220 F-38043 Grenoble, France

Local Structure of Dilute Nitrides and Effects of post-Growth Treatments

Gianluca CIATTO

PhD Thesis

March 19, 2004

University Joseph Fourier - Grenoble I

PHYSICS

Advisor : S. Mobilio

Laboratory : G.I.L.D.A. Collaboration Research Group

European Synchrotron Radiation Facility

Remerciements

Je remercie M. Settimio Mobilio, directeur du laboratoire Gilda CRG - ESRF pour m'avoir accueilli dans son équipe et pour avoir dirigé cette thèse.

Je remercie M. Henri Mariette pour m'avoir fait l'honneur de présider le jury de ma thèse, ainsi que Mme Michèle Sauvage-Simkin et M. Jean-Christophe Harmand pour avoir accepté d'en être les rapporteurs, enfin M. Federico Boscherini et Mme Maria Grazia Proietti pour avoir fait partie du jury.

J'adresse mes remerciements aux membres du groupe Gilda CRG (du présent et du passé) et en particulier à F. D'Acapito, F. Boscherini, S. Colonna, P.L. Solari et C. Maurizio pour le suivi, l'aide et la compagnie.

Je remercie H. Mariette, A. Polimeni, M. Capizzi et D. De Salvador pour leur collaboration et pour nos fructueuses discussions sur les semi-conducteurs III-V.

Les expériences vitales ont été réalisées sur la ligne Gilda de l'ESRF, l'équipe technique doit être grandement remerciée et notamment F. La Manna et F. D'Anca.

Je remercie aussi R. Midtank et D. Batchelor pour leur aide dans les expériences sur Bessy II (ligne Cottbus); L. Floreano et A. Morgante pour l'assistance pendant les expériences à Elettra (ligne Aloisa).

Merci à H. Renevier et à M. G. Proietti pour l'aide et la compagnie lors des manips DAFS sur la ligne D2AM de l'ESRF ainsi que pour leur disponibilité à la discussion.

Un grand merci à L. Grenouillet du CEA pour la croissance des échantillons (couches épaisses) effectuée à la fin août, juste à temps pour les expériences XAFS les plus importantes sur la ligne Gilda; merci aussi à M. Fischer et à A. Forchel (Université de Würzburg) pour la croissance de puits quantiques.

Je remercie L. Ortega pour l'aide précieuse lors des manips XRD au CNRS. Je remercie G. Bisognin, D. de Salvador, C. Mattevi pour la caractérisation des échantillons à Padova (NRA, XRD, PL). Merci aussi à V. Calvo (CEA) et à A. Polimeni (Université Rome I) pour la caractérisation des échantillons par PL.

Je remercie les étudiants avec lesquels j'ai passé un peu de temps sur la ligne: Giorgio, Matteo, Roberta, Nicoletta, Stephen, Lisa.

Un grand merci à Sylvie Monfraix pour avoir corrigé mes résumés en français (en ajoutant beaucoup de virgules !!) et à Denis Testamale pour les précisions.

J'exprime mes remerciements à Pier Lorenzo Solari et Roberta Angelini pour leur aide et soutien lors de mes premiers jours à Grenoble.

Je salue amicalement et remercie les thésards et amis de l'ESRF: Manu (pour beaucoup de cafés, le vol des trucs pour relier la thèse et plein d'autres choses...), Eva (surtout pour les cinémas à 22:00 heures pendant la rédaction), Aurélien (histoire de batteries et de bagnoles...), Sylvie, Elodie, Laurent, Fabrizio, Laurence, Denis, etc., ainsi que les vieux copains de Ravenne et Bologne car ils sont (presque) toujours là quand je rentre en Italie (Ti, Walsh, Grego, Alessandra, Chiara, Agnese, Matteo, Max, Pit, Raffaele, etc.). Je salue aussi les "Grenobloises" plus ou moins "métèques": Junko, Laetitia, Jocelin, Gurio, Sara, Anna. Finalement je remercie ma famille pour le soutien moral pendant ces trois années et d'être venue de loin assister à la soutenance; cette thèse est dédiée à mon grand-père Domenico (qui était coiffeur et conteur de fables).

" *Véga et Deneb étincelaient entre les faîtes des arbres; les troncs et les branches occultaient les étoiles placées plus bas dans le ciel. Le clerc pensa à Pythagore, à Nicolas de Cusa, à un certain Copernic dont les théories récemment exposées étaient ardemment accueillies ou violemment contredites à l'Ecole, et un mouvement d'orgueil le prit à l'idée d'appartenir à cette industrieuse et agitée race des hommes qui domestique le feu, transforme la substance des choses, et scrute les chemins des astres.*"

De " **l'Œuvre au Noir** "
Marguerite Yourcenar

Contents

Introduction

Ce travail de thèse a le but de fournir une caractérisation structurale des semi-conducteurs III-V $GaAs_{1-y}N_y$ et $In_xGa_{1-x}As_{1-y}N_y$, matériaux de grande importance technologique pour la réalisation d'émetteurs lasers à 1.3 et 1.55 μm sur substrat GaAs, et d'offrir une assise pour mieux comprendre les propriétés optiques et électroniques anomales qui ont été observées il y a huit ans et qui sont désormais exploitées dans la réalisation des composantes optoélectroniques. Les techniques principales que nous avons utilisées dans ce but sont l'absorption de rayons X (XAS) avec rayonnement de synchrotron (les expériences ont été réalisées sur les installations de troisième génération ESRF à Grenoble, Elettra à Trieste et Bessy II à Berlin) et la diffraction de rayons X (XRD), réalisée en laboratoire avec des anodes rotatives et des tubes. La spectroscopie de diffraction anomale (DAFS) a eu un rôle limité, mais néanmoins significatif dans ce travail de thèse. Des autres techniques complémentaires comme la photoluminescence (PL), certaines techniques de physique nucléaire (NRA) et simulations théoriques (DFT) ont aussi fourni des informations importantes pour l'interprétation des résultats sur la structure locale et globale des alliages $(In_x)Ga_{1-x}As_{1-y}N_y$.

Ce travail expérimental commence par la vérification des plus récentes attentes théoriques sur la structure des nitrures d'éléments III-V, en choisissant dans chaque cas particulier la technique la mieux adaptée, l'installation de lumière de synchrotron la plus performante, le seuil le plus adapté pour les expériences d'absorption de rayons X, etc. Certaines modélisations théoriques ont été modifiées et adaptées à notre cas pour comprendre le panorama expérimental qui résulte de notre travail et de travail d'autres groupes. Toutes les anomalies des nitrures d'éléments III-V ont une origine commune, qui doit être recherchée dans les caractéristiques très différentes (dimensions, énergies orbitales, électronégativité) des deux anions As et N.

Je voudrais remarquer ici que, face à la prolifération des études de spectroscopie optique sur ces matériaux, peu d'informations expérimentales existaient au début de ce travail de thèse au niveau de la structure de l'alliage, soit à l'échelle de la maille, soit à l'échelle locale (deux premières couches de coordination), même si des calculs théoriques envisageaient que les changements structuraux, en particulier les phénomènes d'ordre chimique, influencent considérablement les propriétés d'émission. Par conséquent, les résultats sur les propriétés structurales de l'alliage $In_xGa_{1-x}As_{1-y}N_y$ présentés dans ce travail de thèse, au-delà de l'importance scientifique, ont aussi un intérêt technologique en fournissant des informations utiles pour la croissance de nouveaux composants optoélectroniques aux caractéristiques améliorées.

Trois principaux sujets ont été abordés pendant cette thèse:

1. l'ordre local en alliages $In_xGa_{1-x}As_{1-y}N_y$ et les effets du recuit post-croissance sur la structure locale;

2. l'étude des distances interatomiques en $GaAs_{1-y}N_y$ dans la limite de dilution pour l'azote;

3. les effets de l'hydrogénation sur la structure locale et globale de nitrures $GaAs_{1-y}N_y$ et $In_xGa_{1-x}As_{1-y}N_y$.

Le premier point est celui de déterminer dans le cas de l'alliage $In_xGa_{1-x}As_{1-y}N_y$ le nombre relatif des liaisons In-N et In-As, et de le comparer avec les prédictions des récentes simulations. En fait, dans un alliage quaternaire le nombre relatif de liaisons n'est pas fixé par la stœchiométrie et une certaine liaison peut être favorite par rapport à une autre. Dans le cas particulier de l'alliage $In_xGa_{1-x}As_{1-y}N_y$, un excès de liaisons In-N par rapport au cas de distribution aléatoire des liaisons a été prévu à l'équilibre par des calculs Monte Carlo. Afin d'obtenir une détermination expérimentale du degré d'ordre, différentes expériences XAS au seuil de l'indium et de l'azote ont été nécessaires. Toutes ces expériences XAS étaient aux limites des possibilités techniques à cause de la faible épaisseur des échantillons, de la dilution en concentration d'azote et indium, de la faible section efficace d'absorption dans les hautes énergies et de la contamination de la surface des échantillons par azote et oxygène. Nous montrons que le recuit post-croissance cause une ordonnance de type In-N + Ga-As; cela vient du fait que le recuit entraîne les échantillons vers la condition d'équilibre. D'ailleurs le degré d'ordre mesuré est très inférieur par rapport à la prédiction (un ordre de grandeur). Nous montrons aussi que le degré d'ordre local mesuré par XAS justifie les propriétés d'émission des échantillons recuits.

En ce qui concerne le deuxième point, nous avons comparé la dépendance de la composition de la distance de liaison Ga-As avec les prédictions théoriques classiques VFF (valence force field), afin de comprendre si les modélisations normalement exploitées pour décrire la structure locale des alliages semi-conducteurs s'adaptent dans le cas d'un système caractérisé par la nature très différente des deux anions As et N et, par conséquent, par les propriétés élastiques très différentes des composants binaires GaAs et GaN. Nous avons comparé nos résultats expérimentaux et nos calculs VFF avec les rigoureuses prédictions de la théorie de la fonctionnelle densité (DFT, density functionals theory). Nous avons trouvé que certaines modélisations VFF sont mieux que d'autres et nous avons lié ce fait aux différentes formulations du potentiel VFF couplé avec les spécificités du système $GaAs_{1-y}N_y$. En raison des difficultés expérimentales, ce sujet n'a pas été abordé précédemment et il n'existait pas d'autres déterminations expérimentales de changements des distances de liaison causés par l'incorporation d'azote dans la structure, malgré l'intérêt considérable adressé à ces matériaux.

Quant au dernier point, l'hydrogénation a été très étudiée d'un point de vue optique car elle amène à une "passivation" des effets liés à l'introduction d'azote et, en

particulier, à une annulation du décalage vers le rouge de la bande interdite. Même dans ce cas, nous avons étudié les effets structuraux de l'irradiation avec hydrogène atomique en $GaAs_{1-y}N_y$ et $In_xGa_{1-x}As_{1-y}N_y$. Nous montrons par XRD que la passivation électrique des effets de l'azote est accompagnée par une étonnante relaxation de la maille soit en $GaAs_{1-y}N_y$, soit en $In_xGa_{1-x}As_{1-y}N_y$. Les effets structuraux et optiques de l'hydrogénation peuvent être en même temps justifiés par la formation de spécifiques complexes N-H. Des simulations théoriques réalisées par mes collaborateurs et d'autres groupes prévoient en effet que ces complexes sont énergiquement favorisés. Les résultats de diffraction de rayons X reportés dans ce travail de thèse représentent une parmi les premières observations d'un changement si remarquable et en même temps réversible sur la structure d'un semi-conducteur causé par un traitement post-croissance. En passant de la structure de maille à la structure locale, nous avons aussi étudié par XAS et DAFS les effets de l'hydrogénation sur les distances inter atomiques en alliages $GaAs_{1-y}N_y$ et $In_xGa_{1-x}As_{1-y}N_y$.

Ce mémoire se divise en cinq chapitres, les trois premiers constituent la partie théorique tandis que dans les trois derniers présentent nos résultats:

- Dans le premier chapitre nous fournissons une introduction théorique sur la physique des nitrures d'éléments III-V et expliquons l'origine de leur importance au point de vue technologique : les plus récentes et importantes applications techniques sont ici décrites brièvement, la théorie de la structure électronique et les modélisations utilisées pour justifier leurs propriétés optiques sont illustrées; la théorie de l'hydrogénation et les modélisations classiques pour décrire les distances inter-atomiques en semi-conducteurs III-V sont ensuite décrites. Finalement les résultats expérimentaux les plus importants et les quelques informations disponibles sur la structure des nitrures avant la réalisation de ce travail sont énumérées.

- Dans le deuxième chapitre nous décrivons les échantillons, les traitements post-croissance (recuit, hydrogénation) et toutes les techniques expérimentales et théoriques exploitées, avec une attention particulière pour la spectroscopie d'absorption de rayons X (XAS), qui a été la technique la plus utilisée pendant ce travail de thèse. Parmi les autres techniques, la spectroscopie de diffraction anomale (DAFS) et la diffraction de rayons X (XRD) sont aussi expliquées.

- Dans le troisième chapitre nous présentons les résultats au sujet de l'ordre local en couches épaisses et puits quantiques de $In_xGa_{1-x}As_{1-y}N_y/GaAs$; les techniques principales exploitées dans ce chapitre sont le XAS (aux seuils de l'indium et de l'azote) et le DAFS (au seuil du gallium).

- Le quatrième chapitre présente une étude expérimentale des distances de liaison en $GaAs_{1-y}N_y/GaAs$ (couches épaisses) à la limite de dilution pour l'azote en comparaison avec des modélisations théoriques. Même dans ce cas le XAS (au seuil du gallium) a été la technique expérimentale la plus utilisée.

- Le dernier chapitre montre les résultats sur les effets de l'hydrogénation sur les propriétés structurales des alliages $GaAs_{1-y}N_y$ (couches épaisses) et $In_xGa_{1-x}As_{1-y}N_y$ (couches épaisses et puits quantiques). Dans ce chapitre la XRD a été la technique la plus utilisée pour obtenir des informations sur le paramètre de maille; le XAS a tout de même joué un rôle important dans l'étude de ces effets à l'échelle locale.

Un appendice (A) suit les cinq chapitres et présente les résultats d'une étude technique finalisée à l'amélioration du XAS en détection de fluorescence, technique normalement exploitée sur la ligne de lumière au sein de laquelle j'ai préparé cette thèse: le laboratoire GILDA de l'ESRF. Il s'agit d'une étude du régime non-linéaire des détecteurs à l'état solide et des corrections de temps mort: en particulier le cas du détecteur ORTEG à treize éléments de germanium hyper pur équipé avec une électronique digitale XIA de la ligne GILDA a été étudié, mais les stratégies de corrections ici élaborées ont une validité plus générale. Même si cette analyse n'a été pas strictement nécessaire pour l'étude des échantillons $In_xGa_{1-x}As_{1-y}N_y$ (l'acquisition a été ici réalisée en conditions linéaires), je présente ces résultats dans cette thèse en raison de l'intérêt potentiel qu'ils pourraient avoir pour la part de la communauté XAS adonné à l'étude d'échantillons dilués (en particulier les implantations et dopant en semi-conducteurs et les nanostructures des semi-conducteurs mêmes) et par conséquent à la détection de fluorescence.

Dans le cadre de ce projet, différentes demandes de temps machine ont été acceptées sur les installations de rayonnement synchrotron de ESRF (Grenoble), Elettra (Trieste, Italie) et Bessy II (Berlin, Allemagne). Les différentes contributions à ce travail sont ci-après énumérées:

Les expériences à l'installation européenne de rayonnement de synchrotron (ESRF) ont été réalisées sur la ligne italienne GILDA (BM08) en ce qui concerne le XAS (aux seuils de l'In et du Ga) et sur la ligne française D2AM (BM02) pour le DAFS. Les expériences XAS au seuil de l'azote ont été réalisées sur la ligne de lumière de ALOISA du synchrotron de Elettra (Trieste) et sur la ligne Cottbus du synchrotron BESSY II (Berlin). Les expériences XRD ont été réalisées au CNRS de Grenoble (LdC) et à l'Université de Padova (I), celles NRA aux Laboratoires Nationaux de Legnaro (I). Les expériences de photoluminescence ont été réalisées à l'Université de Padova (I), au CEA de Grenoble (DRFMC) et à l'Université de Rome "La Sapienza". La croissance des échantillons a été effectuée au CEA de Grenoble (LETI) et à l'Université de Würzburg (D). Les recuits post-croissance ont été effectués au CEA (LETI) et l'hydrogénation des échantillons à l'Université de Rome "La Sapienza". Enfin les simulations théoriques ont été achevées à l'Université de Cagliari (I) et au CNR (ISM) à Rome.

Ma contribution personnelle à ce projet a été celle de jouer un rôle considérable dans la planification de la recherche, de mettre à point et réaliser toutes les expériences XAS sur la ligne GILDA, de prendre partie active dans toute les autres expériences XAS et DAFS, d'effectuer personnellement partie des expériences XRD (en particulier celles sur les échantillons hydrogénés décrites dans le chapitre V). Ma contribution a été aussi celle de réaliser toute l'analyse des données XAS, DAFS et les simulations du spectre

d'absorption de la région du seuil (XANES) de l'azote en analyse de diffusion multiple (FMS); d'utiliser et d'adapter à notre cas certains modèles théoriques classiques et plus récents pour les distances inter-atomiques en semi-conducteurs et pour les décalages de la bande interdite dus à l'ordre local. Enfin, j'ai réalisé l'analyse de données des expériences XAS reporté dans l'appendice; dans ce but j'ai développé un logiciel en Fortran utilisé pour l'inversion de la formule de temps mort du système d'acquisition.

Introduction

This thesis work addresses the issue of a structural characterization of the technologically important III-V dilute nitrides $GaAs_{1-y}N_y$ and $In_xGa_{1-x}As_{1-y}N_y$, providing an useful frame to better understand the anomalous optical and electronic properties that have been observed for eight years and are nowadays exploited in optoelectronic devices design. The main techniques used were X-Ray Absorption Spectroscopy (XAS) and X-Ray Diffraction (XRD). Diffraction Anomalous Fine Structure (DAFS) took also a limited but meaningful role in this work, as other complementary techniques (Photoluminescence Spectroscopy, Nuclear Reaction Analysis and Theoretical Simulations) that provided an important feedback to contextualize the results.

This experimental work starts with an attempt to verify the most novel theoretical predictions in the field of III-V nitrides by using the fittest samples and the most suitable structural investigation techniques, exploiting the high brilliance of third generation synchrotron radiation sources. Some theoretical models were adapted to our case in order to interpret the experimental panorama that came out. All the peculiar properties of such nitrides have a common origin and are basically due to the very different physical characteristics (size, orbital energies, electronegativity) of As and N. I want to stress here that, despite the number of investigations of the optical behavior of dilute nitrides, very little experimental information was available on the structure of these crystals (both at the unit cell and at the local scale) before the beginning of this work, even if structural changes were predicted to dramatically affect the emission properties. The achievements on the structural properties of $In_xGa_{1-x}As_{1-y}N_y$ presented in this work, as a consequence, have not only a scientific interest, but also a technological valence: they provide the samples growers with useful physical information for improving the components of optoelectronic devices.

The main subjects addressed in this thesis are :

1. the short range ordering (SRO) in $In_xGa_{1-x}As_{1-y}N_y$ and the effects of post-growth annealing on the local structure;

2. the composition dependence of the bond lengths at the nitrogen dilute limit in $GaAs_{1-y}N_y$;

3. the effects of hydrogenation on the long- and short-range structure of dilute nitrides.

The first and most challenging point consists in determining the degree of short range order in the quaternary alloy $In_xGa_{1-x}As_{1-y}N_y$, and in comparing it with recent predictions. In order to obtain such information X-Ray Absorption measurements were performed both at the nitrogen and the indium edge. Such XAS measurements were not trivial because of the small thickness of quantum wells samples and the high dilution of the absorber in epilayers samples, because of the low absorption cross section at high energies (In K-edge) and the superficial N contamination (N K-edge). Our results gave evidence for the presence of a preferential In-N bonding over In-As in $In_xGa_{1-x}As_{1-y}N_y$ driven by thermal annealing, which brings the system towards the equilibrium condition where an ordering of the same kind is predicted. The measured short range order parameter resulted however much smaller (about one order of magnitude) than the value predicted by theoretical calculations. We also found a quantitative connection between the measured SRO and the optical behavior of these alloys.

For what concerns the second point, we compared the composition dependence of the Ga-As bond length measured by XAS with the classic Valence Force Field (VFF) predictions. The purpose was to understand whether the theoretical models usually employed in describing the local structure of semiconductor alloys work also in the case of $GaAs_{1-y}N_y$, whose constituent binary compounds (GaAs and GaN) have very different elastic properties due to the deeply different characteristics of the two anions. We compared also our results to first principles calculations performed in the frame of the density functional theory (DFT). Our results show that some VFF models reproduce the experimental distances distributions better then others. We related this different performance to the different formulations of the elastic force field in the peculiar case of $GaAs_{1-y}N_y$. Despite the extremely high interest devoted to these materials, this subject has not been treated before; to the best of our knowledge no experimental determination of the changes in the bond lengths of $GaAs_{1-y}N_y$ induced by N incorporation existed previously to this work.

As regards the third and last issue, hydrogenation has been largely studied since it induces, from an optical viewpoint, the passivation of the nitrogen effects. In this case, we supplied information on the effects of atomic hydrogen irradiation on the structure of $GaAs_{1-y}N_y$ and $In_xGa_{1-x}As_{1-y}N_y$ alloys. We showed how the electrical passivation of nitrogen is accompanied by a remarkable relaxation of the unit cell both in In-free and in In-containing alloys. Our XRD results represent one of the first observations of such a dramatic (and reversible) change induced on the structure of a semiconductor by a post-growth treatment. The effects of hydrogenation on the optical and structural properties are accounted for by the formation of particular N-H complexes; as a matter of fact according to recent *state of art* theoretical simulations the formation of such complexes is energetically favored. We studied also by XAFS and DAFS the effects of hydrogenation on the bond lengths and interatomic distances both in $GaAs_{1-y}N_y$ and $In_xGa_{1-x}As_{1-y}N_y$ alloys.

This thesis is composed of five chapters; the first two give the theoretical basis of the work, the others report the results obtained on the three main issues referred above:

- *Chapter I* provides an overview on the physics of III-V nitrides and explains the origin of their technological interest: the most important present and potential applications are briefly described; the theory of the electronic structure and the models elaborated to account for the optical behavior are discussed along with the theory of hydrogenation and the classic models usually exploited to describe the local structure of ternary and quaternary semiconductor alloys. Furthermore the major experimental achievements and the structural information available in literature previously to this work are here listed.

- *Chapter II* reports a description of the samples, of the growth and post-growth treatments (annealing, hydrogenation) and of all the experimental techniques exploited, paying particular attention to X-Ray Absorption (XAS), which was the main investigation tool of this work; among the other techniques DAFS and XRD are briefly addressed. For each experimental technique exploited the relative experimental station is also described.

- *Chapter III* reports the results achieved on the issue of Short Range Ordering (SRO) in $In_xGa_{1-x}As_{1-y}N_y$ epilayers and quantum wells, using mainly XAS (In and N edge) and DAFS (Ga edge).

- *Chapter IV* presents the behavior of the bond lengths in $GaAs_{1-y}N_y$ at the N dilute limit obtained by XAS; the experimental trend is compared to theoretical predictions.

- *Chapter V* illustrates results on the effects of hydrogenation on the structural properties of $GaAs_{1-y}N_y$ and $In_xGa_{1-x}As_{1-y}N_y$; XRD is the main tool exploited in this chapter to extract information on the unit cell, however XAS provided useful information on the local scale structure.

Appendix (A) reports a technical study finalized to the refurbishment of the beam line of the European Synchrotron Radiation Facility that hosted me as a PhD Student (the Gilda CRG beamline - BM8): an investigation of the non linear regime for solid state detectors exploited for XAS in fluorescence mode.

During the present research, different experimental proposals were awarded beam time at the European Synchrotron Radiation Facility (ESRF) in Grenoble, France, at the Elettra Synchrotron in Trieste, Italy, and at the Bessy II Synchrotron in Berlin, Germany.

The various contributions to the work are so outlined :

Experiments at ESRF were performed at the Italian Gilda CRG beam line (BM8) for what concerns XAS (In and Ga K-absorption edge) and at the French D2AM CRG beam line (BM2) for DAFS (Ga edge). XAS measurements at the N K-edge were performed at the ALOISA beam line of the Elettra facility and at the Cottbus CRG beam line of Bessy II. XRD experiments were performed at the Crystallography Laboratory of the French National Center for Scientific Research (CNRS) in Grenoble and at the

Department of Physics, University of Padova (I). Nuclear Reaction Analysis (NRA) and Rutherford Backscattering Spectrometry (RBS) were performed at the Italian National Nuclear Physics Laboratories in Legnaro. Photoluminescence (PL) measurements were performed in part at the University of Padova (room temperature), in part at the Department of Fundamental Research on Condensed Matter (DRFMC) of the French Institute for Atomic Energy research (CEA) in Grenoble (l0 K) and finally at the Department of Physics, University of Rome I "La Sapienza" (10 K, 150 K and RT); Hydrogenation of the samples was also undertaken at the University of Rome I. Samples were grown at the Department of Optoelectronics (LETI) of CEA in Grenoble and at the University of Würzburg, Germany. Rapid thermal annealing was also performed at CEA/Leti. First principles supercell calculations were performed at the Department of Physics, University of Cagliari (I) and at Italian National Council of Research (CNR), Institute of Condensed Matter (ISM), Rome.

My personal contribution to this project consisted in taking a relevant part in the research planning and developing, in setting up and performing all the XAS experiments at the BM8 beam line of the ESRF and taking active part in all the other XAS and DAFS experiments, in undertaking part of the XRD measurements and data reduction (in particular those on the hydrogenated samples reported in chapter 5), in carrying out all the X-Ray Absorption Fine Structure (XAFS) and DAFS data analysis, and all the X-Ray Absorption Near Edge Spectroscopy (XANES) simulations in the full multiple scattering approach. It consisted also in adapting some classic theoretical models for the bond lengths behavior in semiconductors and very recent models for the changes in the $In_xGa_{1-x}As_{1-y}N_y$ band gap driven by SRO phenomena, in order to interpret the entire experimental panorama. Finally I performed the XAFS analysis of the data whose results are reported in the appendix and wrote the Fortran code therein exploited in order to numerically invert the throughput of the pulse counting electronics.

Part I

Theory of the materials and of the investigation techniques

Chapitre 1: Théorie et applications des nitrures d'éléments III-V

Dans ce chapitre, nous expliquons premièrement l'origine de l'intérêt technologique des nitrures d'éléments III-V et en particulier de l'alliage $In_xGa_{1-x}As_{1-y}N_y$. Cet intérêt est dû au fait qu'ils permettent la croissance de composants à cavité verticale émettant à 1.3 et 1.55 m, épitaxiés sur substrat GaAs. Ces longueurs d'onde correspondent aux deux minima pour l'atténuation du signal dans les fibres en silice et permettent de très longues distances de transmission. La croissance sur substrat GaAs est assez économique et permet d'obtenir des dispositifs d'une très bonne stabilité en température [1, 2]. Au-delà de leur usage dans la production des lasers, ces nitrures vont aussi être utilisés dans la construction de nouvelles cellules solaires d'un rendement très élevé [3].

L'obtention de longueurs d'onde si élevées est possible grâce au paramètre de courbure géant de ces alliages, qui permet de décaler la bande interdite vers le rouge en augmentant la concentration d'azote. Un modèle assez simple (d'anticroisement de bande [4]) explique ce paramètre de courbure anomale par l'interaction entre un niveau isoélectronique lié à l 'introduction d'azote et les états étendus du minimum de la bande de conduction (représentés par un deuxième niveau électronique). L'interaction donne naissance à deux sous-bandes dont l'énergie dépend de la concentration d'azote; la répulsion entre les deux niveaux est à l'origine de la diminution de l'énergie de bande interdite avec l'incorporation d'azote. Ce modèle, qui reproduit bien les observations expérimentales, a été successivement critiqué et un couplage plus complexe parmi différents niveaux du fond de la bande de conduction a été proposé, en tenant compte à la fois de la distribution statistique des différents agrégats d'azote [5].

Nous présentons ensuite la théorie assez récente des effets de l'irradiation des alliages $GaAs_{1-y}N_y$ et $In_xGa_{1-x}As_{1-y}N_y$ par hydrogène. L'hydrogénation est un processus bien connu dans les semi-conducteurs dopés, par contre on dispose de peu d'information sur l'interaction de l'hydrogène avec des impuretés isoélectroniques, comme l'azote dans ce cas. La formation des différents complexes N-H a été proposée dans le but d'expliquer la conduite optique des échantillons hydrogénés; parmi ces complexes deux sont privilégiés d'un point de vue de l'énergie de formation: le $H(BC_N^+)$ dans lequel un seul atome d'hydrogène est impliqué, et le $H_2^*(N)$ qui nécessite la présence de deux

atomes d'hydrogène pour chaque azote [6, 7].

Nous introduisons après la thématique de l'ordre local dans les alliages III-V ternaires et quaternaires. Dans le premier cas, on parle de la probabilité mineure ou majeure par rapport à celle indiquée par la stœchiométrie que des atomes identiques ont de se trouver l'un dans la première couche de coordination de l'autre dans le sous-réseau mixte (anionique dans de cas du $GaAs_{1-y}N_y$) [8]. Dans le deuxième cas, on parle du nombre relatif des différentes liaisons cation-anion et des possibles liaisons énergiquement avantagées comme celles In-N et Ga-As dans le cas de l'$In_xGa_{1-x}As_{1-y}N_y$ [9].

Enfin, on met en évidence le manque d'information sur la structure de ces nitrures, soit à l'échelle de la maille, soit à l'échelle locale et on introduit de cette manière le but de ce travail de thèse; le chapitre se conclue en fournissant des modèles théoriques normalement exploités pour reproduire la structure locale de semi-conducteurs III-V et qui seront rapportés au cas du $In_xGa_{1-x}As_{1-y}N_y$ dans les chapitres suivants.

Chapter 1

III-V nitrides : applications and theory

1.1 Technological interest of $In_xGa_{1-x}As_{1-y}N_y$

1.1.1 Telecommunications

III-V dilute nitrides and in particular $In_xGa_{1-x}As_{1-y}N_y$ alloys have been awarded a great technological interest in the last decade because they allow lasing at 1.3 μm and 1.55 μm on GaAs substrate. The emission at such wavelengths is very important because corresponds to the minima for attenuation of the signal into silica optical fibers; the use of such wavelengths could allow to reach transmission distances longer than 10 km at a network speed of 10 Gigabit/s, solving the problem of the "last mile" for Internet at a local and metro area. In Fig. 1.1 the attenuation (dB/Km) of monochromatic radiation in a silica optical fiber is reported in the wavelength range 0.7 μm - 1.7 μm.

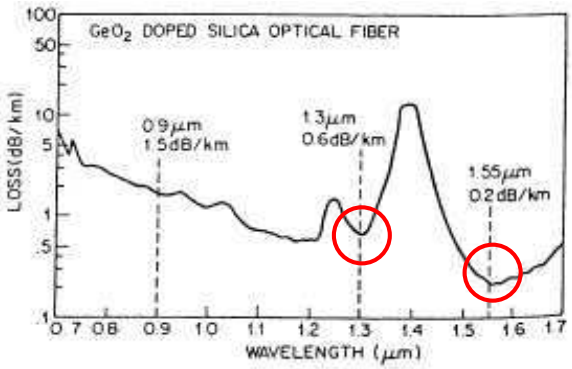

Figure 1.1: Attenuation of the signal in a silica optical fiber in the range 0.7 μm - 1.7 μm ; red circles indicate the two minima of interest at 1.3 and 1.55 μm.

Optical data-transmission must moreover be sure for users' sight : emission at 850 nm (near infra-red), obtained exploiting $In_xGa_{1-x}As$ alloys, is particularly insidious since it is invisible to human sight and can easily damage the eyes at high intensity. For this reason maximum limits (several hundred μW) are fixed for the power of optical modules working at 850 nm; at 1.3 μm the power can be increased by an order of magnitude for the same danger level. Finally at 1.3 μm alimentation voltages for the emitters are comparable to those used for CMOS systems, which would permit the hybridizing of optical devices on Si-based integrated circuits.

Emission at 1.3 μm was first achieved by using $In_xGa_{1-x}As_{1-y}P_y$ alloys grown on InP substrate; several problems are on the other hand related to the InP technology : first of all it is more expensive, secondly $In_xGa_{1-x}As_{1-y}P_y$ /GaAs devices have a poor temperature behavior and should be cooled to properly work. This poor temperature characteristics come from the low electron confinement due to the small mismatch between the conduction bands of $In_xGa_{1-x}As_{1-y}P_y$ and InP.

The mismatch between $In_xGa_{1-x}As_{1-y}N_y$ and GaAs conduction bands is, on the other hand, relevant and a very high confinement of the electrons in the active layer can be obtained; by using $Al_{0.1}Ga_{0.9}As$ barrier-layers it is possible to induce also a slight mismatch of the valence band confining holes as the same time (see Fig. 1.2).

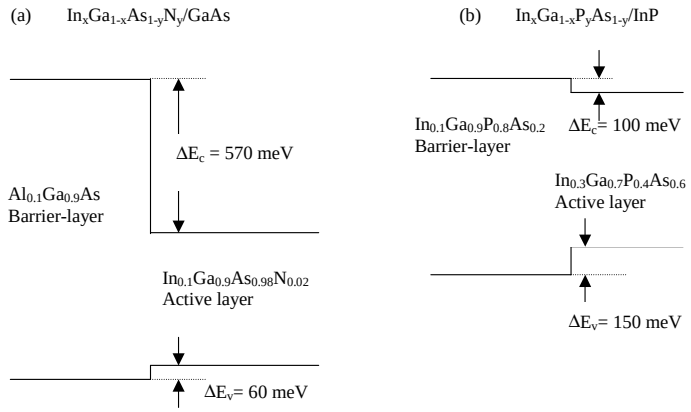

Figure 1.2: Band lineshapes for materials emitting at 1.3 μm : you can notice the greater mismatch between active and barrier layers conduction bands in the case of $In_xGa_{1-x}As_{1-y}N_y$.

The state of art technology employed to build emitters coupled to optic fibers is given by the vertical- cavity surface-emitting lasers (VCSELs). A scheme of a VCSEL [10] is reported in Fig. 1.3. A VCSEL differs from a classic edge emitting laser because the Fabry-Pérot cavity is vertical and very thin, the active layer (red line in the figure) consists of quantum wells for a total thickness of a few tens of nanometer. Since the thickness of the cavity is very little the light wave has to pick up all its energy along the short path to achieve sufficient gain to induce stimulate emission. In order to obtain this, VCSELs need mirrors layers (the green lines in Fig. 1.3) with reflectivity

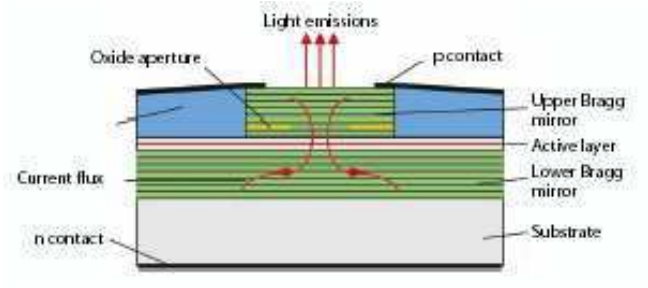

Figure 1.3: From *Infineon* web site (modified) : VCSEL design.

higher than 99 %. For emission on GaAs substrate mirrors are usually obtained by AlGaAs/GaAs bilayers arrays, the higher is the number of bilayer and the difference between the refraction index of the two constituents of the bilayer, the higher is the reflectivity of the mirrors. A further limitation of the InP substrate approach is that the difference between the refraction index of InGaAsP and InP, which constitutes the mirrors layer, is very small, so a great number of repetitions is necessary in order to obtain a sufficient total reflectivity.

The light emitted by edge emitting lasers has an asymmetric beam characteristic and a relatively large angle of divergence. On the other hand in VCSELs, due to the small dimension of the cavity, the beam, which is longitudinal mono-mode, is symmetric and can product a far field with a small angle of divergence. The shape of the active area can be easily modified in order to obtain a laser spot of the desired geometry (for example circular); the low divergence permits to directly couple the radiation into the fiber via a 45° deflection mirror without using additional optical components like focusing optics [10] (see Fig. 1.4).

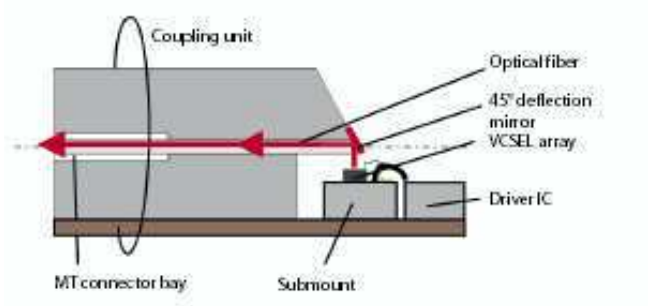

Figure 1.4: From *Infineon* web site (modified) : VCSEL coupled to an optic fiber.

The biggest advantage of VCSELs is the low cost of fabrication and packaging, which results from the fact that the technology used is the same as that used for the fabrication of integrated circuits. In fact the emission from the surface allows both

the entire fabrication process and testing stage to take place on the wafer level; large two-dimensional arrays of VCSELs can be used to generate high optic powers by simply increasing the active area.

Having now understood the importance of the emission at 1.3 μm and 1.5 μm on GaAs substrate let's say that different III-V alloys are eligible for such applications [11]. The first example is given by Sb based III-V quantum wells : GaAsSb/GaAs GaAsSbN/GaAs and GaInAsSbN; the second by InGaAs/GaAs quantum dots; the third and at the present most promising is given by $In_xGa_{1-x}As_{1-y}N_y$ /GaAs quantum wells, which is the object of this PhD thesis. All these approaches, with more or less clamor, have already given noticeable practical results and some components based on these alloys are already commercialized by Infineon Technologies.

It is clear from this how the concepts of nanostructures and in particular quantum wells are extremely important for III-V nitrides technology. The low dimensionality is necessary in order to better control the emission wavelength which in the quantum mechanical regime can be easily tailored by modifying the well width and to enhance the confinement of the charge carriers in the active layers. It is also necessary in order to assure that epilayers grown with a lattice parameter significantly larger than that of the substrate don't inelastically relax via dislocations, which would cause a degradation of the emission proprieties. Finally, low dimensionality will be required in the frame of the hybridization on integrated circuits that become smaller and smaller as the time goes by and computer science develops.

1.1.2 Photovoltaic cells

A solar cell must convert solar radiation into electron-hole pairs and separate electrons from holes. The solar energy is in form of electromagnetic "black body" radiation and the sun spectrum is consistent with that of a black body at a temperature of 5800 K. Part of the solar radiation is in the visible (400-700 nm), but the intensity peak of the spectrum falls in the near infrared (about 1550 nm i.e. 0.8 eV). In order to be absorbed, a photon must have an energy larger than the band gap of the semiconductor that constitutes the solar cell; in case of a multi-junction solar cell, where different semiconductors are employed to optimize the efficiency, the energy absorption range is limited by the element with smallest band gap.

Another constrain is given by the fact that different semiconductors in a multi-junction have to be as far as possible lattice matched i.e. they should posses slightly different lattice constants so that the epitaxial growth doesn't result in an inelastic relaxation via dislocations or other defects. The presence of defects is in fact a cause of severe energy losses in the conversion.

Because of all that, it is evident the need of a large range of semiconductors, which can cover the entire solar spectrum and which can be lattice matched each other. A well designed multi-junction solar cell should in fact match the solar spectrum with the band gaps of the individual junctions. If each junction is tuned to a specific limited wavelength range, this reduces the fraction of above gap photons that dissipates the energy excess via heat production. In particular it is important to dispose of semicon-

ductors with band gaps smaller than 1.0 eV and down to 0.8 eV, like $In_xGa_{1-x}As_{1-y}N_y$, in order to match the region of the solar spectrum peak.

III-V nitrides enormously extend the possible band gap - lattice parameter combinations as you can infer from Fig. 1.5. $In_xGa_{1-x}As_{1-y}N_y$ with 1.0 eV band gap can

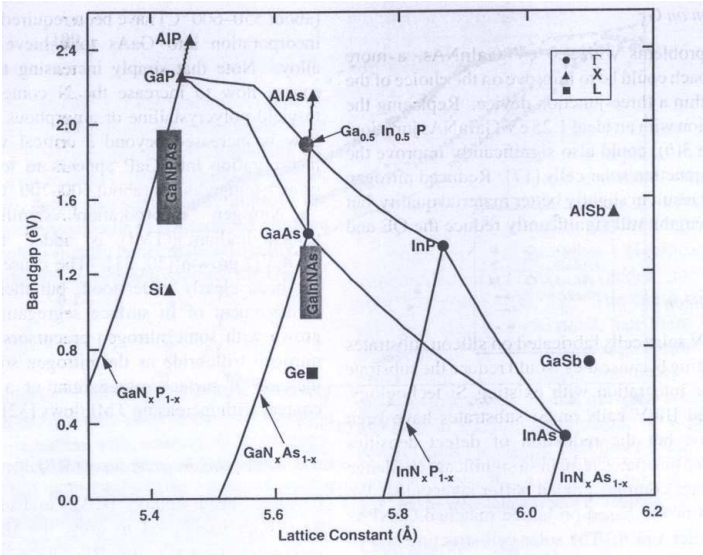

Figure 1.5: From J. F. Geisz and D. J. Friedman (modified) [3]: Band gap as a function of lattice parameter, the boxes indicated III-V nitrides which can be grown lattice matched to Ge and Si.

be so far coupled and lattice matched to 0.7 eV Ge and, on the high energies side, to 1.4 eV GaAs and then to 1.8 eV GaInP obtaining a four junction cell (see Fig. 1.6) with potential efficiency near 40 % at air mass equal zero (AM0 1 sun, spatial applications). Another interesting nitride, 1.7 eV GaNPAs, can be lattice matched to 1.1 eV Si, resulting in a solar cell of great potential interest for integration with the existing and cheaper Si-based technology.

Despite these great expectations for III-V nitrides, at the present the record holding solar cell is a InGaP/GaAs tandem solar cell, which has an AM0 efficiency of about 30 % [12]. In order to understand the problems in building N-based components it is necessary to briefly explain how a solar cell works. In a solar cell the electrons and holes generated by the photons are separated by the field of a p-n junction, the physics proprieties of interest are the optical absorption and the electronic transport proprieties. The absorption coefficient $\mu(E)$ is inversely proportional to the distance within which a photon is likely absorbed, the thickness of the solar cell has to be for this reason larger than $\frac{1}{\mu(E)}$ to collect a relevant fraction of photons and in a sufficiently large energy range. Not only the thickness of the cell, but also the collection length (depletion width plus "diffusion" width) has to be sufficiently large. The most interesting semiconductors for solar cells are so far direct band gap semiconductors : since phonons are not involved

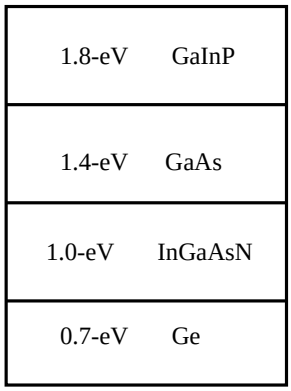

Figure 1.6: Multi-junctions solar cell predicted to give up to 40 % total efficiency.

in this case in the absorption process, this results in a greater $\mu(E)$ which is mandatory for engineering thin-film solar cells.

From the transport proprieties viewpoint the most interesting characteristic is the minority carriers diffusion length. In fact, if an electron-hole couple is created inside the depletion region, the electron and the hole can be immediately separated by the electric field, but also couples created in the free-field region (around the depletion region) where some carriers gradient persists can give a contribution, providing that the diffusion lengths are sufficient to take minority carriers inside the depletion region. This is true in case of high quality semiconductors where the concentration of defects like dislocations or impurities, which can act like traps causing non-radiative recombination of electrons and holes, is very low. If the crystal quality is not optimal and/or the minority carriers diffusion lengths are too short the collection is limited to the depletion region, resulting in a not optimized cell efficiency.

The main trouble associated with $In_xGa_{1-x}As_{1-y}N_y$-based solar cells is given by the relatively low diffusion length of the charge carriers; the origin of that has not been well understood yet, but it is related to a combination of low mobility and short lifetime. In a multi-junction the currents between the different components have to be matched since the lowest current acts like a bottleneck. In order to match the $In_xGa_{1-x}As_{1-y}N_y$ junction current with the others in Fig. 1.6 an internal quantum efficiency of about 100 % would be required for the single $In_xGa_{1-x}As_{1-y}N_y$ component, while at the present only the 70 % has been obtained, due to the poor diffusion length. This is the reason for which nowadays, basing on the performance of the best single-junction $In_xGa_{1-x}As_{1-y}N_y$ solar cell, calculations indicate that the four-junctions one is near the overtaking of the record holding InGaP/GaAs and InGaP/GaAs/Ge, but a real breakdown has not occurred yet. Nevertheless $In_xGa_{1-x}As_{1-y}N_y$ has to be considered the most promising contender among the small-gap components for next generation solar cells, providing to improve in the next future the minority carriers transport proprieties, in part surely limited at the present by the not yet optimal material quality.

1.2 The origin of the giant optical bowing

In this paragraph we list the most important achievements obtained in the last decade on the electronic properties of dilute nitrides. We refer mainly to photoluminescence measurements and theoretical supercell calculations. The former technique, described in section 2.5.3, allows to measure in a semiconductor the energy difference between the top of valence band and the lowest levels near the conduction band minimum; in particular it permits to give an estimation of the band gap, and in some case to measure the energy levels of states that are inside the band gap and arise from defects, impurities or particular atomic arrangements like the nitrogen pairs and clusters which will be described in this section. Calculations are performed by using very large supercells inside which the atomic positions are not obtained via a first-principles approach, but by exploiting a Valence Force Field potential (similar to that described in section 1.5.2); a pseudopotentials approach is used in order to reproduce the electronic levels observed by photoluminescence. Even if the semiconductors described in this paragraph have generally a band gap in the near infrared, in the following we will refer to an increase of the band gap with the term *blue shift* and to a decrease of the same with the term *red shift*.

1.2.1 First observations and theories

Conventional alloys as III-V semiconductors (Al,Ga,In)(As,P) can be grown over the entire composition range and their properties vary smoothly and linearly with composition. Mixed-group V nitrides such as Ga(In,Al)AsN should in principle close the gap between the nitrides and the arsenides, enabling the fabrication of III-V light emitting devices covering the entire visible spectrum. The first obstacle to deal with in order to grow such nitrides was the limited solubility of nitrogen in the host lattice. First investigations were in fact limited to the N doping region ([N]$< 10^{19}$ cm^{-3}). GaP:N isoelectronic doped systems have been exhaustively studied in the impurity limit during the seventies and eighties [13]; for N-doped GaAs only few reports on the optical properties were published [14, 15]. More recently, heavily doped GaAs:N, InGaAs:N, GaP:N and InP:N, with nitrogen concentration reaching few percents, have been grown using novel growth techniques such as metalorganic chemical vapor deposition (MOCVD) and molecular beam epitaxy (MBE) : for such high concentrations these compounds can be described in the framework of alloys [16].

The first Photoluminescence (PL) measurements [17] (see section 2.5.3) performed on $GaAs_{1-y}N_y$ with $y = 0.03$ revealed an intriguing behavior : instead of the expected blue shift, these alloys showed a considerable red shift of the PL peak. This indicated a strongly nonlinear dependence of the band gap on the composition in these alloys; the red shift was observed also for $In_xGa_{1-x}As_{1-y}N_y$ in 1996 [1]. These observations on the one hand precluded the initial idea of covering the entire visible spectrum, by alloying III-V semiconductors with N; on the other hand showed the possibility of building GaAs-lattice matched infrared emitters, whose importance has been enlightened in the previous section.

1.2. The origin of the giant optical bowing

Even by the MBE technique III-V mixed-anion nitrides can be grown only in a narrow composition range near the endpoint constituents (maximum N content about 5%); they exhibit anomalous composition dependent electronic properties. Generally the band gap $E_g(x)$ of a binary $A_{1-x}B_x$ semiconductor alloy deviates from the average gap $\overline{E}_g(x) = (1-x)E_g(A) + xE_g(B)$ of the constituent solids A and B. Both measurements [18] and calculations [19, 20] report that the deviation $\Delta E_g(x) = E_g(x) - \overline{E}_g(x)$ can be well approximated as :

$$\Delta E_g(x) = bx(x-1) \tag{1.1}$$

b is the bowing coefficient, which normally does not depend on composition and is quite small (a fraction of an eV). For ternary alloys, equation 1.1 is still valid with $E_g(A)$ and $E_g(B)$ as the gaps of the constituent binary compounds.

Wei and Zunger [21], via first-principles Density Functional Theory (DFT) calculations in the local density approximation (LDA) (see section 2.5.4) showed that, unlike in conventional III-Vs, in $GaAs_{1-y}N_y$ alloys b is giant and composition dependent (i.e. larger at dilute concentrations). They calculated bowing coefficient of *16 eV* for bulk and *17 eV* for epitaxially strained dilute alloys. These values agree with the experimental determinations of Kondow *et al.* [22] (b=*20 eV* at $x < 1.6\%$) and Weyers *et al.* [17] (b=*14 eV* at $x < 1.5\%$). Wei and Zunger proposed that this anomalous behavior was linked to the localization of the band edge wave functions in the dilute limit, on the As sublattice for the valence band and on the N sublattice for the conduction band. This localization was reported for the first time by Rubio *et al.* [23] and Neugebauer *et al.* [24]; it is due to the large difference of the atomic orbital energies and of the sizes between As and N atoms. Several works [21, 5] discussed the physical origin of the bowing coefficient in $GaAs_{1-y}N_y$, decomposing the high value of b into physically distinct contributions:

1. *Volume deformation*; it represents changes in the band gaps of the constituent GaAs and GaN that are compressed and dilated, respectively, from their natural lattice constants to the average value a(x). This deformation raises the gap of the materials with the larger lattice constant (GaAs) and reduces the band gap of the material with smaller lattice constant. The resulting effect of the two opposite terms on b is negative and quite little (< 1 eV in absolute value).

2. *Charge exchange*; it represents the change in the band gap upon bringing together the constituents, already prepared at a(x), without permitting sublattice relaxation. This terms is proportional to the As-N atomic orbital energy differences and includes charge-transfer effects resulting from band mixing in an ideally unrelaxed lattice.

3. *Structural relaxation*; it represents the change in band gap due to sublattice relaxation if we fix the lattice parameter a(x). This term includes atomic relaxation-induced band mixing. In mixed-cation alloy the major relaxation occurs in the cation sublattice, which couples the cation-localized conduction band states, causing the lowest to move to yet lower energies. In $GaAs_{1-y}N_y$ nitrides this effect is

particularly strong for the quite large cation displacement, due to the large size mismatch between As and N.

In the case of $GaAs_{1-y}N_y$ the two latter terms are positive and much larger than in other mixed anion systems, therefore they control the giant bowing in such alloys.

1.2.2 The anticrossing model

In order to explain these anomalous properties (in particular those of $In_xGa_{1-x}As_{1-y}N_y$) Shan *et al.* [4] proposed in 1999 a simple two levels-model. According to these authors the introduction of N causes a strong interaction between the conduction band and a narrow resonant band formed by nitrogen states; the conduction band edge is formed by extended states, while nitrogen states are localized. The interaction induces a splitting of the conduction band resulting in a reduction of the band gap. The physics of this interaction was modelled simply considering one energy level associated with the extended states of the $In_xGa_{1-x}As$ matrix (E_M) and one level associated with the localized N states (E_N). The interaction was treated within the first order perturbation theory, that leads to the following eigenvalue problem :

$$\begin{bmatrix} E - E_M & V_{MN} \\ V_{MN} & E - E_N \end{bmatrix} = 0 \tag{1.2}$$

V_{MN} is the matrix element describing the interaction and leading to the mixing of these states. Equation 1.2 gives two solutions :

$$E_{\pm} = \frac{E_N + E_M \pm \sqrt{(E_N - E_M)^2 + 4V_{MN}^2}}{2} \tag{1.3}$$

These two solutions indicate a splitting of the conduction band into two sub-bands with the energy minima at E_- and E_+. Such a splitting was observed by Shan *et al.* in photo-modulated reflectance (PR) measurements.

By assuming the insensitivity of E_N to an external pressure and the pressure behavior of the ternary $In_xGa_{1-x}As$ for E_M, they succeeded in very well reproducing the dependence of the band gap on pressure as shown in Fig. 1.7. In absence of interaction the E_M level crosses E_N at 4.4 GPa; as the pressure increases E_- and E_+ first get closer and, in correspondence of the crossing point, repel each other. At higher pressure E_- saturates to the values of E_N and E_+ shows a linear behavior with pressure like E_M. The intensity of the E_+ line in PR measurements increases with respect to E_-, since the former acquires extended character, while the latter takes the localized character of E_N. This two levels approximation is referred to in literature as the *anticrossing model*. At zero pressure the strong repulsion between the two levels causes E_- to move downward for increasing N content (while E_+ moves upwards) originating the giant optical bowing.

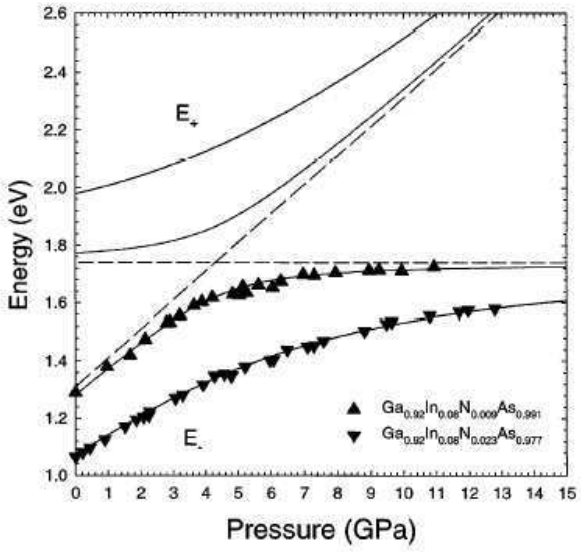

Figure 1.7: From Shan *et al.* (modified) : comparison of the experimental results with model calculations (solid lines) for the band anticrossing in $In_{0.08}Ga_{0.92}As_{0.991}N_{0.009}$ and $In_{0.08}Ga_{0.92}As_{0.977}N_{0.023}$. Dashed lines show the positions of E_M and E_N.

1.2.3 Critics of the anticrossing model

In a detailed band structure calculation Mattila *et al.* [25] heavily criticized the *anticrossing* model, showing how the physics of the giant optical bowing is actually more complex. In the framework of the *anticrossing* model in the *alloy* limit (few % of N) the lowest E_- state is a delocalized state ($a_1(\Gamma_{1c})$-like), while calculations show that it is rather a nitrogen-localized state. Furthermore Shan *et al.* assumed that the nitrogen-induced defect level ($E_N = a_1(N)$), interacting with the $a_1(\Gamma_{1c})$ CBM, originates the anticrossing behavior; actually $a_1(N)$ raises in energy with concentration and, for N content of $\approx 1\%$, it is too high to act as the principal cause of the repulsion.

Anticrossing is instead explained by the breaking of the translation symmetry of the host lattice due the strong perturbation induced by N incorporation. This causes the states near the conduction band minimum Γ_{1c}, L_{1c} and X_{1c} to mix and split into new states. An N substitution at a T_d symmetry site modifies the Γ_{1c} state $a_1(\Gamma_{1c})$, splits the L_{1c} valley into $a_1(L_{1c})$ and $t_2(L_{1c})$ representations and splits the X_{1c} valley into $a_1(X_{1c})$ and $e(X_{1c})$. All the states with a_1 symmetry interact together (also $a_1(N)$ would be in principle allowed to interact) creating the states E_- and E_+. In particular, at 1% of N, E_- derives from a mixing of $a_1(\Gamma_{1c})$ ($\approx 58\%$) and $a_1(L_{1c})$ ($\approx 12\%$) states with a weak contribution from $a_1(X_{1c})$; the $a_1(N)$ level i.e. E_N does not give a direct contribution to the interaction at these concentrations, contrary to what proposed by the *anticrossing* model. The E_- state resulting from this mixing is ≈ 230 meV shifted down in energy for $y = 1\%$, showing that the large band bowing observed at small y is contributed mostly by the conduction band; the shift is due to repulsion from non-a_1

symmetry states. The mixing of a_1-symmetric levels implies also a localization in the real space so explaining the increase in the effective mass of the electron, which is larger for L states. Also the change with pressure in the relative weight of the E_- and E_+ states as observed in PR spectra as well as the saturation of E_- at high pressure is well accounted for by this model.

1.2.4 Polymorphous models : the role of N pairs and clusters

Both the anticrossing model and the calculations of Mattila *et al.* [25] did not considered the role of N pairs and clusters in these alloy. For pair we mean a configuration where a N atom is located as second neighbor of another N (NN1 pair), forth neighbor (NN2), sixth neighbors (NN3), etc. Each configuration, even in a random distribution of atoms, has a non zero probability to occur. For clusters we mean configurations in which two, three, four N atoms are first neighbors of the same cation; even these possibilities become more likely as the N concentration increases. In the *ultra-dilute* regime ($y < 0.01\%$) only localized single impurity levels appear near the band gap (33 meV below CBM in $GaP_1 - yN_y$ and 180 above CBM in $GaAs_1 - yN_y$); at *intermediate* concentrations ($0.05\% < y < 0.1\%$) sharp photoluminescence lines are observed and interpreted as due to the presence of pairs and clusters. In particular the formation of these complexes explains the observed red shift between optical absorption (that involves perturbed host states in the conduction band) and PL emission (that comes from cluster states). Some groups [26, 27] gave a great importance to the role of pairs and clusters in explaining the electronic properties of dilute nitrides. They attributed the red shift of the band gap to the formation of an "impurity" band following the progressive overlap of the different pairs and clusters wave functions (cluster states) with increasing N content. However Kent and Zunger [5] showed that the levels of cluster states (CS) manifest composition pinning i.e. their emission lines remain at a fixed energy at increasing N concentration. This indicates that they don't interact sufficiently each other to create a band and can't justify the giant bowing of the band gap. On the contrary according to Mattila's calculations the conduction band states, perturbed by the symmetry breaking, move downwards for increasing y and sweep in one by one all the pairs levels; when all the CS states disappear into a single broad emission line, the conduction band edge shows a dual nature where localized states coexist with semi-localized and more extended states.

From above we can conclude that the red shift of the band gap is basically due to perturbed host states (PHS) rather than to CS states. As a matter of fact Mattila *et al.* and Kent *et al.* demonstrated that single impurities in GaAs induce the giant bowing, also in absence of pairs. However in order to explain all the electronic properties of these nitrides it is necessary to keep into account both the homogeneous bulk-like features (PHS) and the heterogeneous (CS) behavior in a *polymorphous* model. The formers cause band gap bowing, rigidly shift the conduction band with temperature and pressure and split the conduction band into two sub-bands E_- and E_+; the latter is linked to the formation of localized centers, such as the various nitrogen pairs and clusters, whose levels are in the forbidden gap, and cause the absorption versus emission

Stokes shifts and band tails with asymmetric line shapes.

1.2.5 Supercell approach to a polymorphous model

The most natural approach to a polymorphous model was exploited by Kent and Zunger [5] that used large supercells where one isolated nitrogen atom mimicked the nitrogen impurities and more N atoms randomly distributed simulated clustering. In this way it was possible to take into account at the same time both the symmetry breaking and the formation of N complexes. The use of very large supercells (more than 10^4 atoms) is necessary for very low nitrogen concentrations. Since a first-principles approach like that of the Density Functional Theory (DFT) in the Local Density Approximation (LDA) (see section 2.5.4) is impossible with such large supercells, the authors relaxed atomic positions within the supercell using a Valence Force Field (VFF) potential [28, 29]. The atomic positions obtained in this way agreed with bond lengths and positions extracted by DFT calculations performed on smaller (64-atoms) cells. In order to obtain the electronic properties at the relaxed positions the authors solved the Schrödinger equation

$$[-\frac{1}{2}\nabla^2 + \sum_{\alpha,m} v_\alpha(r - R_{\alpha,m})]\psi_i(r) = \epsilon_i\psi_i(r) \tag{1.4}$$

where α indicates the atomic species, m runs over all atoms, v_α are the screened empirical pseudopotentials and $\mathrm{R}_{\alpha,m}$ is the position of atom m of kind α. As concern the pseudopotentials, they adopted an alternative approach to DFT utilizing in equation 1.4 empirical functions v_α, properly chosen in such a way to reproduce the bulk band structures of the binary alloys GaN, GaAs, GaP at equilibrium, their pressure dependence, band offsets and effective masses.

Equation 1.4 was solved using the linear-scaling folded method [30] which consists on solving for few eigenstates around a specific energy; to have the most important states for the physics of the system it is enough to solve for the conduction and valence band edges. By decomposing the calculated states into the unperturbed Block's states $\phi_{n,k}$ it is possible to determine their Γ, L and X components; and by calculating the distance from each nitrogen site at which 20 % of the amplitude of the eigenstate $\phi_{n,k}$ is enclosed, it is possible to distinguish between localized, quasi-localized and extended states.

1.2.6 Results of polymorphous calculations

These calculations showed that in the N impurity limit the wave functions of the first three levels of the conduction band in GaAs:N exhibit a strong localization (see Fig. 1.8). In the same way Kent and Zunger calculated also the energy levels and wave functions of various pairs and clusters. The energy of pairs is predicted to be lower than that of isolated N impurities and varies non-monotonically with the pair separation. The deepest states are the (110)-oriented pairs (NN1, NN4); these states are predicted

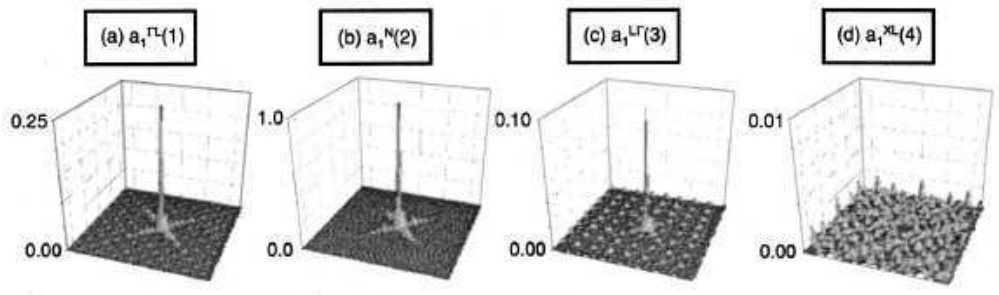

Figure 1.8: From Kent and Zunger (modified) : the squared wave functions of the lowest energy a_1 conduction states of GaAs:N.

to reside into the gap, while other pair states are resonant within the conduction band (see Fig. 1.9).

Moreover, from the calculation of the interaction energy of the different pairs it was possible to show that only the formation of NN2 pairs (100 oriented) is energetically favorable with respect to random statistics, in agreement with the experimental observation of McKay *et al.* [32]; the deep (110)-oriented pairs are less favorable than random statistics while all the other pairs exist randomly. The deepness of the (110)-oriented pairs reflects the fact that when two N substitute As atoms along a (110) oriented zig-zag chain, the replacing of the long Ga-As bond by the short Ga-N one causes adjacent Ga atoms to interact.

Recent experiments on high N-content samples have revealed the presence of deeper levels within the band gap attributed to the formation of N clusters [33, 34]. One kind of these clusters, the N-N-N triplet proposed by Gil and Mariette [31], gives probably origin in the case of $GaP_{1-y}N_y$ to the line historically attributed to the NN2 pair, explaining the big discrepancy between observations and predictions. This structure (Fig. 1.10a) consists of the [110] pair plus a third atom placed at [011], the level of such cluster calculated by Kim and Zunger is 41 meV above the deepest pair level (NN1), in agreement with the experiment. Other examples of nitrogen clustering are given by the Ga-centered tetrahedrons $Ga(As_{4-p}N_p)$ with $0 \leq p \leq 4$ (Fig. 1.10b for $p = 3$). The levels of these clusters become deeper as p increases, consistent with the fact that the conduction band minimum of GaN is lower than that of GaAs. Extended [110]-oriented chains of increasing length (a three atom chain is reported in Fig. 1.10c) are further deeper in energy as shown in Fig. 1.11 and can explain the long "low-energy tail" observed at the conduction-band edge of samples with an high nitrogen content [35, 36, 26].

It is worth noting that, even if these calculations reproduce the overall trend of observations (the isolated impurity is shallower, the pairs deeper, the clusters even deeper), in some case the complexity of the physics and the limit of the calculations (for example the lack of many body corrections) don't allow to definitely assign all the levels to a particular N pair or cluster; moreover quantitative discrepancies exist

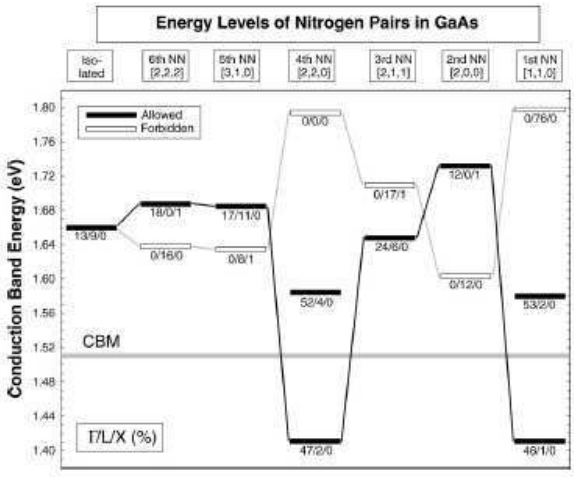

Figure 1.9: From Kent and Zunger (modified) : the energy levels of isolated N and N-N pairs in GaAs, together with the pair name the orientation with respect to one nitrogen at the origin is reported.

between calculations and experiments. However the knowledge we have at the present of the electronic properties of such materials allowed to clarify the actual origin of the giant optical bowing (that does not reside in the pairs) and to interpret several features of the photoluminescence spectra of these alloys on the whole concentration range, whose origin is mainly due to the presence of N pairs and clusters.

1.2.7 Summary : the transition from localized to delocalized states

In order to summarize the theory of electronic structure in $(In_x)Ga_{1-x}As_{1-y}N_y$ we can distinguish three concentration regimes. At very low concentration (*impurity limit*) we have very localized sharp emitting clusters states inside the band gap and quasi-localized states near the CBM. For increasing y the conduction band minimum moves

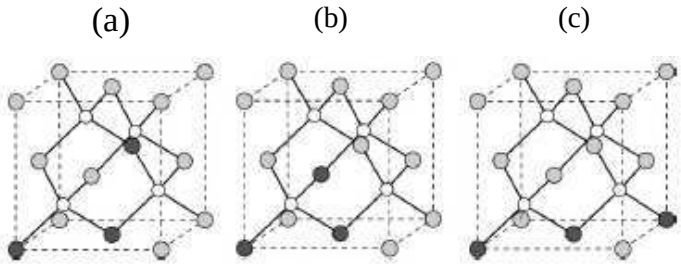

Figure 1.10: Nitrogen triplets : a) Gil and Mariette's triplet[31]; b) $GaAsN_3$ cluster i.e. three nitrogen around a single Ga atom; c) (110)-oriented triplet.

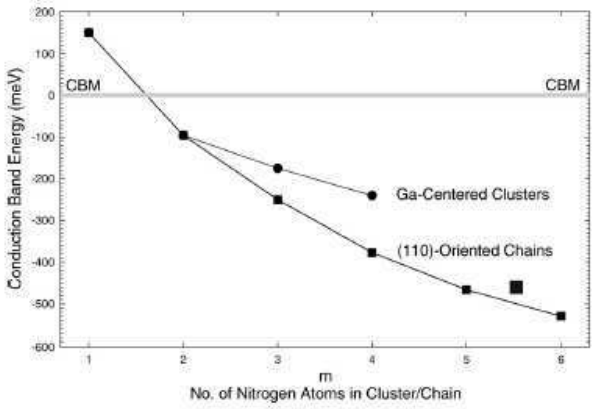

Figure 1.11: From Kent and Zunger (modified) : energy levels of Ga-centered nitrogen clusters and (110)-directed nitrogen chains in GaAs, calculated in a 4096 atom cell.

towards lower energies because of the increasing repulsion among N-perturbed host states. By increasing the N content we reach a concentration limit y_c ($\approx 0.6\%$ for $GaAs_{1-y}N_y$) at which the CBM sweeps in all the CS levels. These states have not sufficiently extended wave functions to overlap and create a band, so we are in an amalgamation of localized and quasi-localized states near the CBM. This limit ($y \approx y_c$), at which the localized to delocalized transition begins [37], has been referred to as *amalgamation limit*.

As the concentration increases again CBM states progressively acquire delocalized (Bloch-like) character, with the CS swept deeper into the continuum. The alloys investigated in this thesis have concentrations between 0.8 % and 5 %, so in the range between the *amalgamation* region and the third regime, the *high concentration* limit, characterized by $y >> y_c$. As a consequence in our samples cluster states in the band gap should not be present. High concentrations are the most interesting from the viewpoint of applications, unluckily up to now not reached by state of art growth techniques because of phase separation and precipitation of N compounds. However if we could move inside the third regime saving a random distribution of N atoms, a continued large downward bowing of the band gap is foreseen by theoretical calculations, with the gap completely closed at y $\approx$ 50 % for $GaAs_{1-y}N_y$ and at y $\approx$ 12% for $In_xGa_{1-x}As_{1-y}N_y$ [38].

1.3 The effects of hydrogenation

Hydrogen is a common impurity in semiconductors being its incorporation likely in state of art growth techniques as metal organic chemical vapor deposition [39] or (to a minor extend) gas-source molecular beam epitaxy [40, 41]. Because of its high chemical reactivity, hydrogen dramatically affects the electronic properties of semiconductors [42]: it can neutralize dangling bonds in the lattice wiping out non-radiative recom-

bination centers, shallow impurities and deep defect levels from the gap of crystalline materials. In carbon-doped Gallium arsenide, for example, hydrogen strongly interacts with carbon and passivates its electrical activity, both in the donor and acceptor case, by forming stable H-C complexes [43].

1.3.1 Interaction with isoelectronic impurities

More complicate and not entirely known is the interaction of hydrogen with isovalent impurities, like substitutional N in $GaAs_{1-y}N_y$ and $In_xGa_{1-x}As_{1-y}N_y$ alloys. Recent experiments [40, 41] have shown that hydrogen incorporation increases with N concentration. Xin *et al.* suggested that H acts like an isolated donor in as grown $In_xGa_{1-x}As_{1-y}N_y$ making these alloys slightly n-type and compensating the p-doping due to the presence of Be and Si impurities. This is different from the role of H in usual semiconductors, since it doesn't act as a passivation agent, but as a doping source itself. Annealing reduces the hydrogen concentration and renders the samples (Si or Be doped) p-type. Baldassarri *et al.* [44] observed via photoluminescence measurements (section 2.5.3) that post-growth hydrogenation of $In_xGa_{1-x}As_{1-y}N_y$ quantum wells revers the huge band gap reduction caused by the incorporation of nitrogen. They attributed this effect to the formation of some unidentified N-H compound. Thermal annealing at 550° for one hour removes the hydrogenation effect and restore the band gap of as-deposited $In_xGa_{1-x}As_{1-y}N_y$ samples.

Very recently three different groups [7, 6, 45] studied the formation of N-H complexes in $GaAs_{1-y}N_y$ via first-principles total energy calculations using the density functional theory [46, 47] in the local density approximation [48, 49]; they reported interesting results concerning the single and two hydrogen-configurations that minimize the formation energy.

1.3.2 Monohydride complexes

As for monoatomic hydrogen Janotti *et al.* [7] and Amore Bonapasta *et al.* [6] studied the donor (+), neutral (0) and acceptor (-) charge states in the different monohydride configurations: the bond center site next to N (BC_N) and far away from N (BC_{As}), the N and Ga antibonding sites (AB_N and AB_{Ga}) and tetrahedral interstitial sites. In the BC_N site (Fig. 1.12a) H occupies a position between N and the Ga atom whose bond has been broken following the introduction of hydrogen. In the AB_N site (Fig. 1.12b) H is located on the same direction of this bond, close to N, but in the opposite verse. Janotti *et al.* calculated that the BC_N is the lowest energy configuration site for all charge states. We reported the calculated formation energy for each charge state as a function of the Fermi energy in Fig. 1.13. The formation energy of BC_N^+ is always the lowest one and crosses that of BC_N^- only beyond the CBM (i.e. where we don't deal with a semiconductor any more); this implies that monoatomic H in $GaAs_{1-y}N_y$ acts only as a donor. That contrasts with the case of the parent compounds GaAs and GaN, where H is an amphoteric impurity and it is positively charged in p-type samples and negatively charged in n-type samples [50, 51]. The peculiar behavior of $GaAs_{1-y}N_y$

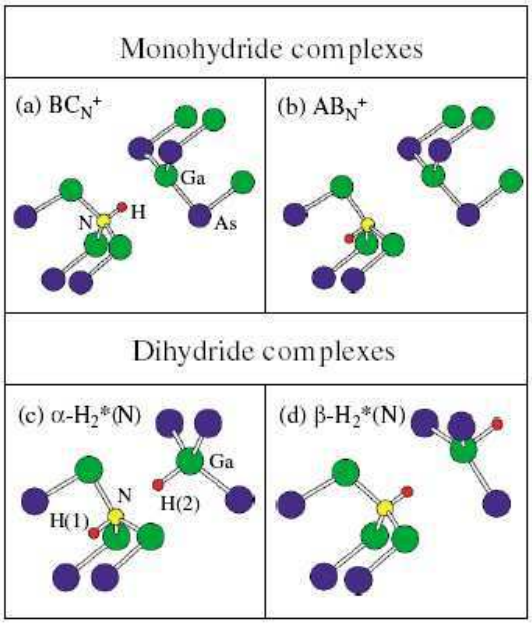

Figure 1.12: From Janotti *et al.* (modified) : models for H-N complexes in $GaAs_{1-y}N_y$, configurations involving one hydrogen {(a) and (b)} and two hydrogens {(c) and (d)}.

is related to the red shift of the band gap due the giant optical bowing described in section 1.2; the interaction between the lowest conduction band states, perturbed by N incorporation, lowers in fact the energy level of CBM below the H (+/-) level. In the case of $In_xGa_{1-x}As_{1-y}N_y$ the presence of Indium further decreases the CBM so that, even in this case, H can be only positive charged.

Having acquired that H is positive charged, let us understand why the BC_N^+ configuration is the most stable. In this configuration, characterized by an online Ga-H-N geometry, Ga and N relax outward with displacement of 0.63 and 0.45 Å with respect to the positions they have in absence of H (according to Amore Bonapasta *et al.*); H binds to the N atom with a H-N bond length of 1.06 Å, while the Ga-H distance is 2.43 Å. These values have to be compared with the sum of the atomic covalent radii which are 1.07 Å and 1.58 Å respectively. That suggests the formation of a strong N-H bond and of a very weak H-Ga interaction. Also in the positive charged AB_N^+ configuration the H atom strongly binds to the N atom (bond length of 1.05 Å according to Janotti *et al.*); however this configuration has a formation energy 0.37 eV higher than BC_N^+, because the charge density of the host at the BC_N^+ site is higher than that at the AB_N^+ site.

In fact, the proton H^+ tends to locate in sites where electron density is higher i.e. where its Coulomb binding energy is larger. For this reason in classical semiconductors like Si or GaAs bond center (BC) sites are favored for H^+ : due to the strong covalent

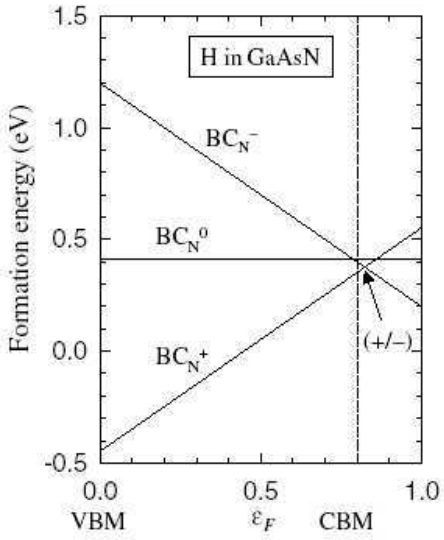

Figure 1.13: From Janotti *et al.* : Formation energy of monoatomic H in $GaAs_{1-y}N_y$ as a function of the Fermi energy ε_F for all charge states; the vertical dashed line indicates the calculated band gap of GaAs.

character of the bond, charge density has in fact a maximum near the bond center. On the contrary in GaN the bond is ionic and charge is spherically localized around the N atom; in this case the AB_N^+ site is preferred, in fact in the BC position an additional energy is needed to relax the Ga and N atoms outward [50]. In $GaAs_{1-y}N_y$ the Ga-N bond is longer, the BC site is less strained and becomes preferred.

1.3.3 Dihydride complexes

Both experimental works and theoretical calculations suggest that charged monoatomic H-complexes cannot explain all the hydrogenation physics in $GaAs_{1-y}N_y$ and $In_xGa_{1-x}As_{1-y}N_y$. Xin *et al.* [41, 40] measured the total H concentration and the free electron concentration in *n*-doped $In_xGa_{1-x}As_{1-y}N_y$ showing that the first is higher : hydrogen is present also in inactive states such as interstitial H_2 molecules and/or H_2^* complexes. Furthermore first-principles calculations [7, 6] show that formation of $H(BC_N^+)$ has only a minor effect on the optical properties and in particular does not explain the reopening of the band gap upon post-growth hydrogenation observed by Baldassarri *et al.* [44] and by Polimeni *et al.* [52]. The reopening is on the other hand explained by the formation of H_2^* complexes; these involve two hydrogen atoms adjacent to a dopant or an isoelectronic impurity. The formation of H_2^* complexes have been firstly proposed by Chang and Chadi for hydrogen incorporation in crystalline Si [53, 54].

In the case of $GaAs_{1-y}N_y$ Janotti *et al.* have calculated the formation energies for different kinds of $H_2^*(N)$, with hydrogen atoms adjacent to nitrogen. The α-$H_2^*(N)$

reported in Fig. 1.12c has the lowest formation energy; in this complex one H atom (H(1)) is at the N antibonding site, with a H-N bond length of 1.05 Å; the second H atom (H(2)) is at the bond-center site with a Ga-H bond length of 1.54 Å. No chemical bond is formed between this latter H atom and N (the N-H separation is 2.06 Å vs. 1.07 Å expected from their respective ionic radii). The β-H_2^*(N) complex of Fig. 1.12d has a slightly higher formation energy. Contrary to what happens in GaAs, α-H_2^*(N) is also strongly energetically favored with respect to the formation of an interstitial H_2 molecule.

The preference for the H(BC_N^+) or the α-H_2^*(N) configuration depends on the Fermi energy. We have showed in Fig. 1.13 that the formation energy of H(BC_N^+) increases

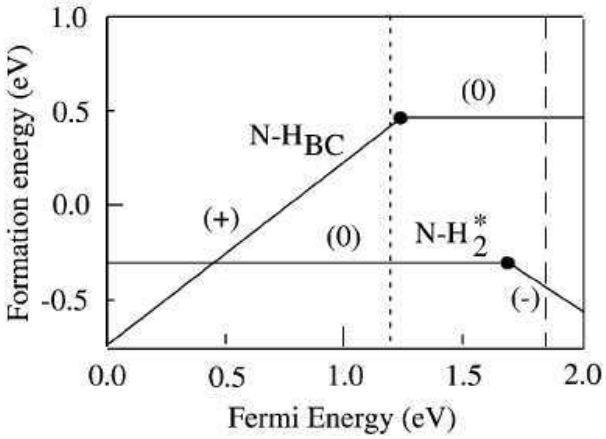

Figure 1.14: From Amore Bonapasta *et al.* (modified) : Formation energy as a function of Fermi energy for the monoatomic hydrogen complex H(BC_N^+) and for the diatomic hydrogen complex α-H_2^*(N), vertical dashed lines correspond roughly to the band gap of $GaAs_{0.97}N_{0.03}$ and GaAs.

with the Fermi energy (E_F); on the contrary the formation energy of α-H_2^*(N) is sensibly steadier (Fig. 1.14) and crosses that of H(BC_N^+) at about $E_F = 0.5$ eV. Doping favors the formation of H(BC_N^+) in p-type and of α-H_2^*(N) in n-type materials; the two complexes may coexist in semi-intrinsic $GaAs_{1-y}N_y$. Actually Amore Bonapasta *et al.* [6] predicted the coexistence of the two complexes also in p-type semiconductors since the formation of H(BC_N^+) is accompanied by the H passivation of shallow acceptors that raises the Fermi level, favoring the formation of α-H_2^*(N). The relative concentration $[H^+]/[H]$ is calculated to decrease with [H] while $[H_2^*]/[H]$ increases, the Fermi energy itself increases with [H] so that neutral self-compensated H_2^*(N) complexes appear to be energetically more favorable at higher hydrogen concentrations.

1.3.4 Effects on the band gap

As already envisaged before, H_2^*(N) complexes explain the complete reversal of the red shift of the band gap induced by N addition: the H_2^*(N) formation can push the

CBM of $GaAs_{1-y}N_y$ back to that of GaAs. The different effects of the $H(BC_N^+)$ and $H_2^*(N)$ complexes on the optical bowing can be explained as follows. In the case of $H(BC_N^+)$ the H^+ ion takes the place of the Ga atom no longer bonded to the N atom that still keeps its five electrons to form four chemical bonds; so the insertion of H doesn't affect so much the unoccupied molecular orbitals distribution, characterized by a strong localization around N. In the case of $H_2^*(N)$ a new unoccupied level appears near the top of the valence band, due to the formation of Ga-H and N-H bonds. This leads to a quite different N bonding where orbitals geometry around N is not conserved and where the N-H bond is not perturbed any more by the dangling bond of Ga, now saturated by the second H atom. The mechanism by which $H_2^*(N)$ formation reopens the band gap has been schematized by Janotti *et al.* with a three-step process (Fig. 1.15).

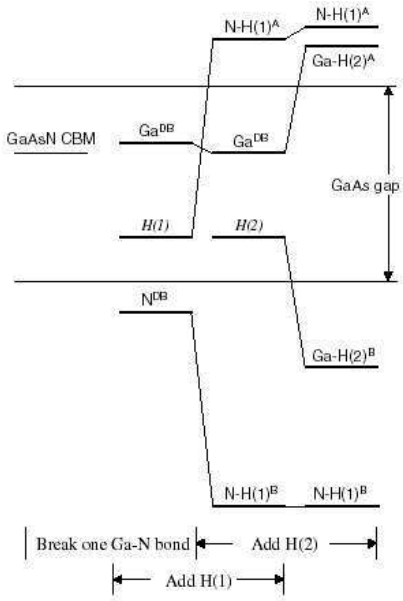

Figure 1.15: From Janotti *et al.* (modified) : Schematic three step-process of the effect of α-$H_2^*(N)$ complexes on the band gap of $GaAs_{1-y}N_y$.

First the bonding of hydrogen to N leads to a large atomic displacement along the [111] direction, breaking one of the Ga-N bonds. This eliminates one of the N-induced $GaAs_{1-y}N_y$ CBM states and creates a N dangling bond (DB) state in the valence band and a Ga DB state near the CBM. Secondly, the binding of H(1) to the N-DB state creates a N-$H(1)^B$ bonding state deep in the valence band and a N-$H(1)^A$ antibonding state in the GaAs conduction band. Third, the binding of H(2) to the Ga-DB state creates a bonding Ga-$H(2)^B$ state below the GaAs VBM and an antibonding Ga-$H(2)^A$ state inside the conduction band of GaAs. In conclusion one $GaAs_{1-y}N_y$ CBM state is completely removed by the formation of a $H_2^*(N)$ complex and the band gap of GaAs is restored.

In conclusion for what concerns the interaction of hydrogen with isoelectronic impurities and the particular case of $GaAs_{1-y}N_y$, hydrogen neutralizes the N effect as it does also in case of defects and shallow acceptors; the passivation process is on the other hand unusual and involves the formation of dihydride complexes. The same has been predicted by the groups cited above also for $In_xGa_{1-x}As_{1-y}N_y$.

1.4 The short range ordering

Spontaneous ordering and preferential bonding are well known phenomena in materials science and in particular in semiconductors and occur mostly when the sizes of the atomic constituents of an alloy are rather different one from the other. Short range ordering (SRO) may occur during the epitaxial growth [55] and in some case is predicted to persist up to very high temperatures, close to the alloy melting point [56]. The main interest in studying SRO in semiconductors is due to the fact that ordering phenomena affect the electronics properties, therefore their understanding is mandatory in order to realize efficient optoelectronic components.

1.4.1 Ternary alloys : clustering and anticlustering

In a ternary alloy of the type $A_yB_{1-y}C$ for SRO we mean that the probability of finding a second A (let's suppose it is a cation) in the first, second, n-cationic neighbors shell of a central atom A is different from the random one (given by the stoichiometry). Bellaiche and Zunger [8] studied this kind of ordering in GaAsN, GaInN and GaInAs via large supercells calculations; they used a set of *Cowley's* parameters to define SRO :

$$\alpha_j(y) = 1 - \frac{P(j)}{y} \tag{1.5}$$

In the case of $GaAs_{1-y}N_y$, for example, P(j) is the probability of finding a nitrogen atom as jth nearest neighbor of an arsenic atom in the mixed anion sublattice. $\alpha_j > 0$ corresponds to an association of like atoms (e.g. clustering), while $\alpha_j < 0$ corresponds to an association of unlike atoms (e.g., anticlustering). In the case of the perfect random alloy $\alpha_j \equiv 0$ for all j's.

By calculating the difference in strain energy due to the formation of the different kind of pairs of impurities, Bellaiche and Zunger found out that the incorporation of NN1 and NN4 pairs increases the strain energy with respect to the random case (approximated, at the dilute limit, by the non-existence of pairs) while the formation of NN2 and NN3 lowers the strain energy of the supercell and in particular the NN2 pair is the most favorable. If the impurities are placed in strain energy-minimizing positions an increase in the band gap occurs with respect to the random alloy, while if they are placed in strain-energy raising positions the gap is reduced : the difference in the bowing coefficient with respect to the random case is as large as 1.5 eV for N-N pairs in GaAs.

Let's now focus on the first *Cowley's* coefficient α_1. It is a general characteristic of zincblende semiconductors that the strain energy increases with α_1 (see Fig. 1.16) i.e. at the equilibrium these alloys adopt anticlustering.

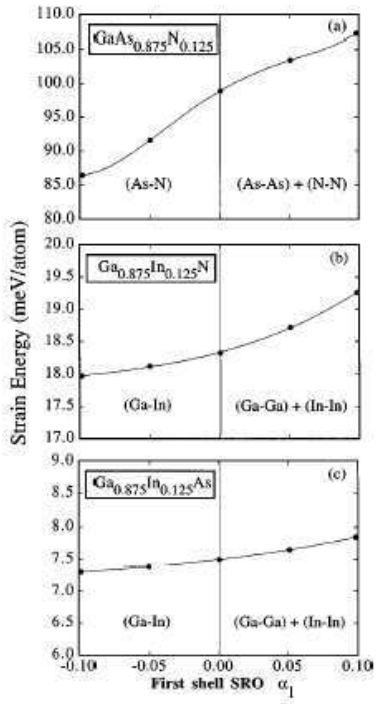

Figure 1.16: From Bellaiche and Zunger (modified) : dependence of the strain energy on α_1 for (a) $GaAs_{0.875}N_{0.125}$, (b) $Ga_{0.875}In_{0.125}N$ and (c) $Ga_{0.875}In_{0.125}As$. The parameters α_i, with $i \geq 2$ are set to their random values (i.e. zero).

On the other hand, in samples grown out of equilibrium (as happens for example by the MBE technique) clustering rather than anticlustering has been observed, especially for relative high N content samples [57, 58]. The increase in strain energy with α_1 is proportional to the lattice mismatch of the bulk constituents of the alloys. In $GaAs_{0.875}N_{0.125}$, which is 20% lattice mismatched, the difference in strain energy is 20 meV/atom when α_1 varies from -0.10 to 0.10. In $Ga_{0.875}In_{0.125}N$, which is 10 % lattice mismatched, the change in the strain energy is 1.3 meV/atom and it is only 0.5 meV/atom in the 7 % lattice mismatched $Ga_{0.875}In_{0.125}As$.

As shown in Fig. 1.17, in zincblend semiconductors anticlustering leads to an increase of the band gap, while clustering decreases the band gap with respect to a random alloy. In nitride alloys the optical bowing is particularly sensitive to the short range ordering; in the case of $GaAs_{0.875}N_{0.125}$ a variation of α_1 from -0.10 to 0.10 decreases the band gap of 122 meV, while in $Ga_{0.875}In_{0.125}As$ the reduction is only 6 meV. This is basically due to the fact that $GaAs_{1-y}N_y$ has localized band edge states, conduction band minimum is localized on the N atoms and valence band maximum on

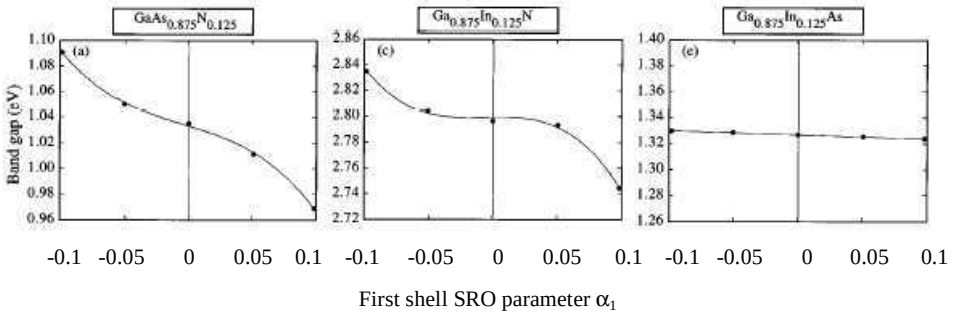

Figure 1.17: From Bellaiche and Zunger (modified) : dependence of the band gap on α_1 for (a) $GaAs_{0.875}N_{0.125}$, (b) $Ga_{0.875}In_{0.125}N$ and (c) $Ga_{0.875}In_{0.125}As$.

the As atoms, so the energy levels of these states are strongly influenced by the local configuration around N and As atoms, respectively. On the other hand, in $Ga_{1-x}In_{\ x}As$ band edge states are extended and therefore less sensitive to the local configuration and order.

1.4.2 Quaternary alloys : bond distribution

In quaternary alloys short range ordering has a different meaning : in fact, in a ternary alloy the number of bonds of each kind is fixed by the composition; on the contrary in a quaternary alloy it can vary. For example let us consider the theoretical case of a $In_{0.5}Ga_{0.5}As_{0.5}N_{0.5}$ alloy; the bonds distribution has two limits, one in which the material can be thought as an InAs + GaN (with no In-N bonds), the other corresponding to a InN + GaAs configuration (with no Ga-N bonds). In principle the system can assume any configuration between these two limits showing a partial degree of order, which can be described by introducing a short range order parameter. As pointed out by Saitta *et al.* in $Zn_xMg_{1-x}S_ySe_{1-y}$ some configurations may be unstable; Fig. 1.18 shows on a *x-y* diagram how the forbidden regions evolve as a function of the temperature for this compound. SRO in quaternary alloys generally refers to the relative number of bonds of each type rather than to the clustering and anticlustering effects. Of course the two concepts are linked since the presence of a preferential bonding between two elements reflects into an increasing probability for clustering.

The issue of short range ordering and its effects on the electronics properties in $In_xGa_{1-x}As_{1-y}N_y$ was recently addressed by Kim and Zunger [9]. On the basis of a previous work [59], they introduced a SRO parameter ξ to describe the distribution of bonds :

$$\xi = n_{In-N}/M - xy \tag{1.6}$$

where n_{In-N} is the number of nearest-neighbors bonds involving In and N atoms, and M is the total number of bonds in the alloy. In a perfect random alloy $\xi = 0$; $\xi > 0$ means that In-N (and Ga-As) bonds are favored with respect to the random case, while

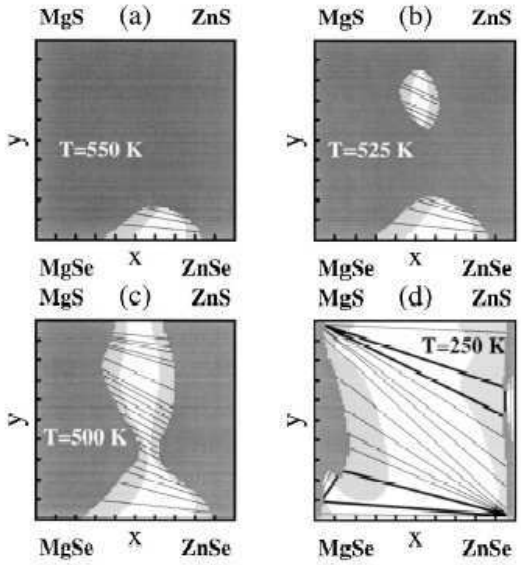

Figure 1.18: From Saitta *et al.* (modified) : Phase diagram of $Zn_xMg_{1-x}S_ySe_{1-y}$ at four different temperatures. The dark gray (binodal) regions are thermodynamically stable, the light gray (spinodal) regions are only locally stable, the white regions are completely unstable.

$\xi < 0$ indicates a prevalence of In-As (and Ga-N) bonds . ξ (x,y,T) is a function of composition and temperature and can be calculated by minimizing the total free energy. Two terms contribute to the total energy : the bond (chemical) energy and the strain energy. In the binary zincblende solids the chemical term follows this sequence : GaN > InN > GaAs > InAs (respectively 2.24, 1.93, 1.63 and 1.55 eV per bond), so the Ga-N + In-As configuration is preferred in terms of bond energy. On the other hand Ga and N atoms are smaller, respectively, than In and As; therefore the "small atom - large atom" configuration In-N + Ga-As is better lattice matched and favored in terms of strain.

Kim and Zunger applied a finite temperature Monte Carlo method to an energy functional describing the strain plus chemical energy of $In_xGa_{1-x}As_{1-y}N_y$ for any configuration. The functional depends both on site occupancy variables S_c and S_a and on the atomic positions R_i of all the M atoms in the supercell:

$$E[\{S_c; S_a\}; \{R_i, i = 1, ..., M\}] = E_{chem} + E_{strain} \tag{1.7}$$

$S_c = 1$ (-1) if Ga (In) is on the cation site c, and $S_a = 1$ (-1) if As (N) is on the anion site a; for the chemical energy they used the expression :

$$E_{chem} = \frac{1}{2} \sum_{i}^{n} \sum_{j}^{n} n_{i-j} e_{ij} \tag{1.8}$$

where n_{i-j} is the number of bonds of type ij and e_{ij} is the energy of that bond (the authors used the experimental cohesive energy of the binary ij compound [60]). For the strain energy the classical Valence Force Field (VFF) formulation (section 1.5.2) was exploited, introducing appropriate bond-stretching and bond-bending force constants [29, 61].

As shown in Fig. 1.19a at zero temperature the free energy of the strain-minimizing configuration In-N + Ga-As is much lower than that of the highly strained, but chemical favored Ga-N + In-As. The opposite situation is true if the coherence condition is removed i.e. if the *in plane* lattice parameter of the $In_xGa_{1-x}As_{1-y}N_y$ epilayer is not forced to assume the value of the lattice parameter of the substrate (GaAs), so that $E_{strain} = 0$. In Fig. 1.19 the authors considered alloys whose concentrations allow to lattice match the GaAs substrate, this constraint is traduced into a relationship between x and y.

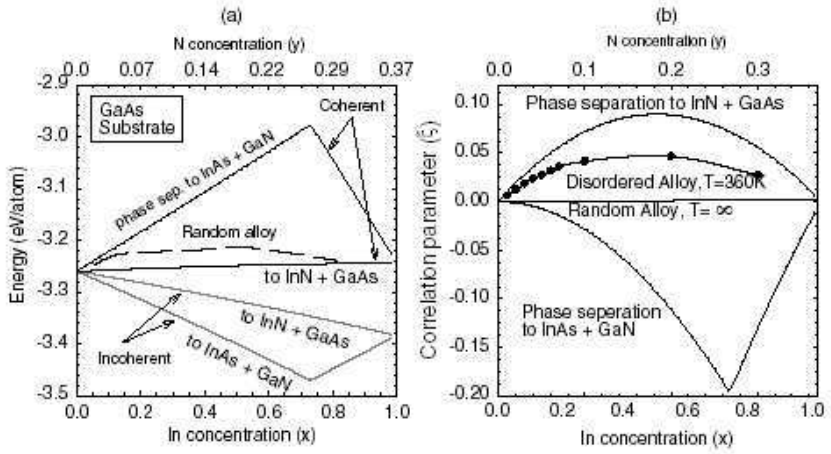

Figure 1.19: From Kim and Zunger (modified) : (a) The energies of some limiting thermodynamic states of InGaAsN lattice matched to GaAs at T = 0; (b) The SRO parameters ξ for the two limit cases of phase separation into InAs + GaN and InN + GaAs, for a random alloy and for an alloy with SRO (positive) calculated at 360 K.

At finite temperature the calculated ξ is positive, i.e. the In-N + Ga-As configuration is still preferred. ξ is about 0.013 and 0.004 for $x = 0.06$, $y = 0.02$ at $360K$ and $1200K$ respectively and 0.042 and 0.031 for $x = 0.25$, $y = 0.09$ at $360K$ and $1200K$ respectively. Fig. 1.19b reports the results at $360K$, together with the calculated behavior for the two opposite limit configurations, here referred to as "phase separation" [1]. As it can be seen in Fig. 1.19b the short range order in the simulated system is quite strong, the calculated points are fitted by a curve that situates, roughly, at the middle

[1] In the following we prefer using the term "maximum ordering" in case of an alloy of composition different from $x, y = 0.5$ since in the samples analyzed in our work we experimentally exclude the hypothesis of an actual phase separation into two distinct crystallographic phases and just look for preferred atomic arrangements.

between the random and the In-N + Ga-As maximum ordering trends.

The main characteristic of this short range ordering is an increased concentration of N-centered In_3Ga_1 clusters with respect to the random case, while the concentration of In_0Ga_4 clusters is lower (Fig. 1.20) than the random one. Also, the first neighbor N-N pairs (NN1) are depleted while NN3 are enhanced.

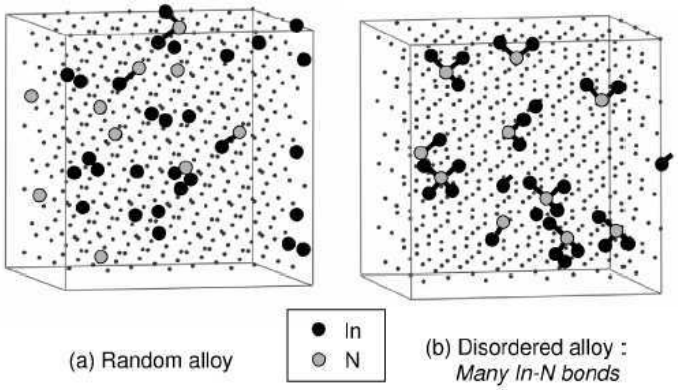

Figure 1.20: From Kim and Zunger (modified) : Visualization of the real space supercell of an InGaAsN alloy for (a) a random configuration and (b) with SRO determined by MC simulation at T = 360 K. In the latter case is evident the preponderance of N-In_3Ga_1 clusters.

The SRO parameter of Equation 1.6 can be written in a different notation [62], more useful for our purpose. Let us introduce the quantity y_{In-N} given by the In-N relative coordination number divided by four; it estimates the probability for a single In-nearest neighbor site to host a N atom ($1 - y_{In-N}$ for an As atom). In terms of y_{In-N}, ξ becomes :

$$\xi = x(y_{In-N} - y) \tag{1.9}$$

The relative coordination of In atoms around N can be calculated from y_{In-N} as:

$$x_{N-In} = \frac{x\ y_{In-N}}{y} \tag{1.10}$$

If y is smaller than x, as it is the case in all the alloys studies in this thesis, the maximum ordering values for y_{In-N} compatible with a given concentration can be extracted by imposing $x_{N-In} = 1$. The SRO parameter calculated by Kim and Zunger for the composition $x = 0.06$, $y = 0.02$ at $360K$ corresponds in our notation to $y_{In-N} = 0.24$ and $x_{N-In} = 0.71$; for these concentrations the maximum ordering value of y_{In-N} is 0.33, the random value is, trivially, 0.02 [2].

[2]Another definition for SRO one can find in literature, and frequently used in case of disordered system, is that given by Cargill and Spaepen [63]; in our case where each atom is four coordinate we

Now let's focus on the effect of SRO on the electronic properties of $In_xGa_{1-x}As_{1-y}N_y$. By applying a plane-wave pseudopotential calculation to the supercell with the SRO obtained by Monte Carlo simulations, Kim and Zunger found out that the $In_xGa_{1-x}As_{1-y}N_y$ band gap increases by ~ 100 meV relative to the random alloy. That is due to the increased statistical presence of N-centered In_3Ga_1 clusters with respect to In_0Ga_4 clusters. The formers result in higher energy L-like levels which interact less with the conduction band minimum states leading to a diminished downward repulsion of the conduction band minimum and to a diminished optical bowing compared to the random case (Fig. 1.21).

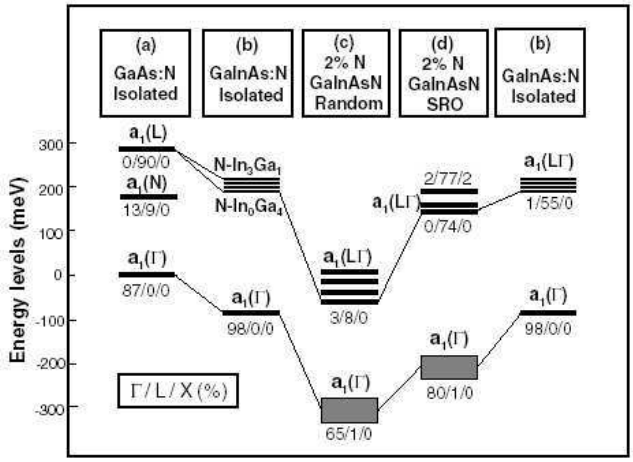

Figure 1.21: From Kim and Zunger (modified) : Energy levels with $\Gamma\backslash L\backslash X$ percentages calculated for (a) isolated N in GaAs, (b) isolated N-In_mGa_{4-m} clusters, (c) random alloy with y = 0.02, x = 0.06 and (d) SRO alloy with the same concentration; shaded areas denote band tails.

Quaternary alloys are interesting mainly because it is possible to independently tune the band gap and the lattice constant varying the composition; it is worth noting that SRO is an important parameter to control the electronic properties and the SRO parameter ξ can be changed by varying the growth conditions.

---

can write :

$$\Gamma_{In-N} = \frac{y_{In-N} - y}{y} \tag{1.11}$$

This parameter, differently from the former of equation 1.6, is normalized by the random In-N relative coordination; in the following we will not refer any more to the Cargill's definition, preferring the Kim's more recent one.

1.5 What about information on the structure ?

1.5.1 Lack of structural information for $GaAs_{1-y}N_y$ and $In_xGa_{1-x}As_{1-y}N_y$

Despite the number of theoretical and experimental studies on the electronic properties of III-V nitrides few works have been made on the global and local structure of $GaAs_{1-y}N_y$ and $In_xGa_{1-x}As_{1-y}N_y$ and many questions are still open. For example there is no clear evidence on the exact location of N inside the lattice, i.e. if it substitutes As in the anion sublattice of the zincblend cell or not. The poor PL intensity of the as grown samples and its increase upon rapid thermal annealing has been attributed to the formation of N-related non radiative defects. Some groups identified these defects with the presence of isolated N-interstitials [64], others proposed the formation N-As and N-N split interstitial complexes [65] (illustrated later in Fig. 3.6). Concerning the long range order structure of these alloys, Neugebauer and Van de Walle [24], on the basis of the Density Functional Theory (section 2.5.4), predicted that Vegard's rule is valid for lattice parameters; nevertheless remarkable deviations from this law were observed by different groups and explained in terms of formation of N-related defects [65, 66]. Another phenomenon which makes the situation more puzzling is the blueshift of the PL line observed systematically upon annealing, which has been attributed either to the diffusion of nitrogen out of the sample [64] or to the removal of potential fluctuations linked to the non-homogeneous concentration of N in the epilayer plane [67].

As regards hydrogenated samples nothing is known about the effect of the formation of monohydride and dihydride complexes on the lattice parameter i.e. if the passivation of the optical properties related to N doping is followed or not by a relaxation of the lattice upon hydrogenation. Stutzmann *et al.* [68] found out that in boron-doped silicon (a completely different system) the formation of H-N complexes leads to a relaxation of the lattice, something similar could be envisaged to happen in the case of $GaAs_{1-y}N_y$, where the formation of H_2^* complexes (section 1.3.3) implicates the breaking of the Ga-N bond and a following increase of the Ga-N distance. No XRD investigation of a possible lattice relaxation induced by H on $GaAs_{1-y}N_y$ and $In_xGa_{1-x}As_{1-y}N_y$ was available in literature before this thesis work, no investigation was as well performed on the effects on the structure of H removal by soft annealing .

Concerning the local structure at the beginning of this work even less was known in literature. An unique experimental work [69] reported XAS measurements (see section 2.2) at the In and N K-egdes; the quality of data was not sufficient to make the measurements sensitive to the weak In-N coordination and In-As bond-lengths were not distinguishable from those of $In_xGa_{1-x}As$. Moreover as concerns the Ga-As bond length no experimental determination has been ever performed both for $GaAs_{1-y}N_y$ and for $In_xGa_{1-x}As_{1-y}N_y$.

A theoretical study of the composition dependence of the Ga-As and Ga-N bond lengths was undertaken by Bellaiche *et al.* [70] via supercell calculations, exploiting a Valence Force Field potential [28] (see section 1.5.2) in order to relax the atomic posi-

tions inside the cell. These authors found an anomalous behavior near the percolation thresholds (see Fig. 1.22) i.e. the concentrations at which a continuous wall to wall chain of given bonds (for example Ga-N-Ga-N...) first forms in the cell of $GaAs_{1-y}N_y$. However even with state of art growth technique it is nowadays possible to insert only

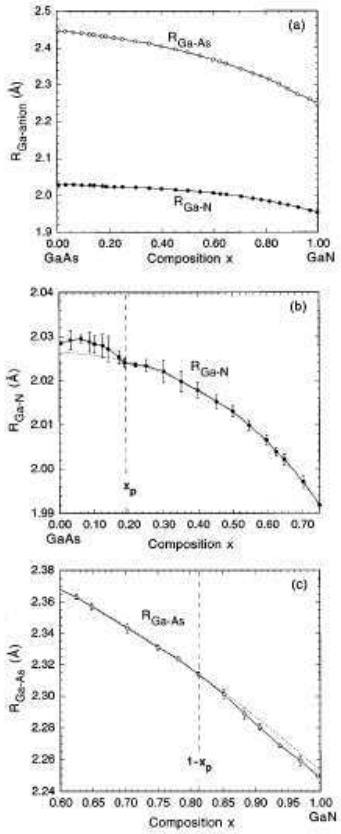

Figure 1.22: From Bellaiche *et al.* : calculated composition dependence of Ga-As and Ga-N bondlengths in $GaAs_{1-y}N_y$; dashed lines correspond to a fit with a fourth-order polynomial, x_p the percolation threshold.

a few percent of substitutional N into the $GaAs_{1-y}N_y$ and $In_xGa_{1-x}As_{1-y}N_y$ alloys, therefore an experimental check of these results is outside the present possibility. It is possible only to investigate the dilute limit ($0 < y < 0.0265$) where it is worth remarking that Bellaiche's curves are not so different from straight lines.

Since almost no information was available on the local structure, no experimental evidence and quantification of the short range ordering referred to in section 1.4 has been also ever given, neither in terms of clustering and anticlustering nor in terms of bond distribution. During the developing of our work Kurtz *et al.* [39], basing on infrared absorption measurements, proposed that annealing induces the short range ordering predicted by Kim and Zunger [9], which can also explain the blue shift of the

band gap upon annealing; however they were not able to precisely quantify the effect. Finally nothing on the effects of hydrogenation on the local coordination and bond lengths is known : does hydrogenation enhance or reduce the short range ordering (if actually present) ? Does it affect in some way the values of In-As and Ga-As bond lengths, for example reducing the epitaxial strain or in some other way ? What is its effect on the width of the bond lengths distribution ?

The main goal of this experimental thesis work is to fill this lack of structural information : by X-Ray diffraction to study the long range order and X-Ray Absorption Spectroscopy to study the local environment of three of the four elements constituting the $In_xGa_{1-x}As_{1-y}N_y$ alloy. As a matter of fact as discussed above the structure dramatically affects the optical properties of these systems and a full knowledge of all the structural aspects is mandatory in order to control the emission properties of nitrides-based lasers. This knowledge is needed for tailoring the band gap of the emitters in order to obtain optimized emission spectra; it can also be very useful in order to understand what are the significant aspects to engineer more efficient materials. Moreover the knowledge of the long range and of local order is very interesting, from a fundamental physics standpoint, to find out "what actually happens" when the two fcc sublattices of this zincblend structure, that host such different atoms (for weight, size, electronegativity), merge one into the other forming the alloy : in particular how the atoms arrange themselves, how they preferentially link each other, if bond lengths can be explained or not in the frame of the most classical models proposed for semiconductors. About the last point in the next section I will briefly list some of these models, which have been useful in order to understand the results of this work.

1.5.2 Local structure of semiconductors

It has been known since a long time that bond lengths in ternary semiconductors cannot be calculated from the lattice parameter using the Virtual Crystal Approximation (VCA) i.e. by a simple linear combination of the binary constituents. This behavior is different from that of the lattice constants, which roughly follow the well known Vegard's law [71]. As a matter of fact X-Ray Absorption experiments [72] have clearly shown in the past, in the case of $In_xGa_{1-x}As$, how the first neighbors distances assume values quite constant and close to the Pauling's limit [73], i.e. to the sum of the elements ionic radii. The presence of two different elements in the cation or in the anion sublattice linearly increases the shorter anion-cation bond length as a function of the composition with respect to the binary compound and decreases the longer one only a bit [72]. These XAFS results were successively simulated in the frame of the Valence Force Field (VFF) model for the potential [28, 74], using force parameters derived from the macroscopic elastic constants C_{11} and C_{12}.

We report here the formulation for the Keating's VFF potential given by Martin and Zunger [29] and applicable to a zincblende cell:

$$U = \sum_l \sum_{m=1}^{4} \frac{3}{8d^2}\alpha \left[\vec{r}_m(l,1)\cdot\vec{r}_m(l,1) - d^2\right]^2 + \qquad (1.12)$$

$$+\sum_{l}\sum_{s=1}^{2}\sum_{m=1}^{3}\sum_{n=m+1}^{4}\frac{3}{8d^2}\beta\left[\overrightarrow{r}_m(l,s)\cdot\overrightarrow{r}_n(l,s)+\frac{d^2}{3}\right]^2 \tag{1.13}$$

where d = R_{ij}^0 is the equilibrium interatomic distance between the atoms i and j, $\overrightarrow{r}_m(l,s)$ is the vector connecting atom s in unit cell l to its mth nearest neighbor. The first sum extends over all nearest neighbors pairs, whereas the second sum extends over all bond angles around every atom, α and β are the bond stretching and the bond bending force constant respectively, related to the macroscopic elastic constants of the material in the following way :

$$\alpha = \frac{a}{4}(C_{11}+3C_{12}) \tag{1.14}$$

$$\beta = \frac{(C_{11}-C_{12})a}{4} \tag{1.15}$$

where a is the lattice parameter. Martins and Zunger [29] (1984) minimized the VFF potential of equation 1.13 for clusters of 64 atoms around a substitutional impurity in a binary matrix. This first Valence Force Field approach was able to reproduce the experimental trends and to give good quantitative results at the impurity limit for several compounds; we will refer in the following to this approach as *MZ* model.

Later a more rigorous analytical method developed by Cai and Thorpe [75] (1992) allowed to fit quite well the experimental findings for a very large variety of semiconductors on the whole concentrations range. In the latter model a rigidity parameter a** has been introduced to describe the resistance of a given lattice to a radial expansion. The rigidity parameter a** is related to the VFF bond stretching and bending constants by the following the relationship:

$$a^{**} = \frac{1+1.25(\frac{\beta}{\alpha})}{1+3.6(\frac{\beta}{\alpha})+1.17(\frac{\beta}{\alpha})^2} \tag{1.16}$$

Note how a**=1 indicates a floppy lattice with each bond length fixed at its natural value (Pauling's limit), a**=0 indicates a perfectly rigid lattice with bond lengths accommodating the average value (VCA's limit). Covalent semiconductors like III-V are characterized by smaller values of a** (0.63 for GaAsP [76] and 0.80 for InGaAs [75]), while more ionic systems as II-IV exhibit higher values (0.90 for CdMnTe [77]), in any case the floppy limit gives a better approximation than the rigid one. For all the $(In_x)Ga_{1-x}As_{1-y}(N_y)$ alloys investigated in this thesis, the rigidity parameter a** values are between 0.69 and 0.72.

Without entering the formalism of this model (we will refer to it as *CT* in the following), which employs Green functions to calculate the length distribution function for the nearest-neighbors distances of a quaternary alloys, I just report the final results for the case of $In_xGa_{1-x}As_{1-y}N_y$:

$$\begin{aligned} R_{Ga-As} &= R_V + a**[x\Delta_{GaIn} + y\Delta_{AsN}] \\ R_{Ga-N} &= R_V + a**[x\Delta_{GaIn} + (1-y)\Delta_{NAs}] \\ R_{In-As} &= R_V + a**[(1-x)\Delta_{InGa} + y\Delta_{AsN}] \\ R_{In-N} &= R_V + a**[(1-x)\Delta_{InGa} + (1-y)\Delta_{NAs}] \end{aligned} \tag{1.17}$$

$\Delta_{AB} = R^0_A - R^0_B$ i.e. the difference between atomic radii of atoms A and B, while R_V is the VCA bond length of the quaternary alloy defined as :

$$R_V = (1-x)(1-y)R^0_{Ga-As} + (1-x)yR^0_{Ga-N} + \\ +x(1-y)R^0_{In-As} + xyR^0_{In-N} \tag{1.18}$$

R^0_{A-B} are the bond-lengths in the binary AB constituent compounds.

Another VFF model was elaborated in 1985 by Balzarotti *et al.* [78] (we will refer to it as *B* in the following); the authors considered that XAFS gives the average of the bond length values in a macroscopic volume, so they explicitly considered all the possible nearest neighbors configurations around a central absorber, giving to each configuration a statistical weight. They considered a ternary alloy $AB_{1-y}C_y$ where B and C are, for example, the anions (as in the case of $GaAs_{1-y}N_y$) assuming that the anion sublattice remains rigid while the cation A moves making longer or shorter bonds with the two different kind of anions. Considering all the possible tetrahedra $B_{4-n}C_n$, $0 \leq n \leq 4$ around the central atom A they expressed, via geometrical considerations, the A-C distances in function of the A-B distances for all the three mixed anion-clusters (the remaining two are not distorted and the distances completely defined by the lattice parameter).

Assuming that distribution of the anions in the sublattice is random, the probability for any vertex to host a B-type anion is *1-y* while the probability to host a C-type anion is y; as a consequence the probability of finding a tetrahedron with n C-type anions is given by the binomial Bernoulli distribution :

$$P(n,y) = {}^{[4]}_{[n]}y^n(1-y)^{4-n} \\ (n = 0,1,2,3,4) \tag{1.19}$$

This probability distribution is visualized in Fig. 1.23 (Woicik *et al.* [79]).

Having defined the geometry of the clusters and their probabilities, Balzarotti *et al.*, properly weighting the different configurations, calculated the average A-C and A-B distances (what measured by EXAFS) in function of the A-B distances for the three different mixed anion clusters. The values of these variables were extracted by minimizing a VFF potential for the three clusters, assuming significant only the bond stretching terms. This method, whose input at the end are only the bond stretching constants of the binary constituents and the lattice constant of the alloy a(x), yields good results when applied to $In_xGa_{1-x}As$ and $Cd_xMn_{1-x}Te$ alloys. Balzarotti *et al.* remarked also that if the assumption of rigidity of the anion sublattice is relaxed, bond bending terms should be also included.

Despite the unquestionable success of these models not all the existing semiconductors are "well-behaving" and deviations from the linearity of the concentration dependence have been observed, typically at the dilute limit. Even for a "model" alloy like the binary SiGe, where the two elements were supposed to randomly occupy the different sites in the cell, the Ge-Ge distance was observed to vary not linearly at the Ge dilute limit [80]. Also, a different composition dependence of the Ge-Ge and Ge-Si

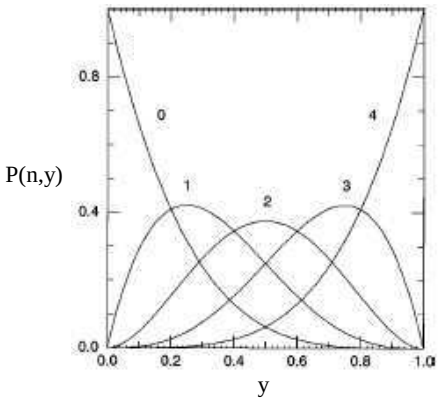

Figure 1.23: From J. Woicik (modified) : probability of occurrence for each different tetrahedron with $0 \leq n \leq 4$ C-type nearest neighbors around a central A atom as a function of C concentration y.

distances [81] was observed, although CT model predicts an unique linear slope for all the bond lengths. However, the relatively large experimental error bars do not usually allow to draw definitive conclusions. We remember here also the discontinuity and the non linearity at the percolation threshold in $GaAs_{1-y}N_y$ predicted by Bellaiche *et al.* and showed in the previous section. Finally a modification of the CT model [82] predicts a slight bowing both in the lattice parameter and in the bond lengths of ternary alloys when disorder in the force constants is considered, nevertheless this modified CT model fails when applied to $In_xGa_{1-x}As$ while better stands for $Zn_{1-x}Cd_xTe$.

Additional considerations have to be taken into account when an alloy is epitaxially grown onto a substrate. In fact in the case of pseudomorphic growth of an epilayer (typically of nanometric dimension) onto a substrate, the lattice constant $a_\perp$ of the layer perpendicular to the interface is either expanded or contracted in response to the distortion of its lattice constant $a_\parallel$ parallel to the interface ($a_\parallel$ is equal to the substrate lattice constant $a_{substrate}$ for a perfectly coherent growth). For an isotropic cubic layer grown on a (001) substrate the fractional strains of the epilayers relative to the interface $\varepsilon_\parallel = \frac{a_\parallel - a_f}{a_f}$ and $\varepsilon_\perp = \frac{a_\perp - a_f}{a_f}$ are related each other through the elastic constants C_{11} and C_{12}, where a_f is the "free" lattice constant of the epilayer.

Assuming that macroscopic strain deformation is transferable to the local scale (not only to the lattice parameter but also to the single bond lengths) i.e. that distortion of the bond lengths induced by strain is uniform despite the two inequivalent bond lengths observed and predicted in a ternary alloys, Tormen *et al.* [83] found a simple formulation for the bond length variation induced by the epitaxial constrain :

$$\delta r^{st} = \frac{a(x)}{2\sqrt{3}} \left[1 - \frac{C_{12}}{C_{11}}\right] \frac{a_\parallel - a_f}{a_f} \tag{1.20}$$

It is evident how, for a completely pseudomorphic growth, if the lattice constant of the

epilayer a_f is smaller that of the substrate $a_{substrate} = a_{\|}$ (tensile strain), as in the case of $GaAs_{1-y}N_y$, bond lengths are increased with respect to the bulk by the tetragonal distortion. In case of $In_xGa_{1-x}As_{1-y}N_y$ roughly $a_f \geq a_{substrate}$ (compressive strain) when $x \geq 3y$, so that for these concentrations strain reduces the bond lengths.

It is worth remarking that, in any case, the effect of strain is opposite in direction and contrasts the alloying effect observed by Mikkelsen and Boyce [72] and predicted by Cai and Thorpe [75] and Balzarotti *et al.* [78] . That can lead, in case of tetragonal distortion, to a reversal in the composition dependence of the bond lengths which can slightly decrease while the lattice constant increases as a function of the composition, as observed by Woicik *et al.* [79] in case of $In_xGa_{1-x}As$ epitaxially grown (with compressive strain) on (001) GaAs (Fig. 1.24), and to the opposite situation in case of tensile strain.

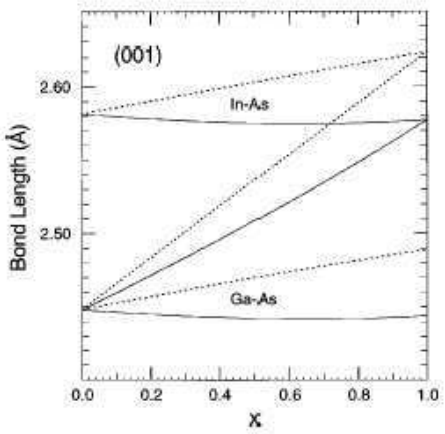

Figure 1.24: From Woicik *et al.* (modified): In-As and Ga-As bond lengths as a function of x for an $In_xGa_{1-x}As$ epitaxially grown on GaAs (low slope full lines); the two low slope dashed lines represent the bond lengths dependence in bulk $In_xGa_{1-x}As$ firstly observed by Mikkelsen and Boyce, the high slope dashed line represent the Vegard's approximation.

If *CT*'s model is used in order to calculate the bond lengths, the tetragonal distortion can be taken into account by adding the δr^{st} term reported in equation 1.20 to the expressions of equation 1.17 and a similar approach can be used for *MZ*'s model. If *B*'s model is otherwise employed, the effects of the tetragonal distortion of the cell on the bond lengths can be directly evaluated using a tetragonal unit cell and calculating from it the bond lengths for each of the three mixed anion distorted tetrahedra. This procedure has already proved to be effective in describing strained $In_xGa_{1-x}As$ alloy dots on $GaAs(001)$ [84].

Chapitre 2 : Les techniques expérimentales

Dans ce chapitre, nous décrivons en bref la croissance des échantillons et les traitements post-croissance (recuit et hydrogénation), puis nous traitons plus ou moins en détail les différentes techniques expérimentales utilisées. Nous dédions beaucoup d'espace à la spectroscopie d'absorption de rayons X (XAS), qui a été la technique expérimentale la plus utilisée pendant ce travail de thèse: à partir des premières observations et interprétations du phénomène des oscillations après-seuil, jusqu'à la formulation dans le cas de diffusion simple du photoélectron et, enfin, à la formulation de diffusion multiple. Les différentes stratégies de mesure de la structure fine du coefficient d'absorption utilisées pendant cette thèse sont ici décrites ensemble aux lignes de lumières sur lesquelles les différentes expériences ont eu lieu, en passant par les techniques d'analyse des données XAS et de simulation du coefficient d'absorption dans la région du seuil (XANES).

En suite la diffraction de rayons X est traitée, cette fois de façon assez simple et fonctionnelle aux expériences effectuées dans ce travail: on commence avec une introduction des concepts de base pour passer à une description de la géométrie de nos expériences et à une revue des différents équipements expérimentaux avec lesquels elles ont été réalisées.

La spectroscopie de diffraction anomale (DAFS) est présentée en commençant avec les idées fondamentales et en portant suffisamment d'attention au sujet de l'analyse des données; enfin, même dans ce cas, nous décrivons brièvement la ligne de lumière sur laquelle ces expériences ont été réalisées.

La dernière partie du chapitre est dédiée à une description plus rapide des techniques complémentaires exploitées dans cette thèse. Trois techniques expérimentales ont été utilisées pour la caractérisation des échantillons : la spectrométrie de retrodiffusion Rutheford (RBS), l'analyse de réactions nucléaires (NRA) et la photoluminescence (PL). La description de la spectroscopie d'absorption dans l'infrarouge et des simulations théoriques selon la Théorie de la Fonctionnelle Densité (DFT) concluent le chapitre.

Chapter 2

Experimental techniques

2.1 Growth and post-growth treatments of the samples

In this thesis work we analyzed the samples grown by two different groups by molecular beam epitaxy, a technique developed during the eighties and nowadays well established for the growth of nitrides [85]. This technique permits to minimize background doping and as the same time to control with great efficiency the layer thickness, even when very small; this makes it the eligible tool for engineering quantum nanostructures. For the growth of $In_xGa_{1-x}As_{1-y}N_y$ MBE is preferable to metalorganic chemical-vapor deposition (MOCVD) due to the high hydrogen contamination in the latter technique. As it has been explained in section 1.3 and will be shown in chapter 5, hydrogen dramatically affects the optical and structural properties of these alloys.

$In_xGa_{1-x}As_{1-y}N_y$ single quantum wells and $GaAs_{1-y}N_y$ epilayers have been grown on undoped Ga (001) substrate at the University of Würzburg (Germany) by solid source molecular beam epitaxy; a radio frequency or an electron-cyclotron resonance plasma source was used for N_2 cracking [86]. $In_xGa_{1-x}As_{1-y}N_y$ and $GaAs_{1-y}N_y$ epilayers have been deposited on Ga (001) at CEA/Leti in Grenoble by gas-source molecular beam epitaxy, using a radio-frequency plasma source to decompose N_2 into the N active species [67]. The N_2 flux was controlled by a mass flow regulator, temperature of the substrate during the growth was 400-430 °C.

Post-growth thermal annealing of the samples was performed in a RTA furnace under N_2 flow at 700 °C, for different annealing times (90, 300 and 1800 s); during the annealing a GaAs wafer covered the samples to prevent any arsenic desorption. Post-growth hydrogenation of the samples [44] was obtained by ion beam irradiation from a Kaufman source with the samples held at 300 °C for 6 hours. The ion energy was about 100 eV and the current density was few tenth of $\mu A/cm^2$; the H impinging dose was of 2.5 10^{18} ions/cm^2. Hydrogen removal could be obtained upon an annealing of 1800 s at 500 °C.

2.2 X-Ray Absorption Fine Structure

2.2.1 The history and the present

The term *X-ray Absorption Fine Structure* (XAFS) refers to oscillations in the absorption coefficient on the high energy side of an absorption edge. Such oscillations, first observed in 1931 [87], can extend up to 1000 eV above the edge, may have a magnitude of 10 % of the absorption jump (see Fig. 2.1) and are not present in the gaseous phase.

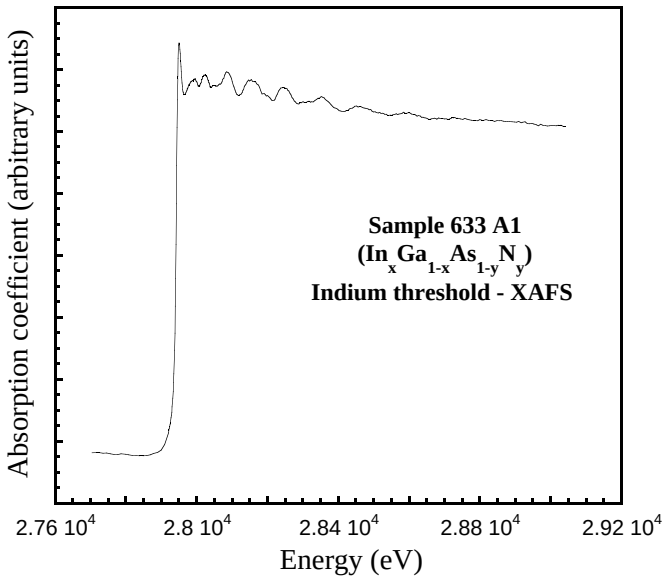

Figure 2.1: XAFS oscillation in the absorption coefficient of the $In_xGa_{1-x}As_{1-y}N_y$ sample 633 A1.

It took a long time to achieve a coherent physical explanation of this effect. At the very beginning both a short range order theory (SRO) [87], according to which oscillations were due to the modification of the final state wave function of the photoelectron caused by back scattering from the surrounding atoms (Fig. 2.2), and a long range order (LRO) one [88], which considered the energy gaps at the Brillouin zone boundaries, were proposed. The LRO approach was shown to be in error, but only 40 years after [90] the first observation of the phenomenon; the long delay was due to the fact that, at the beginning, predictions made with the both theories didn't match well the experimental data.

The first breakthrough occurred in 1971, when Sayers *et al.* [91] pointed out that a Fourier transform of XAFS with respect to the photoelectron wave number should peak at distances related to the atomic neighbors of the absorber. This discovery disclosed the possibility to extract structural information by means of XAFS, like bond distances and coordination numbers. It also clarified the SRO origin of the effect,

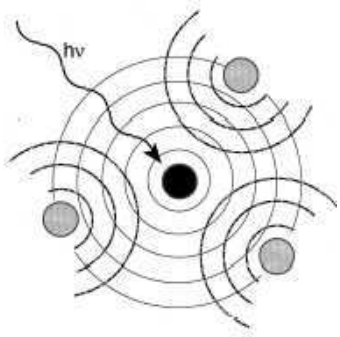

Figure 2.2: From C. Maurizio [89] (modified) : pictorial view of the photoelectron self-interference effect, the atom in black absorbs the photon, the outgoing photoelectron wave is partially backscattered by the neighboring atoms.

since the transform revealed only the first few shells of neighbor atoms. The second breakthrough was the availability of Synchrotron Radiation Sources [92], that delivered X-ray intensities orders of magnitude greater than rotating anodes, and reduced the time for acquiring a spectrum on a concentrated sample from one week to the order of minutes.

Nowadays it is established that a single scattering short range order theory is adequate under most circumstances, if we exclude the energy range immediately above the edge (up to about 30 eV). In this range, which is referred to as XANES region (acronym for *X-ray Absorption Near Edge Spectroscopy*), the energy of the photoelectron is very small (its wavelength is comparable with the interatomic distances),while its mean free path is quite high (some tenths of Å); as a consequence the probability for the photoelectron to be scattered from more than one atom in the surroundings of the absorber increases.

XAFS, with the use of state of art analysis tools, provides information on the local structure around the absorber which is energetically selected; by using this technique it is possible to measure the bond lengths distribution and to determine the number of neighbors of the absorber. In some particular case, XAFS permits also to identify unknown neighbors and/or to measure the relative number of different neighbors in a mixed shell. It can provide information on the bond angles and on the geometry of the photoabsorber site, by studying multiple scattering (section 2.2.3) and exploiting the polarization dependence (section 2.2.2).

As a result, XAFS has become a very important investigation technique in different scientific fields, such as physics, material science, chemistry, biology and biophysics; the local character of the probe made it complementary to X-Ray Diffraction, which provides on the contrary information on the long range order. Since it has been the most exploited technique in this work, XAFS will be addressed in details in the following.

2.2.2 Single scattering XAFS formula

If an homogeneous sample of thickness x is hit by X-ray radiation with intensity I_0 normal to its surface, the outgoing intensity I is attenuated exponentially:

$$I = I_0 exp(-\mu x) \tag{2.1}$$

The linear absorption coefficient μ, related to the photoelectric effect, monotonically decreases as a function of energy. That is true except at the energies corresponding to the photoelectric absorption from electronic core levels; at these energies characteristic sharp edges are observed. μ is the reduction in the energy density u carried by the electromagnetic field, due to the interaction with the material, which can be also expressed as :

$$\begin{aligned} \mu(\omega) &= -\frac{1}{u}\frac{du}{dx} \\ u &= \frac{\epsilon_0 E_0^2}{2} = \frac{\epsilon_0 w^2 A_0^2}{2} \end{aligned} \tag{2.2}$$

where A_0 is the amplitude of the vector potential associated to the electric field, whose maximum amplitude is E_0; ϵ_0 is the dielectric constant of vacuum.

$\mu(\omega)$ depends on the atomic density of the sample n and on the probability of transition W_{fi} for the photoabsorber from the initial state $|\psi_i>$ to the different possible final states $|\psi_f>$, corresponding to possible different core holes or multiple excitations:

$$\mu(\omega) = \frac{2\hbar}{\epsilon_0 \omega A_0^2} n \sum_f W_{if} \tag{2.3}$$

In order to calculate the probability of transition W_{fi}, the time dependent perturbation theory is exploited, which permits to expand in series the interaction potential between the atom and the electromagnetic field, and to use the only first term of the series if the interaction is weak. The transition probability is in this way determined by the Fermi's golden rule:

$$W_{fi} = \frac{2\pi}{\hbar} |\langle \psi_i | \hat{H}_I | \psi_f \rangle|^2 \rho(E_f) \tag{2.4}$$

where $\rho(E_f)$ is the final density of states and $\hat{H}_I$ is the interaction Hamiltonian operator for photoelectric absorbtion which, at the first order, can be written as :

$$\hat{H}_I = i\hbar \frac{e}{m} \sum_j \overrightarrow{A}(\overrightarrow{r_j}) \cdot \overrightarrow{\nabla}_j \tag{2.5}$$

where j labels the electrons inside the atom and $\overrightarrow{\nabla}_j$ their linear momentum.

By using equations 2.5 and 2.4, we find the probability of transition for the photoelectric absorption of photons belonging to a monochromatic, polarized and collimate beam:

$$W_{fi} = \frac{\pi \hbar e^2}{m^2} |A_0|^2 |\langle \psi_i | \sum_j e^{i \overrightarrow{k} \overrightarrow{r}_j} \widehat{\eta} \cdot \overrightarrow{\nabla}_j | \psi_f \rangle|^2 \rho(E_f) \tag{2.6}$$

$\widehat{\eta}$ and $\overrightarrow{k}$ are the polarization unity vector and the electric field vector ($k = 2\pi/\lambda$). If we use the first order term of the series expansion for the exponential, we obtain the transition probability in the dipole approximation (valid for $|\overrightarrow{k}\,\overrightarrow{r_j}|^2| \ll 1$):

$$W_{fi} = \frac{\pi\hbar e^2}{m^2}|A_0|^2|\langle\psi_i|\sum_j \widehat{\eta}\cdot\overrightarrow{\nabla}_j|\psi_f\rangle|^2\rho(E_f) \tag{2.7}$$

If we substitute the momentum with the position operator :

$$W_{fi} = \frac{\pi e^2}{\hbar m^2}|A_0|^2|\langle\psi_i|\sum_j \widehat{\eta}\cdot\overrightarrow{r}_j|\psi_f\rangle|^2\rho(E_f) \tag{2.8}$$

In the dipole approximation the following selection rules are valid for the angular momentum:

$$\Delta l = \pm 1; \Delta s = 0; \Delta j = \pm 1, 0; \Delta m = 0 \tag{2.9}$$

If the transition involves only one electron, the first rule implies that, in case of symmetry s (i.e. $l = 0$) for the initial state, the final state has p symmetry (i.e. $l = 1$). This is the case of all the edges (K) investigated in this thesis work.

In order to calculate the transition probability of equation 2.8 and hence the absorption coefficient, it would be necessary to know the final state $|\psi_f\rangle$ (the initial state is simply the fundamental state of the absorbing atom). This is a priori difficult, since the final state involves all the electrons in the atom and, furthermore, it is perturbed by the local environment of the absorber. An approximation used to simplify the situation is the *single electron* one, based on the fact that a large fraction $\mu_{el}(\omega)$ of the absorption coefficient is due to transitions where only one electron modifies its state and the others $N-1$ just relax their orbitals to accomplish the new potential created by the presence of a core hole. The remaining fraction of μ is due to inelastic transitions, where the excitation of the primary core electron takes to the excitation of more external electrons, which can occupy higher energy states (shake up process) or leave the absorber atom (shake off process); the photon energy is in this case shared by all these excited electrons. The absorption coefficient, following this approximation, can be written as :

$$\mu(\omega) = \mu_{el}(\omega) + \mu_{anel}(\omega) \tag{2.10}$$

$$\mu_{el}(\omega) \propto |\langle\psi_i^{N-1}\psi_i|\widehat{\eta}\cdot\overrightarrow{r}|\psi_f^{N-1}\psi_f\rangle|^2\rho(\epsilon_f) \tag{2.11}$$

where ψ^{N-1} is the Slater representation for the wave functions of passive electrons while ψ, $\overrightarrow{r}$ and ϵ_f are the wave function, position vector and final energy of the active electron.

If the photoelectron has sufficiently high kinetic energy, it takes such a short time in leaving the absorber atom that its motion is not affected by the slower relaxation of the passive electrons [93]. In this case, we can separate the contribution of the active

and passive electrons in the initial and final wave functions (*sudden* approximation):

$$\mu_{el}(\omega) \propto |\langle\psi_i|\widehat{\eta}\cdot\overrightarrow{\overrightarrow{r}}|\psi_f\rangle|^2 S_0^2\rho(\epsilon_f) \tag{2.12}$$

$$S_0^2 = |\langle\psi_i^{N-1}|\psi_f^{N-1}\rangle|^2 \tag{2.13}$$

S_0^2 represents the overlap integral of the passive electrons wave functions in the initial and final states. The sudden approximation, which reduces the calculation of the final state to the final state for the only photoelectron, is rigorous starting from some tenth of eV above the edge. In general S_0^2 varies between 0.7 and 1, and can be experimentally determined by measuring a standard compound with local environment similar to that of the sample under investigation, as done during this work. If there is no relaxation of the $N-1$ electrons, i.e. $S_0^2 = 1$, $\mu_{el}(\omega)$ in equation 2.12 has to be equal to $\mu(\omega)$ of equation 2.10: this means that S_0^2 measures the fraction of absorption due to the only elastic transitions.

The XAFS function is defined as:

$$\chi(E) = \frac{[\mu(E) - \mu_0(E)]}{\Delta\mu_0} \tag{2.14}$$

where $\mu_0(E)$ is the smooth atomic background absorption, which can be simulated by a spline, and $\Delta\mu_0$ is the jump in the absorption coefficient at the edge. Since in the Extended-XAFS region (EXAFS) (starting from about 30 eV above the edge) the final density of states varies slowly and monotonically with energy, the oscillations contained in $\chi(E)$ come only from the matrix element. Different derivations for the single scattering XAFS formula have been proposed (see for example ref. [94]); they normally use a Muffin Tin approximation for the atomic potential, i.e. radial inside a sphere surrounding each atom and constant between the atoms. Even if this approximation is quite crude, it works well in the EXAFS region, where the high energetic photoelectron is essentially scattered by the inner part of the potential and moves almost freely in the interstitial region [95]; the high energy makes it less sensitive to the potential details.

If spherical photoelectron wave functions are employed, the single scattering XAFS formula, as a function of the photoelectron wave number $k = \sqrt{\frac{2m(E-E_0)}{\hbar^2}}$, is:

$$\chi(k) = -3S_0^2(k)\sum_j \frac{N_j}{kR_j^2}|f_j(k,R_j)|sin(2kR_j + 2\delta_c(k) + \phi_j(k,R_j)) \\ e^{-2k^2\sigma_j^2}e^{-2R_j/\lambda_j(k)}(\widehat{\eta}\cdot\widehat{R_j})^2 \tag{2.15}$$

The sum is performed over j-different atomic shells which contain each N_j identical neighbors; in case of mixed shells, linear combinations have to be used. R_j is the vector which links the absorber to the j-neighbors, $|f_j(k,R_j)|$ is the modulus of the backscattering function of the atoms in the shell j, while $\phi_j(k,R_j)$ is its phase; in the spherical wave-approach they depend on R_j. $\delta_c(k)$ is the phase shift of the photoelectron wave induced by the central atom, this phase shift is counted twice (the photoelectron leaves the atom and come back after the scattering from the neighbors). $e^{-2k^2\sigma_j^2}$ is the

Debye-Waller factor which measures the broadening of the distances distribution, σ_j^2 is the mean square fluctuation of the bond lengths R_j. If the distribution of the distances is gaussian (*harmonic* approximation), σ_j^2 can be expressed in terms of vibrational normal modes using the Debye's or Einstein's models [96].

$\lambda_j(k)$ measures the mean distance covered by the photoelectron before losing coherence with its initial state; it causes a damping in the XAFS amplitude since only photoelectrons which do not lose coherence with the initial state give a contribution to the signal. The relative lifetime is $\tau = \lambda/v$, where v is the speed of the photoelectron; the lifetime can be written as the sum of two contributions :

$$\frac{1}{\tau} = \frac{1}{\tau_h} + \frac{1}{\tau_e} \tag{2.16}$$

The first is related to the core hole and diminishes with increasing atomic numbers, since the number of possible final states increases; this term is energy-independent. The second contribution is related to the photoelectron and is due to inelastic interaction with electrons of the absorber neighbors; this term is energy-dependent.

The product $\widehat{\eta} \cdot \widehat{R_j}$ between the polarization and position unitary vectors takes into account the fact that the photoelectron is preferentially ejected in the direction of the field. For isotropic samples as polycrystalline powders, amorphous materials, or single crystals with a cubic symmetry (the case of the samples studied in this thesis), this product can be substituted by the angular average $\frac{1}{3}$. As far as the photoelectron is sufficiently energetic and interacts only with the inner orbitals, we can consider the scattering centers as point-like and neglect the curvature of the spherical wave. As a consequence, the scattering process can be treated in the plane-wave formalism, the complex backscattering amplitude can be expanded in series of partial waves and does not depend on R_j any more:

$$f(k,\pi) = \frac{1}{k}\sum_{t=0}^{\infty}(-1)^l(2l+1)e^{i\delta_l}sin\delta_l \tag{2.17}$$

δ_l are the phase shifts of the partial waves. In the *isotropic* and *small atom* approximation the single scattering XAFS formula becomes:

$$\chi(k) = -S_0^2(k)\sum_j \frac{N_j}{kR_j^2}|f_j(k,\pi)|sin(2kR_j + 2\delta_c(k) + \phi_j(k)) \\ e^{-2k^2\sigma_j^2}e^{-2R_j/\lambda_j(k)} \tag{2.18}$$

For non Gaussian distances distributions, the XAFS formula can be written in series of cumulants C_k [97]; the odd cumulants determine the phase of the signal, while the even ones determine the amplitude. In this case the contribution to XAFS of the j-th atomic shell is:

$$\chi_j(k) = \frac{S_0^2}{k}N_j|f_j(k,\pi)|exp(C_0 - 2k^2C_2 + \frac{2}{3}k^4C_4...) \\ sin[2kC_1 - \frac{4}{3}k^3C_3... + \phi(k)] \tag{2.19}$$

In the formulation of equation 2.18, relative to the *harmonic* approximation, S_0^2 can be determined by measuring a standard compound, $|f_j(k,\pi)|$ and $2\delta_c(k)+\phi_j(k)$ can be either calculated *ab initio* or extracted from standard compounds with similar local environment; $\lambda_j(k)$ can be also estimated. As a consequence three quantities remain unknown and can be determined by fitting the experimental data: the number of atoms for each shell N_j, the distances R_j and the Debye-Waller factors. Different approaches to the first principles calculation of amplitudes and phases, and different fitting procedures were proposed in order to extract structural information; in section 2.2.5 we will describe in more details the procedure chosen in our analysis.

2.2.3 Multiple scattering

In the XANES region, the energy of the photoelectron is small with respect to the interaction potential, so that the probability to be scattered by more than one atom becomes higher; the simple expression of equation 2.18 is not valid any more and multiple scattering has to be taken into account. The inclusion of multiple scattering (MS) contributions is mandatory in the XANES region, but also in the EXAFS one some of them have quite high amplitude and have to be included in order to analyze data. In particular, triangular paths involving a second neighbor atom and a first neighbor one resulted in some case important for the samples analyzed in this work. Also longer collinear paths are in some case predicted to give quite high contributions due to the enhanced forward scattering caused by the intermediate atom. This phenomenon is referred to as *focusing* or *shadowing* effect [98].

The XAFS function can be expanded in series of sums, each of ones accounts for all contributions of multiple scattering involving a definite number of atoms [99] :

$$\chi = \sum_{j\neq 0} \chi_2^{0i0} + \sum_{i\neq j; i,j\neq 0} \chi_3^{0ij0} + \sum_{i\neq j\neq k; i,k\neq 0} \chi_4^{0ijk0} + ... \tag{2.20}$$

In the sum, the term $\chi_\Gamma^{0ijk...0}$ represents the contribution to XAFS of the multiple scattering involving $\Gamma-1$ scatterers (labelled i,j,k, etc); the first sum stands for the single scattering. If an ad-hoc effective Debye-Waller factor is associated to each path Γ, together with a scattering amplitude f_Γ (including the damping due to the finite mean free path), the XAFS function can be written in a form similar to that one of the single scattering equation 2.18:

$$\chi_\Gamma(k) = S_0^2 \frac{N_\Gamma}{kR_\Gamma^2} |f_\Gamma(k)| sin(2kR_\Gamma + 2\delta + \phi_\Gamma(k)) e^{-2k^2\sigma_\Gamma^2} \tag{2.21}$$

The majority of these paths have usually a negligible amplitude and a preliminary estimation and filtering is necessary in order select the useful ones for the fit procedure. The series expansion of equation 2.21 is rigorous in the EXAFS region, but unluckily cannot be applied very close to the edge (few tenth of eV), since the series is not convergent for very small k. In this case the problem has to be treated in a more general way, for example by expressing the absorption cross section in terms of Green's functions.

The Green's function for a system described by an hamiltonian H is:

$$G(E) = lim_{\xi \to 0^+} \frac{1}{E - H - i\xi} \tag{2.22}$$

The absorption cross section σ, proportional to the absorption coefficient μ, can be written in Rydberg unities ($e = \hbar = 1$) as :

$$\sigma = 4\pi^2 \alpha \hbar\omega Im < \psi_i | (\widehat{\eta}^\star \cdot r' \frac{1}{\pi} G(E_i + \hbar\omega)(\widehat{\eta} \cdot r) | \psi_i > \tag{2.23}$$

where $|\psi_i >$ is the single electron initial state, and G the "single particle" Green's function:

$$G(\overrightarrow{r}, \overrightarrow{r}', E_i + \hbar\omega) = \sum_f \int ... \int \prod_{i=1}^{N-1} d^3 r_i \prod_{i=1}^{N-1} d^3 r_i' \psi_i^{N-1^\star}(\overrightarrow{r}', \overrightarrow{r}'_1, ..., \overrightarrow{r}'_{N-1})$$
$$\frac{\psi_f^{N^\star}(\overrightarrow{r}', \overrightarrow{r}'_1, ..., \overrightarrow{r}'_{N-1}) \psi_f^N(\overrightarrow{r}, \overrightarrow{r1}_1, ..., \overrightarrow{r}_{N-1})}{E_i + \hbar\omega - E_f - i\eta} \psi_i^{N-1}(\overrightarrow{r}, \overrightarrow{r}_1, ..., \overrightarrow{r}_{N-1}) \tag{2.24}$$

This function describes the propagation of the photoelectron in the final state of energy E_f from point r to point r', the formalism takes into account the many body character of the process. The single particle Green function satisfies the following Dyson's equation:

$$(\nabla^2 + E - V_c(\overrightarrow{r}))G(\overrightarrow{r}, \overrightarrow{r}', E) -$$
$$- \int d^3 r'' \sum(\overrightarrow{r}, \overrightarrow{r}'', E) G(\overrightarrow{r}'', \overrightarrow{r}', E) = \delta(\overrightarrow{r} - \overrightarrow{r}') \tag{2.25}$$

$\sum(\overrightarrow{r}, \overrightarrow{r}'', E)$ is called self-energy and has a role of exchange-correlation potential which is, in the most general case, energy dependent and not local. $V_c(\overrightarrow{r})$ is the local Coulomb-Hatree potential due to the electrostatic interaction with nuclei and other electrons.

A simplification often used in the calculation is the *Muffin Tin* symmetry for the potential; the Green function around a site n can be written as:

$$\frac{1}{\pi} G(\overrightarrow{r}_n, \overrightarrow{r}'_n, E) = \sum_{LL'} R_L^n(\overrightarrow{r}_n, E) \tau_{LL'}^{nn} R_{L'}^n(\overrightarrow{r}'_n, E) +$$
$$\sum_L R_L^n(\overrightarrow{r}_n, E) S_L^n(\overrightarrow{r}'_n, E) \tag{2.26}$$

Here L is the couple of quantum numbers (l, m), R_L^n and S_L^n are the radial solutions, respectively regular and irregular at the origin ($r_n = 0$), of the Schrödinger equation for r_n, r'_n inside the Muffin Tin sphere. The angular part is given by the spherical harmonics $Y_L(\overrightarrow{r_{ij}})$. These solutions link with continuity on the sphere surface with the combinations of Bessel, Neumann and Hankel functions which are necessary to describe the wave function in the flat-potential region. $\tau_{LL'}^{nn}$ are the so called *scattering-path operators*[100] and represent scattering by site n from an incoming wave L to an

outgoing wave L'. These operators are defined by the Lippmann-Schwinger equation $G(E) = G_0 + GVG_0$, where $H = H_0 + V$ is the hamiltonian of the system and by the transition matrix $TG_0 = VG(E)$, which is linked to the scattering path operators by :

$$T = \sum_{i,j} \tau^{ij}_{LL'} \tag{2.27}$$

The *scattering path operators* can be written in function of the scattering matrix T_a and the propagators matrix G:

$$\tau^{ij}_{LL'} = [T_a^{-1} - G]^{-1} = [I - T_a G]^{-1} T_a \tag{2.28}$$

The scattering matrix describes the scattering amplitude of a spherical wave of angular momentum L into an outgoing wave of angular momentum L'; due to the spherical symmetry of the potential the matrix is diagonal on the L indexes and it can be written by using the operator t^i_l, which depends on the atomic "phase shifts" δ^i_l :

$$T_a|^{ij}_{LL'} = t^i_l \delta_{ij} \delta_{LL'} = exp(i\delta^i_l) sin(\delta^i_l) \delta_{ij} \delta_{LL'} \tag{2.29}$$

As it can be inferred from this expression, the matrix is also diagonal on the site indexes. The propagator matrix G, as well diagonal on the site indexes, is defined by :

$$G^{ij}_{LL'} = 4\pi i \sum_{L''} i^{l+l''-l'} C^{L'}_{L,L''} h^+_{l''}(kr_{ij}) Y_{L''}(\widehat{r_{ij}}) \tag{2.30}$$

where the Gaunt's coefficients $C^{L'}_{LL''}$ are :

$$C^{L'}_{LL''} = \int d\Omega Y_L(\theta,\varphi) Y_{L'}(\theta,\varphi) Y_{L''}(\theta,\varphi) \tag{2.31}$$

while $h^+_l(kr_{ij})$ are the spherical Hankel functions.

Due to the strong localization of $< \psi_i|$ on the photoabsorber site, for a K-edge it is sufficient to calculate the Green function inside the photoabsorber sphere in order to evaluate the absorption cross section of equation 2.23; this means considering only the absorber site (n=0) in equation 2.26.

The evaluation of the Green function on the absorber site, and so of the cross section, can be rigourously performed by numerically inverting the matrix $[I - T_a G]$ of equation 2.28; the inversion of this matrix can be generally done only through its knowledge on all the site and momentum indexes. For $k \to 0$ the Hankel's function modula which enter the expression for G are in fact large and $[I - T_a G]$ has large out-of-diagonal elements, so that its inversion gives terms which couple the different atoms and structural configurations, and only the total signal makes sense.

If the photoelectron energy is quite high, $T_a G$ can be treated as a perturbation of I and expanded in geometric series:

$$(I - T_a G)^{-1} = \sum_n (T_a G)^n \tag{2.32}$$

The series converges only if its spectral radius (the modulus of the biggest eigenvalue) is smaller that 1; this condition roughly fixes the limit of the validity of the series expansion representation, and it is normally satisfied starting from few tenth of eV above the threshold [101]. The quadratic term in the expansion gives the contribution of all the scattering paths which start from the absorber and involve only one scatterer, the cubic term stands for paths involving scattering from two neighbors, etc. This formalism permits to uncouple the contributions of different atomic configurations. It could be demonstrated that, introducing the series expansion 2.32 in the expression of the scattering path operators, of the Green function and finally of the absorption coefficient, the XAFS function can be written in the multiple scattering form of equations 2.20 and 2.21, defining effective Debye-Wallers and backscattering amplitudes. A more complete and "step to step" derivation of the general XAFS formulation in the multiple scattering approach can be found in references [102, 99, 103].

The numerical inversion of the matrix $(I - T_a G)$ gives the first method to simulate the XAFS signal in the near edge region; since in this way all the paths are implicitly summed by the inversion, this strategy is referred to as Full Multiple Scattering (FMS) approach. The XANES of $GaAs_{1-y}N_y$ and $In_xGa_{1-x}As_{1-y}N_y$ samples at the nitrogen edge which will be presented in the following have been simulated in FMS approach; this strategy allows to simulate XANES starting from the geometric configuration of a cluster of atoms surrounding the photoabsorber.

The geometric structure of a site is deeply linked to the electronic structure of the material, as a matter of fact a completely different approach based on band structure calculations could be adopted in order to reproduce XANES, at least the in case of a periodic structure [104, 105]. Near the edge the absorption coefficient describes the transitions of the photoelectron to the lowest unoccupied states compatible with the selection rules for the angular momentum. In the case of a semiconductor these transition have, as final states, some unoccupied state in the bottom of the conduction band. If we consider a K-edge in the dipole approximation, the final state must have a p-symmetry; the XANES signal is in this way proportional to the p-projected local density of states in the bottom of the conduction band. The equivalence of the band structure calculation and the full multiple scattering approach has been demonstrate by J. E. Muller *et al.* [106].

2.2.4 Detection schemes

The simplest detection scheme for XAFS measurements is the transmission mode, where the X-ray flux impinging on the sample I_0 and the transmitted flux I of equation 2.1 are directly measured, using for example ionization chambers, and give the total absorption coefficient:

$$\mu = -\frac{ln(I/I_0)}{x} \tag{2.33}$$

In case of an uniform sample, the total absorption coefficient can be divided into the absorption of the atoms of interest and the other atoms $\mu_T = \mu_A + \mu_B$. In order to

evaluate the *signal to noise* ratio, we have to consider that the structural information is carried by the only modulations of μ_A ($\Delta\mu_A$). If the expression of the signal to noise is maximized as a function of the sample thickness [94] we find $\mu_T X = 2.55$ and

$$\frac{S}{N} = 0.736 \frac{\Delta\mu_A}{\mu_T} I_{inc}^{1/2} \tag{2.34}$$

The *signal to noise* is maximized when the thickness of the sample is of the same order of magnitude of the photoelectron mean free path, typically about $10\mu m$. The higher is the ratio $\frac{\Delta\mu_A}{\mu_T}$, proportional to the concentration of the absorber, the better is the *signal to noise*. Transmission measurements are fast and accurate if concentrate, sufficiently thin and homogeneous samples are available. In this thesis work, detection in transmission has been exploited in order to measure InAs and GaAs standard compounds, at the In and Ga edges, useful to estimate S_0^2 before analyzing the samples.

In case of high dilution of the absorber the detection of fluorescence radiation, which origins from the relaxation of the excited state, becomes more favorable over transmission [107]. When the core hole is filled by an electron from an higher energy level, the energy in excess, corresponding to the difference between the two electronic levels, can be delivered by the creation of a photon X (fluorescence photon) or by the expulsion of another electron from an higher energy level (Auger electron). The two processes are in competition: for light atoms the Auger effect is more probable, while for heavy atoms fluorescence emission becomes more likely (Fig. 2.3 for K, L and M edge). The relative weight of the two processes is measured by the fluorescence yield :

$$\eta_s = \frac{X_s}{X_s + A_s} \tag{2.35}$$

where X_s and A_s are the probability of emission of one fluorescence photon or Auger electron.

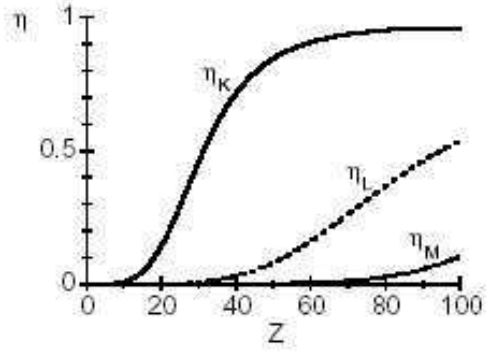

Figure 2.3: From P. Fornasini [108] (modified) : average fluorescence yield η_s for K, L and M edges as a function of the atomic number Z.

The fluorescence photons corresponding to a particular electronic transition taking place in the atoms of interest, can be selected in energy by using an energy resolving

detector (see appendix A) and can give, upon definite conditions, a signal that is proportional to the absorption coefficient. If a solid state detector is employed, the choice of an energy range is carried out electronically; in our measurements at the In K-edge on $In_xGa_{1-x}As_{1-y}N_y$, for example, we selected the In K_α fluorescence line among the fluorescence lines of Ga and As, the elastic scattered and Compton scattered radiation (Fig. 2.4).

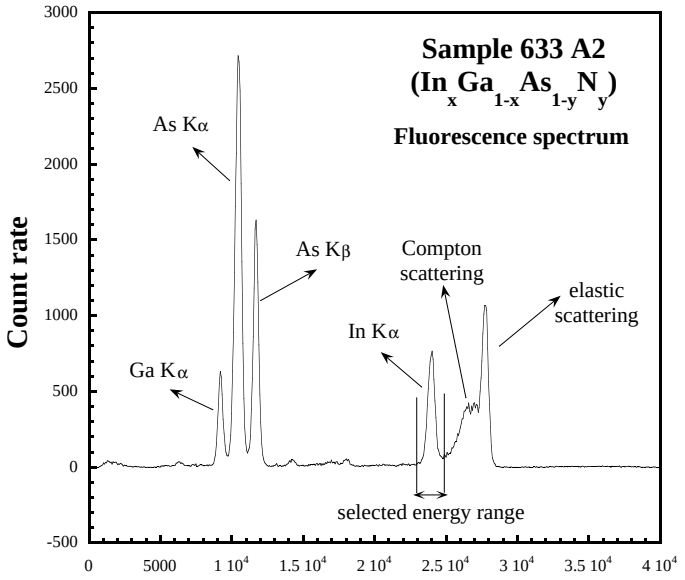

Figure 2.4: Whole fluorescence spectrum of the photons impinging the detector.

For an infinitely thick sample and an incidence angle of 45°, the intensity of fluorescence radiation on the detector with solid angle acceptance $\Omega/4\pi$ is:

$$I_f = \frac{I_0 \eta_s (\Omega/4\pi) \mu_A(E)}{\mu_T(E) + \mu_T(E_f)} \tag{2.36}$$

Here E is the energy of the incident photon and E_f is the characteristic fluorescence energy. If the element under investigation is dilute enough, the denominator in equation 2.36 does not sensibly oscillate as a function of energy and I_f is proportional to $\mu_A(E)$. Fluorescence yield detection has been successfully extended even to the case of concentrated samples, providing to self absorption is either minimized by an appropriate low exit angle-geometry or accounted for using appropriate corrections [109, 110, 111, 112].

Starting from equation 2.36 the *signal to noise* ratio for the fluorescence detection scheme is:

$$\frac{S}{N} = \left(\frac{I_0 \eta_s (\Omega/4\pi) \mu_A(E)}{\mu_T(E) + \mu_T(E_f)} \right)^{1/2} \frac{\Delta\mu_A}{\mu_A} \tag{2.37}$$

If $\eta_s\Omega/4\pi$ is greater than μ_A/μ_T, the fluorescence scheme is more suitable than transmission; this means that roughly[1] fluorescence is preferred for $\mu_T/\mu_A > 10^2 - 10^3$. The transmission scheme can be further complicated in case of epilayers grown on a substrate (like in our case). In this condition the thick substrate can absorb all (or a great part of) the radiation transmitted by the epilayer, forbidding the use of equation 2.33 in the evaluation of the absorption coefficient; otherwise fluorescence yield approach is possible if the element whose threshold is investigated is not present in the substrate.

An extension of equation 2.36 to the case of inhomogeneous samples and to the case in which the fluorescence of interest gives a very weak signal, comparable with background radiation, can be found in the paper of Lee *et al.* [94]; an extension to the case of not infinitely thin samples is given in the paper of Jaklevic *et al.* [107]. Fluorescence yield detection has been employed for the majority of the XAFS measurements of this thesis, both for the indium and the nitrogen threshold.

A third possible strategy is given by the detection of Auger and secondary electrons; in this case the intensity of the electrons signal I_e is similar to that of fluorescence radiation :

$$I_e = \frac{I_0(1-\eta_s)(\Omega/4\pi)\mu_A(E)}{\mu_T(E)+n(E)} \tag{2.38}$$

$n(E)$ represents the exponential attenuation of the non-radiative signal, i.e. the inverse of the sampling depth for electrons. The total electron signal is dominated by that of secondary electrons which have typically energies of some eV and a mean free path shorter than 10 nm (Fig. 2.5). The short sampling depth of electrons makes non-radiative detection unfavorable with respect to fluorescence for thick samples; in case of very thin samples (a few nanometers) all depends on the solid angle acceptance for fluorescence/electron detectors and on the fluorescence/electron yield.

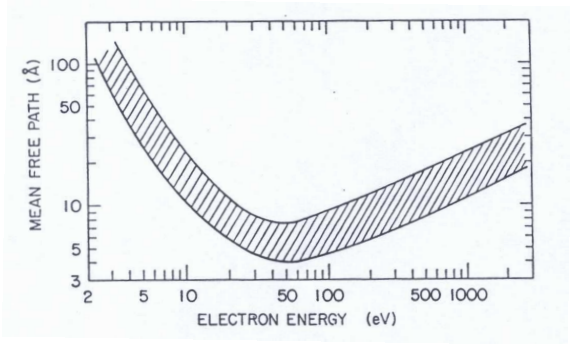

Figure 2.5: From P. Fornasini [108] (modified) : Mean free path for electrons as a function of energy, values for the different materials fall inside the hatched area.

Sometimes non-radiative detection can be employed while fluorescence detection is impossible: that is the case of quite thick epilayer (few thousands of nm) deposited

[1]The precise value depends on the atomic species and the solid angle acceptance.

on a substrate containing the element whose edge is under study. In this way one can exploit the non-radiative short mean free path in order to select electrons that come only from the most superficial region, and that are produced upon photo-excitation of atoms that reside in the epilayer. In this case the fluorescence signal would contain a contribution by atoms residing in the substrate, due to the longer photons mean free path (around 10 μ m at 10 KeV). For thinner deposited epilayers or quantum nanostructures of the same kind, XAFS is not fit and the use of a spatial-site selective technique like Diffraction Anomalous Fine Structure (section 2.4) is mandatory.

It is worth observing that even in case of concentrated-thick samples electron yield detection is suitable; in fact, since in the denominator of equation 2.38 $n(E)$ is by far larger than $\mu_T(E)$ and does not oscillate, the non-radiative signal I_e remains proportional to $\mu_A(E)$. In this work the total electron yield detection scheme, in which electrons are not selected in energy, has been exploited to study the gallium K-edge of 300 nm-thick $GaAs_{1-y}N_y$ epilayers grown on GaAs substrate.

2.2.5 Data analysis

XAFS data analysis usually follows three steps: first the XAFS function is extracted from equation 2.14, then an evaluation of the backscattering amplitudes and phase shifts is done, and finally a fit to the data varying some of the structural parameters in equation 2.18 is performed. The analysis software exploited in this work was the FEFF package, elaborated at the University of Washington, Seattle.

For the background extraction the Autobk code was exploited [113]. This program first performs a pre-edge background removal using a linear function; in this procedure most of the energy dependence of the absorption other than that from the absorption edge of interest is eliminated. Then it carries out normalization to the edge jump and, finally, it performs a post-edge background removal. The last procedure consists in subtracting from $\mu(E)$ a smoothly varying background function $\mu_0 E$, which approximates the absorption from the isolated embedded atom, obtaining in this way $\chi(E)$. The function exploited to approximate the post-edge background is a fourth-order polynomial spline whose knots are equally spaced in k space, the flexibility of the spline is determined by the number of knots. The spline and its first two derivatives are required to be continuous at the knots and one degree of freedom is associated to each knot; the background function is not required to go through the experimental curve at the knots.

The basic idea of the program is that no signal in the Fourier transform of the EXAFS function $\widetilde{\chi}(k)$ can have a physical meaning below a quite small threshold value of R, so the free coefficients of the spline are chosen in order to minimize the R components below a fixed R value R_{bkg}. This means that the method chooses the spline to best fit only the low-frequency components of $\mu(E)$, and not the whole absorption spectrum as other codes use to do. The value of R_{bkg} can be chosen by the user, a good choice being about half the distance of the first shell peak, and determines the maximum number of knots i.e. the stiffness of the spline. As a matter of fact, from

information theory ideas [114] the number of independent points for an EXAFS fit is:

$$N_{ind} = \frac{2\Delta R \Delta k}{\pi} \tag{2.39}$$

where ΔR and Δk are the K- and R- range of useful data.

If the fit is performed from $R = 0$ to $R = R_{bkg}$, as in the case of the background removal, the number of independent points is :

$$N_{ind}^{bkg} = \frac{2R_{bkg}\Delta k}{\pi} \tag{2.40}$$

Since each knot is associated with one degree of freedom, the maximum number of knots is the integer part of N_{ind}^{bkg} in equation 2.40; the program uses a number of knots equal to $N_{ind}^{bkg} - 1$. In Fig. 2.6 an example of post-edge background modelling is reported for the $In_xGa_{1-x}As_{1-y}N_y$ sample 712V.

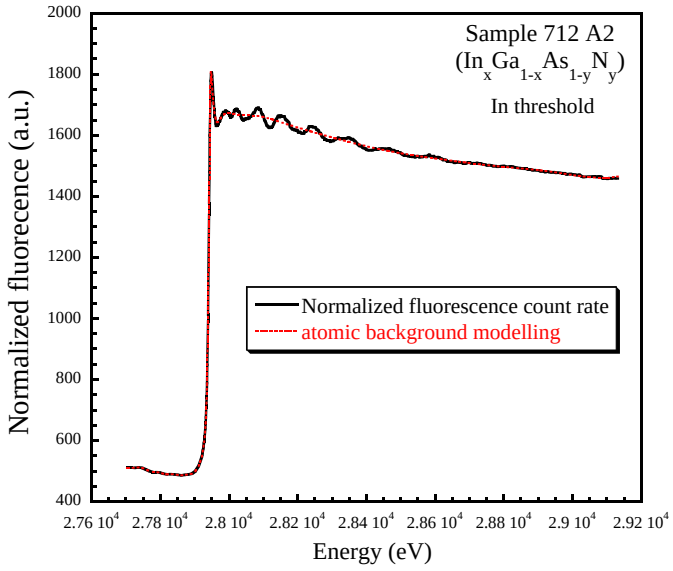

Figure 2.6: Example of post-edge background modelling by the code Autobk.

After background removal, all the atomic clusters which are useful for simulating EXAFS and multiple scattering signals are generated starting from the knowledge of their lattice parameters and spatial groups. This is done by the code atoms [115], which produces a list of coordinates for all the atoms inside a cluster of chosen dimension. For example, in case of the analysis of an $In_xGa_{1-x}As_{1-y}N_y$ spectrum at the indium edge, a zincblend $In_{0.5}Ga_{0.5}As$ cluster was used to model backscattering amplitudes and phase shifts for the first (and third) shell In-As paths, for In-(As)-Ga and In-(As)-In second shell paths, and for multiple scattering paths involving only As anions. In order to generate N-related paths a zincblend InGaN cluster was exploited, which permitted to generate first (and third) shell In-N paths as well as In-(N)-Ga and In-(N)-In second

shell single scattering paths[2]. In the same way this last cluster could be used to model multiple scattering triangular paths involving N anions.

For each cluster an *ab initio* modelling of the absorption cross section was done by exploiting the FEFF 800 code [103], which implements a Green function approach similar to that explained in section 2.2.3. For EXAFS analysis a Dirac-Fock atomic code [116, 117] was exploited to obtain the free-atom electronic densities, which were successively overlapped (following the Mattheiss's prescription [118]) in order to obtain a total electron density and to construct a Coulomb potential . A ground-state Von Barth-Hedin [119] potential was exploited for exchange-correlation potential and the Hedin-Lundqvist (HL) energy-dependent self-energy correction [120] was added. Then the total potential was approximated with a Muffin-Tin one, and the Dirac equation in the spinor relativistic approximation [121] was solved to obtain radial wave functions and partial wave shifts, that are necessary to construct the single particle Green function of equation 2.26. Finally the Green function was calculated in the multiple scattering approach, paths with negligible amplitudes were rejected, and amplitudes and phases for all paths inside a definite cluster were recorded in different files as a function of the energy. They have been used successively during the fitting procedure.

The code implements two further procedures, which are necessary for the simulation of XANES, and which have been exploited in this work for the N-edge analysis: the full multiple scattering approach (FMS) and a self consistent calculation of the potentials. The first consists in the numerical inversion of the matrix of section 2.2.3; the time required for this inversion scales with the cube of the number of atoms in the cluster and the calculation is possible only by using powerful computing resources. Simulations of the nitrogen XANES region of $In_xGa_{1-x}As_{1-y}N_y$ required the use of very large clusters, and the FEFF800 code was modified in order to deal with clusters containing up to 400 atoms (the original version allowed an upper limit of 87). For each XANES simulation, three days of machine-time were necessary on a Xeon double-cpu 2.4GHz Linux workstation (belonging to ESRF, Gorilla Mosix cluster).

The self consistent calculation is performed by using the above-quoted values of potential in the first step for the calculation of the Green function; then the calculated Green function is integrated in energy to obtain the new total electron density $\rho(r)$, from which a new potential is calculated :

$$\rho(\overrightarrow{r}) = -\frac{2}{\pi}\int_{-\infty}^{E_f} d(E)G(\overrightarrow{r}, \overrightarrow{r}, E) \tag{2.41}$$

The spatial instead of energy integration in equation 2.41 gives the electronic density of states, which gives access to the absorption cross section if the presence of the core hole is taken into account. The process is iterated until the series of the calculated electron densities converges, and the final density of states is exploited to evaluate the absorption cross section in the XANES region. In order to save time, the self consistent-field (SCF) evaluation of the potential can be performed within a radius by far smaller than the

[2]As for these second shell paths, the next-nearest neighbor (Ga,In) is coordinated to the central In via a N atom in the first shell.

full multiple scattering one. In the simulations reported in this work the SCF radius contained only the nearest and next-nearest neighbors around each unique site, while FMS was extended to the whole cluster of 20 atomic shells around the photoabsorber (that means 381 atoms for the zincblend structures under study).

The theoretical amplitudes and phases generated by FEFF800 were successively exploited to construct a model function

$$\chi_{model}(k) = \sum_{Path} (k, Amp(k), Phase(k), Path\ parameters) \tag{2.42}$$

which was fitted to the data[3]. The fitting program exploited was the Feffit code [123]. Possible free parameters for each path are the path length and Debye-Waller, the threshold energy shift, the third and the fourth cumulants and an amplitude factor which includes S_0^2. Usually S_0^2 is determined measuring a standard compound and kept fixed during the fit, and a global $e0$ variable is used for all paths. Cumulants beyond the second are used only in case of strong disorder in the bond distances distribution, which is not the case of the samples in this work. Both the experimental and theoretical signals were opportunely k-weighted, apodizated with a Gaussian window [122] and Fourier-transformed in the R-space; then a non-linear least square routine of the kind Levenberg-Marquardt was exploited to find the best set of variables which minimizes the χ^2 statistic for the difference between the experimental and theoretical signals:

$$\chi^2 = \frac{N_{ipd}}{2N_{pts}\epsilon^2} \sum_{i=1}^{N_{pts}} \{(Re[\widetilde{\chi}_{data}(R_i) - \widetilde{\chi}_{model}(R_i)])^2 + \\ +(Im[\widetilde{\chi}_{data}(R_i) - \widetilde{\chi}_{model}(R_i)])^2\} \tag{2.43}$$

N_{pts} is the number of data points in the R space range, N_{idp} is the number of independent points in the data range and ϵ is the average uncertainty in the measurement of $\widetilde{\chi}_{data}(R_i)$; both theory and imaginary parts of $\widetilde{\chi}(R)$ are used in the fit.

In order to estimate ϵ, the program evaluates the RMS value of $\widetilde{\chi}(R)$ between 15 Å and 25 Å where fluctuations are assumed to be white noise. This allows to take into account statistic errors; on the other hand systematic errors due the theoretical modelling of amplitudes and phase shifts are impossible to estimate. As a consequence the χ^2 estimated by equation 2.43 are often by far bigger than the degree of freedom in the fit [124], even in case of very good fit.

Since a good estimation of ϵ is necessary to estimate errors on the structural parameters, the program uses the following strategy. It assuming that, if the fit is visually very good, the reduced chi-square χ^2_ν needs to approach 1; this can be obtained by scaling ϵ by a factor $\sqrt{\chi^2_\nu}$. The new value for the uncertainty on the measurement is exploited to calculate the errors on the structural parameters. Uncertainties are estimated by inverting the Jacobian $N_{nvarys}\ x\ N_{nvarys}$ matrix of the second derivatives of χ^2, with respect to the N_{nvarys} free variables of the fit. The diagonal terms of the inverse matrix give the errors on the structural parameters, the out of diagonals elements

[3]Further details on the modelling can be found on the program manual available on the web site [122].

give the correlations between the variables. Clearly this procedure of error evaluation can work only for fit that are visually very good, which is the case of the most of the analysis in this work.

2.2.6 Experimental stations

In K-edge measurements were performed at the European Synchrotron Radiation Facility in Grenoble (Bending Magnet 8 -GILDA CRG beamline[4]), exploiting a sagittally focusing monochromator equipped with Si [311] crystals, run in the dynamical mode [126]. High order harmonics were rejected by detuning the crystals. Energy range of interest was $[27700 - 29400]$ eV; at such energies the absorption cross section is very low (see Fig. 2.7), which makes the measurement of dilute samples quite challenging and needs an extremely accurate alignment. Flux on the sample was about $3*10^{10}$ photons/s on a spot of 1 mm^2, the In Kα fluorescence signal was monitored using a thirteen-element hyper pure Ge detector (see appendix A).

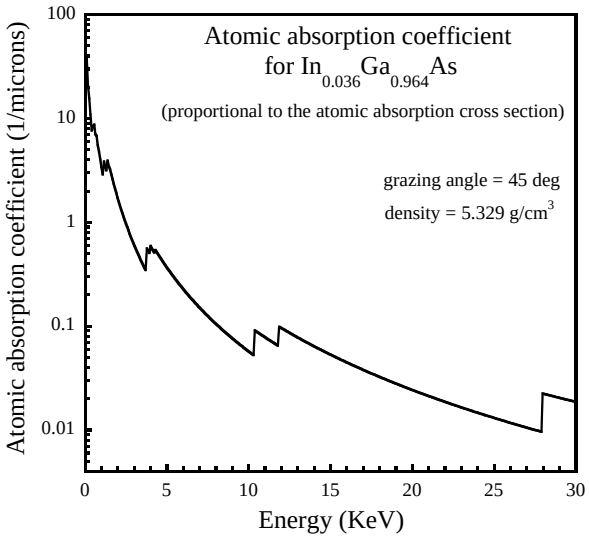

Figure 2.7: Simulation of the atomic absorption coefficient as a function of energy for a $In_xGa_{1-x}As$ with the concentrations of sample 710V; discontinuities correspond to the different absorption edges.

Samples were kept at 77 K in order to reduce the thermal damping of the signal, and an oscillating sample holder (Fig. 2.8) was exploited to limit the effects of the spurious peaks due the occurrence of Bragg reflections. As a matter of fact in our samples the high crystalline quality of the substrate alters the absorption signal in two ways: either reaching directly one or more detector elements and saturating them, or by modulating the fluorescence intensity with the excitation of X-ray standing waves (the

[4]A complete description of the beamline can be found on the PhD thesis of F. D'Acapito [125]

latter effect, opposite to the former, is present in the signal from all detector signals at the same time). The exploitation of parallel acquisition via thirteen detectors elements allows to overcome the detection saturation problem, by averaging the signals from the different elements after the exclusion of the saturated channels. The vibrating sample holder [83] reduces the excitation of standing waves by continuously changing the Bragg condition during data collection and smoothing out the spurious peaks. The signal was normalized point by point by recording the flux incident on the sample with a ionization chamber filled with Argon gas.

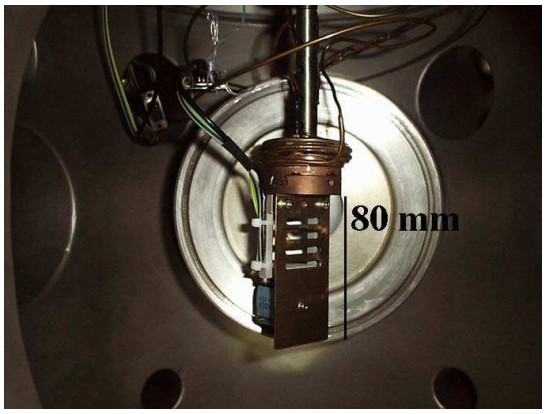

Figure 2.8: Picture of the vibrating sample holder, located inside the XAFS chamber of the Gilda beam line (ESRF).

N K-edge measurements were performed at the ELETTRA facility in Trieste (Aloisa beamline [127]) and at the BESSY II facility in Berlin (U49/2-PGM2, Cottbus beamline [128]). Flux on the sample by using the third harmonic of the undulator was about 10^{12} photons/s at the Aloisa station and $3*10^{12}$ photons/s at the Cottbus one. At the latter station, we were able to rotate the sample and to exploit the polarization dependence of the XAFS signal for studying the symmetry of the N site. The spot size at the center of the experimental chambers was about $30(ver)\ x\ 200(hor)\ \mu m$ at Aloisa, $30(ver)\ x\ 500(hor)\ \mu m$ at Cottbus. Also in case of N K-edge, fluorescence detection was exploited in order to guarantee bulk sensitivity and to limit surface contamination effects, using a window-less single element hyper pure germanium detector. The fluorescence counts were normalized by using the drain current from a gold mesh located before the sample. In case of the N K-edge, we were forced to limit our investigation to the XANES region ($[390 - 440]$ eV) because of the closeness of the oxygen edge and the natural oxidation of the epilayers surfaces.

Ga K-edge measurements were also undertaken at the GILDA CRG beamline of the ESRF using the same dynamical sagittally focusing Si (311) monochromator [126]. High order harmonics were in this case rejected by exploiting two Palladium covered mirrors [125] and detuning the crystals. Absorption coefficient at the Ga threshold was measured by recording the total electrons yield signal via the drain current from the

sample, which is proportional to the non radiative intensity of equation 2.38. Fluorescence yield detection would have not been possible due to the longer free mean path of photons with respect to electrons, combined with the presence of the absorber in the substrate. Flux on the sample was about $3*10^{10}$ photons/s on a spot of 1 mm^2, the energy range was $[10200 - 11300]$ eV.

2.3 X-Ray Diffraction

2.3.1 A bit of theory

X-Ray Diffraction (XRD) is the ideal tool to investigate the periodic structure of materials and to measure the lattice parameters of ordered structure. The long range order character of the probe makes it complementary to XAFS, which on the contrary gives information on the short range order. We will not spend too much words in order to describe a well known and acquired technique such XRD, whose first patterns where recorded at the beginning of century by Friedrich *et al.* [129] in the transmission (Von Laue) geometry and by Bragg [130] in the reflection geometry (Bragg). A description of the basic principles of XRD and of the equivalence of the Von Laue and Bragg's approach can be found in solid state textbooks (see for example Ashcroft and Mermin [131]), and to give a complete overview of the theory and technical developments in this field is beyond the purposes of this work. We will limit to remind here the few basic concepts which are mandatory in order to understand the present results.

Diffraction condition by a family of parallel crystallographic planes occurs when the waves scattered by the single planes interfere constructively each other. This fixes a relationship among the distance between the crystallographic planes d_{hkl}, the wavelength λ and the incidence angle θ :

$$2d_{hkl}sin\theta = \lambda \tag{2.44}$$

We used the subscript hkl because, for each family of planes, there are perpendicular vectors in the reciprocal space, the shortest of which has a length $\frac{2\pi}{d}$. The coordinates of this vector (h, k, l), referred to as "Miller indices", define the family of planes under study; in case of absence of high order harmonics (they are neglected in equation 2.44), this vector (let's call it $\overrightarrow{q}$) is the exchanged wave vector of the scattering process.

For cubic crystals, the relationship between the lattice planes distances and their corresponding Miller indices is particularly simple and, if we indicate with a the lattice parameter of the crystal, the diffraction condition is:

$$2asin\theta = \lambda\sqrt{h^2 + k^2 + l^2} \tag{2.45}$$

This provides a vary simple way to measure a, setting a well defined wavelength and performing an angular scan to determinate the maximum of the diffraction peak.

The intensity of the Bragg's peak is proportional to the square of the absolute value of the diffracted wave amplitude. In case of a zincblend crystal, as $Ga_{1-x}As_{1-y}N_y$ and $In_xGa_{1-x}As_{1-y}N_y$, a basis consisting of one-two cations placed at $(0, 0, 0)$ and two

anions placed at $(\frac{1}{4}, \frac{1}{4}, \frac{1}{4})$ is necessary in order to describe the position of all atoms inside the unit cell. As a consequence a *unit cell structure factor* F_{cell} appears in the expression of the diffracted wave amplitude F; since the single ions inside the unit cell are chemically different, they are weighted each by its atomic form factor f_j :

$$F = \sum_{\alpha \equiv \ cell}^{over\ whole\ crystal} e^{i\overrightarrow{Q}\cdot\overrightarrow{r_\alpha}} \sum_{j\ \in\ cell} f_j e^{i\overrightarrow{Q}\cdot\overrightarrow{r_j}} e^{-M_j Q^2} = I\left(\overrightarrow{Q}\right) F_{cell} \tag{2.46}$$

Here $\overrightarrow{Q} = 2\pi\overrightarrow{q}$, I is the interference function, also referred to as *form factor* of the crystal; if $\overrightarrow{Q}\cdot\overrightarrow{r_\alpha}$ is multiple of 2π the different unit cells scatter in phase and diffraction takes place. In some case, for definite values of $\overrightarrow{Q}$ and particular arrangements of the ions inside the cell (described by the term F_{cell}), cancellations can occur and inhibit diffraction. F_{cell} can make the diffraction amplitude vanish or sensibly decrease for a particular choice of the Miller indices, some reflections result in this way forbidden or weakened for a particular structure. The term $e^{-M_j Q^2}$ is the Debye-Waller factor and takes into account thermic and structural disorder in the atomic distribution.

The relationship 2.46 is valid in case of the *kinematical approximation*, which is rigorous for thin crystals characterized by not excellent periodic quality [132]. In this approximation the photon is described by a plane wave, the scattering is elastic and the photons are scattered only once, i.e. multiple scattering is neglected. A theory which goes further the kinematical approximation, the *dynamical theory*, has been elaborated in the seventies [133]; this theory is mandatory in order to describe the behavior of "perfect" and thick crystals.

If the quality of the crystal is very high, it becomes also more likely that the diffraction condition of equation 2.45 is satisfied by two families of planes, characterized by different Miller indices. In this case, if we look at one of the two reflection, its Bragg intensity can be decreased (Aufhellung process) or also increased (Umweganregung process) due to the presence of the second one [134]. This phenomenon, called *multiple diffraction*, is particularly tedious when analyzing the fine structure of the diffracted intensity near an absorption edge (section 2.4), while does not create problems if we are only interested in determining the angular position of the diffracted peak.

2.3.2 Geometry of the experiments

All the samples investigated in this work have been characterized by XRD; we exploited the so called $\theta - 2\theta$ or Bragg-Brentano geometry in which, as the sample rotates of an angle θ about an horizontal axis perpendicular to the X-ray incident beam, the detector moves by an angle 2θ about the same axis in order to catch the reflection. A pictorial view illustrating the θ and 2θ circles together with the others degrees of freedom necessary for our measurements is reported in Fig. 2.9.

Samples were analyzed choosing the (004) and the (006) Bragg's reflections, this choice permitted to measure the distance between lattice planes along the growth axis; our samples are in fact grown on GaAs (001). In order to perform these measurements the χ angle of Fig. 2.9 was set to $0°$, while θ and 2θ were rotated simultaneously. Being

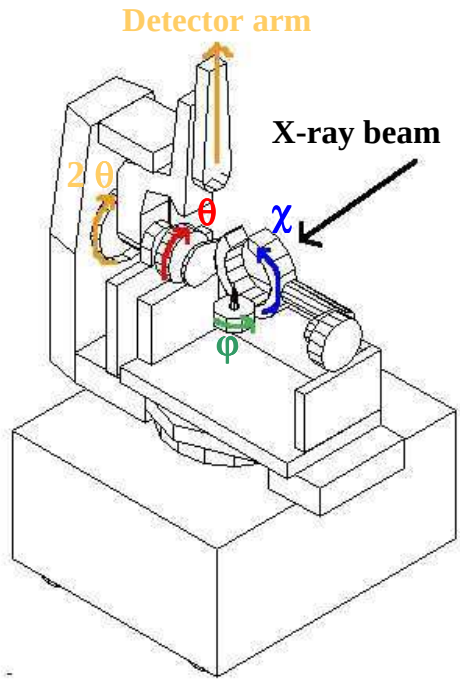

Figure 2.9: Pictorial view of a diffractometer for XRD in Bragg-Brentano geometry. The figure reports a modified scheme of the diffractometer of the D2AM CRG beamline of the ESRF; only the circles of interest are indicated. The sample is located on the tip, χ (blue) represents the rotation around the axis of the incident X-ray beam, ϕ (green) the rotation around the vertical axis.

the unit cell of the investigated epilayers and quantum wells not rigourously cubic, but tetragonally distorted (section 1.5.2), the (004) and the (006) crystal plane reflections give directly access to the *out of plane of growth* lattice parameter $a_\perp$, applying equation 2.45.

The (006) reflection is forbidden for the diamond lattice, as well as all reflections for which the sum of the Miller indices is twice an odd integer [131]. In the case of the zincblend structure, which is similar to the diamond except for the fact that a basis is necessary to account for the presence of chemically different elements; the different atomic form factor between anions and cations forbids the structure factor to completely vanish. Nevertheless this factor is consistently reduced and the (006) is called a "weak" reflection; this is the case of dilute nitrides investigated in this work.

Several samples were measured in the vicinity of the (224) crystal plane reflection, which has an *in plane* component. This was useful to extract the lattice parameter *in the plane of growth* $a_\parallel$, once $a_\perp$ is known from (004) XRD measurements. $a_\parallel$ is used in equation 1.20 to calculate the distortion of the bond-lengths induced by strain; in particular the knowledge of $a_\parallel$ allows to verify if samples are coherently grown on the substrate. In order to select the (224) reflection, the angle χ was fixed at 35.264° for

the substrate peak.

2.3.3 Experimental stations

The X-ray diffraction experiments in this work have been performed on four different experimental station. The first was a Rigaku 12 kW molybdenum rotating anode X-ray generator of the CNRS in Grenoble, where the Mo Kα_1 fluorescence line (wavelength =0.7092 Å) was selected as incident wavelength by using a Si (111) channel cut monochromator, set in front of a linear X-ray focus (0.05 x 10 mm2). The scattered intensity was detected by using a GMI diffractometer equipped with a NaI(Tl) scintillation detector, resolution in terms of FWMH of the substrate peak in angle θ was 0.005°. Some samples were measured at the CNRS by using a copper rotating anode, not provided with a channel cut, and referring to the Cu Kα_1 fluorescence line for the determination of the lattice parameters. In this case doubled Bragg's peaks, due to the presence of the Kα_2 was observed in the spectra. In this case the FWMH in θ was larger (0.03°).

Part of the samples was measured by a 16 kW Philips X'Pert PRO MRD copper anode diffractometer at the University of Padova (Italy), a Bartels monochromator consisting of four Ge (220) crystals (two channel-cut) was here exploited to select the Cu Kα_1 fluorescence line (wavelength =1.54088 Å). In this diffractometer a parabolic mirror collects the beam before it impinges the monochromator, reducing the divergence and increasing the intensity. In the *triple axis configuration* the diffracted beam encounters again two (220) reflections by a Ge channel-cut analyzer before entering the detector. These multiple reflections allow reducing the angular acceptance and mapping in details the reciprocal space; the resolution in terms of FWMH of the substrate peak in angle θ was 0.003°. In the *standard configuration* the diffracted beam is collected without using the analyzer, and placing slits in front of the detector; in this case FWMH in θ was 0.006°. The detector exploited was a proportional counter using Xenon gas.

Finally some $\theta - 2\theta$ scans were performed by using the seven circle-diffractometer of the French D2AM CRG beamline of the European Synchrotron Radiation Facility, choosing X-ray energies in the vicinity of the Gallium absorption threshold (wavelength =1.19595 Å). This experimental apparatus will be described in the next section dedicated to Diffraction Anomalous Fine Structure (2.4).

2.4 Diffraction Anomalous Fine Structure

2.4.1 The basic ideas

Diffraction anomalous fine structure (DAFS) refers to a fine structure in the intensity of an X-ray diffraction peak, as a function of the incident X-ray energy, in the vicinity of an absorption edge. This phenomenon, first observed by Y. Cauchois [135] in 1956, finds its physical origin in the proportionality between the imaginary part of the atomic form factor f introduced in equation 2.46 and the total atomic cross section. The last

is defined as the sum of the atomic cross sections for elastic scattering and absorption :

$$\sigma_{A,total(E)} = \sigma_{elesticscatt.} + \sigma_{absorption} \tag{2.47}$$

If we call f_{Aj} the atomic form factor (also referred to as atomic scattering factor) for an atom A on a site j, the relationship with $\sigma_{Aj,total(E)}$ is given (in the forward scattering limit) by the optical theorem [136] :

$$f''_{Aj}(\overrightarrow{Q} = 0, E) = \frac{E}{2hcr_0}\sigma_{Aj,total} \tag{2.48}$$

r_0 is the classical electron radius, f''_{Aj} is the imaginary part of f_{Aj} :

$$f_A(\overrightarrow{Q}, E) = f_{0A}(\overrightarrow{Q}) + f'_A(E) + if''_A(E) \tag{2.49}$$

For a non-forward scattering the relation 2.48 is valid in the dipole approximation; some studies have recently addressed the issue of the limit field of application for this relationship [137].

The absorption cross section $\sigma_{absorption}$ is proportional to the absorption coefficient, which shows oscillations in the vicinity of the absorption edges; the amplitude and frequency of these oscillation contain information on the local environment of the absorber (section 2.2). Due to the optical theorem, these oscillatory structures propagate into f''_{Aj} and also into the energy-dependent real part of the atomic form factor f'_A, since it is related to f''_{Aj} via the Kramers-Kronig relationships [138] :

$$f'(E) = \frac{2}{\pi}P\int_0^\infty \frac{E'f''(E')}{E^2 - E'^2}dE' \tag{2.50}$$

$$f''(E) = -\frac{2E}{\pi}P\int_0^\infty \frac{f'(E')}{E^2 - E'^2}dE' \tag{2.51}$$

P indicates here the principal part of the integral. $f'_A(E)$ and $f''_A(E)$ are called anomalous contributions of the atomic form factor; elsewhere they are very low, but become relevant near an absorption edge. Since they enter the expression of the structure factor of the cell F_{cell} and of the diffracted intensity, which is proportional to the square of F_{cell}, the oscillatory XAFS-like behavior propagates in the energy dependence of the the Bragg peak amplitude. The same information available from an XAFS analysis can be in principle obtained studying the fine structure of the diffracted peak in the vicinity of an absorption edge.

The fundamental idea which aimed the developing of DAFS was to unify the chemical selectivity of XAFS to the spatial and site selective of XRD. By means of DAFS it is possible, despite a more elaborate experimental set up and data analysis compared to XAFS, to select the contribution of a particular absorber (choosing the X-ray energy near an absorption edge) embedded in a specific long range structure (choosing a particular Bragg peak). This allows, for example, to study the local structure of a particular element present both in the active layer and in the substrate/cap of a thin quantum wells, by selecting the Bragg peak of the only active layer thanks to the mismatch

between the lattice parameters. This spatial selectivity of DAFS was exploited in the present work to study the local environment of Ga in thin $In_xGa_{1-x}As_{1-y}N_y/GaAs$ quantum wells.

The site selectivity of DAFS, instead, allows to discriminate the contributions of the different sites of an unique crystallographic structure in which an absorber can be located. In this case the different sites contribute to the same Bragg peak, but for a particular choice of the reflection the contribution from some of them cancel in the expression of the structure factor, so that only information about the local structure of the others is obtained. That is the case studied by Pickering *et al.* [139], which separated the contributions of the tetrahedral and octahedral sites of Co in the spinel Co_3O_4 structure, using the (222) crystal plane reflection to enhance the contribution of the former site and the (220) reflection to enhance that of the latter.

2.4.2 Data analysis

Next step is to show how XAFS-like information can be extracted from a DAFS spectrum. A demonstration of the DAFS spectroscopy was advanced by Stragier *et al.* [140] in 1992, while an explanation of the DAFS data analysis in the extended region above an absorption edge was provided by Proietti *et al.* [141]; we will mostly refer to the last paper in the following. The anomalous contributions to the atomic form factor can be divided into a non-oscillating component and an oscillating one :

$$f'_{Aj} = f'_{0A} + \Delta f''_{0A}\chi'_{Aj} \tag{2.52}$$
$$f''_{Aj} = f''_{0A} + \Delta f''_{0A}\chi''_{Aj} \tag{2.53}$$

so that

$$f_A(\overrightarrow{Q}, E) = f_{0A}(\overrightarrow{Q}) + f'_{0A}(E) + if''_{0A}(E) + \Delta f''_{0A}[\chi'_{Aj}(E) + i\chi''_{Aj}(E)] \tag{2.54}$$

$\chi'_{Aj}(E) + i\chi''_{Aj}(E)$ is the complex fine structure i.e. the correction due to the local environment of the anomalous atoms. The cell structure factor F_{cell} of equation 2.46 can be written in this way for a general non-centrosymmetric cell with N_A anomalous atoms in the basis:

$$F_{cell}(\overrightarrow{Q}, E) = F_T(\overrightarrow{Q}, E)e^{i\varphi_T\left(\overrightarrow{Q}\right)} + \sum_{j=1}^{N_A} |\alpha_{Aj}(\overrightarrow{Q})|e^{i\varphi_{Aj}(\overrightarrow{Q})}\left[f'_{Aj}(E) + if''_{Aj}(E)\right] \tag{2.55}$$

$F_T(\overrightarrow{Q}, E)$ is a complex structure factor of phase φ_T, that includes the net contribution of all non-anomalous atoms and the Thompson scattering of all anomalous atoms, $\alpha_{Aj}(\overrightarrow{Q}) = c_{Aj}e^{-M_{Aj}Q^2}e^{i\varphi_{Aj}\left(\overrightarrow{Q}\right)}$, where c_{Aj} is the occupation factor of atom A on site j and $e^{-M_{Aj}Q^2}$ is the Debye-Waller factor, $\varphi_{Aj}(\overrightarrow{Q}) = \overrightarrow{Q} \cdot \overrightarrow{r_j}$ and $|\alpha_{Aj}(Q)| = \sqrt{\alpha_{Aj}\alpha^*_{Aj}}$.

If we call $F_0(\overrightarrow{Q}, E)$ the complex smooth structure factor, calculated without taking into account the complex fine structure, and assuming that f'_{0A} and f''_{0A} are identical for all anomalous atoms, from equation 2.55 it follows that :

$$|F_0(\overrightarrow{Q}, E)|^2 = |F_T|^2\{[cos(\varphi_T - \varphi_A) + \beta f'_{0A}]^2 + [sin(\varphi_T - \varphi_A) + \beta f''_{0A}]^2\} \quad (2.56)$$

$\beta = |\alpha_A|/|F_T|$ and $|\alpha_A|e^{i\varphi_A} = \sum_{j=1}^{N_A} \alpha_{Aj} e^{i\varphi_{Aj}}$. The energy dependent non-oscillatory variation of the diffracted intensity near an absorption edge, to which $|F_0(\overrightarrow{Q}, E)|^2$ is proportional, depends on the only two parameters $\Delta\varphi = \varphi_T - \varphi_A$ and β. These parameters determine the shape of the DAFS spectrum, and their experimental determination through a fit of the smooth DAFS line shape by equation 2.56 gives access to important information on the crystallographic structure. In case only one anomalous site contributes to the reflection, equation 2.56 remains valid for F_{cell}, if we substitutes f'_{0A} with f'_{Aj} and f''_{0A} with f''_{Aj} (now the index j becomes superfluous).

Two procedures can be now used in order to extract XAFS-like information. If we have a single anomalous site contribution, an iterative Kramers-Kronig procedure can be used to extract χ'_A and χ''_A from equation 2.56, assigning f'_A and f''_A the initial values f'_{0A} and f''_{0A}. The extracted oscillatory signal χ''_A can be analyzed with the standard XAFS tools. As a matter of fact, even if f''_{Aj} (equation 2.48) is proportional to the total cross section $\sigma_{Aj,total}$, it is virtually proportional to the absorption cross section, being this one by far greater than the atomic cross section for elastic scattering in the energy range of our DAFS experiments [108]. This method needn't the use of crystallographic information, but cannot be applied in case of multiple anomalous sites. An alternative procedure consists in taking only the first order terms in the expansion of the square modulus of F_{cell}, approximation which has been demonstrated to be valid for DAFS analysis [141]; the expression of $|F_{cell}|^2$ becomes:

$$|F_{cell}(Q, E)|^2 = |F_0|^2 + 2|F_0||\alpha_A|\Delta f''_{0A} \sum_{j=1}^{N_A} w_{Aj}[cos(\varphi_0 - \varphi_{Aj})\chi'_{Aj} + sin(\varphi_0 - \varphi_{Aj})\chi''_{Aj}] \quad (2.57)$$

From this it follows for the Extended-DAFS oscillations $\chi_{\overrightarrow{Q}}(k)$, given a scattering vector $\overrightarrow{Q}$:

$$\chi_{\overrightarrow{Q}}(k) = \sum_{j=1}^{N_A} w_{Aj}[cos(\varphi_0 - \varphi_{Aj})\chi'_{Aj} + sin(\varphi_0 - \varphi_{Aj})\chi''_{Aj}] = \frac{|F_0|}{2|\alpha_A|\Delta f''_{0A}} \left(\frac{|F_{cell}|^2 - |F_0|^2}{|F_0|^2} \right) \quad (2.58)$$

where K is the photoelectron wave number.

$|F_{cell}|^2$ is proportional to the measured diffracted intensity through different correction factors :

$$I(\overrightarrow{Q}, E) = SD(E)A(Q, E)L(Q, E)P(Q)|F_{cell}(\overrightarrow{Q}, E)|^2 \quad (2.59)$$

S is a scale factor, A is the correction accounting for the absorption of the incident and diffracted beams including geometrical effects (i.e. variation of the spot on the samples varying the incident angle), L and P are the Lorenz and Polarization corrections. If we call I_{expt} the experimental intensity corrected for what listed above and for the fluorescence background, equation 2.58 becomes:

$$\chi_{\overrightarrow{Q}}(k) = \sum_{j=1}^{N_A} w_{Aj}[cos(\varphi_0 - \varphi_{Aj})\chi'_{Aj} + sin(\varphi_0 - \varphi_{Aj})\chi''_{Aj}] = \frac{|F_0|}{2|\alpha_A|\Delta f''_{0A}} \left(\frac{|I_{exp}| - |I_{0\ exp}|}{|I_{0\ exp}|} \right) \tag{2.60}$$

$I_{0\ exp}$ is the smooth background of the experimental DAFS oscillations. The net amplitude of DAFS oscillations is proportional to the ratio $\frac{|\alpha_A|}{|F_0|}$. We will call S_d the DAFS normalization factor, which has to be taken into account in order to analyze the experimental DAFS into a XAFS formalism :

$$S_d = \frac{|F_0|}{2|\alpha_A|\Delta f''_{0A}} \tag{2.61}$$

The phase differences $\varphi_0 - \varphi_{Aj}$ in the equation 2.60, the weights w_{Aj} and S_d can be calculated via the crystallographic structure. S_d, using equation 2.60 and equation 2.56, is :

$$S_d = \frac{\sqrt{[cos(\Delta\Phi) + \beta f'_{0A}]^2 + [sin(\Delta\Phi) + \beta f''_{0A}]^2}}{[2\beta\Delta f''_{0A}]} \tag{2.62}$$

In other words S_d is expressed in function of $\Delta\Phi$ and β and can be calculated by fitting the smooth part of the corrected experimental intensity with equation 2.56, without a precise knowledge of the crystallography.

The complex fine structure due to an atom A on site j may be written, according to Stragier *et al.* [140], as an expansion over the scattering paths of the photoelectron around the absorbing atom :

$$\chi'_{Aj} + i\chi''_{Aj} = -\sum_{\Gamma} Amp^{\Gamma}_{Aj}(k) exp\{-i[2kR^{\Gamma}_{Aj} + \delta^{\Gamma}_{Aj}(k)]\} \tag{2.63}$$

where χ''_{Aj} is equivalent to the XAFS signal and χ'_{Aj} is related to it via the Kramers-Kronig transform; Γ indicates a photoelectron scattering path, $Amp^{\Gamma}_{Aj}(k)$ is the amplitude of the scattering process along the path Γ, $\delta^{\Gamma}_{Aj}(k)$ is its phase shift and R^{Γ}_{Aj} is the effective path length. The real part χ'_{Aj} of the complex fine structure is a sum of cosine function and the imaginary part χ''_{Aj} is a sum of sine functions. From equations 2.60 and 2.63 the DAFS oscillations can be expressed in a way which is very similar to that one of XAFS :

$$\chi_{\overrightarrow{Q}}(k) = \sum_{j} \sum_{\Gamma} w_{Aj}(\overrightarrow{Q}) Amp^{\Gamma}_{Aj} sin[2kR^{\Gamma}_{Aj} + \delta^{\Gamma}_{Aj}(k) + \varphi_0(\overrightarrow{Q}, k) - \varphi_{Aj}(\overrightarrow{Q}) - \frac{\pi}{2}] \tag{2.64}$$

Equation 2.64 introduces a parametrization of the DAFS oscillations which can be treated like XAFS, if the crystallographic weights w_{Aj} are calculated and the phases $\varphi_0 - \varphi_{Aj}$ added to the photoelectron phase shift.

In case of a single anomalous site, the phase difference $\varphi_0 - \varphi_A$ in equation 2.64 can be expressed in function of the only variable β and $\Delta\Phi$ of equation 2.56.

$$cos(\varphi_0 - \varphi_A) = \frac{[cos(\Delta\Phi) + \beta f'_{0A}]}{\sqrt{[cos(\Delta\Phi) + \beta f'_{0A}]^2 + [sin(\Delta\Phi) + \beta f''_{0A}]^2}} \tag{2.65}$$

$$sin(\varphi_0 - \varphi_A) = \frac{[sin(\Delta\Phi) + \beta f''_{0A}]}{\sqrt{[cos(\Delta\Phi) + \beta f'_{0A}]^2 + [sin(\Delta\Phi) + \beta f''_{0A}]^2}} \tag{2.66}$$

This means that, for a single anomalous site, $\varphi_0 - \varphi_A$ can be obtained, as was the case of S_d, from a fitting of the smooth part of the DAFS spectrum with equation 2.56. As a consequence the XAFS-like information, whose variables appear parameterized in equation 2.64, can be obtained directly from the experimental intensity as suggested by equation 2.60, determining S_d and $\varphi_0 - \varphi_A$ without using the knowledge of the crystallography.

In case of measurements on $In_xGa_{1-x}As_{1-y}N_y$ quantum wells at the Ga K-edge we dealt with a non-centrosymmetric zincblend structure whose basis consisted of four elements: two cations located in position (0,0,0) and two anions located in position $(\frac{1}{4},\frac{1}{4},\frac{1}{4})$. The only anomalous atom of the basis was the Ga (0,0,0), which allowed us to determine $\varphi_0 - \varphi_A$ and S_d by fitting of the smooth part of DAFS as shown in Fig. 2.10. The fits were performed by the code DPU, developed by P. Wolfers *et al.* at CNRS-Grenoble, without exploiting the knowledge of the crystallographic structure. The

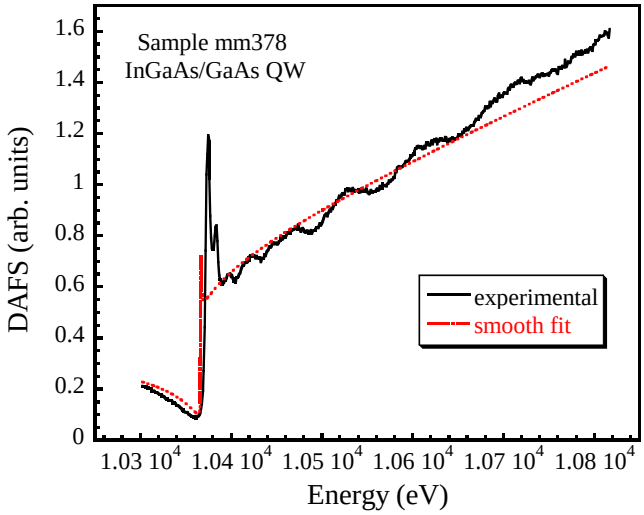

Figure 2.10: Normalized raw experimental DAFS and fit of the smooth part performed by DPU.

chosen reflection was the weak (006) one, where the Thompson scattering contributions of Ga and As almost cancel out. This causes the anomalous effect to be quite large : diffracted intensity at the Ga edge is about a factor 5.5 larger than 80 eV below the edge.

In order to evaluate the amount of the absorption correction, this value has to be compared with the relative variation through the Ga edge of the factor $A(\overrightarrow{Q}, E)$ appearing in equation 2.59. This correction comes from the fact that the absorption of photons near an edge can introduce structures which distort the diffracted intensity on the peak of interest. For a sample of thickness t, in reflection geometry, with the diffraction vector perpendicular to the surface (symmetric reflection), $A(\overrightarrow{Q}, E)$ is [142]:

$$A(\overrightarrow{Q}, E) = \int_0^t e^{-2\mu z/sin\theta_B} dz = \frac{1 - e^{-2\mu t/sin\theta_B}}{2\mu/sin\theta_B} \tag{2.67}$$

For a 10nm $In_xGa_{1-x}As_{1-y}N_y$ film with concentrations in the range of our samples and a beam incident at an angle θ of about 39, as in case of our measurements, the relative variation of $A(\overrightarrow{Q}, E)$ at the gallium edge (calculated via equation 2.67) virtually doesn't distinguish from 1 (1.0007). For this reason we could neglect absorption correction in this work. The relative jump in $A(\overrightarrow{Q}, E)$ would be 1.07 for a 1 μm-thick sample and 1.72 for a 1 cm-thick sample; this shows how also for bulk samples the absorption correction is not a concern in the case of a weak reflection.

The polarization correction $P(Q)$, in case of an electric field perpendicular to the plane of incidence, as in the $\theta - 2\theta$ geometry, is:

$$P = p + (1 - p)cos^2(2\theta) \tag{2.68}$$

where p is the polarization rate in the plane perpendicular to the scattering plane, which was close to unity (95 %) at the bending magnet of the D2AM beam line of ESRF (polarization almost entirely linear); as consequence also P was close to 1 and this correction could be neglected. The Lorenz correction given by $L = \frac{\lambda^2}{sin2\theta}$ was not necessary too, since we were interested only in DAFS oscillation. Finally, the fluorescence background, which in case of a weak reflection is comparable to the diffracted intensity, was eliminated by using a crystal analyzer (see following section).

Once evaluated $(\varphi_0 - \varphi_A)$ and S_d as a function of k, the first was added to the phase of the theoretical paths calculated by Feff800 [103] as described in section 2.2.5, XAFS-like oscillations were extracted from the normalized diffracted intensity with the Autobk code [113], but without subtracting a pre-edge and without normalizing by the jump as in section 2.2. Then, the DAFS oscillating signal has been k-weighted, apodizated and Fourier-transformed in the R-space. After that a fit was performed by the Feffit code [123], varying the structural variables in the parameterized equation 2.64 and introducing the previously evaluated S_d factor in order to reproduce the experimental amplitudes.

2.4.3 The experimental station

DAFS experiments were undertaken at the D2AM CRG bending magnet beam line (BM02) of the European Synchrotron Radiation Facility, exploiting a Si(111) double crystal monochromator. Sagittal focusing was obtained by bending the second crystal, while vertical focusing by using two mirrors. The first mirror (placed before the monochromator) collimated the beam, while the second (placed after the monochromator) focalized it. The two mirrors were coated with platinum and allowed also to reject high order harmonics. Normalization of the diffracted intensity was obtained by measuring the fluorescence intensity emitted by a pure Ti foil mounted in vacuum at 45° with respect to the beam path. A more complete description of the beam line can be found in the PhD thesis of S. Grenier [143].

Samples were mounted on a 7-circle diffractometer (illustrated in Fig. 2.9) where three Euler circles (θ, φ, χ) were dedicated to sample movements; the other circles were the vertical motion 2θ of the detector arm (same rotation axis of θ), the horizontal motion of the detector arm α, the vertical motion of the analyzer crystal θ_A (carried by the detector arm) and the vertical motion of the detector after the analyzing crystal $2\theta_A$. The angular movements had a resolution better than 0.001°, the tracking of the Bragg's peak during an energy scan was obtained by previously determining the θ and 2θ angles for three or four points equally spaced in the energy range of interest, and by applying a linear regression.

Elimination of the sample fluorescence background, which is a concern when dealing with weak reflections, was achieved by the utilization of a (002) flat graphite single crystal analyzer. In Fig. 2.11 note how the diffraction peak (on the right side) can be separated, after the edge, from the Ga Kβ fluorescence one (on the left side), by an opportune energy calibration of the analyzer. Elimination of the Ga Kα fluorescence is by far less problematic, due to the larger energy shift of the related peak with respect to the diffraction one.

Since on the (006) weak reflection we had less than 2000 photons/s on the detector, the use of a photomultiplier (Cyberstar) combined with a NaI scintillator crystal was sufficient to avoid dead time distortions (which arise when exceeding 100000 photons/s). We used a PIN silicon photodiode (Canberra-Eurysis, PD 300-15-300 CB) for performing some $\theta - 2\theta$ scan in the vicinity of the (004) crystal plane reflection. A final refurbishment was the use of a vibrating sample holder, necessary to limit the distortions introduced into the DAFS spectra by multiple diffraction, averaging the probability to satisfy the Bragg's condition for two families of crystal planes (see section 2.3). As a matter of fact our quantum wells were of excellent crystalline quality, and subjected to dynamical effects despite their low thickness (less than 10 Å).

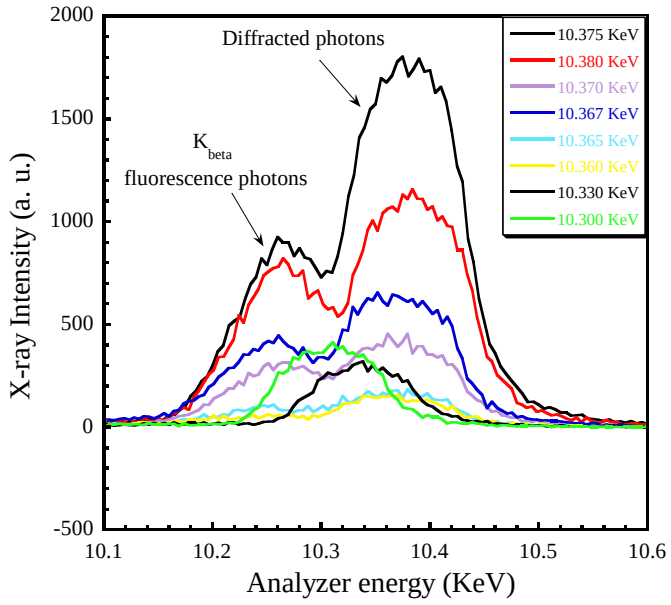

Figure 2.11: Energy scans performed with the crystal analyzer for different values of the incident beam energy (reported in the legend): after the edge (E = 10.367 KeV) the Ga Kβ fluorescence radiation can be separated from diffraction.

2.5 Complementary techniques

2.5.1 Rutherford Back-scattering Spectrometry

Rutherford backscattering Spectrometry (RBS) is the study of the energy spectra of α-particles backscattered from a target [144]. From these spectra it is possible to obtain information about the concentration of the atomic elements in a material and on the thickness of an epilayer. As a matter of fact, for a given geometry, the energy of ions scattered from an atom at the sample surface is a function of the atom mass; as a result the different elements can be identified by the energy values of the edges in the RBS spectra (RBS yield vs. energy). The thickness of a layer is determined by measuring the energy lost by the ions from the surface to the layer/substrate interface, and the concentration of the elements is obtained from the heights of the spectra in the energy range relative to the scattering from each element. RBS spectra were collected with a 2 MeV $^4He^+$ beam at the CN accelerator of the *Legnaro National Laboratories* (Padova, I), in order to determine the In concentration and thickness of the $In_xGa_{1-x}As_{1-y}N_y$ and $In_xGa_{1-x}As$ epilayers.

In case of a low mass atom in a heavy matrix, conventional RBS is not suitable because the signal related to the light atom is too weak; that was the case of N in the alloys studied in this work. Resonant Back-Scattering spectrometry (r-BS) [145], using energetic He beams, has been developed in order to enhance the cross section

over the Rutherford for the light element, and to extract its backscattering signal from the background. Unfortunately, in the case of nitrogen, the reported ratios of the N elastic resonant cross section with respect to the Rutherford are all below 100 and this is not sufficient to detect 1 at % N in GaAs ; in consequence r-BS couldn't be exploited in our case.

2.5.2 Nuclear Reaction Analysis

Nuclear Reaction Analysis (NRA), which is also a well established technique for material analysis [146], allows to select the contribution of the only nitrogen, exploiting deuteron induced nuclear reactions [147]. In particular the better choice in this case was the $^{14}N(d,\alpha_1)^{12}C$ reaction, which involves as final state the first excited state of carbon; this reaction channel is more probable than that involving the fundamental state of C (α_0) and was tested to be completely unaffected by substrate contributions [148]. In this reaction α particles are detected.

N concentration can be determined from the reaction yield, calibrating previously the reaction on a standard whose concentration is extracted with an independent technique; in the present case the standard was a Si_3N_4/Si sample and its N concentration was determined by RBS. By exploiting the channelling technique, aligning the deuteron beam along the main crystallographic planes and comparing the reaction yield with that of NRA performed in a random geometry, it was possible to study the lattice location of N atoms. The reaction yield in fact, if N is substitutional to As in the zincblend cell, is supposed to diminish consistently when the beam is aligned along a definite planes family with respect to a random geometry, while it diminishes less if the beam finds on its track a fraction of interstitial N atoms.

NRA in channelling geometry was used in this work to determine the substitutional fraction of N atoms in $In_xGa_{1-x}As_{1-y}N_y$ and $GaAs_{1-y}N_y$ epilayers. NRA was also exploited in order to achieve a direct measurement of the nitrogen concentration in our epilayers; these concentrations were associated to the lattice parameters measured by XRD in order to verify the validity of the Vegard's law, often questioned for III-V nitrides.

The N substitutional fraction f_{001} along the (001) crystallographic direction is defined as :

$$f_{001} = \frac{1-\chi_N}{1-\chi_M} \tag{2.69}$$

Where χ_N is the ratio between the (001) channelling and random yield for the N impurities, while χ_M is that one for the GaAs matrix, measured by parallel RBS (2.5.1). In Fig. 2.12, NRA spectra in the range of the α_1 peak (on the right) corresponding to the reaction of interest $^{14}N(d,\alpha_1)^{12}C$, taken in the random and (001) aligned geometries, are reported for a $GaAs_{1-y}N_y$ sample and a GaAs reference. It is evident the decrease of the yield in the channelling mode in the case of $GaAs_{1-y}N_y$ and how the substrate does not contribute to the reaction.

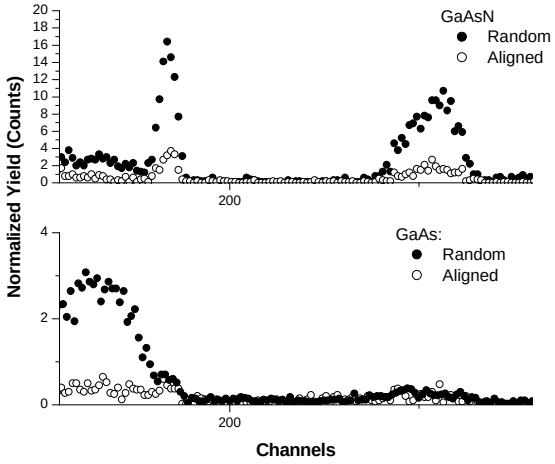

Figure 2.12: NRA energy spectra in the range of the α_1 reaction product (peak on the right) for $GaAs_{1-y}N_y$ and GaAs samples in random and aligned geometries.

NRA was performed with a deuterium beam in the energy range (900 - 1250) KeV at the CN accelerator of the *Legnaro National Laboratories* (Padova, I), exploiting a silicon solid state detector positioned at a scattering angle of 150° (IBM geometry). A parallel RBS acquisition, exploiting another silicon detector, was also set up; NRA and RBS spectra were collected both in the random and channelling geometry. Random spectra, in order to avoid any channelling, were acquired rotating the sample around a selected axial direction with an azimuth angle of 5°. Further information on the experimental setup can be found in the paper of Bisognin *et al.* [148] and references within.

2.5.3 Photoluminescence Spectroscopy

Photoluminescence spectroscopy (PL) is the technique normally employed to measure the band gap of semiconductors. Radiation of suitable energy emitted from a laser is exploited to generate electron-hole pairs in the material; the radiation emitted following the recombination is analyzed in energy via a diffraction reticle monochromator and collected, obtaining spectra in which the PL intensity is reported as a function of energy. PL is not a bulky technique, since it measures the energy difference related to transition between the top of the valence band and the lowest energy states of the conduction band. In case of not homogeneous samples, PL measures the band gap of the part of the sample whose conduction band states are lowest in energy. If a low temperature is set in order to minimize thermal vibration and to enhance the signal, PL can be sensitive to localized states near the conduction band edge, which are on the contrary ionized at room temperature. In this sense a low temperature PL measurement can be less indicative than a room temperature one in order to give an estimation of the gap.

All the samples analyzed in this work were characterized by PL spectroscopy. Room

temperature PL on $(In_x)Ga_{1-x}As_{1-y}(N_y)$ epilayers was performed at the University of Padova (I) by using the 488 nm line of a Ar^+ laser and collecting the emitted radiation by a liquid nitrogen cooled photomultiplier tube. PL measurements at low temperature (10 K) were performed at CEA/DRFMC in Grenoble (F), by using a liquid helium cryostat and exploiting as incident radiation the 702 nm line of a Ar^+ laser. The laser worked at 20 mW and scans were recorded with a wavelength step of 10 Å. PL on quantum wells and hydrogenated epilayers have been performed at the University of Rome "La Sapienza" (I), always at T = 150 K and T = 10 K, employing the 515 nm line of a Ar^+ laser and a N_2 cooled Ge detector.

2.5.4 Supercell Simulations

Supercell simulations were undertaken at the National Research Council (CNR) in Rome (I), in order to investigate the possible relaxation of the lattice upon hydrogenation in $GaAs_{1-y}N_y$ epilayers and $In_xGa_{1-x}As_{1-y}N_y$ quantum wells, due to the formation of $H_2^*(N)$ complexes (section 1.3.3). Simulations were performed in the framework of the density functional theory (DFT) [46, 47] in the local density approximation (LDA) [48, 49]. Total energies were calculated using supercells, separable *ab initio* pseudopotentials, plane-wave basis sets, the special-points technique for K-space integration, and the exchange-correlation functional of Ceperley-Alder [149]. Ultrasoft pseudopotentials were used in the case of nitrogen [150] and nonlinear core corrections were introduced in the case of indium. Convergence tests were done by using plane-wave cutoffs ranging from 18 to 28 Ry, supercells of 32 and 64 atoms, and k-point meshes equivalent to a (4,4,4) or (8,8,8) Monkhrost-Pack mesh in the zincblend cell. The results presented in this work were achieved by using 64-atom supercells, the (4,4,4) K-point Monkhrost-Pack mesh, and cutoffs of 22 Ry. In particular, $GaAs_{1-y}N_y$ epilayers were simulated by using a 64-atom supercell of GaAs, which included one or two N atoms, thus corresponding to y values of 0.03 and 0.06, respectively [151]. The value of the lattice parameter in the growth plane was fixed to that calculated for GaAs (5.557 Å), while the value of the lattice parameter along the growth direction, c, was allowed to range from 5.292 to 5.662 Å. For each c-value considered, the supercell geometry has been fully optimized. The c-value corresponding to the total-energy minimum has been evaluated through a Murnaghan fit [152] of the total energy values corresponding to the sampled values of c.

Supercell simulations were also performed at the University of Cagliari (I), in order to estimate the average Ga-As distance and its distribution in bulk and epitaxial $GaAs_{1-y}N_y$ as a function of y, and to compare it with the experimental results. These first-principles calculations were carried out also within the density functional theory in the local density approximation, using the all-electron projector augmented wave (PAW) method [153, 154] as implemented in the VASP code [155, 156], with a plane-wave basis cut off at 250 eV, and k-points summations on a (4,4,4) Monkhorst-Pack mesh. Ga 3d electrons were included in the valence manifold. The calculated GaAs lattice constant is a_{th}=5.610 Å. We used 64-atom simple-cubic GaAs supercells (occasionally, 256-atom body-centered cubic cells, for the lowest concentrations), GaAs

supercells containing a variable number of nitrogen atoms substituting an As atom at randomly chosen zincblende anion lattice sites, in order to mimic a disordered sample. (Care was taken to ensure that artificial spatial correlations, e.g. line-up of atoms along 110 chains, were not present, and a few configurations were compared for selected N concentrations, finding the results to be insensitive to the detailed disposition of N atoms). For the calculations in 256-atom supercells, which include up to 1150 doubly-occupied electron states and are therefore at the limit of present computational capabilities, we used the single-k-point sampling suggested [157] by Makov *et al.* . For each N concentration, we considered two realizations of GaAsN, namely bulk free-standing GaAsN and GaAs-epitaxial GaAsN, simulated in tetragonal cells with the in-plane lattice constant fixed at the calculated GaAs bulk value. In each case, we optimized the lattice constant of the system (the orthogonal component, in the GaAs-epi case) simultaneously relaxing the atomic positions using Hellman-Feynman force until the maximum force component is under 0.01 eV/Å. To avoid Pulay stresses, we relax each system for a set of fixed volumes, and obtain the equilibrium volume and ground state energy by a standard Murnaghan equation-of-state fit [152].

2.5.5 Infrared Absorption

Absorption of radiation in the infrared by a material occurs for particular frequencies whose propagation through the crystal lattice is forbidden, because they are resonant with characteristic properties of the lattice material. The energy of the radiation is in this case transferred as thermal energy to the material, exciting electrons and atoms. The vibrational modes of the lattice which absorb radiation may be rather complicate, consisting of several type of fundamental vibrations. In order that a vibrational mode can absorb, a mechanism for coupling the vibrational motion to the electromagnetic radiation must exist. In case of a III-V semiconductor, in which bonds maintain a certain degree of ionicity, the coupling mechanism can be provided by the interaction between the dipole moment of the anion-cation bond and the electric field of the electromagnetic radiation. The vibrational stretching of the bond induces an oscillating dipole moment which can be driven by the electric field, and the energy of this latter is converted into vibrational motion of the atoms.

Far infrared absorption spectra peak at the wavelength corresponding to the vibrational energy of a particular mode, which allows to identify the bonds in a given structure and to understand under which condition they break; in this case the signal disappears in the frequency range of interest. Since the energy of a vibrational mode is inversely proportional to the length of the related bond, infrared absorption can also give information on the variation of the bond lengths due to different strain conditions or different local configurations [39].

Far Infrared absorption spectra were acquired in an extended wave vector range around the Ga-N stretch (440 - 500 cm^{-1}), in order to investigate the breaking of the Ga-N bonds upon atomic hydrogen irradiation [151], first step of the formation of H_2^* complexes (see section 1.3.3). Infrared absorption measurements were performed at the Lehigh University, Bethlehem, Pennsylvania (USA) at liquid He temperature by using

a Bomem DA3 spectrometer (spectral resolution 1 cm^{-1}) with a Si bolometer.

Part II

Results

Chapitre 3: L'ordre local dans l'alliage $\mathbf{In}_x\mathbf{Ga}_{1-x}\mathbf{As}_{1-y}\mathbf{N}_y$

Dans ce chapitre, nous présentons les résultats des expériences dont le but est de vérifier si l'ordre atomique préférentiel In-N + Ga-As prévu à l'équilibre par des calculs Monte Carlo [9] dans l'alliage $In_xGa_{1-x}As_{1-y}N_y$ est ou non réel. Cet ordre a été aussi proposé comme une cause possible du décalage vers le bleu de la bande interdite observée dans les cas d'échantillons $In_xGa_{1-x}As_{1-y}N_y$ après recuit. Les expériences EXAFS (extended X-ray absorption fine structure) au seuil K de l'indium permettent de mesurer directement le nombre de coordination relatif In-N (y_{In-N}) i.e. la probabilité de chaque site dans la première couche de coordination autour d'un indium d'accueillir un atome d'azote. Dans le cas de distribution aléatoire de liaisons, y_{In-N} est équivalent à la concentration d'azote y; sinon il est plus ou moins élevé dans le cas d'ordre préférentiel In-N + Ga-As ou In-As + Ga-N respectivement. On a pu comparer la valeur de y_{In-N} déterminée par EXAFS avec celle prévue à l'équilibre et celle correspondante à la condition d'ordre maximal (chaque atome d'azote complètement entouré par atomes d'indium). Les expériences EXAFS au seuil K de l'indium (27940 eV) présentés dans ce chapitre sont à la limite des actuelles possibilités techniques à cause de la petite section efficace pour le processus d'absorption à hautes énergies, de la petite concentration d'azote (au maximum 5%), de l'épaisseur très limitée de la couche $In_xGa_{1-x}As_{1-y}N_y$ dans les puits quantiques et de la dilution de l'indium dans les cas des couches épaisses.

En raison du fait que les simulations selon la théorie de la diffusion multiple (FMS, full multiple scattering) du coefficient d'absorption dans la région du seuil K de l'azote (XANES) révèlent que cela serait très différent dans les cas de distribution aléatoire des liaisons et d'ordre maximal, nous avons réalisé des expériences XANES (X-ray absorbtion near edge spectroscopy) au seuil K de l'azote (409 eV). Par contre une extension à la région EXAFS n'a pas été ici possible à cause de la proximité du seuil de l'oxygène (543 eV). Même ces expériences au seuil K de l'azote sont très difficiles à réaliser à cause de la courte longueur d'atténuation des photons à ces petites énergies (presque 100 nm en GaAs à 400 eV) et à la faible concentration d'azote, et ont nécessité le flux très intense d'une ligne de lumière d'ondulateur.

Le chapitre commence avec la présentation des caractéristiques des échantillons analysés, nous présentons ensuite les résultats d'une étude de la localisation des atomes d'azote dans la structure, afin de vérifier s'ils substituent les atomes de As ou s'ils

occupent des sites différents. En exploitant la dépendance de la polarisation du signal XAS (dans le cas particulier dans la région du seuil de l'azote) ainsi que des techniques de physique nucléaire (NRA) nous montrons que la symétrie du site de l'azote est cubique et que N est toujours substitutive à As, que les échantillons soient recuits ou pas. L'évaluation de la concentration d'azote obtenue à partir du rendement d'une réaction nucléaire qui implique sélectivement les atomes d'azote et l'estimation du paramètre de maille par diffraction de rayons X à haute résolution nous a permis de vérifier que la loi de Vegard, souvent mise en doute pour les nitrures III-V, est parfaitement valide [148].

Apres l'étude de la symétrie du site de l'azote nous présentons les résultats sur l'ordre local en couches épaisses $In_xGa_{1-x}As_{1-y}N_y$ et montrons que y_{In-N} est plus grand que y dans les échantillons recuits tandis que les deux valeurs ne sont pas distinguables dans le cas d'échantillons non traités. Cela signifie que l'ordre local prévu existe, même si au point de vue quantitatif les paramètres d'ordre mesurés par XAS sont beaucoup plus petits par rapport à ceux calculés à l'equilibre. Cela signifie aussi que le recuit amène les échantillons vers l'état d'équilibre, mais que le processus n'est pas complet. Ces résultats fournissent la première détermination quantitative de l'ordre local en $In_xGa_{1-x}As_{1-y}N_y$ [62].

Nous présentons ensuite la même étude sur l'ordre local dans le cas des puits quantiques $In_xGa_{1-x}As_{1-y}N_y$/GaAs, qui sont effectivement exploités dans la fabrication de composants optoélectroniques. Ici la détermination de l'ordre local est beaucoup plus difficile car la contrainte sur les concentrations, due à la nécessité d'optimisation des propriétés d'émission, rend les conditions de distribution aléatoire des liaisons et d'ordre maximal très proches entre eux du point de vue de la coordination locale y_{In-N}. Cependant, les résultats semblent indiquer un ordre de type In-N + Ga-As dans les puits quantiques hydrogénés [158]. Dans le cas des puits quantiques, une analyse du seuil de l'azote a été impossible à cause de la faible épaisseur de la couche $In_xGa_{1-x}As_{1-y}N_y$ et de la contamination superficielle d'azote. Au contraire la spectroscopie de diffraction anomale (DAFS), grâce à sa sélectivité spatiale ainsi que chimique, a permis d'étudier l'ordre local autour d'un atome (le gallium) présent aussi dans le substrat; XAS au seuil K de l'In et DAFS au seuil K du Ga montrent que les distances de liaison cation-As s'allongent en conséquence de l'hydrogénation; cet effet sera ensuite expliqué dans le chapitre 5.

Enfin, nous montrons, dans le cas des couches épaisses de $In_xGa_{1-x}As_{1-y}N_y$, que le degré d'ordre local mesuré par XAS peut justifier le comportement optique des échantillons recuits (sur la base des récents modèles théoriques [159]) et que l'augmentation du nombre de liaisons In-N (par rapport à celles In-As) amenée par le recuit peut être par conséquent à l'origine des décalages de la bande interdite observés par différents groupes.

Chapter 3

The Short Range Ordering in $\mathbf{In}_x\mathbf{Ga}_{1-x}\mathbf{As}_{1-y}\mathbf{N}_y$

3.1 Introduction

In this chapter I present the results of experiments performed to verify the predicted In-N preferential bonding [9] described in section 1.4.2. XAFS (section 2.2) at the In K-edge allows to directly measure the probability for a In nearest-neighbor site to host an N atom (the variable y_{In-N} introduced in section 1.4.2). Such measurements are at the limit of the present possibilities for the low absorption cross section at high energy (around 28 KeV), the low N content (max 5%) in the investigated samples, the very low thickness of the quantum wells (6-8 nm) and the dilution of In absorber in the epilayers (concentration about 4 %).

We also performed a study of the N K-edge XANES because Full Multiple Scattering (FMS) simulations indicate they are qualitatively very different in case of random or strongly ordered alloys. XANES have a role in assisting XAFS results at the Indium K-edge. Also these measurements are very difficult requiring an high flux undulator beam line because of the high N dilution and the short attenuation length for low energy photons (around 100 nm in GaAs at 400 eV). Due to the small energy interval between the nitrogen and oxygen K-edges (409 eV, 543 eV), it was not possible to extend the spectra to the EXAFS region.

In the following we first present a study on the location of N in the lattice in order to verify if it is substitutional to As or not, performed by NRA (2.5.2) and incident angle-dependent XANES measurements. Then we address the issue of the SRO in $In_xGa_{1-x}As_{1-y}N_y$ epilayers, by means of XAFS at the In and N K-edges; subsequently we do the same for the quantum wells (QWs) employed in lasers manufacturing, by means of XAFS at the In K-edge and DAFS (2.4) at the Ga K-edge. In case of quantum wells a N K-edge analysis was impossible because of the high N dilution and of the nitrogen surface contamination. DAFS, due to its spatial selectivity, allows to study the local environment of the Ga atoms located in the active layer even if this element is also present in the substrate (GaAs), which would be impossible by means

of XAFS. Finally on the basis of our results we discuss on the possibility that the SRO originates the blue shift of the PL (2.5.3) peak observed upon annealing as proposed, during the development of this work, by different groups [39, 159, 160].

3.2 The investigated samples

We investigated two series of $GaAs_{1-y}N_y$, $In_xGa_{1-x}As$ and $In_xGa_{1-x}As_{1-y}N_y$ epilayers whose characteristics are reported in the upper part of table 3.1. Epilayers have been specifically designed in order to highlight the effects of SRO. The In and N concentrations are similar ($x \approx 0.04$, $y \approx 0.02$ in the first series and ≈ 0.03 in the second series), so the expected relative In-N coordination number should be very high in case of maximum In-N + Ga-As ordering (about 50% for series I and 90% for series II). As deposited samples are referred to as *V*, samples treated with RTA (section 2.1) at 700 °C for 90 s as *A1*, and samples treated with RTA at 700 °C for 300 s as *A2*. With the concentrations at play, the small difference between the lattice parameters of the $(In_x)Ga_{1-x}As_{1-y}N_y$ epilayers and the GaAs substrate allowed to grow the samples with a thickness as large as 140 nm (in average) avoiding relaxation via dislocations.

We investigated also three series of $In_xGa_{1-x}As$ and $In_xGa_{1-x}As_{1-y}N_y$ single quantum wells (lower part of table 3.1) optimized for the emission; in this case the In content is quite high, so that maximum ordering corresponds to a relatively small y_{In-N} (see table 3.1), which makes difficult the quantitative determination of SRO. Each of the three series consists of three samples: a ternary $In_xGa_{1-x}As$, a quaternary $In_xGa_{1-x}As_{1-y}N_y$ and an hydrogenated $In_xGa_{1-x}As_{1-y}N_y$. Hydrogenated quantum wells are referred to

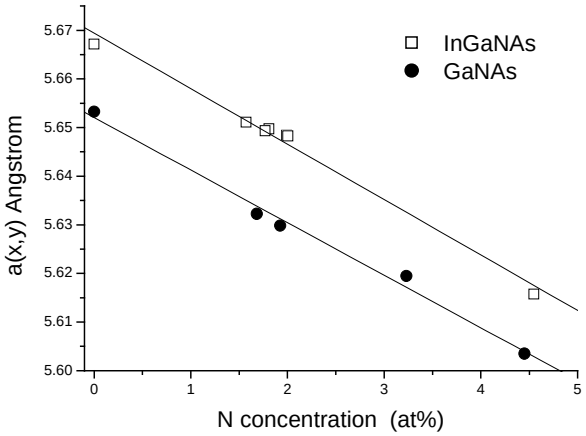

Figure 3.1: Relaxed lattice parameter of epilayers as a function of nitrogen concentration. The two continuous lines represent linear fits to the two data sets.

as *d/4*, corresponding to the hydrogen impinging dose reported in section 2.1.

In case of the epilayers In concentrations were determined by RBS (section 2.5.1). NRA (section 2.5.2) measurements of the N concentration allowed to verify the valid-

ity of the Vegard's law for the lattice parameter, often questioned for dilute nitrides [65, 66, 64]. As it is evident in Fig. 3.1, plotting the relaxed lattice parameter as a function of the N concentration, a linear relationship is observed both for $GaAs_{1-y}N_y$ and $In_xGa_{1-x}As_{1-y}N_y$ alloys.

Verified that the Vegard's law is rigorously valid, N concentration has been subsequently obtained from the lattice parameter measured by X-ray Diffraction. XRD data collected in the vicinity of the (004) reflection provided the *out of plane* lattice parameter $a_\perp$, while XRD in the vicinity of the asymmetric (224) reflection provided the *in plane* lattice parameter $a_\parallel$. We verified that all the epilayers were virtually completely pseudomorphic on the substrate ($a_\parallel = a_{substrate}$). This permitted to calculate the relaxed lattice constant a_f of the epilayers from $a_\perp$, $a_{substrate}$ and the elastic constants C_{11} and C_{12} [161] :

$$a_\perp = a_f + 2\frac{C_{12}}{C_{11}}(a_f - a_{substrate}) \tag{3.1}$$

and then to calculate the N concentrations reported in table 3.1 from the Vegard's law.

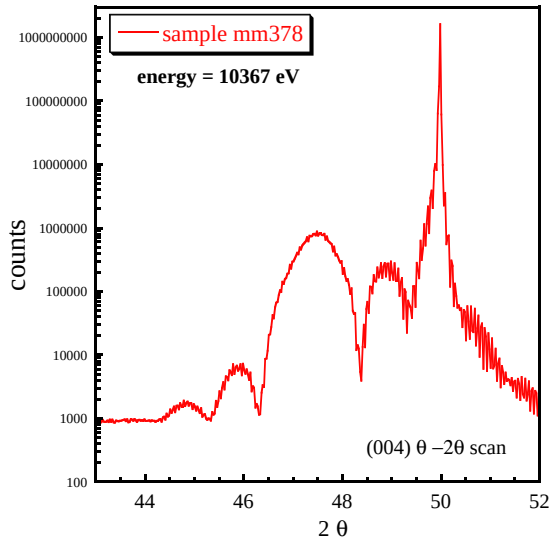

Figure 3.2: θ - 2θ scan in the vicinity of the (004) crystal plane reflection, the Pendellossung fringes are clearly distinguishable.

The In and N concentrations reported in table 3.1 for QWs come from MBE calibration. In concentration (x) values of ternary alloys are in agreement with values determined by XRD (assuming the validity of the Vegard's law) within $\Delta x = \pm\, 2\%$; N concentration values (y) within $\Delta y = \pm\, 1\%$. From the periodicity of the Pendellossung fringes we determined also the thickness of the epilayers and QWs (table 3.1). The presence of the fringes demonstrate the high crystalline quality of the material. In Fig. 3.2 (XRD scan for sample $InAs_{1-y}N_y$ QW 378), two different frequencies are distinguishable: the lower one is related to the finite thickness of the the epilayer while the

Table 3.1: Samples concentrations and thickness, maximum values for y_{In-N} compatible with concentrations, PL at different temperatures and N substitutional fraction; for the epilayers error on In concentration is 0.1 at%, on N concentration is 0.05 at%, for QWs respectively 2 at% and 1 at%; error on thickness is 2 nm, while error on f_{001} is 0.02. The column referred to as *low temperature PL* reports values taken at 10 K for epilayers and at 150 K for QWs.

Sample	y (%)	x (%)	thickness (nm)	max SRO y_{In-N}(%)	PL RT (eV)	PL low T (eV)	f_{001}
$(In_x)Ga_{1-x}As_{1-y}(N_y)$ epilayers							
series I							
632 V	2.10	0.0	147	0	x x x	x x x	1.03
632 A1	1.42	0.0	146	0	1.204±0.002	1.227±0.001	1.02
632 A2	2.10	0.0	140	0	1.138±0.003	1.165±0.001	xxx
633 V	2.08	4.3	145	48	x x x	x x x	1.04
633 A1	1.52	4.3	140	35	1.172±0.003	1.193±0.001	0.96
633 A2	2.00	4.3	152	47	1.140±0.003	1.154±0.002	1.01
series II							
711 V	3.04	0.0	145	0	x x x	1.033±0.008	xxx
711 A2	4.58	0.0	130	0	0.977± 0.007	0.997±0.004	1.00
710 V	0.0	3.6	144	0	x x x	x x x	xxx
712 V	3.35	3.8	136	88	x x x	1.13±0.07	1.01
712 A2	3.27	3.8	150	86	1.053± 0.002	1.087±0.001	xxx
$In_xGa_{1-x}As_{1-y}(N_y)$ quantum wells							
series I							
225	0.0	32	6.4	0	1.099±0.002	1.153±0.001	
227	2.7	32	6	8.4	0.935±0.003	0.983±0.002	
227d4	2.7	32	6	8.4	xxx	1.112±0.004	
series II							
260	0.0	38	7	0	1.064±0.002	1.090±0.001	
241	4.2	38	6.5	11.1	0.838±0.004	0.875±0.003	
241d4	4.2	38	6.5	11.1	xxx	1.060±0.030	
series III							
378	0.0	38	8	0	1.067±0.002	1.123±0.001	
383	5.2	38	8.2	13.7	0.800±0.004	0.841±0.003	
383d4	5.2	38	8.2	13.7	xxx	1.097±0.012	

higher one is linked to that of the cap layer (about 100 nm). Thickness is obtained by a fit of the XRD spectra with the Takagi-Taupin equations; the error on the thickness is about 2 nm.

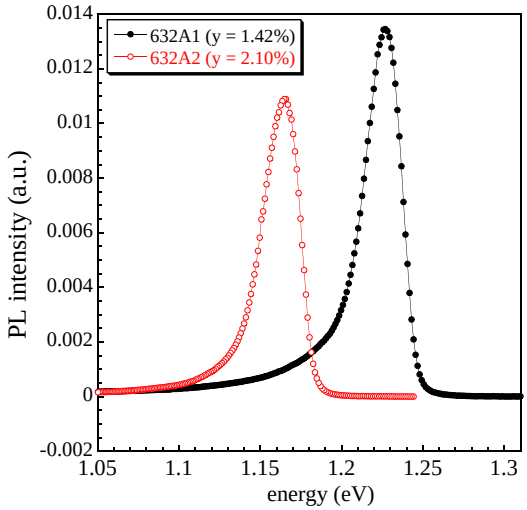

Figure 3.3: PL spectra taken at T = 10 K for two annealed samples, the energy value corresponding to the peak is an estimation of the band gap.

Samples have been characterized by Photoluminescence at different temperatures (see section 2.5.3); the observed energy position of the peaks is also reported in table 3.1. In case of annealed samples the PL intensity is quite strong and very good spectra are obtained (see Fig. 3.3); note the red shift due to an higher N incorporation and the asymmetric low energy tail due to the presence of localized states described in section 1.2.7. On the contrary as grown samples present a very poor PL efficiency and an estimation of the band gap is hardly achievable even at T = 10 K. Nevertheless PL values for these samples are reported in table 3.1 when the measurement was possible.

3.3 The substitutional character of N

Information on the geometry of the N coordination sites can be obtained by exploiting the polarization dependence of the XAFS signal (equation 2.15), by changing the angle between definite crystallographic directions and the electric field of linearly polarized synchrotron radiation. In presence of a cubic symmetry (like in case of pure substitutional N) no polarization dependence of N K-edge XANES should be present; on the contrary it is significant in hexagonal structures like GaN.

In Fig. 3.4 we report three N K-edge XANES spectra for sample 712 V taken with different incidence angles. The three spectra are virtually identical, evidencing there

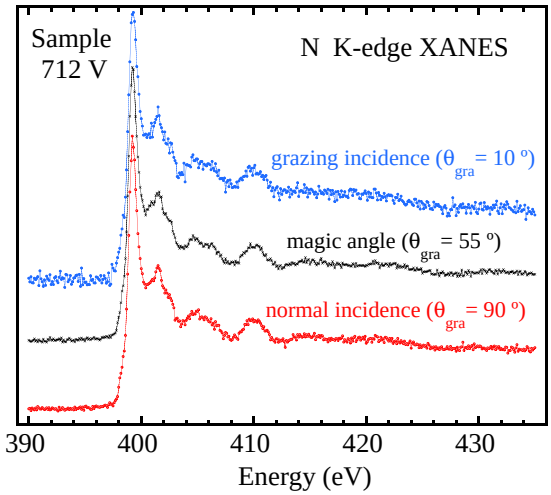

Figure 3.4: N K-edge XANES taken on sample 712V for different grazing angles.

is not a polarization dependence of N K-edge XANES : this is a fingerprint of the cubic symmetry of the N site and gives a strong indication that nitrogen atoms are substitutional to arsenic in the zincblend host structure. For a not-isotropic symmetry group (as the hexagonal) significant variations in the relative intensity of the XANES should be observed, as evident in Fig. 3.5 where two N K-edge XANES spectra for an hexagonal GaN standard sample, respectively taken at $\theta_{gra} = 20°$ and $\theta_{gra} = 55°$, are reported.

The XANES spectra of Fig. 3.4 rule out also the hypothesis of the formation of N-N and N-As split interstitials (Fig. 3.6) proposed by Li *et al.* [65]. In fact the presence of these complexes would give sharp resonances in the pre-edge region of the XANES, not observed in our case. In fact when N is hybridized differently from sp^3, one π^* molecular orbital below the continuum remains unoccupied and a pre-edge sharp line appears in the spectrum due to the transitions from $1s$ to π^* levels [162]. This happens for example in the N_2 molecule, where the two nitrogen atoms use three valence electrons to form three bonds leaving one π^* orbital unoccupied; in a split interstitial complex as those of Fig. 3.6, N atoms bind each other in a similar way and the configuration of molecular

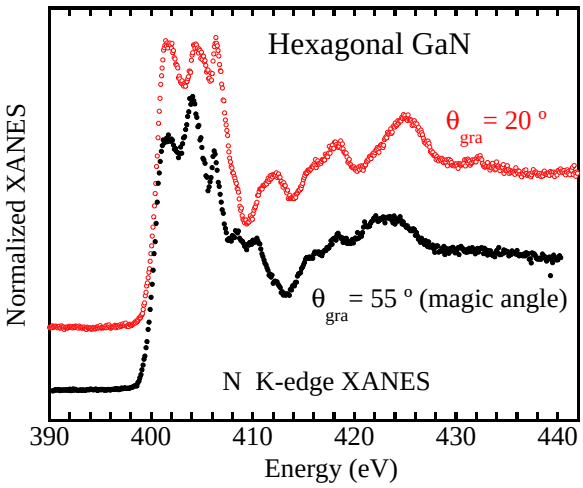

Figure 3.5: N K-edge XANES relative to an hexagonal GaN standard for different grazing angles.

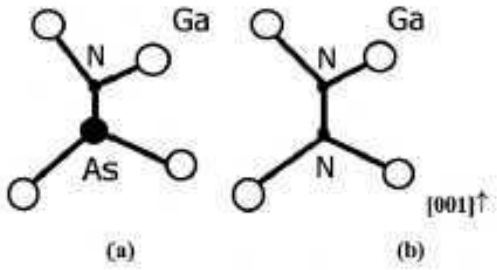

Figure 3.6: From Li *et al.* (modified) : atomic structures for the split interstitial N-N and N-As complexes.

orbitals is similar.

The substitutional character of nitrogen is confirmed by comparing random and channelling NRA spectra along the (001) growth direction. Measured values for f_{001} (section 2.5.2) are reported in table 3.1, similar values were obtained along the (111) crystallographic direction; these values give a substitutional fraction close to 100 % for all epilayers, both as deposited and annealed [148]. These results allow to discard (within an error = ± 0.02) the formation of point defects, except for those aligned along the (001) and (111) directions.

The defects corresponding to N substitutional to Ga instead of As (N_{Ga}) cannot be excluded by NRA, but Orellana *et al.* [163] showed that their formation energy is much higher than that of substitutional N, so they are unlikely. The same is true for tetrahedral isolated interstitial sites that are predicted to have a formation energy higher than N-As and N-N split interstitials [65]. (100) and (110) split interstitials

are significantly displaced from the (001) direction, so they are not shadowed and their formation can be ruled out by NRA analysis; the same holds for (001) split interstitials, which are not shadowed in the (111) direction.

3.4 Epilayers : In K-edge EXAFS

We report in Fig. 3.7 the background subtracted[1] EXAFS spectra taken at the In K-edge on epilayers. Each one is a sum of three or four scans in fluorescence mode two hours long. Just looking at the spectra we see that the predicted short range

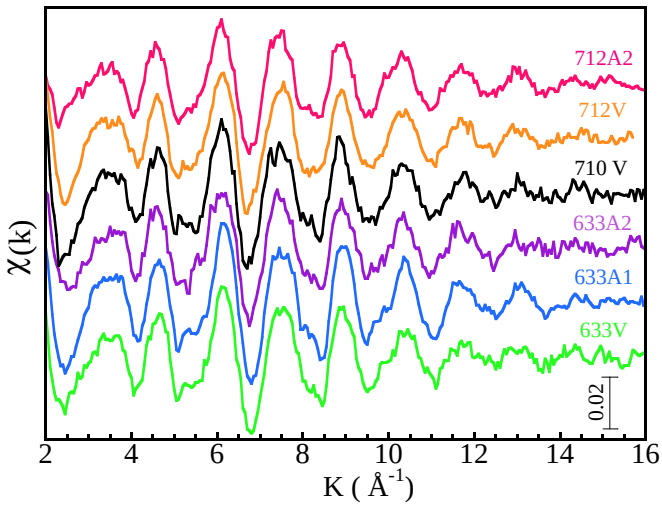

Figure 3.7: Background subtracted XAFS spectra ($\chi(k)$ vs. k) taken at the Indium K-edge on $In_xGa_{1-x}As_{1-y}(N_y)$ epilayers.

ordering, if it exists, is in any case very weak. In fact the XAFS signal behavior for $In_xGa_{1-x}As_{1-y}N_y$ samples does not appreciably differ from that of the ternary $In_xGa_{1-x}As$; the signal appears to be dominated in frequency and envelope by the first shell In-As contribution with a small if any In-N contribution. In case of strong SRO the line shape of XAFS would be completely different as illustrated in the simulations reported in Fig. 3.8. These simulations qualitatively show that in case of maximum ordering the behavior of the signal as a function of k would be characterized by a monotonic decrease due to the N backscattering amplitude, with superposed a frequency due to second shell atoms coordinated to the absorber In via a first shell N. Assuming a SRO as that predicted by Kim and Zunger practically a single oscillation should be present around $K = 4$ Å^{-1}. This differs from the random case and from that of only In-As contribution which show a clear double oscillation.

[1]Data reduction has been performed according to the procedures illustrated in section 2.2.5. A spline with 15 free coefficients has been used to extract the $\chi(k)$ signal from the raw data, R_{bkg} value in the Autobk code [113] was fixed to 1.3 Å for the background subtraction of all spectra.

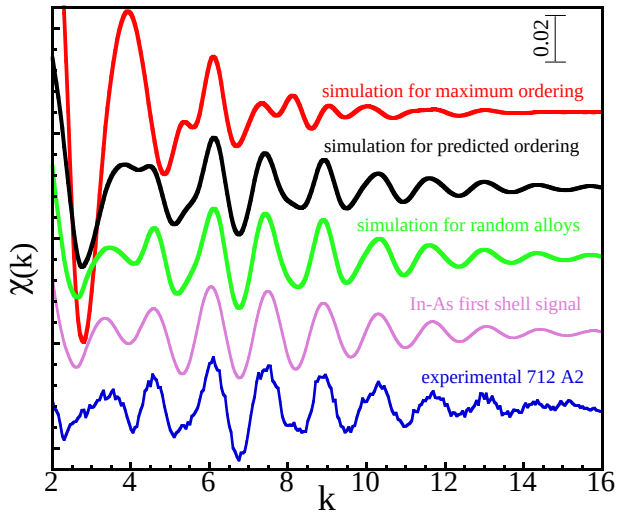

Figure 3.8: Experimental $\chi(k)$ for sample 712 A2 compared to simulations for random, predicted and maximum ordering and to the contribution to the signal of the only first shell In-As single scattering path. These simulations were made by fixing the interatomic distances and Debye-Waller factors to the values obtained from the fit of sample 712 A2 and assigning y_{In-N} the values corresponding to random ordering (3.3%), to the SRO predicted by Kim and Zunger (24 %, extracted from equation 1.9) and finally to the maximum ordering reported in table 3.1 (86%).

In Fig. 3.9 we report the Magnitude of the Fourier Transform (FT) for the three samples of the series 71X; for both the $In_xGa_{1-x}As$ reference sample (710 V) and for the quaternaries the first shell is dominated by the peak due to the In-As correlations. The amplitude of this first shell peak decreases in the annealed quaternary epilayer (712 A2). A small low-R shoulder is present in all data, its amplitude increasing in going from the ternary to the annealed quaternary sample (712 A2). It is tempting to interpret this shoulder as a direct signature of the presence of In-N bonds as very recently suggested by Lordi *et al.* [164]. However, the presence of this shoulder in the N-free InGaAs sample (due to FT termination effects and small, inevitable, errors in background subtraction) indicates that this interpretation is overly simplistic.

Superposed to the spectrum for sample 712 A2 we also show a simulation of the Fourier Transform assuming the degree of ordering predicted by Kim and Zunger (local relative In-N coordination y_{In-N} of 24%). It is apparent that significant differences exist in the overall lineshape of the first shell peak. Moreover the simulated signal presents a higher amplitude in the region $2.9-3.4$ Å due to second shell Ga atoms coordinated via a first shell nitrogen. All this indicates that the actual degree of ordering is significantly less than that predicted.

Data at the In K-edge were fitted with a combination of In-As and In-N signals for the first shell and two distinct In-Ga contributions for the second shell; these two

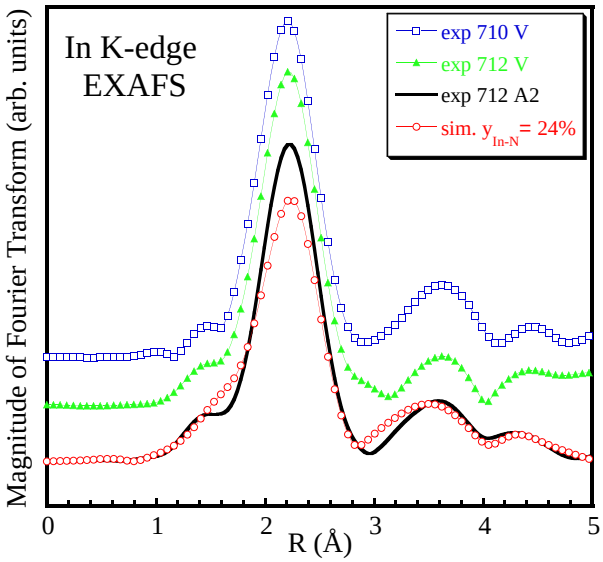

Figure 3.9: Fourier Transform for series II-epilayers and simulation of the predicted y_{In-N}. Data, along with the theoretical signals generated by FEFF [103], have been weighted for K^1, multiplied for a Gaussian apodization window and finally Fourier transformed in the range $k = 3.0 - 13.4$ Å^{-1}.

contributions are due to second shell Ga atoms linked to the central In via either As or N atoms which are located at significantly different distances from the absorber. We neglected the presence of In atoms in the second shell since the introduction of related paths did not bring about a statistic improvement of the fit. The third shell was taken into account by a single In-As signal. The variable y_{In-N} (introduced in section 1.4.2) determines the relative weight of all the N-related structural signals (Fig. 3.10); it is equal to the probability for a single In-nearest neighbor site to host a N atom ($y_{In-N} = \frac{In-N\ coordination\ number}{4}$, since In is fourfold coordinated in the zincblend structure).

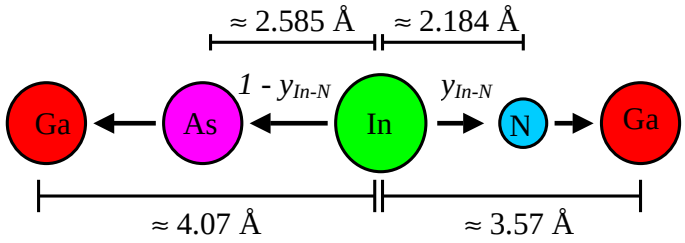

Figure 3.10: Scheme for the fit : first and second shells are divided into two sub-shells, characterized by different distances and weighted by the variable y_{In-N}.

Only the multiple scattering signal due to the triangular atomic arrangement involving the central In, a second shell Ga and a first shell As atom was found to have a significant amplitude and was therefore included in the analysis (see scheme in Fig. 3.11).

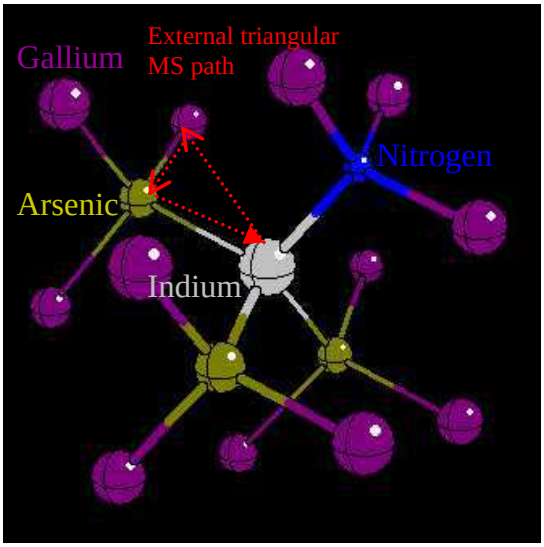

Figure 3.11: First and second atomic shells around a central indium in the zincblend structure of $In_xGa_{1-x}As_{1-y}N_y$, we introduced one N atom in the first shell and just Ga atoms in the second shell; the external triangular MS path exploited in the fit is enlightened. Visualization is obtained with Moldraw 2.0.

Fit variables were y_{In-N} and the In-As first shell distance R_{In-As}; the In-N distance R_{In-N} was fixed to the value predicted by using the *Cai et Thorpe's* model for quaternary bulk alloys and adding the *Tormen's* correction to take into account the tetragonal distortion of the coherently grown epilayers (see section 1.5.2) [2]. A unique Debye-Waller variable was used for the In-N and In-As first shell in order to minimize the total number of variables and correlation. Two distances R^{As}_{In-Ga} and R^{N}_{In-Ga} were used to fit the bimodal second shell distances distribution described above, with a unique second shell Debye-Waller parameter. An independent distance and Debye-Waller parameter were assigned to the triangular multiple scattering and to the third shell. For all shells a common non-structural parameter was the threshold energy shift ΔE (in the range 7-10 eV, see table 3.2); and finally the many-body amplitude reduc-

[2] Concerning parameters employed in the model, lattice constants of the binary compounds InAs and GaAs have been taken from XRD results respectively reported in the paper of Ozolins *et al.* [165] and of Fewster *et al.* [166] while lattice constants of cubic InN and GaN, being the zincblend form instable, have been taken from theoretical determinations by Wright and Nelson [167, 168]; force constants are calculated starting by the bond stretching and bond bending parameters or macroscopic elastic constants (to which α and β are related via equation 1.14) reported in the papers of Martin [169] (GaAs, InAs) and Wright [170] (InN, GaN).

tion factor S_0^2 introduced in section 2.2.2 was fixed to the value found from analysis of an InAs powder sample.

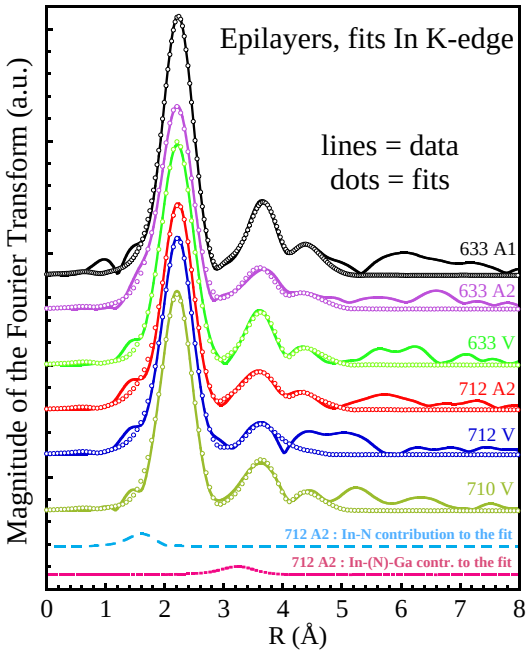

Figure 3.12: Fits performed on the Fourier Transform for all epilayer samples in the range R = 1.6 - 4.8 Å by the Feffit program [123].

In Fig. 3.12 the fits are reported together with the Fourier Transforms for all samples. It is evident the very good agreement achieved, up to the second shell and, in some case, also to the third one. Results of the fits (SRO parameters, interatomic distances and Debye-Waller factors) are reported in Table 3.2.

We start discussing the extracted values of y_{In-N} and the quantification of the short range ordering. The bottom curves of Fig. 3.12 report the two quite weak contributions to the best fit of sample 712 A2 induced by the presence of N. A statistical analysis confirms that the introduction of the extra scattering signals related to N is significant and reliable. This analysis involves a comparison between fits with and without inclusion of the N components. If we include them while fitting the quaternary sample 712 A2, the value of reduced chi-square χ^2_ν significantly diminishes with respect to a fit without them (3.46 $\pm$ 0.47 vs. 4.38 $\pm$ 0.42); on the other hand, if we try to include the N components while fitting the ternary alloy of the same series (710 V), χ^2_ν actually increases (5.23 $\pm$ 0.47 vs. 4.28 $\pm$ 0.43). In case of sample 712 A2 the fit including N-related signals gives also a better agreement in the second shell region, due in particular to the contribution of the In-(N)-Ga signal with distance R^N_{In-Ga}, as shown in Fig. 3.13.

In Fig. 3.14 we report values of y_{In-N} as a function of N concentration for all

Table 3.2: In K-edge fits results : y_{In-N}, x_{N-In}, measured SRO parameter ξ (all definitions have been reported in section 1.4.2), measured and theoretical (*th*) bond lengths, Debye-Waller factors (σ^2) and threshold energy shift ΔE (error ± 1 eV). R_{In-As} distances in the table have been corrected for the systematic error in the theoretical phases generated by FEFF comparing the distance fitted for a bulk InAs standard, measured in transmission mode in the same run of measurements, to the VCA value determined by XRD (2.635 ± 0.003 Å vs. 2.623 Å); systematic errors on the second shell distances are on the other hand by far smaller than the statistic ones (4.288 ± 0.018 Å vs. 4.284 Å for InAs) and can be neglected.

Sample	y_{In-N} (%)	x_{N-In} (%)	ξ	R_{In-As} (Å)	R^{th}_{In-As} (Å)	
$In_xGa_{1-x}As_{1-y}N_y$ - series I						
633 V	0.7 ± 4.3	1.5 ± 8.9	-5.9e-4	2.580 ± 0.004	2.587	
633 A1	4.2 ± 2.6	11.9 ± 8.0	1.2e-3	2.583 ± 0.004	2.587	
633 A2	5.7 ± 4.0	12.2 ± 9.1	1.6e-3	2.579 ± 0.006	2.587	
$(In_x)Ga_{1-x}As_{1-y}N_y$ - series II						
710 V	xxx	xxx	xxx	2.583 ± 0.006	2.586	
712 V	6.1 ± 3.3	6.9 ± 4.0	1.0e-3	2.587 ± 0.004	2.589	
712 A2	9.6 ± 4.3	11.1 ± 5.4	2.4e-3	2.595 ± 0.004	2.589	

Sample	R^{th}_{In-N} (Å)	σ^2_{Ishell} (10^{-3} Å^2)	R^{N}_{In-Ga} (Å)	R^{As}_{In-Ga} (Å)	$\sigma^2_{IIshell}$ (10^{-3} Å^2)	ΔE
$In_xGa_{1-x}As_{1-y}N_y$ - series I						
633 V	2.184	3.9 ± 0.1	xxx	4.067 ± 0.008	9 ± 2	9
633 A1	2.184	2.5 ± 0.2	3.59 ± 0.05	4.076 ± 0.006	7 ± 2	10
633 A2	2.184	3.9 ± 0.4	3.53 ± 0.07	4.056 ± 0.011	11 ± 1	7
$(In_x)Ga_{1-x}As_{1-y}N_y$ - series II						
710 V	xxx	4.0 ± 0.2	xxx	4.079 ± 0.017	12 ± 2	7
712 V	2.185	3.6 ± 0.3	3.53 ± 0.06	4.085 ± 0.009	14 ± 1	8
712 A2	2.185	3.6 ± 0.4	3.62 ± 0.05	4.089 ± 0.024	13 ± 2	9

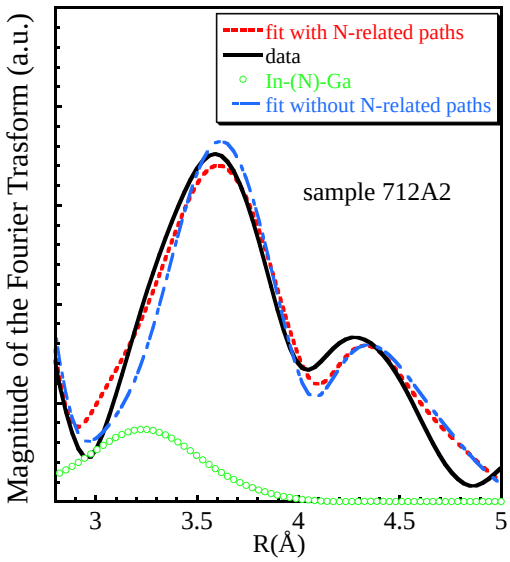

Figure 3.13: Comparison between fits including or not N-related paths. The fit which includes them better simulates the second shell, where the contribution to the signal from Ga atoms coordinated to the absorber via a first shell N (In-(N)-Ga) is not negligible.

samples together with the expected values for a random coordination and a value calculated by Kim and Zunger in our concentrations range. Note how the as grown samples have values for y_{In-N} compatible with the random case, while annealed samples show a small but measurable ordering effect. In fact the y_{In-N} values are systematically higher for annealed samples than for as grown. If we fit a least-squares function [124] of the form $y_{In-N} = by$ to the three values relative to annealed samples and calculate the error on the slope starting by the measured errors on y_{In-N}, we find a slope $b = 2.9$ with a σ value of 0.9. This allows to discard the "random" behavior ($b = 1$) to a 5% confidence level. The quantitatively determined degree of order is, however, quite weak: Kim and Zunger [9] predicted an order parameter ξ as high as 1.3×10^{-2} in case of concentrations similar to those of sample 633 A2, while we have gotten 1.6×10^{-3}, one order of magnitude less.

As for distances, first shell In-As bond lengths are in agreement within less than 0.01 Å with distances predicted by using the *Cai and Thorpe*'s model and keeping into account the effects of the tetragonal distortion of the strained epilayers cell via the *Tormen*'s formulation (see section 1.5.2). As regards second shell distances, they lie within a reasonable range. The R^{As}_{In-Ga} distance, whose average is 4.075 ± 0.012 Å, is smaller than the In-In distance in indium arsenide (4.284 Å) but larger than the VCA value for InGaAs (4.009 Å) due to the fact that the heavier In cation is involved in the bond. The R^{N}_{In-Ga} distance, which is 3.57 ± 0.06 Å, is larger than the VCA value for the In-Ga distance in InGaN (3.17 Å) due to the high overall content of arsenic in

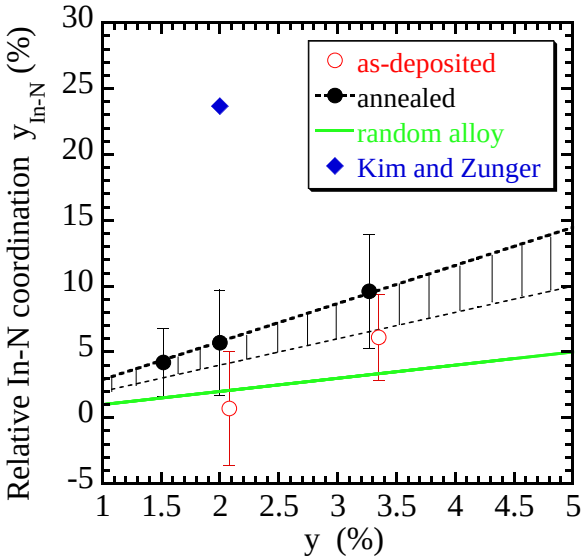

Figure 3.14: y_{In-N} as a function of N concentration for the different quaternary samples. Dotted lines represent a least-squares fit to "annealed" points and its lower error bar (1σ) : random trend falls outside.

the alloys, but smaller than the VCA In-Ga in InGaAsN (3.98 Å) because As atoms are not directly involved in these bonds. We used here $x = 0.04$ and $y = 0.03$ in order to obtain VCA values and the references referred above for the lattice parameters of the cubic constituent compounds. Debye-Waller factors and MS variables have been also found to lie within reasonable ranges. The DW factor of the only sample 633A1 was found rather smaller than for the others; since temperature was the same (liquid nitrogen) during all the experiments, this effect can be due to the lower annealing time (90s) to which only this sample was subjected, which seems to be optimal to minimize the structural disorder around the In site.

3.5 Epilayers : N K-edge XANES

As reported in section 3.1 to provide a complementary probe of SRO we studied the N K-edge XANES on the same quaternary samples and on two reference ternary $GaAs_{1-y}N_y$ samples. The spectra were also simulated with the FEFF code in the full multiple scattering approach using self consistency for the potential [103]. The clusters for simulating $GaAs_{1-y}N_y$ spectra were created by introducing an N impurity in the GaAs structure (GaAs:N); relaxing the first and second shell distances minimizing the total energy, evaluated assuming a valence force field potential [28] with appropriate force constants [169, 170].

The VFF potential minimized was that given by Martins and Zunger [29] (equation 1.13); we considered all the bonds formed by the N impurity (4 bonds with first shell

Ga atoms), those formed by each of its Ga nearest neighbors (1 bond with N and 3 with next-nearest neighbors As) and finally those formed by third shell As atoms (1 bond with a first shell Ga atom, two bonds with third shell Ga atoms and one bond with a fifth shell Ga atom). The elastic deformation energy takes the following expression:

$$
\begin{aligned}
U = 4\,\frac{3}{8}\Bigg[& \frac{\alpha_{GaN}}{\frac{3}{16}a_{GaN}^2}\left(\frac{3x^2}{16}-\frac{3}{16}a_{GaN}^2\right)^2 + 3\frac{\alpha_{GaAs}}{\frac{3}{16}a_{GaAs}^2}\left(\frac{8y^2-8xy+3x^2}{16}-\right. \\
& \left.\frac{3}{16}a_{GaAs}^2\right)^2 + 6\frac{\alpha_{GaAs}}{\frac{3}{16}a_{GaAs}^2}\left(\frac{8y^2-16a_{GaAs}y+11a_{GaAs}^2}{16}-\frac{3}{16}a_{GaAs}^2\right)^2 \\
& +3\frac{\alpha_{GaAs}}{\frac{3}{16}a_{GaAs}^2}\left(\frac{19a_{GaAs}^2-24a_{GaAs}y+8y^2}{16}-\frac{3}{16}a_{GaAs}^2\right)^2\Bigg] + \frac{3\beta_{GaAs}}{8\frac{3}{16}a_{GaAs}^2}\cdot \\
& \Bigg\{4\cdot 3\left(3\frac{x^2}{16}-\frac{xy}{4}+\frac{a_{GaAs}^2}{16}\right)^2 + 12\left[2\left(\frac{8y^2-4xy-8ya_{GaAs}+3xa_{GaAs}}{16}\right.\right. \\
& \left.\left. +\ \frac{a_{GaAs}^2}{16}\right)^2 + \left(\frac{8y^2-4xy-12ya_{GaAs}+7xa_{GaAs}}{16}+\frac{a_{GaAs}^2}{16}\right)^2\right]\Bigg\}
\end{aligned}
\tag{3.2}
$$

The parameters introduced in this formulation have the meaning explained in section 1.5.2, the values of the lattice parameters a_{GaAs}, a_{GaN} and force constants α_{GaAs}, α_{GaN}, β_{GaAs}, β_{GaN} of the binary constituent compounds were taken from references [166, 168, 169, 170]. The two variables x and y correspond to the lattice parameters which, in the virtual crystal approximation, generate the relaxed N-Ga first shell and N-As second shell distances respectively; as a consequence they are linked to R_{N-Ga} and R_{N-As} by :

$$
\begin{aligned}
R_{N-Ga} &= x\frac{\sqrt{3}}{4} \\
R_{N-As} &= \frac{y}{\sqrt{2}}
\end{aligned}
\tag{3.3}
$$

The minimum (x, y) point of the $U(x, y)$ surface was calculated using the Mathematica 4 code (ESRF licence - Indigo cluster).

The same procedure was adopted for a N impurity in InAs (parameters taken from references [165, 167, 169, 170]). To simulate the quaternary alloys with different In contents we made weighted linear combinations of the simulated XANES spectra for GaAs:N and InAs:N. The clusters exploited in the simulations consisted of 20 atomic shells around the central N i.e. of 381 atoms. In order to minimize CPU time the self consistency radius (section 2.2.5) was kept smaller than the full multiple scattering one (up to the second atomic shell) : this approximation does not affect the results, as tested on smaller clusters. Energy step of the XANES was fixed to the smallest value allowed by the FEFF program (0.3 eV), however larger than the experimental step (0.1 eV).

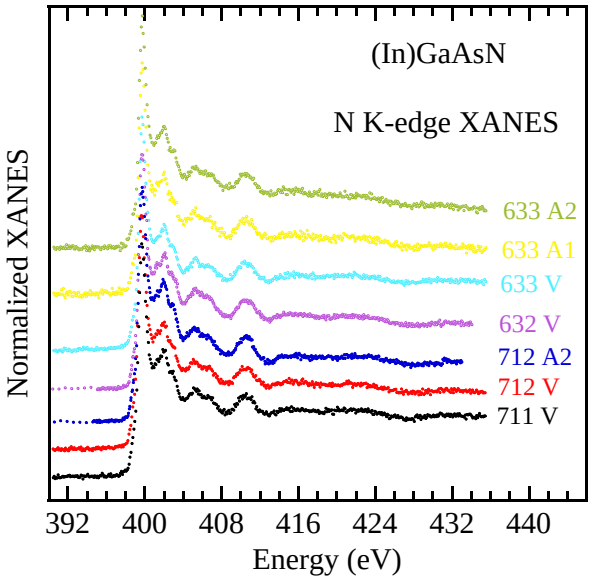

Figure 3.15: Experimental N K-edge XANES spectra.

In Fig. 3.15 we report all the experimental XANES spectra and in Fig. 3.16 a comparison between two of them with the FMS simulations[3]. It is apparent that all the spectra are quite similar to each other and very well simulated by a simple GaAs:N structure. So we conclude that a In-N coordination, if present, is below our sensitivity. This fact is not surprising: as a matter of fact the In K-edge EXAFS data showed that the N-In relative coordination x_{N-In} is 12 % at most (table 3.2); and in Fig. 3.16 it is evident how for quaternary alloys below 20 %, simulations are not significantly modified with respect to GaAs:N. This confirms that the preferential In-N bonding is weak, since a stronger ordering would result in one of the upper lineshapes in Fig. 3.16.

The big dimension of the clusters exploited in the simulation and the utilization of a VFF potential to relax atomic positions was absolutely mandatory. Fig. 3.17 shows the simulations of the XANES spectra at increasing cluster sizes from 7 to 20 atomic shells: it is evident that the simulation presents all the features of the experimental spectra only when the cluster exceeds 18 shells. Fig. 3.18 reports a comparison between a simulation for a cluster (15 shells) in which atomic positions have been relaxed via VFF as referred above, with a simulation for a cluster in which interatomic distances of the GaAs matrix have not been modified either in the first or in the second shell (absence of relaxation), and with a further simulation in which first shell distances have been fixed to the theoretical values for cubic gallium nitride (total relaxation).

[3]Simulated signals were shifted in energy by −0.48 eV and their energy scale was dilated by 6 %; the *ab initio* evaluation of the potential done by FEFF is in fact too brute to perfectly reproduce the value of the band gap, these corrections are in any case well within the limits accepted by the XAFS community.

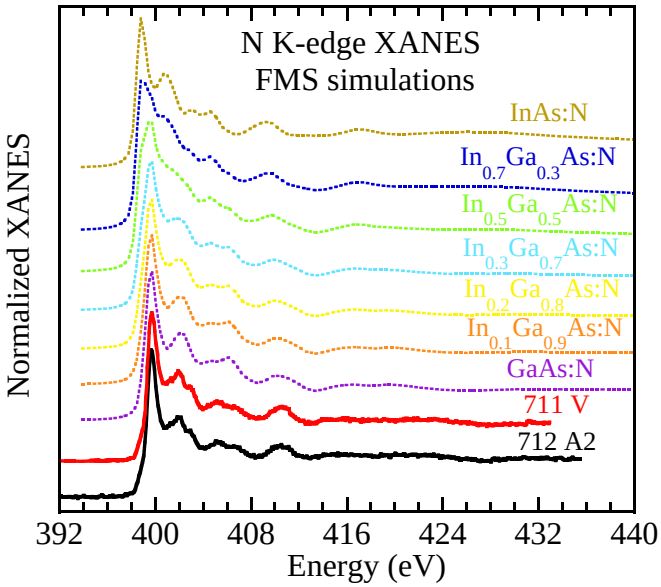

Figure 3.16: Simulated N K-edge XANES: the In content decreases from top to bottom; two experimental spectra (bold lines at the bottom) are also reported for a comparison.

Significant differences in the line shape of the simulations are evident, showing the large effect of the relaxation on the spectra[4].

Our results on the In and N K-edge spectra provide the first quantification of SRO in as-deposited and annealed $In_xGa_{1-x}As_{1-y}N_y$. They strongly disagree from a quantitative viewpoint with recent Monte Carlo simulations. In fact our measured order parameters are about one order of magnitude smaller than those predicted, but are significantly higher than in the random case [62].

[4]On the contrary relaxation beyond the second shell was found to have negligible effects on the simulations.

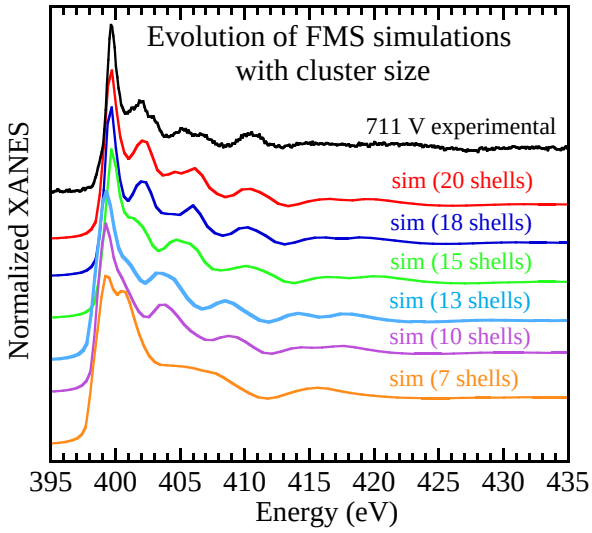

Figure 3.17: Improvement of N K-edge simulations by increasing the cluster size : 18-20 atomic shells around the central N are necessary in order to well reproduce the experimental spectrum.

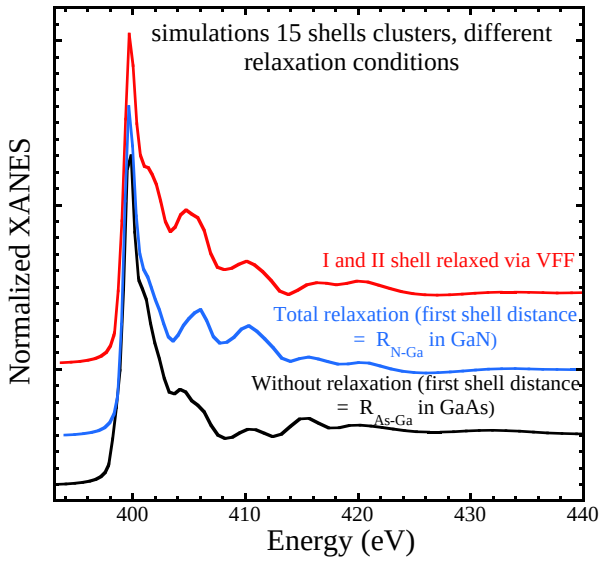

Figure 3.18: Effect of different relaxations of the atomic positions in the cluster.

3.6 Quantum Wells : In K-edge EXAFS

Fig. 3.19 presents the background subtracted XAFS spectra of $(In_x)Ga_{1-x}As_{1-y}N_y$ single quantum wells series described in table 3.1. Each of these spectra is the sum of four scans taken in fluorescence mode, each of which lasted about five hours; in other words each spectrum required about 20 hours of acquisition time exploiting the parallel acquisition of a 13 element detector. The signal to noise ratio of the spectra is very good up to k = 15 $Å^{-1}$, especially considering the experimental difficulties mentioned above.

The behavior of the XAFS signal is rather similar for all the quantum wells; this is not surprising considering the quite low values of y_{In-N} even for the maximum preferential ordering condition (table 3.1) with the concentrations at play in this case.

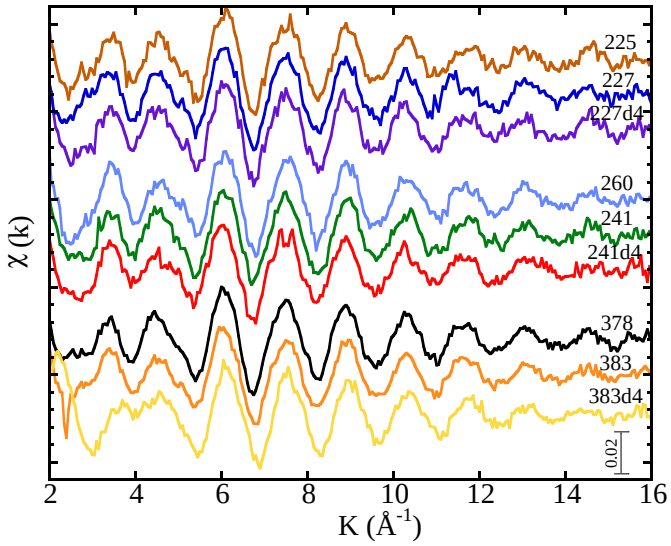

Figure 3.19: Background subtracted XAFS spectra ($\chi(k)$); background extraction has been performed with the Autobk code [113] by exploiting a spline with 17 free coefficients, imposing $R_{bkg} = 1.3$ Å.

On the contrary differences between $In_xGa_{1-x}As$ and $In_xGa_{1-x}As_{1-y}N_y$ samples are well evident in the Fourier transforms (FT) reported in Fig. 3.20. The peak at an apparent distance R of $\sim$ 2.2 Å is due to the first shell atomic correlations, while the structure above 3 Å is due to the second shell. In the series I, characterized by the lowest N content for the quaternary alloys, the amplitude of the first shell peak does not vary so much comparing the ternary and quaternary samples; on the other hand in series II and III, where the N content is higher, the amplitude of the FT is significantly reduced in case of N-containing quantum wells. In series II the hydrogenated $In_xGa_{1-x}As_{1-y}N_y$ has a first shell peak amplitude smaller than the non-hydrogenated one, while the

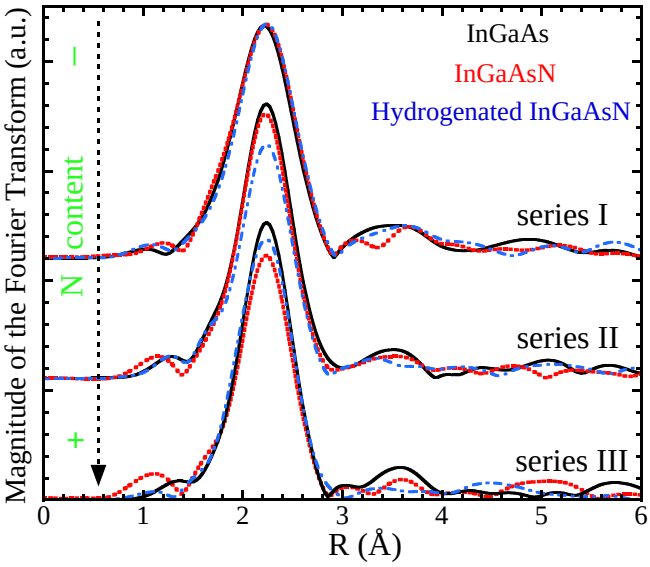

Figure 3.20: Fourier Transforms for all quantum wells samples : black continuous line = $In_xG_{1-x}As$, red dotted line = $In_xGa_{1-x}As_{1-y}N_y$, blue dashed-dotted line = hydrogenated $In_xGa_{1-x}As_{1-y}N_y$. FTs were performed after selecting the (3 - 13) $Å^{-1}$ range of the $k \cdot \chi(k)$ signal and after multiplying it by a Gaussian apodization window.

opposite is true in case of series III.

Samples 241d4 and 383 have the lowest amplitude of the FT first shell peak and present also an overall shift and asymmetry towards low R-values which could due be to the contribution of the In-N coordination as suggested by Lordi *et al.* [164]. Nevertheless we believe that this hypothesis may be wrong because the line shape of the FT in the region of low R-values is dramatically sensitive even to small errors and differences in the background extraction from sample to sample. Furthermore at the concentrations of these quantum wells, very similar to those of Lordi *et al.*, even the biggest possible value of y_{In-N} (table 3.1) is too low to induce shoulders or peaks in FT spectra, as we have already seen in case of the epilayers [5]. A lot of attention has to be payed before associating low-R structures to the In-N coordination; only a rigorous statistical analysis like that performed on the epilayers allows to draw conclusions on the In-N preferential coordination. In case of quantum wells, an evaluation of the error in the determination of the actual y_{In-N} is particularly important since, with the concentrations at play, the values of y_{In-N} corresponding to the random and maximum ordering conditions are very close each other.

As clear from Fig. 3.20, the amplitude of second shell of quaternary samples of series II and III is very low and hardly distinguishable from the noise level; therefore

[5] As reported in Fig. 3.12, the fit performed on epilayer 712A2, whose y_{In-N} is about 10 %, does not show any shoulder.

we limited the analysis to the first shell. This fact made impossible the evaluation of the fraction of second shell In and Ga atoms related to the absorber via a first shell N.

Theoretical signals of the first shell were calculated by FEFF for two cubic InAs and InN model clusters; these signals were Fourier transformed in the same way as the experimental data while performing the Fourier Transform. Then, the first coordination shell (in the range $R = 1.4 - 2.9$ Å) was fitted by a linear combination of the In-As and In-N contributions, determining the variable y_{In-N} i.e. the relative number of N atoms in the first shell of In. The fitting parameters were the mentioned y_{In-N}, the In-As first shell distances R_{In-As}, a unique Debye Waller factor for all first shell paths σ^2_{Ish} and the threshold energy ΔE. The In-N distance was fixed to the theoretical value R^{th}_{In-N} using the criterium described in section 3.4 for epilayers. We treated ΔE as a variable because of the big changes observed in the band gap of these alloys both upon addition of N and hydrogenation (see chapter 1). The many body amplitude S^2_0 was estimated by using a InAs standard.

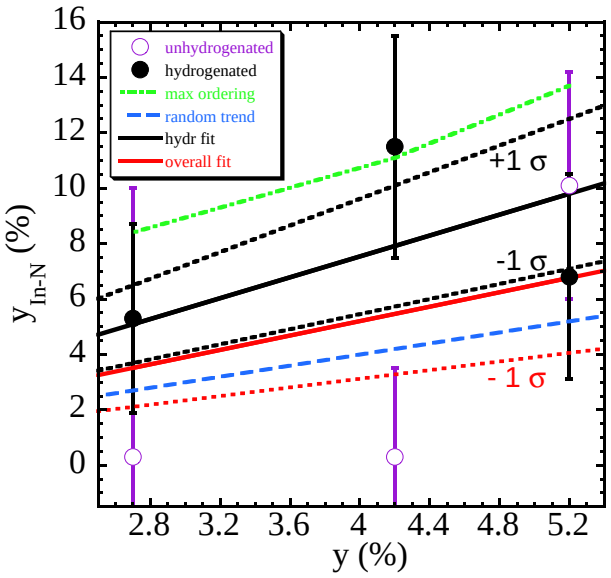

Figure 3.21: y_{In-N} as a function of y for quantum wells samples: violet open circles = un-hydrogenated samples; black full circles = hydrogenated samples; continuous line: linear fits to all data (red) and hydrogenated data (black), respectively; dotted line = 1σ error bars; the trends for random (dashed blue line) and maximum ordering (dashed-dotted green line) are also showed.

The results of the fits are reported in table 3.3, and the extracted values of y_{In-N} as a function of the N concentration y in Fig. 3.21. The introduction of the In-N signal was tested to be statistically significant for samples 227d4, 241d4, 383 and 383d4; on the other hand in case of samples 227 and 241 it resulted to be not significant. In these last cases the value of y_{In-N} was in any case very close to 0. The introduction, for the

sake of argument, of the In-N path while fitting all ternary samples did not improve the statistics.

In Fig. 3.21 it is evident how the y_{In-N} values of quaternary alloys constitute an almost homogeneous cloud distributed around the random trend (dashed blue line). In fact a least-squares [124] linear fit (full red line) to all the data (of the type $y_{In-N} = bx$), without distinguishing between as grown and hydrogenated samples, gives a value of the slope $b = 1.3 \pm 0.5$, which is undistinguishable from the random one ($b = 1$) within a 1σ confidence level [6] (dotted red line). If we consider only hydrogenated samples, all their y_{In-N} values are over the random line; a least-squares linear fit of only these data (continuous black line) gives $b = 1.9 \pm 0.5$; the agreement of this value with the random case value is at the limit of the 95 % confidence level. This result seems to indicate a tendency towards ordering in hydrogenated $In_xGa_{1-x}As_{1-y}N_y$ [158]; however the closeness of the random (dashed blue line) and maximum (dashed-dotted green line) ordering trends, and the experimental uncertainties do not allow us to understand if SRO is in this case stronger than that observed for annealed epilayers or not.

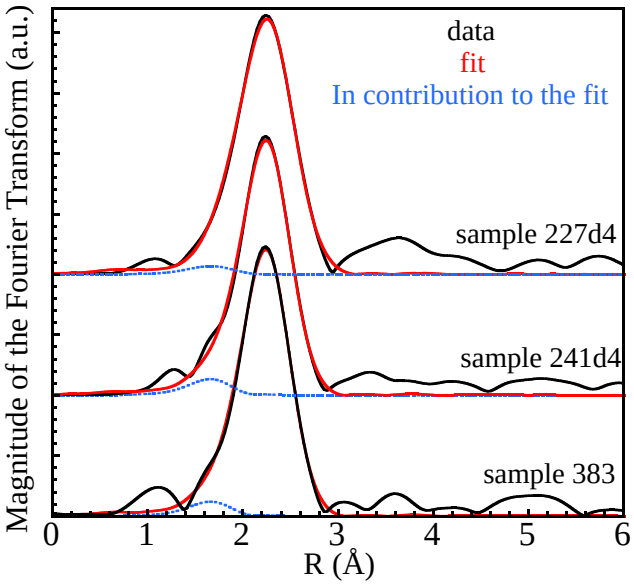

Figure 3.22: Fits on the Fourier Transform for the most ordered samples: black line = experimental spectra; red line = fits; blue dotted line = contribution to the fits of the In-N coordination.

The In-As bond lengths extracted by the fits are reported in table 3.3 together with the predictions of the model of Cai and Thorpe corrected for the local effects of the tetragonal distortion (section 1.5.2). Bond lengths look in overall agreement with the theoretical prediction if we exclude the case of hydrogenated samples; in this case in

[6] Errors on the slope are calculated by considering the different experimental uncertainties as error on the ordinates [124].

Table 3.3: Fitted first shell variables for quantum wells samples and theoretical bond lengths; not significant determinations of y_{In-N} are reported in parenthesis. The interatomic distances, Debye-Waller factors and ΔE for samples 227 and 241 are extracted from the fits which don't include the In-N first shell path. The systematic errors done by FEFF in the calculations of the theoretical phase shifts are taken into account by comparing the distances extracted in case of a bulk InAs to that given by XRD [165] and scaling consequently the experimental distances of the samples.

Sample	y_{In-N} (%)	R_{In-As}(Å)	R^{th}_{In-As}(Å)
$In_xGa_{1-x}As_{1-y}(N_y)$ quantum wells - series I			
225	xxx	2.582 ± 0.005	2.581
227	(0.3 ± 9.7)	2.589 ± 0.008	2.584
227d4	5.3 ± 3.4	2.599 ± 0.004	2.579
$In_xGa_{1-x}As_{1-y}(N_y)$ quantum wells - series II			
260	xxx	2.590 ± 0.005	2.581
241	(0.3 ± 3.2)	2.583 ± 0.004	2.583
241d4	11.5 ± 4.0	2.595 ± 0.004	2.578
$In_xGa_{1-x}As_{1-y}(N_y)$ quantum wells - series III			
378	xxx	2.591 ± 0.005	2.582
383	10.1 ± 4.1	2.589 ± 0.004	2.583
383d4	6.8 ± 3.7	2.589 ± 0.006	2.578

Sample	R^{th}_{In-N}(Å)	σ^2_{Ish} (10^{-3} Å^2)	ΔE (eV)
$In_xGa_{1-x}As_{1-y}(N_y)$ quantum wells - series I			
225	xxx	2.80 ± 0.17	8.4 ± 0.9
227	2.171	2.54 ± 0.27	8.7 ± 1.4
227d4	2.167	2.19 ± 0.29	11.6 ± 0.6
$In_xGa_{1-x}As_{1-y}(N_y)$ quantum wells - series II			
260	xxx	2.22 ± 0.16	9.8 ± 1.0
241	2.169	2.54 ± 0.08	9.4 ± 0.5
241d4	2.164	2.51 ± 0.33	9.2 ± 0.7
$In_xGa_{1-x}As_{1-y}(N_y)$ quantum wells - series III			
378	xxx	2.22 ± 0.13	10.3 ± 0.8
383	2.168	2.32 ± 0.33	10.0 ± 0.7
383d4	2.163	1.92 ± 0.28	10.7 ± 0.6

fact a systematical increase (in the range $0.01 - 0.02$ Å) with respect to the theory has been observed : this effect will be discussed later in chapter 5, which addresses in details the issue of hydrogenation.

In Fig. 3.22 we show the obtained fits for the most ordered samples of each series. The contribution of the weak but statistically significant In-N path is reported (blue dotted line) for each fit. This contribution helps in reproducing the asymmetry present in these FTs at low R-values, even if it is not sufficient to reproduce the shoulder present in the experimental spectrum of sample 241d4. As outlined above, this shoulder comes from errors in the atomic background modelling of the XAFS signal at high K-values rather than from ordering. It is worth noticing how the highest values for y_{In-N} have been obtained on samples for which the amplitude of the first shell peak in the Fourier Transform reported in Fig. 3.20 is smallest. This is due to the lower backscattering amplitude of N atoms which substitute a part of As atoms in the first coordination shell of the absorber rather than to an increased structural disorder. As a matter of fact the value of the Debye-Waller factors reported in table 3.3 does not vary significantly.

3.7 Quantum Wells : Ga K-edge DAFS

We report now DAFS spectra recorded at the Ga K-edge on the three quantum wells of the third series (samples 378, 383 and 383d4) performed to check the results achieved at the In K-edge. As reported in table 3.4, being the concentration of Ga higher than that of In (0.62 vs. 0.38), the value of the local variable y_{Ga-N} (probability of a Ga nearest neighbor site to host a N atom) would assume quite small values (8.4 %) even in the case N atoms were completely surrounded by Ga atoms. In case of random ordering we would expect to obtain for samples 383 and 383d4 a value equal to the N concentration y (5.2 %) and even smaller values in case of In-N + Ga-As short range ordering. In spite of such low values, our results on the In K-edge show that we should be able to measure y_{Ga-N} values with good S/N ratio also at the Ga K-edge and, in particular, we should be sensitive to the Ga-N coordination in case of random ordering.

DAFS data have been recorded following the Bragg peak of the weak (006) reflection scanning the energy in the range (10200 - 11100 eV). The anomalous effect through the Ga K-edge is well visible in the $\theta - 2\theta$ scans reported in Fig. 3.23. Note how the amplitude of the peak at 2θ of about 74-75 °, corresponding to the quantum well *out of plane* lattice parameter, increases while crossing the edge, has a maximum at an energy of 10375 eV and then decreases after the "white line". The increase in the X-ray intensity far from the Bragg condition (at $2\theta = 72°$ for example) is due to the contribution of Ga $K\alpha$ and Ga $K\beta$ fluorescence which have, after the edge, a not negligible magnitude compared to X-ray Diffraction on the weak reflection; during the DAFS measurement fluorescence radiation has been rejected using a crystal analyzer, as described in section 2.4 and illustrated in Fig. 2.11.

In Fig. 3.24 the Background subtracted DAFS spectra (the $\frac{I_{exp}-I_{0\ exp}}{I_{0\ exp}}$ of equation 2.60) are reported for the three quantum wells; each spectrum is an average of three-four spectra recorded with an energy step of 2 eV and a 10 s per point acquisition time.

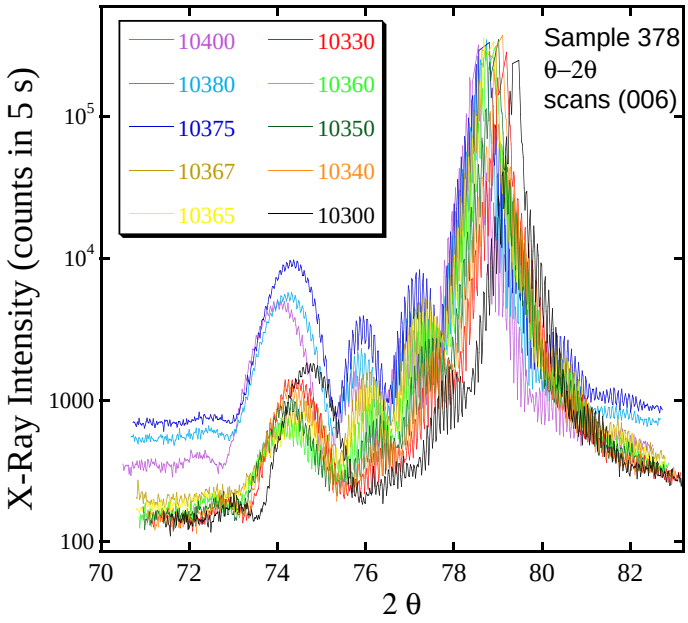

Figure 3.23: $\theta - 2\theta$ scans performed for sample 378 at different energies around the Ga K-edge (10367 eV) in the vicinity of the (006) reflection.

The small differences in the amplitude of the oscillations are due to the different values of S_d for the three samples.

The theoretical signals for fitting the data have been calculated by FEFF, then amplitudes and phases have been corrected by extracting the values of S_d (equation 2.62) and $\varphi_0 - \varphi_A$ (equation 2.64) from a fit of the smooth part of DAFS spectrum, as described in section 2.4; the values obtained are reported in table 3.4. Since the Fourier Transformed signals above the first shell were too low, only a first shell analysis was performed. Two cubic GaAs and GaN clusters were used to model the first shell Ga-As and Ga-N scattering signals.

The experimental and theoretical signals have been weighted for k^3, multiplied by a Gaussian window and then Fourier Transformed in the K-range [3 - 11] Å^{-1} for sample 378, [3 - 12] Å^{-1} for sample 383 and [3 - 10] Å^{-1} for sample 383d4 before performing the fit [7]. The fit was performed in the [1 - 3] Å R-range, with the Ga-As bond length (R_{Ga-As}) and Debye-Waller (σ_{Ga-As}) as fitting parameters. The Ga-N bond length R_{Ga-N} was fixed to the theoretical values and for this coordination the same Debye-Waller factor was used as for the Ga-As one.

The threshold energy shift ΔE was treated as a variable in case of the ternary sample 378, and then fixed to value obtained for this alloy while fitting the two quaternary

[7] the difference in the upper window limit comes from the fact that spectra have not the same quality at high k-values (as you can see in Fig. 3.24) and the spectrum of sample 383d4 in particular presents distortions above $k = 10$, probably due to multiple diffraction effects (section 2.3.1).

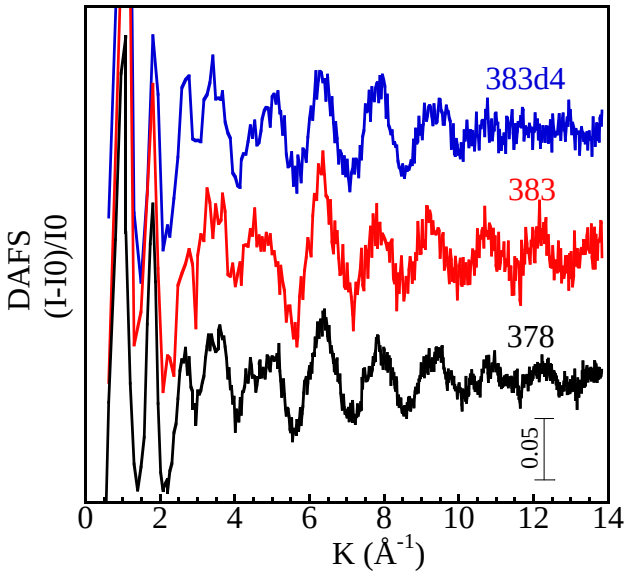

Figure 3.24: Background subtracted DAFS for series III quantum wells; a spline with 11 free coefficients has been exploited for modelling the smooth background I_0 of the experimental DAFS oscillations, fixing the R_{bkg} parameter of the Autobk code [113] to 1.2 Å.

samples (in order to avoid correlation between ΔE and R_{Ga-As}). This choice was justified by the fact that the very delicate correction procedure (via the DPU code) of the phases calculated *ab initio* by FEFF brings an uncertainty in the determination of the bond lengths larger than that induced by a possible different energy shift of the edge between the three samples. The many body amplitude reduction factor S_0^2 was fixed to the value found in a powder GaAs model compound.

First all fits were performed neglecting N atoms i.e. without using the first shell Ga-N signal; then this signal was included, the variable y_{Ga-N} was introduced in order to measure the relative Ga-As and Ga-N coordinations and fits were performed again. In all cases fits that include the N-related scattering path did not bring about an improvement of the statistic, by comparing the two reduced chi squares; conclusion is that we are not sensitive to the Ga-N coordination in these measurements, which is the reason for results for the extracted parameters reported in table 3.4 refer to fits that did not use the Ga-N signal.

The lack in sensitivity to the Ga-N coordination could be due to the small number of nitrogen atoms in the local environment of Ga as a consequence of the preferential In-N bonding observed at the In K-edge in this quantum wells series. In fact the y_{Ga-N} value corresponding to the random ordering condition (5.2 %) should be measurable since a value of $y_{In-N} = 5.3$ % was measured for sample 227d4 at the In K-edge (table 3.3). On the other hand I have to admit that this conclusion is questionable because the quality of DAFS spectra at the Ga K-edge is worse than that of XAFS at the In

Table 3.4: Results of the fit of DAFS spectra at Ga K-edge on series III quantum wells samples, theoretical bond lengths, values of y_{Ga-N} for In-As + Ga-N maximum ordering condition and values of S_d and $\varphi_0 - \varphi_A$ extracted by fitting the DAFS smooth part.

Sample	R_{Ga-As}(Å)	R^{th}_{Ga-As}(Å)	σ^2_{Ga-As} (10^{-3} Å^2)	ΔE (eV)
$In_xGa_{1-x}As_{1-y}(N_y)$ quantum wells - series III				
378	2.439 ± 0.012	2.443	3.05 ± 0.42	8.8 ± 2.7
383	2.446 ± 0.004	2.440	2.74 ± 0.46	8.8 (fixed)
383d4	2.446 ± 0.004	2.434	2.59 ± 0.50	8.8 (fixed)

Sample	max ordering y_{Ga-N} (%)	S_d	$\varphi_0 - \varphi_A$ at 10.37 KeV (deg)	$\varphi_0 - \varphi_A$ at 10.9 KeV (deg)
$In_xGa_{1-x}As_{1-y}(N_y)$ quantum wells - series III				
378	0.0	1.17	89	46
383	8.4	1.09	100	55
383d4	8.4	1.15	91	48

K-edge.

From table 3.4 it is evident how Debye-Waller factors do not significantly vary between the different samples. As concerns the Ga-As bond lengths, the values of samples 378 and 383 are in agreement with the prediction of *Cai and Thorpe* [75] + *Tormen* [83] model, which means that the procedure of correction of the DAFS theoretical phases was correct; the same is not true for the hydrogenated sample 383d4. The error on the Ga-As bond length for sample 378 reported in the table is greater than that for the other samples since in the fit of samples 383 and 383d4 ΔE was fixed to the value extracted for sample 378; since in this way the error associated to the quaternary samples doesn't take into account the uncertainty on ΔE, it is more confident to associate all Ga-As bond lengths the error of ±0.01 Å determined for the ternary alloy. In this sense the theoretical expected value for the hydrogenated 383d4 sample falls outside the 1σ lower experimental error bar, in agreement with In K-edge XAFS results reported in table 3.3, which envisage a stretching of the cation-As bond length upon hydrogenation. This last result will be discussed in the frame of the structural changes induced by hydrogenation in chapter 5.

Finally in Fig. 3.25 we report the fits performed on the first shell Fourier filtered signals *(Q-space)* for all series III quantum wells, which appear of satisfactory quality considering the intrinsic difficulty of DAFS experiments and data analysis.

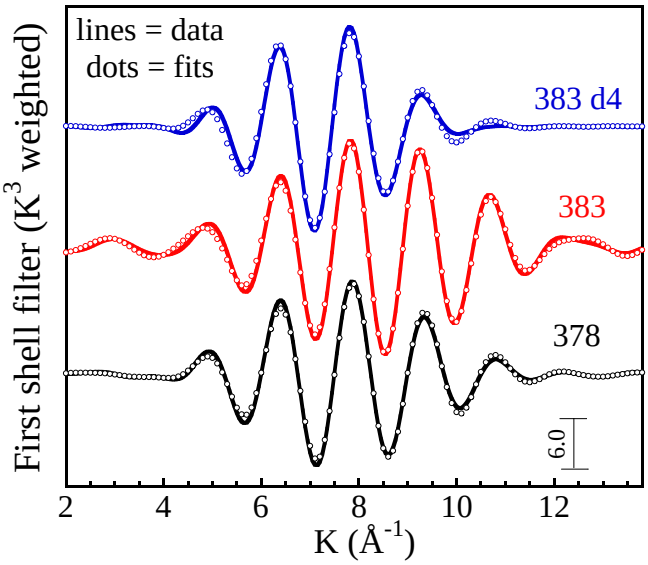

Figure 3.25: Fits on the first shell filter of series III quantum wells.

3.8 The link between optics and SRO

Can SRO justify the effect of annealing on the optical properties ?.

The answer to this final question was actually more complicated than envisaged. In fact if our epilayers, characterized by a quite high N content, are perfectly designed in order to study the local structural properties and the short range ordering phenomena (concentrations, substitutional location of N both in as grown and annealed samples, absence of interstitial defects and of heterogeneous contamination on the concentration scale of N), on the other hand they present a very poor PL efficiency before annealing. The PL signal in as grown epilayers is in fact not measurable at room temperature and extremely low even at 10 K, which made impossible a direct evaluation of the blue shift of the band gap by comparing the annealed samples with the as grown ones. The improvement of the PL signal upon annealing has been observed in all optical experimental studies on these alloys [67, 64, 159, 160] and essentially attributed to a reduction of non-radiative recombination centers (defects or impurities) upon annealing [8].

Due to the lack of quality data on as grown samples we concentrated only on the PL results on the annealed ones and we tried to interpret our results on ternary and quaternary samples in the frame of the method proposed by Duboz *et al.* [159]. These authors considered the effects of the different possible local configurations around N

[8] Due to the sensitiveness of PL even to very small non-radiative defects concentrations, we cannot exclude that this is the actual origin of the phenomenon, even if NRA analysis rules out the presence of N-related defects also in as grown samples down to few percents of the total N concentration (f_{001} in table 3.1) and a fluorescence analysis (Fig. 2.4) rules out the possibility of heterogeneous contamination down to the same concentration scale.

atoms in order to describe the compositional trend of the conduction band minimum in $In_xGa_{1-x}As_{1-y}N_y$. As explained previously in section 1.4.2 and illustrated in Fig. 1.21, the different N-centered clusters N-In_nGa_{4-n} ($0 \leq n \leq 4$) which can occur in $In_xGa_{1-x}As_{1-y}N_y$ induce levels which stand at different energies, whose value increases with n. This leads to a different N-mediated coupling among the conduction band edge states, which causes the increases of the band gap for high-n configurations. Therefore an alloy characterized by In-N + Ga-As SRO, possessing a larger statistical presence of In-rich clusters around the N atoms with respect to a random alloy, is predicted to show a blue shift of the band gap.

Tight-binding supercell calculations [160] showed that the E_N level, which enters the BAC formulation (equation 1.3), differs by 220 meV between the In_0Ga_4 configuration (E_{Ga} =1.65 eV for $x \approx 4\%$) and the In_4Ga_0 one (E_{In} = 1.85 eV); the other cluster configurations are equally spaced (by about 50 meV) between the two limit cases. The same calculation gives for the matrix element V_{MN}, which enters equation 1.3 and links the N resonant state and the conduction band-edge state, values of 2.00 $eV * \sqrt{y}$ for the 4-Ga nitrogen nearest neighbors (NNs) configuration and of 1.35 $eV * \sqrt{y}$ for the 4-In NNs. Experiments [171, 172] have shown that a value of $V_{Ga} = 2.4\ eV$ is more suitable than 2.0 eV in the ternary $GaAs_{1-y}N_y$. Therefore we have used this experimental value and the consequently scaled $V_{In} = 1.75\ eV$ in our work.

The BAC expression for the E_- conduction band is:

$$E_- = 0.5\{(E_N + E_C) - \sqrt{(E_N - E_C)^2 + 4yV^2}\} \tag{3.4}$$

As E_C we chose the experimental band gap value of GaAs (1.425 ± 0.002) when describing the CBM of $GaAs_{1-y}N_y$ alloys and a theoretical value for the band gap of $In_xGa_{1-x}As$ [173] (E_C^{InGaAs}) when considering the quaternary $In_xGa_{1-x}As_{1-y}N_y$. The exploited theoretical composition dependence of the $In_xGa_{1-x}As$ band gap was:

$$E_C^{InGaAs} = 1.425 - 1.53x + 0.45x^2 \tag{3.5}$$

This expression has been modified in order to take into account the band gap increase due to the compressive strain [173] which origins from the epitaxial growth on GaAs substrate :

$$E_C^{InGaAs} = 1.425 - 1.53x + 0.45x^2 + 0.42x \tag{3.6}$$

As E_N level in Eq. 3.4 we used the expression proposed by Duboz *et al.* [159]:

$$E_N = E_{Ga} + \frac{i}{4}(E_{In} - E_{Ga}) - x\beta \tag{3.7}$$

where β is a slope parameter fixed to 0.56 eV and i indicates the average number of Indium atoms in the NNs shell of nitrogen. In case of random arrangement of the atoms $i = 4x$, while in case of short range ordering i can be more generally expressed via our previously defined short range order parameter : $i = 4x_{N-In}$; in this way equation 3.7 leads to the following formulation 3.8 :

$$E_N = E_{Ga} + x_{N-In}(E_{In} - E_{Ga}) - x\beta \tag{3.8}$$

Also the potential V which enters equation 3.4 can be expressed via x_{N-In}:

$$V = V_{Ga}(1 - x_{N-In}) + V_{In}x_{N-In} = [2.4(1 - x_{N-In}) + 1.75(x_{N-In})] \tag{3.9}$$

The difference between the band gap of the quaternary (ternary) $(In_x)Ga_{1-x}As_{1-y}N_y$ samples and that of the relative N-free ternary (binary) alloys can be written as:

$$\Delta E = \frac{1}{2}\{E_N - E_C - \sqrt{(E_N - E_C)^2 + 4yV^2}\} + 0.42\frac{\Delta a_N}{\Delta a_{In}}y \tag{3.10}$$

The last term added in equation 3.10 accounts for the tensile strain due to the addition of nitrogen. $\Delta a_N = a_{GaN} - a_{GaAs}$ and $\Delta a_{In} = a_{InAs} - a_{GaAs}$ where a_{GaN}, a_{GaAs} and a_{InAs} are the lattice parameters of the binary compounds and the coefficient 0.42 is the same exploited for the compressive strain of $In_xGa_{1-x}As$; the negative contribution to ΔE due to the tensile strain induced by N has been in this way calculated by evaluating the equivalent In concentration which would produce the same (compressive) strain. In these alloys in fact, as it has been tested for InGaAs [173], the optical effects of an opposite strain are supposed to be identical in magnitude.

By introducing the expression of E_n of Eq. 3.8 and that of the potential of Eq. 3.9 into Eq. 3.10, the change in the band gap can be written as a function depending on the concentrations x and y and on the SRO parameter x_{N-In} :

$$\Delta E = \frac{1}{2}\{\ 0.269 + 0.2x_{N-In} - 0.56x - \sqrt{(0.269 + 0.2x_{N-In} - 0.56x)^2 + 4y(2.4 - 0.65x_{N-In})^2}\ \} - 1.242y \tag{3.11}$$

By imposing $x = x_{N-In} = 0$ we can compare the prediction of Eq. 3.11 with the experimental ΔE values of $GaAs_{1-y}N_y$ samples; fixing the In concentration to the average value of $x = 0.04$ (the actual x in our epilayers is in the range $0.038 - 0.043$) and assigning x_{N-In} different values, we can compare the expected dependence of ΔE on y for different short range ordering situations with the experimental change in band gap for the quaternary alloys. This is shown in Fig. 3.26, where we report the experimental ΔE for ternary (black squares) and quaternary (red circles) samples and prediction of equation 3.11 for different values of x_{N-In}. The condition $x_{N-In} = 0.04$ corresponds to the quaternary random alloy, $x_{N-In} = 0.12$ corresponds to the average SRO measured by XAFS (x_{N-In} values reported in table 3.2 are in the range $11.1-12.2$ %); finally the condition $x_{N-In} = 0.48$ corresponds to the SRO predicted by Kim and Zunger [9, 62] ($x_{N-In} = \frac{x \cdot y_{In-N}}{y} = \frac{0.04 \cdot 0.24}{0.02}$).

We can also treat x_{N-In} in equation 3.11 as a free parameter and fit the experimental ΔE data for the annealed quaternary alloys (this fit is reported in Fig. 3.26 too). This procedure allows to extract the value of x_{N-In} from PL data and to compare it with the XAFS determination. This fit yields a value of $x_{N-In} = (16 \pm 4)\%$, which is in agreement with XAFS data inside the 1σ error bar and shows how the change in the band gap of annealed $In_xGa_{1-x}As_{1-y}N_y$ with respect to the ternary $In_xGa_{1-x}As$ can be quantitatively described in the frame of the short range ordering theory with

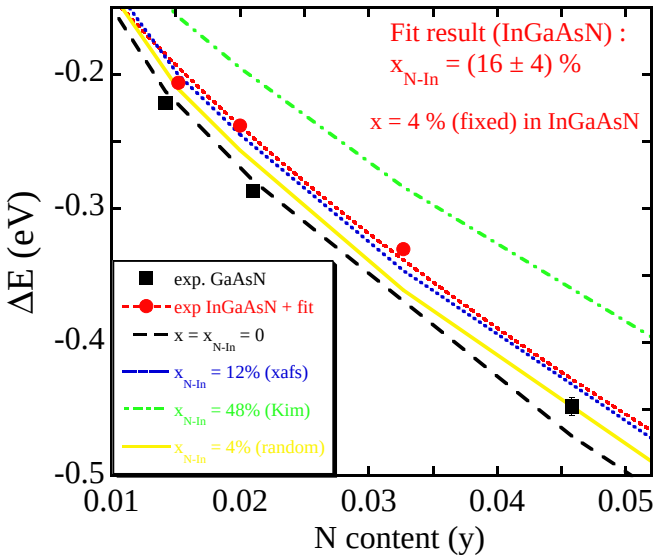

Figure 3.26: Experimental change in the band gap with respect to the N-free alloy in $(In_x)Ga_{1-x}As_{1-y}N_y$, along with the fit performed with equation 3.11 (red dotted line) and the trends for random alloy (yellow continuous line), SRO measured by XAFS [62] (blue dotted line), and SRO predicted by Kim and Zunger [9] (green dashed-dotted line); x is fixed to 4% in quaternary alloys. The Duboz's predicted trend for $GaAs_{1-y}N_y$ is also reported (black dashed line); experimental errors are smaller than the dimension of the symbols.

the information achieved by our XAFS experiments. In fact the curve representing the SRO measured by XAFS ($x_{N-In} = 12\%$) well reproduces the experimental data, closely following the least-squares fit of equation 3.11. On the contrary the experimental ΔE for all quaternary epilayers fall over the curve corresponding to the random configuration and well below the curve which represents the SRO predicted at the equilibrium by Monte Carlo calculations, showing again that the preferential In-N bonding driven by annealing is actual but quite week.

As regards ternary samples, equation 3.11 with $x = 0$ well reproduces the experimental ΔE observed in $GaAs_{1-y}N_y$ in the range $0.01 \leq y \leq 0.02$. The discrepancy between experimental data and prediction at higher y (around 0.045) can be due to changes in the concentration profile [86] of the samples or to homogenization of the nitrogen composition fluctuations [67] upon annealing as recently proposed by different groups.

3.9 Conclusions

We addressed in this chapter the issue of the structural short range ordering (SRO) in $In_xGa_{1-x}As_{1-y}N_y$ alloys, both in the form of epilayers and quantum wells. Even if the In-N + Ga-As configuration has been predicted to be energetically favored via Montecarlo calculations and even if the hypothesis of ordering upon annealing has been advanced basing on Infrared Absorption and Photoluminescence measurements, a lack in literature of a direct determination of the relative number of bonds in these alloys was evident before our work. Combining In K-edge XAFS measurements, N K-edge XANES and simulations of the XANES in the full multiple scattering (FMS) approach, we showed that ordering phenomena actually exist in annealed epilayers and have the same sign of the prediction, but are by far weaker in magnitude (order parameters are about one order of magnitude smaller than the predicted). Our measurements provide the first quantitative experimental determination of SRO in dilute nitrides, information of paramount importance for interpreting and controlling the optical behavior of these high-tech materials.

If situation is clear in case of epilayers, specifically designed in order to highlight the effect of SRO, it is more complicate in case of quantum wells samples, due to concentration constraints which cause the random and maximum ordering situations to be very close each other from the viewpoint of the local In-N relative coordination. In K-edge XANES and Ga K-edge DAFS performed on QWs seem to indicate a tendency towards a preferential In-N bonding in hydrogenated samples, even if we cannot be conclusive here due also to the fact that theory of hydrogenation does not support this result. XAFS and DAFS measurements of the In-As and Ga-As bond lengths respectively indicate that a stretching of the cation-As bond occurs upon hydrogenation, this effect will be explained in chapter 5 in the frame of the formation of particular N-H complexes, theoretically introduced in section 1.3.

The will of rigorously addressing the issue of SRO led us to characterize very well our epilayers from a structural viewpoint. In particular we showed that both in as grown and annealed samples N remains substitutional to As in the zincblend structure. In order to achieve this information we combined a N K-edge XANES analysis, in which spectra were recorded by varying the incidence angle to test the cubic symmetry of the N site, with nuclear physics techniques (NRA) which ruled out the presence of N interstitials in the structure comparing the nuclear reaction yield in random and channelling geometry. The measurement of the N concentration via NRA and of the *out of plane* and *in plane* lattice parameters via HRXRD allowed us to verify that the relaxed unit cell of our samples strictly follows the Vegard's law.

Finally we tried to understand if the SRO quantified by our XAFS measurements can provide a justification of the trend in the band gap of annealed samples. We exploited and adapted models reported in literature which, basing on tight binding calculations, predict the change in the band gap due to the SRO phenomena which are envisaged upon annealing. By inserting the order parameter extracted by XAFS in the formulation of these models we were able to reproduce satisfactory the PL results for annealed $In_xGa_{1-x}As_{1-y}N_y$ epilayers; moreover the value of the SRO parameter

extracted from a fit of PL spectra is consistent with that measured by XAFS. We conclude that SRO ordering can be actually at the origin of the blue shift observed upon annealing and that both structural and optical determinations indicate that SRO is by far weaker than that predicted at the equilibrium.

Chapitre 4 : La structure locale de l'alliage $GaAs_{1-y}N_y$

Dans ce chapitre nous présentons les résultats d'une analyse de la structure locale d'alliages $GaAs_{1-y}N_y$ et en particulier du comportement de la distance de liaison Ga-As à la limite de dilution pour l'azote. Les résultats des expériences XAS réalisées sur couches épaisses (300 nm) au seuil du Ga en détection d'électrons sont ici comparés avec des simulations faites à partir de la théorie de la Fonctionnelle Densité (DFT) et avec les résultats des différents modèles VFF (valence force field) introduits dans le premier chapitre. Le choix du système ternaire (sans indium) pour cette étude est dû au fait qu'il est beaucoup moins désordonné par rapport à l'alliage $In_xGa_{1-x}As_{1-y}N_y$, plus simple et adapté à l'étude des petites variations des distances des liaisons causées par l'incorporation d'une quantité limitée d'azote (y = 2.7 % maximum).

Nous confrontons ici les performances des différents modèles VFF dans la prédiction des longueurs des liaisons qui résultent des deux effets opposés: la diminution du paramètre de maille en fonction de la concentration d'azote et l'augmentation de la contrainte en tension due à la croissance pseudomorphique sur substrat GaAs [83]. Dans le cas de l'alliage $GaAs_{1-y}N_y$, la dimension, les énergies orbitales et l'electronégativité sont très différentes pour les deux anions. Par conséquent les constantes élastiques pour les composés binaires constituants (GaAs et GaN cubiques) et les constantes de force utilisées dans la construction du potentiel VFF [28] sont aussi très différentes. Nous montrons que les modèles VFF qui emploient deux couples de constantes de force [78, 29] (liés aux deux liaisons Ga-As et Ga-N) reproduisent mieux la distance Ga-As en fonction de la concentration d'azote par rapport à un modèle qui utilise un paramètre de rigidité unique dépendant d'un seul couple de constantes de force [75]. Comme le dernier modèle est valable pour la majorité des semi-conducteurs III-V, nous pensons que son échec est ici dû au désordre dans les constantes des forces liées aux très différentes caractéristiques des deux anions. Quand l'effet de la contrainte en tension est pris en compte, la simulation DFT reproduit très bien les données expérimentales pour la distance Ga-As, qui augmente avec la concentration d'azote malgré la diminution du paramètre de maille.

Nous montrons aussi une étude sur la largeur de la distribution de distances Ga-As; soit les expériences XAS, soit les calculs DFT et VFF montrent que cette largeur augmente considérablement en fonction de la concentration d'azote. Cela signifie que

le désordre statique augmente même pour de très petites quantités d'azote incorporées. En particulier les simulations DFT envisagent une distribution bi-modale de la distance Ga-As, où certaines liaisons sont plus longues par rapport à la même distance en GaAs tandis que les autres sont plus courtes. La longueur des liaisons allongées ne varie pas significativement avec la concentration d'azote, donc l'augmentation finale de la distance Ga-As est due à celle du nombre des liaisons allongées.

Les résultats XAS présentés dans ce chapitre constituent la première étude expérimentale de la structure locale et du désordre local causé par l'incorporation d'azote en $GaAs_{1-y}N_y$ [174]. La connaissance de la structure de cet alliage, qui est parmi les plus simples nitrures d'éléments III-V, est très important pour comprendre la physique de base des systèmes plus compliqués et plus intéressants du point de vue technologique comme l'alliage $In_xGa_{1-x}As_{1-y}N_y$.

Chapter 4

Local structure of $GaAs_{1-y}N_y$

4.1 Introduction

In this chapter we present the results of an analysis of the local structure of $GaAs_{1-y}N_y$ and in particular of the behavior of the Ga-As bond length at the N dilute limit. The results of XAFS experiments performed on 300 nm-thick epilayers at the Ga K-edge (in total electron yield detection) are compared with first-principles DFT calculations and with the prediction of the three Valence Force Field (VFF) models described in section 1.5.2. The choice of the In-free alloy for this investigation is due to the fact that this system is less disordered with respect to the quaternary $In_xGa_{1-x}As_{1-y}N_y$. If the N content y is low enough, $GaAs_{1-y}N_y$ is virtually a perturbation of the gallium arsenide crystal and is more suitable for studying subtle effects on the bond length distribution, related to the incorporation of N. We discuss the relative performance of the VFF models in predicting the bond length expansion due to the competitive effects of the decrease of the free lattice parameter and of the tensile strain due to the pseudomorphic growth (section 1.5.2).

In the case of $GaAs_{1-y}N_y$, the very large difference in size and electronegativity between the two anions causes a significant mismatch between the elastic constants of the binary constituent compounds (cubic GaAs and GaN) and, as a consequence, between the force constants employed while constructing the VFF potential. This constitutes a good test of validity for the above referred VFF models, some of which exploit unique rigidity parameters to describe the stiffness of the crystal. Along with the determinations of the average value of the bond length, we present also results obtained on the width of the bond length distribution which increases upon N incorporation, indicating the appearance of significant static disorder despite the low N content in the epilayers.

4.2 The investigated samples

Three 300 nm $GaAs_{1-y}N_y$ epilayers, with y = 0.084, 0.0142 and 0.0268 have been grown on undoped GaAs(001) substrate by solid source molecular beam epitaxy as referred in

Table 4.1: GaAsN epilayers : y, thickness, $a_\perp$, a_f, $a_\parallel$, PL peak position at different temperatures; errors on lattice parameters are different since different XRD setups have been exploited; error on PL data is ± 1 meV; error on y is determined by the quadratic propagation of the error on the lattice parameter.

Sample	y (%)	thickness (nm)	$a_\perp$ (Å)	a_f (Å)
V118	2.68 ± 0.19	310	5.593 ± 0.002	5.622 ± 0.002
V112	1.42 ± 0.19	300	5.621 ± 0.002	5.637 ± 0.002
V106	0.84 ± 0.12	310	5.636 ± 0.001	5.644 ± 0.001
GaAs	0.00	bulk	5.654 ± 0.001	5.654 ± 0.001
Sample	$a_\parallel$ (Å)	PL RT (eV)	PL 150 K (eV)	PL 10 K (eV)
V118	5.654 ± 0.004	xxx	1.132	1.144
V112	5.650 ± 0.004	1.166	1.176	1.177
V106	xxx	1.245	1.271	1.271
GaAs	5.654 ± 0.001	1.425	1.485	1.518

section 2.1. Since theoretical predictions [21] and the NRA channelling measurements [148], performed on similar samples and illustrated in section 3.2, indicate that the lattice constant of $GaAs_{1-y}N_y$ strictly obeys Vegard's law (Fig. 3.1), the N concentration has been measured via High Resolution X-Ray Diffraction (HRXRD) measurements. HRXRD data collected in the vicinity of the (004) crystal plane reflection [151] allowed to determine the *out of plane* lattice parameter $a_\perp$, while XRD in the vicinity of the asymmetric (224) reflection permitted to extract the *in plane* parameter $a_\parallel$, and to verify that the epilayers were virtually pseudomorphic to the substrate ($a_\parallel = a_{substrate}$). This information permitted to calculate the relaxed lattice constant a_f of the epilayers directly from the measured value of $a_\perp$, knowing the elastic constant C_{11} and C_{12} and using the well known equation [161] :

$$a_\perp = a_f + 2\frac{C_{12}}{C_{11}}(a_f - a_{substrate}) \tag{4.1}$$

a_f allows to calculate the stretching of the bond lengths due to the epitaxial tensile strain by using equation 1.20.

Table 4.1 reports, along with the concentration and thickness of the samples, the measured values of $a_\perp$ and the calculated values of a_f. An evaluation of $a_\parallel$ via XRD on the (224) reflection (also reported in the table) has been done only for the two samples whose N concentration is higher (V112 and V118); since the *in plain* lattice parameter

for these samples does not differ from that of GaAs (5.654 Å) inside the experimental 1σ error bar, we are confident that the same is true for the less strained one (V106).

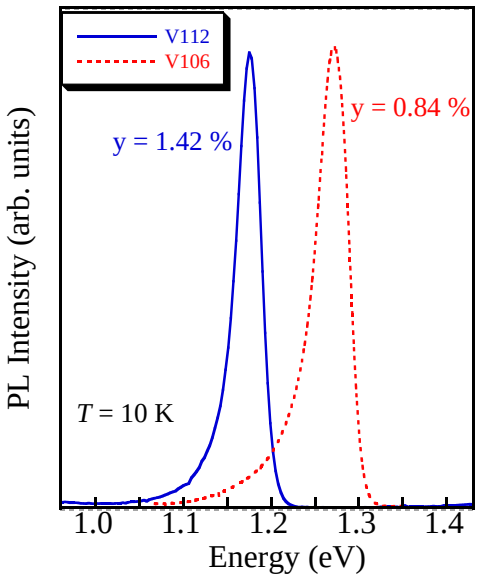

Figure 4.1: PL spectra for samples V106 and V112 at 10 K: it is evident the red shift of the band gap in the sample with higher N content.

We report also the value of the PL peak position at different temperatures: it is evident the progressive red shift by increasing the N content, due to the giant optical bowing discussed in chapter 1. The change in band gap is illustrated in Fig. 4.1, which shows the PL spectra acquired at T = 10 K for samples V106 and V112.

4.3 Ga K-edge XAFS : experiment and data analysis

The energy dependence of the X-ray absorption coefficient at the Ga K-edge was recorded by measuring the drain current from the sample (total electron yield, TEY). We measured the three $GaAs_{1-y}N_y$ epilayers described above plus a GaAs standard, in the same experimental conditions. TEY detection allows to selectively probe only the epilayers, whose thickness is about 300 nm. In fact even though *KLL* Auger electrons are quite energetic, based on a total-electron-yield depth dependence model [175], we estimate the contribution of absorption events taking place in the substrate to the total electron current to be lower than $3-4\%$ in our experiment. This estimation is obtained by considering the contribution $i(x_0)$ to the secondary electron current per Auger electron created at a depth x_0, with Auger escape length R, in case of an homogenous planar sample:

$$i(x_0) = \frac{3}{8}\frac{N}{\alpha R}\left[1 - \left(\frac{x_0}{R}\right)^2 + 2\frac{x_0}{\alpha R^2} - \frac{2}{(\alpha R)^2}\right] \tag{4.2}$$

This relationship is valid for $x_0 \leq R$, while for $x_0 \geq R$ $i(x_0)$ is:

$$i(x_0) = \frac{3}{8}\frac{N}{\alpha R}\left[\frac{2}{\alpha R} - \frac{2}{(\alpha R)^2}\right] e^{-\alpha(x_0 - R)} \tag{4.3}$$

In these equations, N is the average number of secondary electrons produced by an individual Auger electron and α^{-1} is the secondary electrons escape length. In case of GaAs (a good approximation for our samples) the *KLL* Auger-penetration range R has been estimated, via Monte Carlo calculations of the electron trajectories [176, 177, 178], to be about 350 nm, comparable with the thickness of our epilayers; *LMM* and other Auger electrons have escape lengths by far shorter. By integrating equation 4.2 from the surface of the sample ($x_0 = 0$) to the epilayer-substrate interface ($x_0 = 300$), we obtain the contribution of the sample to the secondary electrons current; while by integrating equation 4.2 from the interface ($x_0 = 300$) to R ($x_0 = 350$), and equation 4.3 from R ($x_0 = 350$) to $x_0 = \infty$, we estimate the contribution of the substrate. The latter one is 3 % of the former if a value of $\alpha^{-1} = 10$ Å is used, 4% if we consider α^{-1} = 100 Å ; it is safe to affirm that the actual α^{-1} values fall in this range [179].

XAFS background subtraction and data analysis have been performed according to the procedure described in section 2.2.5. A R_{bkg} value of 1.3 Å has been introduced in Autobk [113] and a spline with 13 free coefficients exploited in order to interpolate the atomic background. Very high quality data were obtained, as it is evident in Fig. 4.2, where the background subtracted XAFS spectra for all the samples are reported. χ(k)

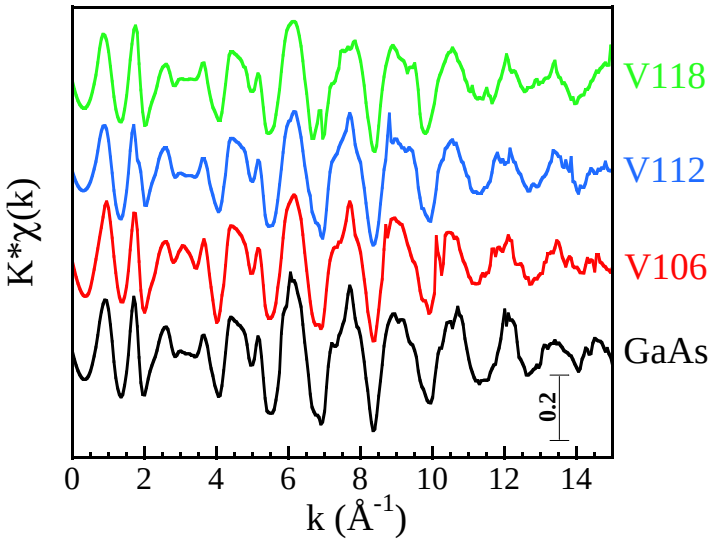

Figure 4.2: Background subtracted XAFS spectra.

signals were multiplied by a weighting function k^1 and a Gaussian window, and then Fourier-transformed in the k-range [3.5-11] $Å^{-1}$. In Fig. 4.3a we report the magnitude of the Fourier Tranforms of the data (lines); the first three peaks correspond to the

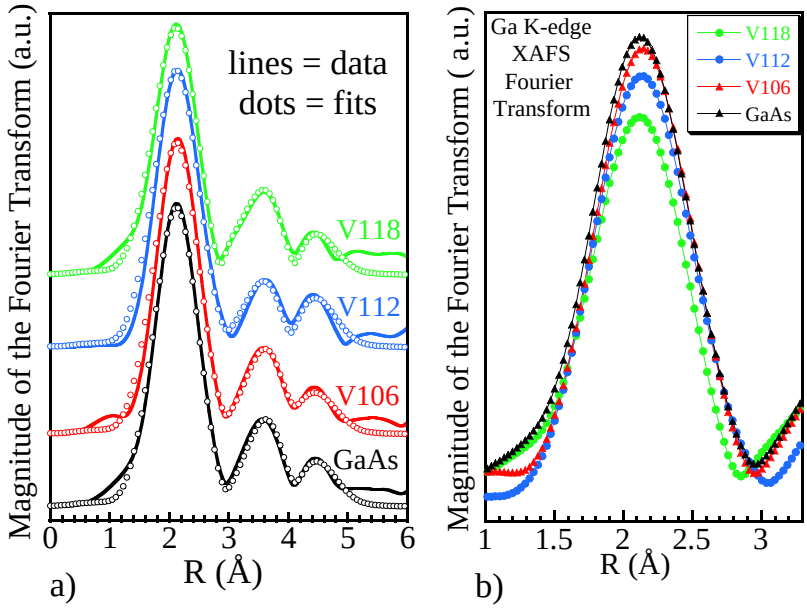

Figure 4.3: a) Fits in R-space for all the samples and the GaAs standard : line = data, dots = fits; b) Zoom on the first shell peak of the Fourier Transform for all spectra (superposed).

first three coordination shells of the zincblende structure. In Fig. 4.3b a detailed view of the first shell peak for all samples is reported; small shifts in the peak position and a significant decrease in the peak amplitude with N concentration are evident. Data analysis was performed by the FEFF 8.00 code using cubic GaAs and GaN model clusters to calculate the theoretical backscattering amplitudes and phase shifts. Data were fitted in R-space by the Feffit program [123] within the window [0 - 4.9] Å , which includes the second and third coordination shells. We were not directly sensitive to the N coordination in the first shell, because of the high N dilution and of low backscattering amplitude of nitrogen atoms; our goal was to measure effects induced by the presence of nitrogen on the average Ga-As bond lengths and their distribution.

First shell variables were the Ga-As bond length (R_{Ga-As}) and the Ga-As Debye-Waller factor (σ^2_{Ga-As}); second shell variables were a unique Ga-Ga distance R_{Ga-Ga} and Debye-Waller (σ^2_{Ga-Ga}). The two shortest triangular multiple scattering (MS) contributions were introduced, the first involving a second shell Ga atom and a first shell As, the second two first shell As atoms. MS lengths were expressed as a combination of the variables R_{Ga-As} and R_{Ga-Ga} ($\frac{2R_{Ga-As}+R_{Ga-Ga}}{2}$), assuming the virtual crystal approximation in case of the internal triangle; this procedure was necessary in order to reduce the total number of variables and to minimize correlation. Debye-Waller factors for MS paths were also treated as dependent parameters and expressed as $\sigma^2_{Ga-As} + \frac{1}{4}\sigma^2_{Ga-Ga}$, neglecting correlation between movements of the single atoms.

Third shell variables were a Ga-As distance and the related σ^2. The many-body amplitude reduction factor $S02$ and the threshold energy shift ΔE were estimated by fitting the GaAs standard in the same conditions as the samples. Fixing ΔE while fitting the samples allows avoiding correlation with the odd cumulants of the distance distribution; this was found to be particularly important in order to minimize the errors in the determination of the Ga-As bond length. This procedure is justified by the similarity of the local environment of Ga, due to the low N concentration, and to the fact that variations in the band gap among the samples (table 4.1) are well within the statistic error on ΔE. Fits in the R-space for the four samples are showed in the left side of Fig. 4.3 (dots), superposed to the experimental Fourier Transforms: note that the first shells are in particular very well reproduced, both from the viewpoint of amplitude and peak position.

Only in the sample with greatest N content a N-related second shell path (Ga-(N)-Ga) was found to be necessary to mimic second shell Ga atoms linked to the absorber via a first shell N atom. The split of the second shell is here detectable, even if the N coordination is not visible on the first shell, due to the higher backscattering amplitude of Ga with respect to N.

4.4 Valence Force Field calculation

In order to provide a theoretical estimate of the Ga-As bond length distribution, we have exploited the three VFF models described in section 1.5.2 (Cai and Thorpe = *CT*, Martins and Zunger = *MZ* and Balzarotti *et al.* = *B*).

According to the *CT* model, equation 1.17 gives for the Ga-As bond length in $GaAs_{1-y}N_y$ (*x=0*) the following relationship:

$$\begin{aligned} R_{\mathrm{Ga-As}} = (1-x)R_{\mathrm{GaAs}} + xR_{\mathrm{GaN}} \\ -a^{**}x(R_{\mathrm{GaN}} - R_{\mathrm{GaAs}}). \end{aligned} \tag{4.4}$$

R_{GaAs} and R_{GaN} are the Ga-As and Ga-N bond lengths in the binary zincblend constituent compounds, and a** is the rigidity parameter introduced in section 1.5.2 and related to the VFF bond-stretching and bending constants α and β. $R_{\mathrm{Ga-As}}$ depends on R_{GaAs} and R_{GaN}, which are related to the relative lattice constants as $R_{\mathrm{GaX}}=\frac{\sqrt{3}}{4}a_{\mathrm{GaX}}$. The GaAs lattice constant is available from high resolution XRD [166], and that of GaN from theory [168], as the zincblend structure is unstable for this compound. If we neglect the presence of N while calculating a** and use the bond bending and bond stretching constants of GaAs (taken from the paper of Martin [169]), the composition dependence of the Ga-As bond length is:

$$R_{Ga-As}(y) = 2.448 - 0.1591\ y. \tag{4.5}$$

We may also perform a weighted average to calculate $\frac{\beta}{\alpha}$, using the values for GaAs and GaN and the N concentration in order to obtain, point by point, the value a** to be used in equation 4.4. Distances predicted in this way do not significantly differ from

those extracted by equation 4.5, because of the small y in our experimental range. The force constants for cubic GaN have been obtained by the elastic constants reported in the paper of Wright [170], the weighted value of a^{**} calculated for the GaAsN epilayers investigated in this work is about 0.69.

In the *MZ* scheme, using the lattice parameters and force constants relevant to $GaAs_{1-y}N_y$ obtained as described above, the composition dependence of the Ga-As bond length is :

$$R_{Ga-As}(y) = 2.448 - 0.1046\ y \tag{4.6}$$

Note here the smaller slope of the predicted linear trend with respect to *CT*'s model. Finally we applied the *B* method for a ternary $AB_{1-y}C_y$ alloys to the case of $GaAs_{1-y}N_y$ (A=Ga, B=As, C=N), weighting the occurrence of all the possible $As_{4-n}N_n$ tetrahedra ($0 \leq n \leq 4$) around a central Ga atom.

In order to take into account the effect of strain due to the tetragonal distortion of the unit cell in our pseudomorphic epilayers, we have modified the three VFF models described above. In case of *CT*'s and *MZ*'s models, we have simply summed to the bulk values the result obtained from equation 1.20; in the following we will refer to these models as *CT + strain* and *MZ + strain* respectively. We have modified the *B* model for unstrained alloys to take into account strain in the $GaAs_{4-n}N_n$ tetrahedra. The anion sublattice is supposed to obey Vegard's law and then the unit cell is strained, following macroscopic elasticity theory, to match the substrate on the growth plane. Within such a strained structure a series of $GaAs_{4-n}N_n$ distorted tetrahedra is defined; the position of Ga in the tetrahedron is determined by minimizing the bond stretch energy. Eventually, average values for $\langle R_{Ga-N} \rangle$ and $\langle R_{Ga-As} \rangle$ are calculated by considering the bond degeneracy within each tetrahedron, as well as the relative number tetrahedra at each concentration value [180]. The variance of the bond length distribution σ^2_{Ga-X} (with X =N or As) is calculated by the usual formula $\langle (R_{Ga-X} - \langle R_{Ga-X} \rangle)^2 \rangle$. The composition dependence of the bond lengths and their standard deviation predicted in this way will be referred to as *B + strain*.

4.5 First-principles calculations

The lattice constant of both strained and unstrained GaAsN were calculated as function of N content according to the first principle supercell approach described in section 2.5.4, revealing in both cases a perfect Vegard-like behaviour, as suggested earlier [21] (For epitaxial GaAsN, this refers to the lattice constant normal to the growth plane). The main structural effect of the N substitution is as expected a local breathing-like inward relaxation of the Ga first neighbours. We studied the Ga-As and Ga-N bond lengths for y between 0 and 0.125. Consistently with the argument of section 1.5.2, in the strained case both the average Ga-As and Ga-N bond lengths increase with N content, whereas they decrease in the unstrained case. These values result from distributions of the Ga-As bond lengths which, as visible in Fig. 4.4, are roughly bimodal in the concentration range studied, with a narrow peak below the average

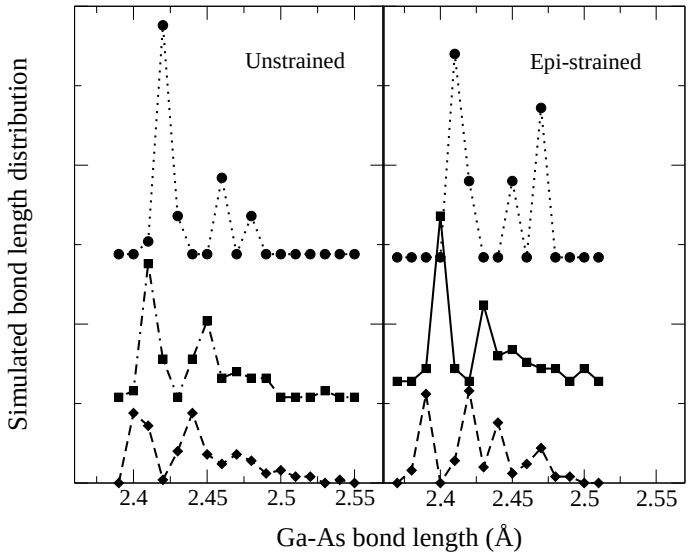

Figure 4.4: Calculated Ga-As bond length distributions at various concentrations.

value and a broad and structured peak group above the average. The bimodal character appears to be progressively smeared out at larger concentrations.

We analized statistically our calculated distributions. They are all positive-skewed (i.e. possessing an asymmetric tail at large length values) and platykurtic (flatter in shape than the normal distribution). Their standard variance σ^2 in units of 10^{-3} Å^2 is 0.5, 0.8, 1.1, and 1.7 for $y \simeq$0.03, 0.06, 0.09, 0.125 respectively. Since the temperature is zero in our simulation, these variances are purely disorder-induced. To compare with experiment, the thermal fluctuation of the underlying GaAs lattice must be accounted for (also, it may be argued that one should use the absolute deviation instead of the standard deviation since the distributions deviate appreciably from gaussian behavior). The resulting total fluctuations in units of 10^{-3} Å^2 for y=0.03, 0.06, 0.09, and 0.12 are respectively 9.8, 10.8, 11.3, and 13.3 using the absolute deviation, and 10.3, 11.8, 12.9, and 14.7 using the standard deviation. These data compare favorably with experimental results and their extrapolation to higher y, as will be discussed below.

The disorder-induced variations in σ^2 and mean value between different-y samples are quite small, although the distributions spread out (at least visually) over more than 0.1 Å. We therefore applied a number of standard statistical tests (paired-distribution t-test, F-test, and χ^2 and KS tests) [181], and verified explicitly that the distributions and their means and variances do indeed differ in a statistically significant sense.

4.6 Behavior of the average Ga-As bond length

In Fig. 4.5 we report the experimental values for the first shell Ga-As distance as a function of the N content y for the different samples, while a summary of the evaluated

Table 4.2: Evaluated structural parameters, ΔE is fixed to the value determined for the GaAs standard sample (7.7 ± 0.8 eV), errors = 1σ.

Sample	R_{Ga-As}(Å)	$\sigma^2_{Ga-As}(10^{-3}Å^2)$	R_{Ga-Ga}(Å)
V118	2.451 ± 0.005	8.1 ± 0.3	3.995 ± 0.012
V112	2.451 ± 0.005	7.1 ± 0.3	3.996 ± 0.013
V106	2.453 ± 0.005	6.6 ± 0.3	3.990 ± 0.011
GaAs	2.448 ± 0.005	6.4 ± 0.7	3.998 ± 0.010
Sample	$\sigma^2_{Ga-Ga}(10^{-2}Å^2)$	$R^{3rd\ shell}_{Ga-As}$(Å)	$\sigma^2_{3rd\ sh}(10^{-2}Å^2)$
V118	1.30 ± 0.09	4.659 ± 0.020	1.83 ± 0.19
V112	1.47 ± 0.10	4.680 ± 0.021	1.70 ± 0.21
V106	1.28 ± 0.07	4.697 ± 0.022	1.98 ± 0.24
GaAs	1.34 ± 0.10	4.688 ± 0.014	1.76 ± 0.16

structural parameters is shown in table 4.2. In the table we report the estimated distances and Debye-Waller factors for the first, second and third shells. The systematic error on the distances, due to that in the *ab initio* calculation of the XAFS phase shifts, has been taken into account by scaling all distances by a common value so as to obtain the known value for bulk GaAs [166]. Errors on the bond lengths reported in table 4.2 are obtained as quadratic combinations of the errors evaluated from the fits of the samples and of the GaAs standard. The black-bold continuous line reported in Fig. 4.5 represents a linear least-squares fit (R_{GaAs} + slope × y) to the experimental points. The two black dotted lines are the 1σ lower and upper error bar on the linear fit slope, extracted *a posteriori* from the data [124]; the dashed line is the 2σ error bar. Also shown in Fig. 4.5 are the average bond lengths calculated using the DFT calculations and the results of application of the VFF models, for both un-strained and strained cases. The values obtained from the first-principles simulations have been corrected for the systematic error by using the theoretical lattice constant (see section 4.5) of bulk GaAs.

Fig. 4.5 shows how the measured Ga-As bond length in $GaAs_{1-y}N_y$ epilayers is longer than the same distance in bulk GaAs, even if the free lattice parameter extracted by XRD decreases as a function of y (a_f = 5.644 Å for sample V106, a_f = 5.637 Å for sample V112, a_f = 5.622 Å for sample V118, a_f = 5.654 Å for GaAs). This can be accounted for by the propagation on the local scale of the tetragonal distortion induced by the epitaxial growth described in section 1.5.2. In the case of $GaAs_{1-y}N_y$/GaAs the strain is tensile, so the Ga-As bond length is increased by the distortion, which

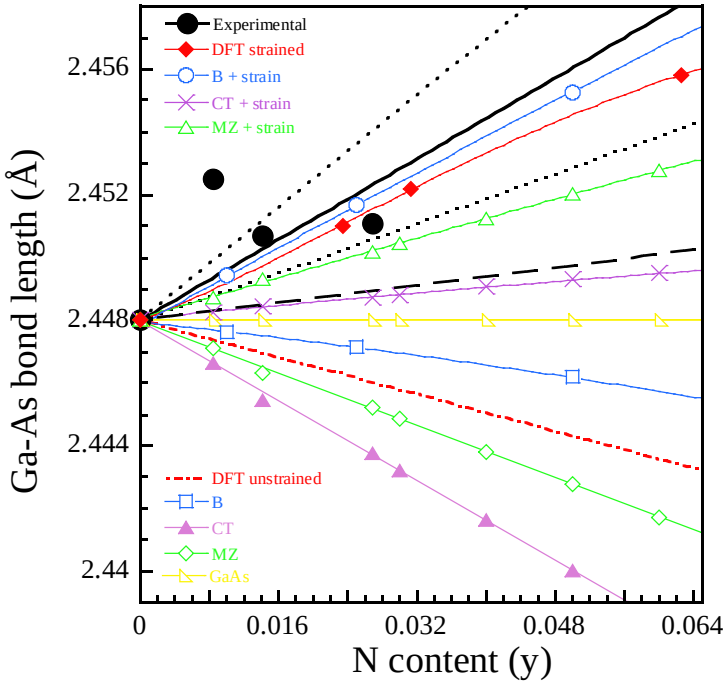

Figure 4.5: Experimental composition dependence of the Ga-As first shell bond length compared with the predictions of the first principles DFT calculation and three different VFF models. Black circles = experimental points, black bold continuous line = least-squares fit, black dotted lines = 1 σ error, black dashed line = 2 σ error; red line = DFT simulations, blue line = B models (with and without strain), violet line = CT, green line = MZ.

contrasts the alloying effect and finally induces the bond length to raise by increasing N concentration.

It is evident from Fig. 4.5 that the DFT simulations for strained alloys and the *B+strain* model quantitatively reproduce the increase in the bond lengths following nitrogen addition, while *CT + strain* prediction falls outside not only the 1σ lower error line but also the 2σ one, underestimating the experimental data; the results of the *MZ + strain* model is close to the experimental 1σ lower error limit.

The difference between the results of the *CT + strain* and *B + strain* models seems to mainly reside not in the modelling of the epitaxial strain effect, but in that of the bulk-like alloying component. This is evident by comparing the CT and B predictions for bulk alloys, the former is given in fact by a linear function with a quite high negative slope, which gives in this case shorter distances also compared with the MZ impurity model.

It is safe to say that CT and its "strained" extension, which are valid for a variety of ternary semiconductors, reproduce with less accuracy the bond lengths in an alloy

characterized by the very different sizes of the two anions and by the very different VFF force constants of its two binary constituent compounds. Considering for example bond stretching, $\alpha = 85.85\frac{N}{m}$ in case of cubic GaN and $\alpha = 41.19\frac{N}{m}$ in case of GaAs; as concerns bond bending $\beta = 14.98\frac{N}{m}$ for GaN and $\beta = 8.95\frac{N}{m}$ for GaAs. The *CT* model employs a unique parameter a^{**} in order to describe the force field; in the definition of a^{**} (equation 1.16) the bond stretching and bond bending force constants enter through their ratio, which compensates their absolute difference. The disorder in the force constants is not taken into account in this way, and this may be the reason for the failure of the approach in a case of great disorder such as the present. In case of $In_xGa_{1-x}As$ alloys, for which the method well reproduces the experimental data, the difference in the bond stretching force constants for the binary constituents is by far smaller ($\alpha = 41.19\frac{N}{m}$ for GaAs vs. $\alpha = 35.18\frac{N}{m}$ for InAs), and the same is true for the bond bending constants.

The *B* model and its "strained" version contain strong approximations since they assume that the cation sublattice is rigid and completely neglect the bond bending terms. Nevertheless in the expression of the VFF potential [78] they include separately the bond stretching terms for the binary constituent compounds. The *MZ*'s impurity model itself includes in its formulation [29], beside a bond stretching term related to the matrix, a second impurity-matrix bond stretching term, in the present case related to the N-Ga bonding. In this way the model allows the presence of two different force constants and better reproduces the experimental trend than *CT*. The *B*'s model, with respect to *MZ*'s, takes also into account the statistics of the possible different local configurations around the absorber atom.

Finally, another factor which can affect the results obtained with the three VFF approaches could be the different propagation of the error on the parameter R_{GaN}, which enters all the formulations. As described above, cubic GaN is unstable so that the R_{GaN} value exploited in this work has been obtained by calculations, which may bring about a large uncertainty in its determination.

Even if our experimental error bars are quite small for an XAFS experiment (about 0.005 Å for the first shell distances, about 0.01 Å for the second and about 0.02 Å for the third shell, as reported in table 4.2), unluckily this is not sufficient to extend our considerations on the relative performance of the different VFF methods to the second and third shell distances.

4.7 Distribution of the Ga-As bond length

A remarkable experimental finding is the decrease of the amplitude of the peak corresponding to the first shell Ga-As coordination in the XAFS Fourier transform by increasing N content. This is evident in Fig. 4.3b, where the Fourier transforms in the R-range [1-3.3] Å for the different samples and the standard are superposed. The effect originates from the progressively increasing structural disorder induced by the inclusion of nitrogen in the GaAs lattice, as it can be inferred looking at the systematic increase of the Debye Waller factor σ^2_{Ga-As} with y (table 4.2). This result is consis-

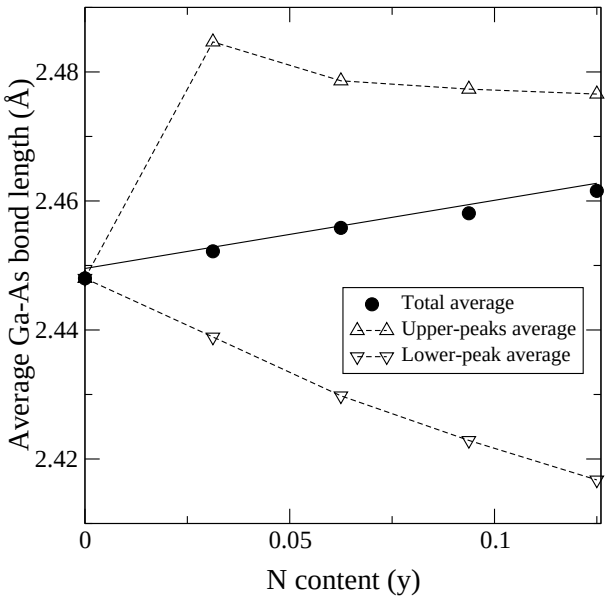

Figure 4.6: Simulated Ga-As distance in epi-strained GaAsN vs. N content. Solid line: linear fit; dashed lines connect data points.

tent with our DFT calculations which suggest to divide, as sketched in Fig. 4.6, the Ga-As distances distribution into two groups: that of the bonds which are stretched following N incorporation (R_s) and that of the bonds which are contracted (R_c). Such a bipartition is plausible on the basis of the calculated bond-length distributions displayed in Fig. 4.4. The total average bond length is then a weighted combination of the two contributions, $R_{Ga-As} = a_1 R_s + a_2 R_c$. As the N content increases, the peaks corresponding to the two groups into which we can roughly divide the distances distribution decrease in intensity and broaden (see Fig. 4.4). While the average length of the contracted bonds steadily decreases for increasing values of y, the average length of stretched bonds seems to saturate in this concentration regime, and the increase in the Ga-As total average bond length with y (see Fig. 4.6) is due to the increase of the relative weight a_1 of the stretched bonds (0.29, 0.47, and 0.67 for y$\simeq$3, 6, 9 %).

If we take for example the case of the 64 atoms supercell containing one N atom (y = 0.03125), the calculation yields the values $a_1 = 0.29$ and $a_2 = 0.71$ for the two weights; the final value for the predicted bond length, after correcting for the systematic error using the GaAs theoretical lattice constant, is $R_{Ga-As} = 2.452$ Å . This value is compatible with an increase of the distance with N content and with the closest experimental point (2.454 Å for y =0.0268). The broadening of the average Ga-As distance observed by XAFS with increasing N content finds a correspondence in the simulated broadening of the bimodal distances distribution illustrated in Fig. 4.4.

As described above we have quantitatively estimated the variances of the Ga-As distance distribution obtained from the DFT simulations. An extrapolation (by a

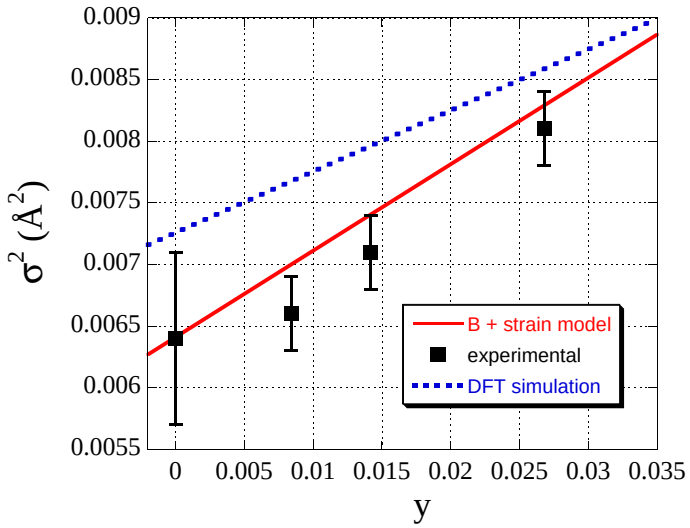

Figure 4.7: Comparison between predicted and calculated variances trend as a function of N concentration y; black symbols: experimental data, continuous red line: prediction by *B+strain* model, dotted blue line: prediction by DFT calculations.

least squares linear fit, R = 0.96) of the simulated variance trend to the experimental concentrations range is reported in Fig. 4.7, along with the experimental values. Also reported in Fig. 4.7 is a least-squares linear fit (R = 0.99) to the bond length variances obtained from model *B+strain*, which were obtained as described in section 4.4; in all cases the effect of thermal disorder estimated from the experimental spectrum of GaAs was summed to the structural effect. It is clear that all estimates of the bond length variance trend are in good qualitative agreement with the experiment and that predicted and measured variances values are in quantitative agreement within less than 0.001 Å^2.

4.8 Conclusions

In this chapter we have presented a combined experimental and theoretical study of the local structure of Ga in $GaAs_{1-y}N_y$ epilayers grown on GaAs [001], using XAFS in total electron yield detection, Density Functional Theory calculations (DFT) and Valence Force Field (VFF) models.

XAFS results reveal as the balance between the alloying and strain effects on the bond lengths results in an increase of the Ga-As bond-length with N concentration; the DFT calculations reproduce wells these experimental results when strain is taken into account. In the framework of VFF models, a good agreement is found if the difference in Ga-As and Ga-N bond stretching and bond bending force constants is taken into account; if force constant disorder is neglected, agreement with the experiment is not satisfying. This is due, in our opinion, to the fact that the force constants of the

binary compounds which constitute the $GaAs_{1-y}N_y$ alloy significantly differ each other with respect, for example, to the case of $In_xGa_{1-x}As$, for which the CT model works very well. The behavior of the bond lengths in $GaAs_{1-y}N_y$ could be common to other ternary systems characterized by a significant disorder in the force constants of the constituent compounds. This is, generalizing, yet another effect of the very different nature of the two cations in $GaAs_{1-y}N_y$, which is, as we explained in section 1.2, also at the origin of the anomalous optical properties of these alloys.

Both measurements and calculations indicate that the distribution of the Ga-As distances progressively broadens for increasing N content, which is a fingerprint of an increased local structural disorder induced by the incorporation of nitrogen. In particular supercell calculations give evidence of a bimodal distribution of the Ga-As distance, whereby a percentage of the bonds are stretched compared to the Ga-As distance in bulk GaAs, while the remaining bonds are contracted. The length of the stretched bonds does not vary appreciably when increasing the N content, so that the increase in the average Ga-As bond length with y is due to the augmented number of stretched bonds.

The XAFS results reported in this chapter constitute the first experimental study of the local structure and of the local structural disorder induced by N incorporation in $GaAs_{1-y}N_y$; a knowledge of the structure of this alloy, which is among the simplest dilute nitrides, is very important in order to understand the fundamental physics of more complicated and interesting systems like $In_xGa_{1-x}As_{1-y}N_y$.

Chapitre 5: Les effets structuraux de l'hydrogénation

Dans ce chapitre nous exposons les résultats sur les effets de l'hydrogénation sur la structure des alliages $GaAs_{1-y}N_y$ et $In_xGa_{1-x}As_{1-y}N_y$, soit à l'échelle de maille, soit à l'échelle locale. La théorie de l'hydrogénation et les effets sur les propriétés optiques ont déjà été discutés dans le chapitre I: l'hydrogénation renverse le décalage vers le rouge de la bande interdite dû à l'incorporation d'azote, et cet effet est complètement réversible par un recuit (30 minutes à 500 C) [52, 44]. Nous montrons ici, en exploitant la diffraction de rayons X (XRD), que l'effet sur l'émission est accompagné par une expansion du paramètre de maille dans la direction de la croissance, réversible par le même recuit. Dans le cas du $GaAs_{1-y}N_y$, le paramètre de maille de l'alliage hydrogéné se relaxe et ne se distingue plus de celui du GaAs, tandis que dans le cas du $In_xGa_{1-x}As_{1-y}N_y$ il se rapproche de celui de l'alliage non nitruré $In_xGa_{1-x}As$ [151].

En même temps la spectroscopie d'absorption dans l'infrarouge montre que l'hydrogénation provoque la rupture des liaisons Ga-N, qui se reconstruisent pendant le recuit. Des méthodes théoriques de minimisation de l'énergie totale (DFT) indiquent que la formation d'un des complexes décrits dans le chapitre I (le complexe $H_2^*(N)$) rend compte de l'effet sur la structure en même temps que de celui sur la bande interdite. Le phénomène est lié à la grande réactivité des atomes d'hydrogène qui, couplée avec l'électronégativité élevée de l'azote, arrive à casser la liaison Ga-N. Le recuit emporte les atomes d'hydrogène du réseau et en conséquence les liaisons Ga-N se reconstruisent. Les résultats que nous illustrons dans ce chapitre et en particulier ceux de XRD ont été très utiles pour discriminer parmi les différents complexes N-H proposés. En effet tous les complexes mono-hydrogéné ne provoquent pas une expansion de la structure selon les prédictions et pourtant leur formation peut être écartée [182].

L'expansion de la structure conséquente à l'hydrogénation explique aussi l'allongement des distances cation-As observé (chapitre III) dans le cas des puits quantiques $In_xGa_{1-x}As_{1-y}N_y$ hydrogéné par rapport aux prédictions VFF (qui tiennent aussi compte de la contrainte due à la croissance épitaxiale). Nous reportons ici aussi les résultats d'expériences XAS au seuil du Ga réalisées en détection d'électrons sur couches épaisses de $GaAs_{1-y}N_y$ hydrogéné; même dans ce cas la distance Ga-As est plus longue que prévu, malgré cette liaison ne soit pas directement impliquée dans la formation des complexes N-H. L'hydrogénation enlève le désordre structural dans la

distribution des distances de liaison Ga-As, observé dans les échantillons non traités (chapitre IV) et dû à la contrainte en tension de la maille conséquente à l'incorporation d'azote.

Les résultats expérimentaux présentés dans ce chapitre fournissent la première détermination des effets structuraux de l'hydrogénation en nitrures d'éléments III-V. En particulier les résultats XRD sur l'expansion du paramètre de maille constituent une parmi les premières observations d'un effet si remarquable (et en même temps réversible) sur la maille d'un semi-conducteur, guidé par un traitement post-croissance.

Ces résultats sont aussi importants du point de vue des applications techniques car l'hydrogène est un contaminant très commun dans les techniques de croissance utilisées pour la production de semi-conducteurs à large échelle comme le dépôt en phase vapeur par organométalliques (MOCVD). La connaissance des effets structuraux de l'hydrogénation montrée dans ce chapitre est pourtant nécessaire car ces effets influencent les propriétés d'émission de manière considérable. En plus, un contrôle amélioré du processus d'hydrogénation pourrait être utilisé pour régler la longueur d'onde d'émission des composants optoélectroniques après la croissance, en exploitant en même temps la réversibilité du phénomène.

Chapter 5

Structural effects of hydrogenation

5.1 Introduction

In this chapter we will present results on the effects of atomic hydrogen irradiation on the local and long range structure of $GaAs_{1-y}N_y$ and $In_xGa_{1-x}As_{1-y}N_y$. The theory of hydrogenation and its effects on the optical properties were discussed in section 1.3. Hydrogenation induces a dramatic reversal of the red shift of the band gap due to N incorporation, completely reversible upon thermal annealing. We show in this chapter, via X-Ray diffraction measurements, that this effect is accompanied by a lattice expansion along the growth direction, completely recovered after the annealing procedure. In the case of the ternary $GaAs_{1-y}N_y$ the *out of plane* lattice parameter $a_\perp$ of the hydrogenated alloy relaxes and becomes almost indistinguishable from that of the substrate; in the case of the hydrogenated $In_xGa_{1-x}As_{1-y}N_y$, $a_\perp$ recovers and also exceeds the value of the N-free $In_xGa_{1-x}As$ [151].

Simultaneously, Infrared Absorption spectroscopy suggests that the Ga-N bonds are broken by hydrogenation and reform upon annealing. The information achieved from our experiments allows to discriminate between the proposed formation of monohydride and dihydride complexes (described in section 1.3). In fact total energy first-principles calculations performed in the frame of our work predict different behaviors of the long range structure of these alloys upon formation of the two kinds of complexes.

The expansion of the *out of plane* lattice parameter upon hydrogenation helps in understanding the underestimation of the local bond lengths present in hydrogenated samples (chapter 3), if one assume that the only effect of hydrogenation is the removal or enhancing of strain; we will discuss also the effects of hydrogen irradiation on the local structure of the $GaAs_{1-y}N_y$ samples already presented in chapter 4. The experimental results presented in this chapter constitute the first determination of the structural effects of hydrogenation in III-N-V semiconductors.

5.2 The analyzed samples

We report results obtained on $GaAs_{1-y}N_y$ epilayers, $In_xGa_{1-x}As_{1-y}(N_y)$ quantum wells and some selected $In_xGa_{1-x}As_{1-y}N_y$ epilayers.

Concerning the $GaAs_{1-y}N_y$, we studied the three samples V106, V112 and V118 described in chapter 4 and for each of them an hydrogenated sample with the same characteristics (indicated with H106, H112 and H118 respectively); hydrogenation was performed according to the procedure described in section 2.1, the same dose was used for all ternary and quaternary samples presented in this chapter.

The hydrogenated samples hereby referred as H106, H112 and H118 were obtained cutting the original samples into two or more parts. As it will be shown later, in the hydrogenated epilayers it is impossible to calculate with precision the concentrations from $a_\perp$ values estimated by XRD; in fact in this case the diffraction peaks related to $a_\perp$ overlap that of the substrate. Therefore we assumed that the concentrations were identical to those of the as grown samples (table 4.1).

On the third piece cut from the original sample V106 we performed also a long heat treatment (section 2.1) identical to that exploited during hydrogenation, but without irradiating the samples: we will refer to this annealing procedure as *A4* and to the sample as V106A4. The fourth and last part of the original sample was first hydrogenated and then annealed in order to remove hydrogen from the structure: we will refer to this annealing procedure as *A5* and to the sample as H106A5.

As for the quaternary quantum wells, listed in table 3.1, we investigated the structure of series II and III samples; furthermore we studied the $In_xGa_{1-x}As_{1-y}N_y$ epilayer 712 A2 and two more samples coming from the same original wafer: the first hydrogenated (712 A2H), the second hydrogenated and then subjected to the *A5* treatment in order to remove hydrogen (712 A2A5).

5.3 Effects of the lattice parameter

5.3.1 XRD results

As already observed by Polimeni *et al.* [52] and Baldassarri *et al.* [44] (Fig. 5.1) the PL peak of an $In_xGa_{1-x}As_{1-y}N_y$ quantum well gradually blue shifts upon hydrogenation while increasing the hydrogenation dose.

As shown in the figure, for a dose of $270H_0 = 0.25 \cdot 10^{19}$ ions/cm^2 (red line) the maximum shift of the band gap is obtained and the PL peak gets close to that of a ternary $In_xGa_{1-x}As$ (black dotted line). All our samples were irradiated with this dose. At higher doses (blue line) the PL peak position saturates and no further blue shift is observed. As can be observed from the figure the PL intensity decreases at increasing hydrogenation doses; the broadening of the PL peak is due to non-radiative defects created by the hydrogen irradiation. The re-opening of the band gap upon hydrogenation has been reported also for In-free samples.

To check if this intriguing optical behavior has or not a structural origin we performed X-ray diffraction $\theta - 2\theta$ scans (section 2.3.2) on the $GaAs_{1-y}N_y$ samples V106,

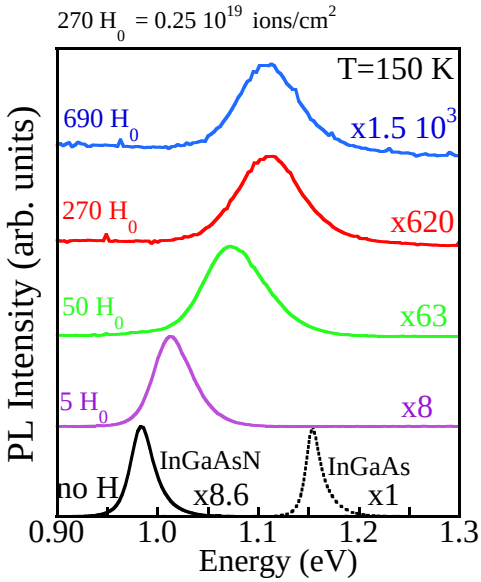

Figure 5.1: PL spectra of $In_xGa_{1-x}As_{1-y}N_y$ quantum wells subjected to different hydrogenation doses; black continuous line = non-hydrogenated QW (sample 227), black dotted line = N-free QW (sample 225).

H106, V106A4 and H106A5 (Fig. 5.2b). XRD data for these samples are reported beside the relative photoluminescence spectra (Fig. 5.2a). The XRD scan of the virgin sample V106 (black continuous line) presents two peaks corresponding to the $a_\perp$ of the substrate (peak on the left, higher intensity) and of the epilayer (peak on the right, lower intensity). The positive angular shift of the N-containing epilayer peak indicates that it has a smaller lattice constant along the growth direction (5.636 ± 0.001 Å) than the substrate ($a_{substrate}$ = 5.654 Å). X-ray diffraction data of the hydrogenated epilayer (red line - sample H106) do not show the diffraction peak associated with the $GaAs_{1-y}N_y$ epilayer. On the contrary a shoulder is present on the lower angle side of the substrate peak. The shoulder is more evident if data are presented in linear scale (Fig. 5.3). It is evident the presence of compressive strain in the hydrogenated $GaAs_{1-y}N_y$ epilayer, with the lattice constant of the hydrogenated sample that exceeds the GaAs one.

We underline that the heat treatment of the sample without hydrogen does not vary the material lattice characteristics (dotted gray line - sample V106A4). Diffraction data recorded on the sample first hydrogenated and then annealed until all H was removed (blue line - sample H106A5) show a full restoration of the $GaAs_{1-y}N_y$ lattice and photoluminescence properties. This indicates that no lattice randomization or N out diffusion occurs due to H irradiation. We conclude that the crystal unit cell of $GaAs_{1-y}N_y$ undergoes a large variation of its size upon H insertion and that this process is reversible.

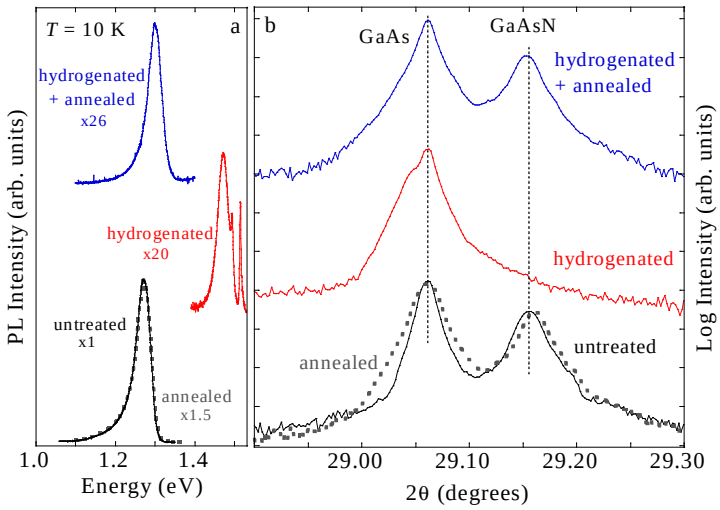

Figure 5.2: Reversible effects of hydrogenation on the emission properties (a) and on the (004) diffraction peak (b) of $GaAs_{1-y}N_y$; black line = V106, red line = H106, blue line = H106A5, gray dotted line = V106A4. Mo Kα_1 line was used for XRD.

Similar results have been obtained for samples V112 and H112, characterized by a higher nitrogen content ($y = 0.0142$) (Fig. 5.4). The *out of plane* lattice parameter of sample V112 results to be $a_\perp = 5.621 \pm 0.002$ Å, smaller than the V106 one, so showing the presence of an higher tensile strain. Also in this case the spectrum of the hydrogenated sample H112 (red line) shows the disappearance of the epilayer related peaks and the appearance of a shoulder on the left side of the substrate peaks. In the present case the shoulder is well separated from the substrate peak, so we can estimate $a_\perp$ for the epilayer (5.661 ± 0.004 Å) which results very close to $a_{substrate}$. As shown in the inset of Fig. 5.4, the relaxation of the unit cell upon hydrogenation is accompanied by the usual blue shift of the band gap.

As anticipated in chapter 4, XRD data collected on the (224) asymmetric crystal plane reflection for sample V112 and V118 showed that the virgin GaAsN epilayers were pseudomorphic to the substrate. We reported these data in Fig. 5.5 (black and red line) together with those of the hydrogenated sample H112 (blue line). The two highest peaks at about $2\theta = 83.6°$ and 84.1° are due to the substrate and origin from diffraction of the Cu Kα_1 and Cu Kα_2 incident radiation. The structures between $2\theta = 84.1° \div 84.9°$ are related to the epilayer. It is evident how the structures related to the epilayers disappear and how the epilayer and substrate diffraction peaks are not separated even on the (224) reflection.

Since the epilayer and substrate peaks are not separated in hydrogenated samples both on the (004) and (224) crystal plane reflections, we conclude that also hydrogenated samples are pseudomorphic. In fact if the difference in $a_\parallel$ of the epilayers and substrate was significant we would observe peaks at two different angular positions on

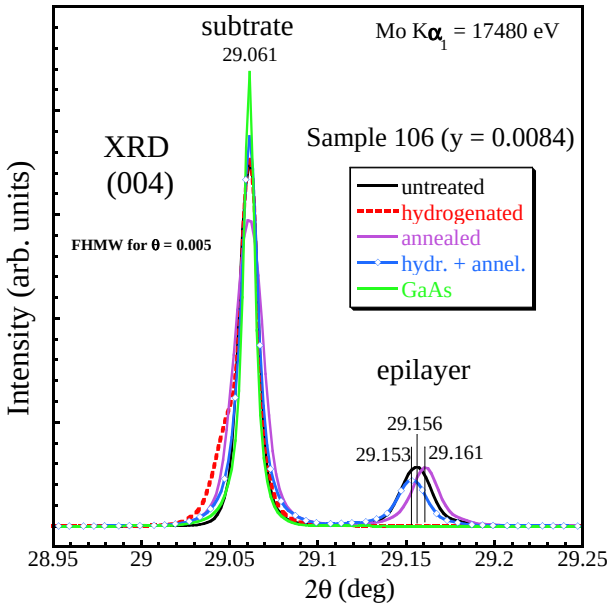

Figure 5.3: Same XRD spectra of Fig. 5.2b, but reported in linear scale.

the asymmetric reflection (224). Furthermore XRD on the (004) reflection indicates that hydrogenated epilayers are virtually unstrained, have the same lattice parameter of the substrate, so likely they are pseudomorphic.

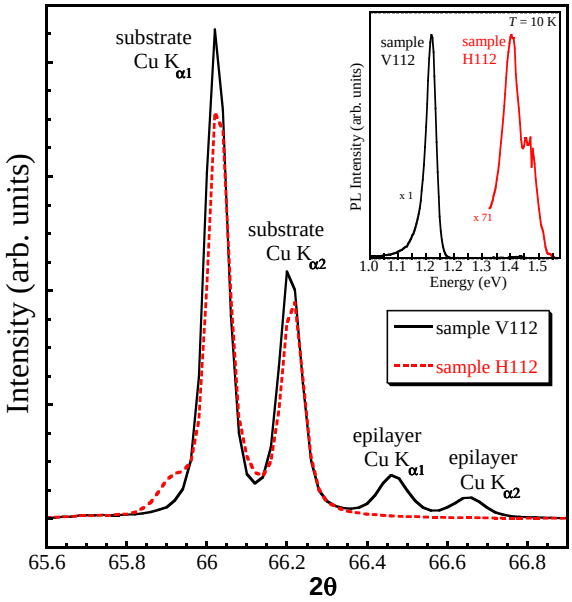

Figure 5.4: (004) $\theta - 2\theta$ scans for sample V112 (black line) and H112 (red line); in the inset the relative PL spectra. The spectra were recorded with a Cu rotating anode, without the use of a monochromator; therefore the diffraction peaks are doubled for the presence of both Kα_1 and Kα_2 fluorescence lines.

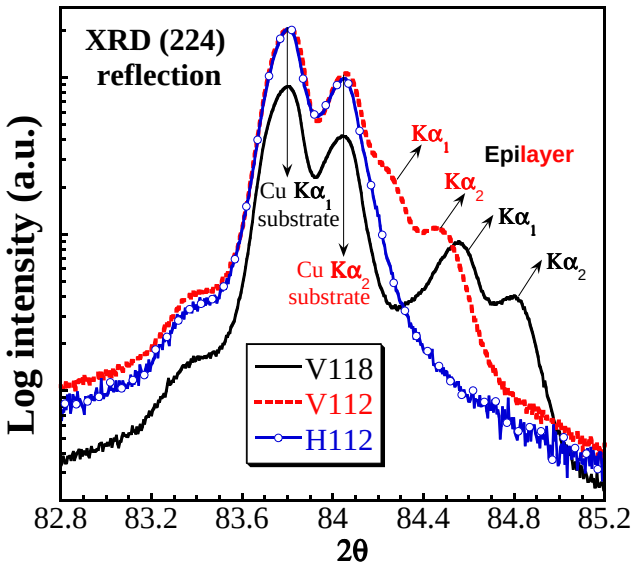

Figure 5.5: XRD $\theta - 2\theta$ scans on the asymmetric (224) reflection; black line = sample V118, red line = sample V112, blue line = sample H112 (hydrogenated).

In order to strengthen our observations we studied the case of the $In_xGa_{1-x}As_{1-y}N_y$ alloy, which is under opposite initial strain conditions (i.e. compressive) for sufficiently large In content (as is the case of our quantum wells). The bottom black curve in

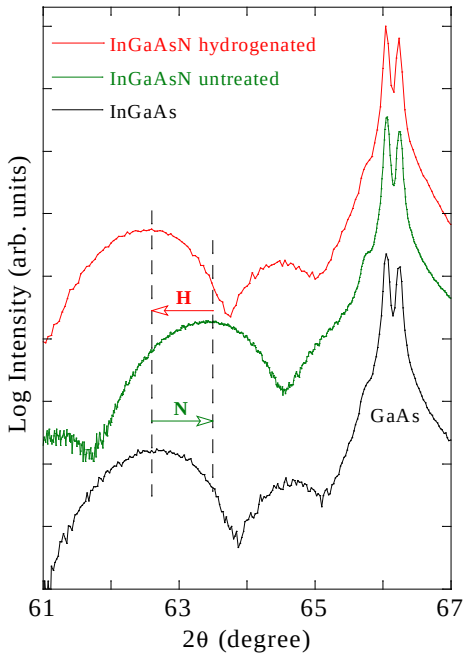

Figure 5.6: XRD rocking curve for series III quantum wells samples; black line = sample 378 ($x = 0.38, y = 0$), green line = 383 ($x = 0.38, y = 0.052$), red line = 383d4 ($x = 0.38, y = 0.052$, hydrogenated). The split of the substrate peak into two peaks at about 66° is due to the fact that also these measurements were performed with a Cu rotating anode without the use of a monochromator, and therefore to the presence of both Cu Kα_1 and Cu Kα_2 fluorescence lines. The two lines are not separated on the quantum well diffraction peak being this latter very broad because of the very small thickness of the active layer.

Fig. 5.6 shows the X-Ray Diffraction curve of a reference N-free $In_xGa_{1-x}As$ quantum well (sample 378). The substitution of 38 % of the Ga atoms with larger In atoms gives rise to compressive strain in the thin quantum well layer with an *out of plane* lattice parameter $a_\perp = 5.929 \pm 0.008$ Å. This compressive strain is partially relieved by adding N (sample 383, middle green curve of Fig. 5.6). The shift of the sample 383 peak with respect to 378 indicates a diminished *out of plane* lattice parameter ($a_\perp = 5.868 \pm 0.007$ Å).

The irradiation of the N-containing sample with H restores the lattice properties of the N-free quantum well (sample 383d4, top red curve) to such an extent that the diffraction curves of the hydrogenated $In_xGa_{1-x}As_{1-y}N_y$ and of the $In_xGa_{1-x}As$ samples are hardly distinguishable. As for the $GaAs_{1-y}N_y$ case, also for this hydrogenated

sample photoluminescence data show a full recovery of the band gap to the value of the N-free $In_xGa_{1-x}As$ quantum well (table 3.1).

The same results have been obtained also from XRD (004) $\theta - 2\theta$ scans with Synchrotron Radiation near the Ga edge. Fig. 5.7a reports the data recorded on the same

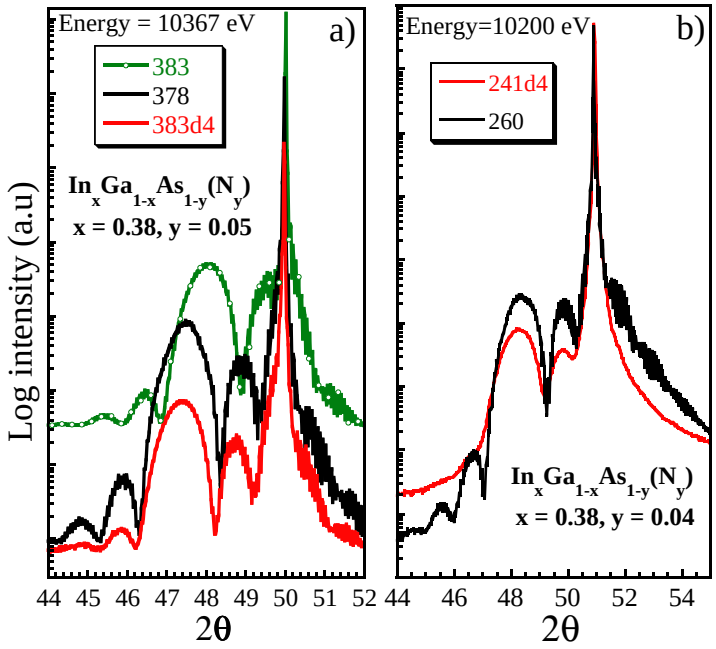

Figure 5.7: (004) XRD scans performed on $(In_x)Ga_{1-x}As_{1-y}N_y$ QWs with Synchrotron Radiation; a) series-III samples, b) series-II samples; black line = N free samples, green line = as grown $In_xGa_{1-x}As_{1-y}N_y$, red line = hydrogenated $In_xGa_{1-x}As_{1-y}N_y$.

series-III samples of Fig. 5.6; the presence of clear Pendellossung fringes is a clue of the high crystalline quality of the QWs and indirectly indicates that samples are pseudomorphic to the substrate; in fact relaxation via dislocations normally induces the disappearance of these structures. Fig. 5.7b reports similar XRD scans performed on series-II quantum wells. In this case data for the as grown $In_xGa_{1-x}As_{1-y}N_y$ sample 241 are not available; nevertheless by comparing data for the N-free 260 and the hydrogenated $In_xGa_{1-x}As_{1-y}N_y$ 241d4 it is clear how the two *out of plane* lattice parameters are very similar, as a result of the expansion caused by hydrogenation of the QW. The quantitative results of XRD experiments reported in table 5.1 show that $a_\perp$ of the hydrogenated $In_xGa_{1-x}As_{1-y}N_y$ QWs and that of the ternary $In_xGa_{1-x}As$ ones characterized by the same In content are equal within the experimental error, while $a_\perp$ of the as grown $In_xGa_{1-x}As_{1-y}N_y$ samples are significantly smaller.

In case of the epilayer 712A2, where the strain is tensile because of the low In content (3.8 %), hydrogenation (Fig. 5.8) induces an expansion of the unit cell which

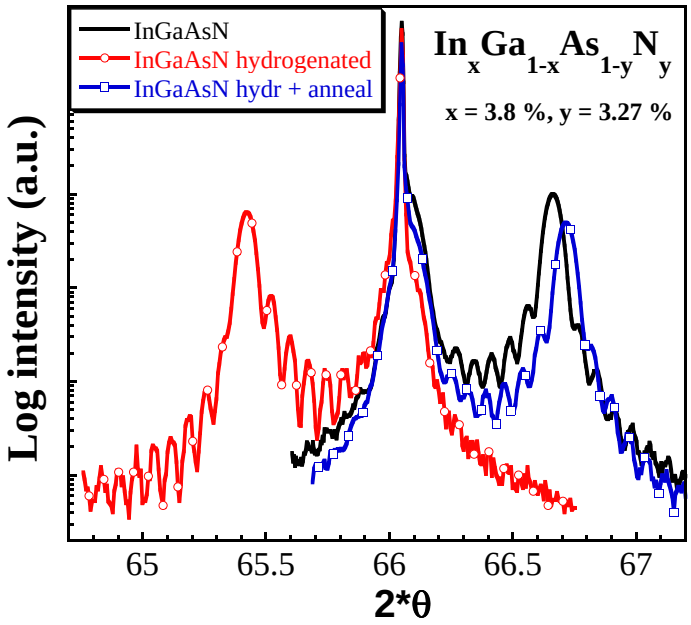

Figure 5.8: Reversible inversion of the strain condition induced by hydrogenation in case of the $In_xGa_{1-x}As_{1-y}N_y$ epilayer 712A2: black line = sample 712A2, red line = 712A2H, blue line = 712A2A5.

causes the strain to switch from the tensile condition (black line) to the compressive one (red line); a thermal annealing of the kind *A5* completely restores the initial tensile condition (blue line).

In case of sample 712A2H it was very difficult to give an estimation of the band gap since the PL peak looks quite broad even at 10 K (Fig. 5.9); in any case, considering the center of mass of the "hydrogenated" curve in Fig. 5.9, the blue shift induced by hydrogenation is significantly smaller than that observed for quantum wells and evident from table 5.1. The difference between the optical behavior of quantum wells and epilayers may be due to the fact that the latter have a more inhomogeneous nitrogen implantation profile, and therefore some regions in the sample may be less affected by the hydrogenation process. PL measures the band gap of the part of the sample whose conduction band states are lowest in energy (see section 2.5.3) i.e. in our case the band gap of the partially hydrogenated region, where a smaller blue shift is present. However, both the non-radiative defects which broaden the hydrogenated curve of Fig. 5.9 and the inhomogeneity in the N concentration profile are not so extended to affect the overall structural quality of the alloys.

In order to summarize our results, table 5.1 reports the measured values of $a_\perp$, the calculated values of a_f (via equation 4.1, using linear combinations of the elastic constants) and the PL emission for all $(In_x)Ga_{1-x}As_{1-y}N_y$ samples investigated in this section. It is worth stressing here that, even if a similar effect of relaxation of the

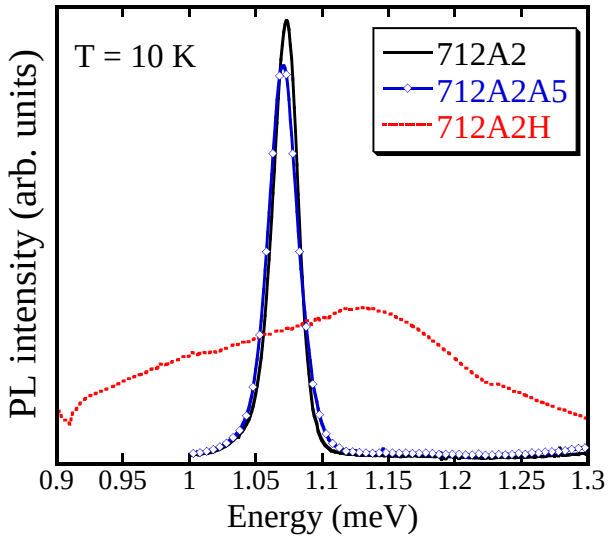

Figure 5.9: PL spectra taken at 10 K for samples reported in Fig. 5.8; black line = sample 712A2, red line = 712A2H, blue line = 712A2A5.

lattice upon hydrogenation has been already observed in case of Boron-doped silicon and attributed to the formation of B-H complexes [68], the XRD measurements presented in this chapter report the first observation of a huge and reversible expansion of the unit cell driven by a post-growth treatment in semiconductors characterized by the presence of an isovalent impurity (N).

5.3.2 Infrared absorption and DFT calculations results

Far infrared absorption measurements have been performed on the same $GaAs_{1-y}N_y$ samples investigated by X-ray diffraction. Fig. 5.10 shows the infrared spectra of the untreated sample V106 (black bottom curve), of the hydrogenated H106 (middle red curve) and of the hydrogenated plus annealed H106A5 (top blue curve) in the energy region of the local vibrational mode of the Ga-N bond (472 cm^{-1}) [183]. The decrease in the absorption intensity of this mode in the hydrogenated sample indicates a decrease in the number of Ga-N bonds present in the sample. Subsequent thermal annealing restores the pre-hydrogenation number of bonds (blue curve). These data provide further evidence for strong changes in the lattice environment around N atoms in $GaAs_{1-y}N_y$ upon hydrogenation, showing how the microscopic mechanism of lattice relaxation involves the breaking of Ga-N bonds.

We tried to account for the experimental panorama assuming that, upon hydrogenation, the N-H complexes (section 1.3) are formed and that, upon the *A5* thermal treatment, such complexes break. Via first-principles total energy calculations (section 2.5.4) we have predicted the effects on the lattice parameter of the two most stable complexes [7, 6]: the monohydrogen $H(BC_N^+)$ complex and the dihydrogen $H_2^*(N)$ one.

Table 5.1: Comparison between XRD and PL results : measured $a_\perp$, calculated a_f and PL peak position (at 150 K for QWs and at 10 K for epilayers); the different errors on the extracted lattice parameters are due to the different thickness of the samples and to a different experimental setup.

Sample	$a_\perp$ (Å)	a_f (Å)	PL (eV)
378	5.929 ± 0.008	5.794 ± 0.008	1.123 ± 0.001
383	5.868 ± 0.007	5.762 ± 0.007	0.841 ± 0.003
383d4	5.936 ± 0.008	5.798 ± 0.008	1.097 ± 0.012
260	5.944 ± 0.008	5.802 ± 0.008	1.090 ± 0.001
241	5.871 ± 0.009	5.764 ± 0.009	0.875 ± 0.003
241d4	5.939 ± 0.008	5.800 ± 0.008	1.060 ± 0.030
712A2	5.607 ± 0.001	5.629 ± 0.001	1.073 ± 0.001
712A2H	5.701 ± 0.001	5.678 ± 0.001	1.089 ± 0.120
712A2A5	5.603 ± 0.001	5.627 ± 0.001	1.070 ± 0.001
H106	$\simeq GaAs(5.654)$	$\simeq GaAs(5.654)$	1.471 ± 0.001
H106A5	5.637 ± 0.001	5.645 ± 0.001	1.298 ± 0.001
V106A4	5.635 ± 0.001	5.644 ± 0.001	1.271 ± 0.001
H112	5.661 ± 0.004	5.658 ± 0.004	1.405 ± 0.001

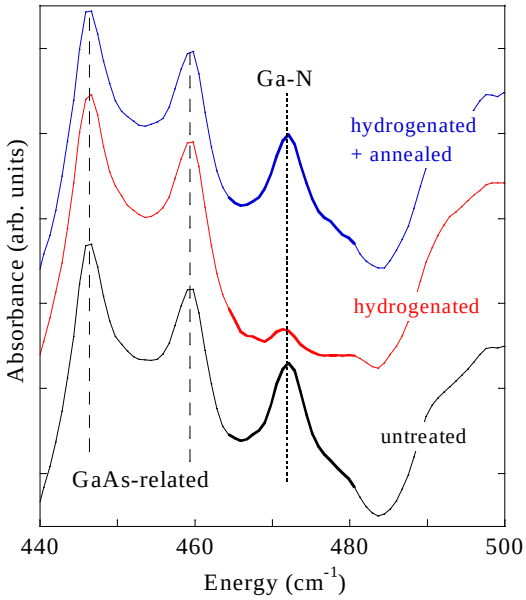

Figure 5.10: Far infrared spectra of the same samples whose photoluminescence spectra and diffraction curves are shown in Fig. 5.2; black curve = sample V106, red curve = H106, blue curve = H106A5.

I remind here that, as anticipated in section 1.3, in the $H(BC_N^+)$ there is only a H_{BC} atom bonded to N at the bond center (BC) position between the Ga and N atoms; in the $H_2^*(N)$ complex two strong Ga-H_{BC} and N-H_{AB} bonds are formed which involve, respectively, a H_{BC} atom in bond center position between the Ga and N atoms, and a H_{AB} atom in opposite position with respect to the same nitrogen atom (Fig. 5.11).

By total energy calculations we evaluated the change in $a_\perp$ induced by the formation of the two complexes in $GaAs_{1-y}N_y$/GaAs epilayers with $y = 0.03$ and $y = 0.06$. For $y = 0.06$ we calculated $a_\perp$ to be equal to 5.406 Å for H-free material, 5.371 Å for a lattice containing $H(BC_N^+)$ complexes, and 5.512 for a lattice containing $H_2^*(N)$ complexes (the calculated lattice constant for GaAs being $a_{GaAs} = 5.557$ Å). These results show that the alloy lattice undergoes a further slight contraction in the case of $H(BC_N^+)$ complexes, while 99.2 % of the GaAs lattice constant is recovered in the presence of $H_2^*(N)$ complexes (that is, 70 % of the change produced by N introduction is recovered by H). For $y = 0.03$, similar results have been obtained and 99.6 % of the GaAs lattice constant is recovered by the formation of the $H_2^*(N)$ complex. Thus the same dihydride complex that accounts for N electronic passivation [7, 6, 45] as illustrated in section 1.3.4 induces also a lattice relaxation similar to that observed after hydrogenation, as schematically shown in Fig. 5.11.

It is worth highlighting some important difference with respect to the case of hydrogenated Si:B [68]: therein a H atom located at the BC site of a Si-B bond induces an outward relaxation of its Si and B neighbors which, in turn, leads to a partial re-

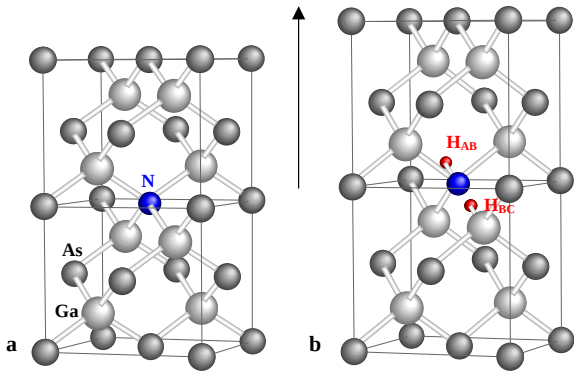

Figure 5.11: Sketch of the $GaAs_{1-y}N_y$ lattice in the vicinity of a nitrogen atom. (a) $GaAs_{1-y}N_y$ lattice (no hydrogen). (b) $H_2^*(N)$ complex. The lattice difference between the H-containing and the H-free $GaAs_{1-y}N_y$ crystals has been exaggerated for clarity; the vertical arrow indicates the growth direction. Dark atoms = As, light atoms = Ga, blue atoms = nitrogen, red atoms = hydrogen.

covery of the undoped Si lattice constant. The present results show, instead, that a H atom located at the BC site of a Ga-N bond in $GaAs_{1-y}N_y$ does not lead to a recovery of the GaAs lattice constant nor to N passivation, which are obtained only when $H_2^*(N)$ complexes are formed. Indeed, the cases of a single H_{BC} atom in Si:B and in $GaAs_{1-y}N_y$ are different because a different chemical bonding occurs. In the former case H_{BC} saturates the Si dangling bond thus leaving the chemical valence of both Si and B fully satisfied. In $GaAs_{1-y}N_y$, H_{BC} too induces an outward local relaxation of the Ga and N atoms [6]. However, the H atom is now bonded to the N atom and this leaves an unsaturated dangling bond on the Ga atom.

A detailed analysis of the chemical bonding of the $H(BC_N^+)$ complex shows that the Ga dangling bond induces a Ga-H bonding interaction, which lowers the total energy of the system when the $GaAs_{1-y}N_y$ lattice constant is reduced [182]. Therefore, the formation of the $H(BC_N^+)$ complex does not lead to a dilation of the $GaAs_{1-y}N_y$ lattice toward that of the GaAs lattice, rather it leads to a lattice contraction. On the ground of the above considerations, one can conclude that the different chemical behavior of a dopant impurity, similar to B in Si, and of an isoelectronic impurity, similar to N in GaAs, accounts for the different effects induced by H-containing complexes in Si:B and $GaAs_{1-y}N_y$ lattices.

5.4 Effects on the local structure

Next step was the study of the effects of $H_2^*(N)$ complexes at the local scale i.e. on the single bond lengths. From above it is evident how upon hydrogenation the N-Ga bonds break and H atoms locate between Ga and N, increasing their relative distance. However open questions remain, concerning the quantitative value of the Ga-N distance and the

effects of hydrogenation on the other interatomic distances present in $GaAs_{1-y}N_y$ and also $In_xGa_{1-x}As_{1-y}N_y$ alloys. We may speculate that the expansion of the unit cell induces a stretch also of the bonds not directly involved in the formation of the N-H complexes, for example the Ga-As and the In-As distances; on the other hand the lattice relaxation is supposed to minimize the tensile strain contribution on the bond lengths in the case of $GaAs_{1-y}N_y$.

We suppose that the Ga-As bond length in hydrogenated $GaAs_{1-y}N_y$ may be different from that of an unstrained $GaAs_{1-y}N_y$ alloy (i.e. hydrogen does not just act as a "strain remover") and, despite the virtual equivalence of the unit cell, may be also different from the Ga-As distance in gallium arsenide. In this section we present an experimental approach to the topic of the effects of the formation of H-N complexes on the bond lengths; we report the Ga-As bond length in hydrogenated $GaAs_{1-y}N_y$ epilayers measured by XAFS at the Ga K-edge and we interpret the XAFS results obtained on all hydrogenated samples (epilayers and quantum wells) in the frame of the H-N complexes theory.

In Fig. 5.12 the background subtracted XAFS for the three hydrogenated $GaAs_{1-y}N_y$ epilayers H106, H112 and H118 are reported; background subtraction as well as data analysis has been performed in a identical way to that described in chapter 4 for virgin epilayers. Even in case of hydrogenated samples we were not sensitive to the direct Ga-N coordination, due to the low N content, so we limited to study the effects of N incorporation and subsequent hydrogenation on the distribution of the Ga-As bond length. It is apparent from Fig. 5.12 the high quality of the data recorded in total

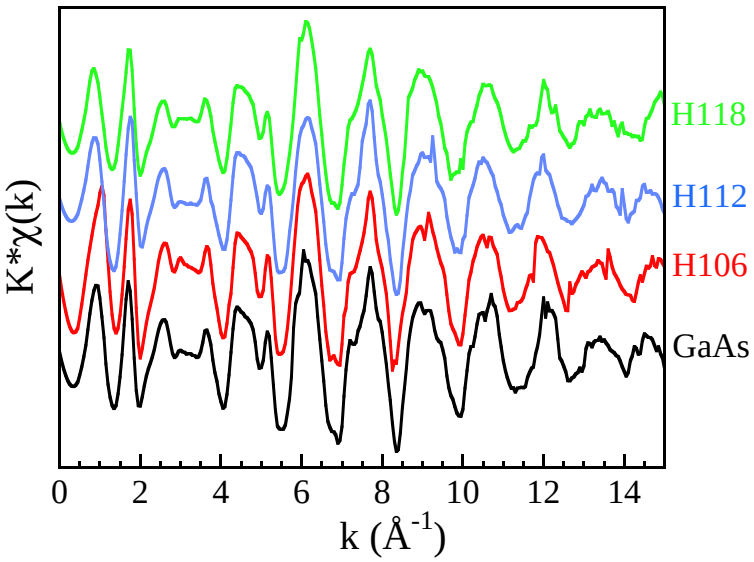

Figure 5.12: Background subtracted XAFS spectra for hydrogenated $GaAs_{1-y}N_y$ and the GaAs reference.

electron yield mode measuring the drain current of the sample; note how, contrary to

the case of virgin $GaAs_{1-y}N_y$ (Fig. 4.2), the amplitude of the XAFS oscillations does not decrease with the N content ($y_{H106} < y_{H112} < y_{H118}$).

In Fig. 5.13b the Fourier transforms of the XAFS signals for hydrogenated epilayers are reported together with those of virgin epilayers (Fig. 5.13a): it is clear how the broadening of first shell peak (corresponding to the Ga-As correlation) for increasing y observed in virgin samples is not present for hydrogenated samples.

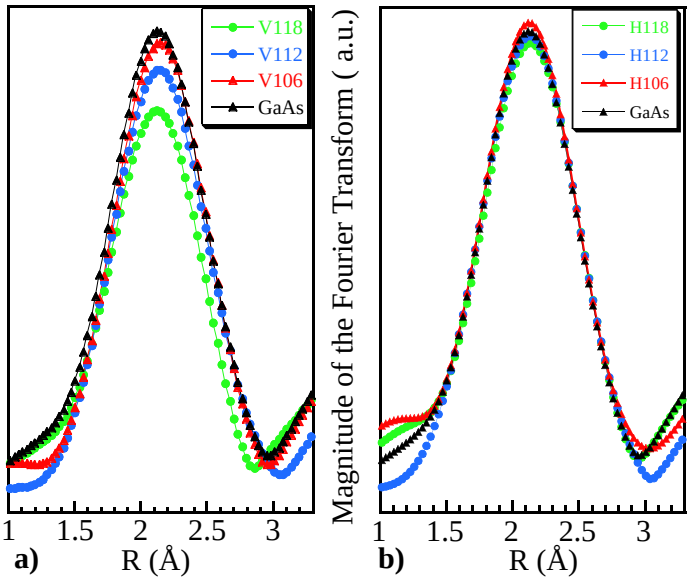

Figure 5.13: Fourier transform (in the R-range [1-3.3]) of the XAFS signal for (a) virgin $GaAs_{1-y}N_y$ epilayers and (b) hydrogenated $GaAs_{1-y}N_y$ epilayers : in the latter case the first shell peak does not broaden at increasing N content.

The amplitudes of the first shell peak do not differ from that measured for the gallium arsenide standard for all hydrogenated $GaAs_{1-y}N_y$ epilayers, qualitatively showing how the GaAs first shell is identical to that of hydrogenated samples. The fits were performed up to the third shell; the results achieved are reported in Fig. 5.14. We stress the good agreement obtained and in particular how the fits perfectly reproduce the signal of the first coordination shell. Table 5.2 reports the values of the distances and Debye-Waller factors extracted from the fits. Errors on the bond lengths are obtained as quadratic combinations of the errors evaluated from the fits of the samples and of the GaAs standard.

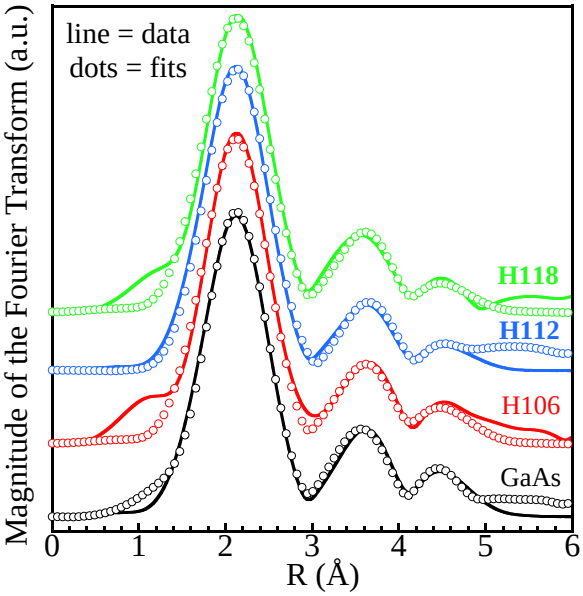

Figure 5.14: Fits in R-space for all hydrogenated samples and the GaAs standard.

Table 5.2: Structural parameters evaluated from the fits for hydrogenated $GaAs_{1-y}N_y$ epilayers, errors = 1σ.

Sample	R_{Ga-As}(Å)	$\sigma^2_{Ga-As}(10^{-3}Å^2)$	R_{Ga-Ga}(Å)
H118	2.451 ± 0.005	6.6 ± 0.3	3.995 ± 0.011
H112	2.447 ± 0.005	6.3 ± 0.2	4.009 ± 0.012
H106	2.450 ± 0.005	6.3 ± 0.3	4.006 ± 0.012
GaAs	2.448 ± 0.005	6.4 ± 0.7	3.998 ± 0.010
Sample	$\sigma^2_{Ga-Ga}(10^{-2}Å^2)$	$R^{3rd\ shell}_{Ga-As}$(Å)	$\sigma^2_{3rd\ sh}(10^{-2}Å^2)$
H118	1.34 ± 0.08	4.688 ± 0.026	2.32 ± 0.33
H112	1.52 ± 0.09	4.735 ± 0.030	2.53 ± 0.39
H106	1.34 ± 0.10	4.720 ± 0.029	2.11 ± 0.36
GaAs	1.34 ± 0.10	4.688 ± 0.014	1.76 ± 0.16

In Fig. 5.15 the experimental distances of hydrogenated epilayers (black points) are reported as a function of the concentration along with those of as deposited epilayers (red points) already showed in Fig. 4.5. The black continuous line is the linear fit (of

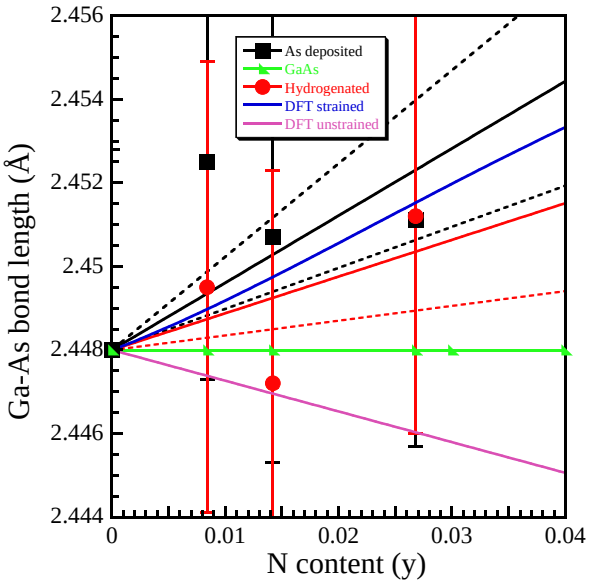

Figure 5.15: Experimental composition dependence of the Ga-As first shell bond length for as-deposited (black points) and hydrogenated (red points) $GaAs_{1-y}N_y$ epilayers compared with the predictions of the first-principles DFT calculations for a strained and unstrained $GaAs_{1-y}N_y$ alloy; black and red continuous lines = least-squares fits, dotted lines = 1 σ error, blue and purple continuous lines = simulated trends.

the kind R_{GaAs} + slope $\times$ y) to the "as deposited" points already reported in Fig. 4.5, while the red continuous line represents a similar fit to the hydrogenated points. The black and red dotted lines correspond to the relative 1σ experimental error bars, for the hydrogenated samples (red dotted) the only -1σ limit is showed. The blue line represents a fit to the distances calculated by DFT simulations for strained $GaAs_{1-y}N_y$ epilayers and its extrapolation to the lowest N contents, the purple line a linear fit and extrapolation of the DFT trend for unstrained $GaAs_{1-y}N_y$ alloys and the green line the Ga-As bond length in gallium arsenide.

For as deposited samples the local distances are well reproduced by the DFT simulation. Bond distances for hydrogenated samples are shorter, due to the lower effect of the tensile strain at a local scale. Nevertheless the fit to the "hydrogenated" points allows to discard (at a 1σ confidence level) both the DFT prediction for an unstrained $GaAs_{1-y}N_y$ alloy (purple line) and the presence of a Ga-As bond length equal to that of gallium arsenide. This means that the proposed formation of N-H complexes not only increases the distances between the Ga and N atoms and expands the *out of plane* lattice parameter, but also increases the Ga-As distances, which are not directly in-

volved in the process. This result is not so obvious as one could naively think; in fact the breaking of the Ga-N bond is not sufficient to cause itself an overall expansion of the structure. In fact, as explained by A. Amore Bonapasta and F. Filippone [182], the presence of a Ga dangling bond in the monohydride $H(BC_N^+)$ complex would cause a Ga-H_{BC} interaction which favors on the contrary a contraction of the unit cell. Our XAFS results, suggesting an increase of the Ga-As distance also over the values of gallium arsenide, are compatible with the formation of $H_2^*(N)$ complexes. Even if a detailed first-principles simulation of the average Ga-As distance is presently missing, the calculations of A. Amore Bonapasta and F. Filippone [182] show that the Ga and As atoms surrounding the $H_2^*(N)$ complex move away one from the other with respect to the virgin $GaAs_{1-y}N_y$ alloy.

Due to the complexity of elastic relaxation and chemical bonding phenomena in the formation of monohydride and dihydride H-N complexes, this direct experimental determination of the bond length values achieved by XAFS provides data of paramount importance in order to determine the precise geometry of selected complexes.

In table 5.2, note how Debye-Waller factors do not show any compositional trend, remaining virtually identical to the gallium arsenide standard value for all the hydrogenated epilayers; this contrasts with the case of the as deposited samples. DFT calculations of the standard variance σ^2 performed for the unstrained Ga-As distance distributions in H-free $GaAs_{1-y}N_y$ show a similar insensitiveness to composition variation. In Fig. 5.16 the first shell σ^2 extracted from the XAFS fits for hydrogenated

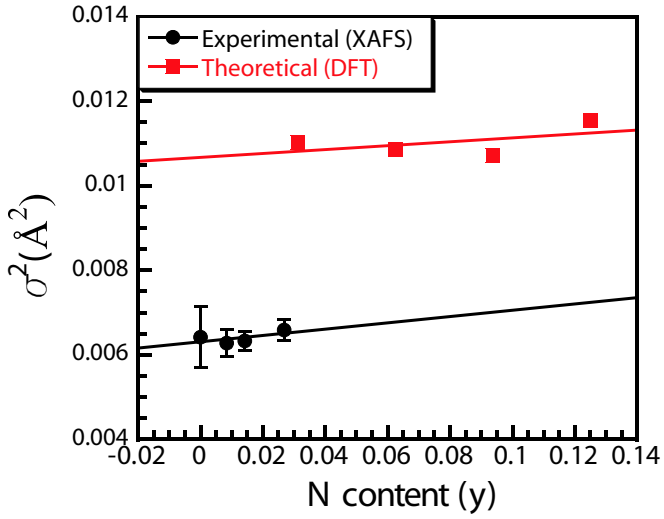

Figure 5.16: Comparison between experimental Ga-As σ^2 trend (black points) for hydrogenated $GaAs_{1-y}N_y$ measured by XAFS and theoretical trend predicted via DFT for bulk H-free $GaAs_{1-y}N_y$ (red points); continuous lines represent linear fits, errors = 1 σ.

samples are reported along with the DFT calculations for the unstrained Ga-As distance

distributions in H-free $GaAs_{1-y}N_y$; it is evident how despite an additive systematic error in the simulated σ^2, the two linear fits to the experimental and theoretical points have very close slopes. The systematic error in the simulated σ^2 could be due to the fact that its thermal component is approximated by the experimental Debye-Waller factor measured in gallium arsenide, assuming that in this case the structural disorder component is zero. Since some structural disorder is present also in GaAs, this assumption leads to an overestimation of σ^2 in $GaAs_{1-y}N_y$. The extrapolation of the DFT trend to $y = 0$ does not yield in fact the Debye-Waller measured for GaAs.

As demonstrated by XRD, hydrogenated $GaAs_{1-y}N_y$ are strain-free alloys. Therefore the similarity between the experimental variance of the Ga- As distance distributions in H-$GaAs_{1-y}N_y$ and the variance calculated for those of unstrained distance in H-free $GaAs_{1-y}N_y$ suggests that the increased structural disorder observed in as deposited $GaAs_{1-y}N_y$ for increasing y in chapter 4 (Fig. 4.7) is not a direct effect of N incorporation, but it is rather a local effect of the tetragonal distortion of the epilayers cell caused by the pseudomorphic growth on GaAs substrate.

The hypothesis of a global expansion of the local bond lengths as a consequence of the relaxation of the unit cell observed by XRD and accounted for by the formation of $H_2^*(N)$ complexes provides us with a key to interpret also the results on hydrogenated $In_xGa_{1-x}As_{1-y}N_y$ quantum wells reported in table 3.3 (In K-edge XAFS) and table 3.4 (Ga K-edge DAFS). In Fig. 5.17a we report the difference between the experimen-

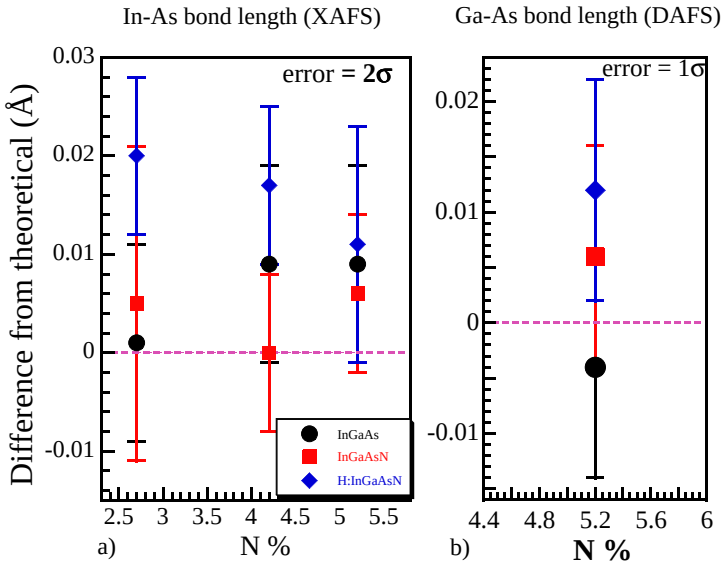

Figure 5.17: Differences between experimental and theoretical determinations of the bond lengths in $In_xGa_{1-x}As_{1-y}(N_y)$ quantum wells; black points = $In_xGa_{1-x}As$, red points = as deposited $In_xGa_{1-x}As_{1-y}N_y$, blue points = hydrogenated $In_xGa_{1-x}As_{1-y}N_y$; a) In-As distances by In K-edge XAFS, b) Ga-As distances by Ga K-edge DAFS.

tal In-As distances extracted from In K-edge XAFS measurements and the theoretical values. These latter (see table 3.3) have been calculated by using the *Cai and Thorpe*'s VFF model [75] for a quaternary $In_xGa_{1-x}As_{1-y}N_y$ alloy correcting for the strain effect by the *Tormen*'s formulation [83] (see section 1.5.2). In case of hydrogenated QWs, as for as deposited ones, the local effects of the tetragonal distortion on the unit cell have been calculated by equation 1.20, using the free lattice parameter values calculated by XRD (table 5.1). In this way we kept into account the increased (compressive) strain component related to the relaxation upon hydrogenation of the lattice parameter, which should induce the bond lengths to be smaller than those of as deposited $In_xGa_{1-x}As_{1-y}N_y$ if H had only the role of a "strain enhancer". In Fig. 5.17b we report in parallel the differences between the experimental Ga-As distances extracted for series III quantum wells from Ga K-edge DAFS and theoretical values calculated in the same way.

It is evident from the figure how, in case of hydrogenated samples (blue points), these differences are systematically larger than in as deposited ones: both the for the Ga-As and the In-As bond length. Hydrogenation apparently induces an overall expansion of the different bonds in the quaternary alloy which cannot be taken into account by attributing to H (as in the prediction of tables 3.3 and 3.4) the only role of strain enhancer. In case of the In-As distance, the better quality of the data for In K-edge XAFS allows us to claim that bond lengths exceed the as predicted values even at a 2σ confidence level, while error bars reported in Fig. 5.17b for DAFS results correspond to a 1σ confidence level. It is worth remarking here how in Fig. 5.17a also the distances in ternary and as deposited quaternary QWs in average exceed the predicted values, even if this is not true at a 2σ confidence level. The discrepancy between experimental data and predictions can be due in this case to the not completely satisfactory adequacy of *Cai and Thorpe*'s [75] model in predicting bond lengths for a system characterized by a strong disorder in the force constants (as already discussed in chapter 4 for the case of $GaAs_{1-y}N_y$); also a systematic error of FEFF in the *ab initio* modelling of the theoretical phase shifts different in case of $In_xGa_{1-x}As_{1-y}(N_y)$ with respect to InAs cannot be excluded.

5.5 Conclusions

In this chapter we have showed how atomic hydrogen irradiation not only passivates the optical and electronic effects induced by nitrogen incorporation in $(In_x)Ga_{1-x}As_{1-y}N_y$, but also induces a dramatic and reversible effect on the long range as well as local structure of these alloys. The *out of plane* lattice parameter relaxes upon hydrogenation to the value of the N-free alloy and an annealing at 500 °C for 30 minutes completely restores the lattice parameter values before hydrogenation. Part of the Ga-N bonds are broken upon hydrogenation and reform subsequently to the thermal annealing.

Total energy minimization methods indicate that a complex involving two hydrogen atoms in the neighborhood of a nitrogen atom accounts for these structural effects. XRD measurements allowed to discriminate between the proposed N-H complexes,

ruling out the formation of monohydride complexes which do not imply an expansion of the lattice parameter. Annealing eliminates H atoms from the lattice and induces the broken Ga-N bonds to reform.

The phenomenon is probably due to the high reactivity of H which, coupled to the high electronegativity of N, manages to break the Ga-N bonds; this behavior may be common also to other alloys characterized by a large difference in the atomic size and electronegativity of the anions.

The expansion of the unit cell leads locally to a relaxation of the In-As and Ga-As bonds, not directly involved in the formation of H-N complexes; furthermore hydrogenation removes the structural disorder in the Ga-As distance distribution related to the tetragonal distortion of the $GaAs_{1-y}N_y$ cell, tensile-strained on GaAs substrate.

The experimental results presented in this chapter represent one of the first observations of such an enormous and reversible change in the unit cell of a semiconductor crystal induced by a post-growth treatment, and the first observation in case of a III-V one characterized by the presence of an isovalent substitutional impurity. These results are of relevance also from the application viewpoint; in fact hydrogen is largely present as a carrier gas in the growth techniques used for large scale semiconductor production such those based on vapor deposition (MOCVD), in which the incorporation of hydrogen in the as grown material is a likely occurrence. If from one side hydrogen incorporation is a concern, on the other hand it could be in principle exploited for tailoring the band gap of $In_xGa_{1-x}As_{1-y}N_y$ after the growth, once the problem of the formation of non-radiative defects induced by the hydrogenation procedure will be overcome.

General Conclusions

This thesis work provides a structural characterization of III-V nitrides, in particular of $GaAs_{1-y}N_y$ and $In_xGa_{1-x}As_{1-y}N_y$ alloys, semiconductors of strategic importance in the manufactory of optoelectronic devices and photovoltaic cells of the next future.

By means of X-Ray Absorption measurements at the In K-edge on $In_xGa_{1-x}As_{1-y}N_y$ alloys, we looked for short range ordering phenomena in the surroundings of the indium site. We found that the relative In-N coordination number is over the stoichiometric values in annealed samples, while its value is equal to the random case in as grown alloys. This indicates that annealing drives a preferential In-N bonding in $In_xGa_{1-x}As_{1-y}N_y$, as recently predicted at the equilibrium by Monte Carlo simulations. On the other hand the measured degree of order is by far smaller (about one order of magnitude) than the predicted one. This can be due to the fact that annealing brings the system towards the equilibrium condition without reaching it; an alternative explication may be the failure of the theoretical modelling. The XAS results at the In K-edge are qualitatively supported by N K-edge XANES measurements and by simulations of the absorption coefficient in the near edge region performed in the Full Multiple Scattering approach (FMS).

The SRO parameters measured by XAS quantitatively account for the changes in the band gap observed upon N incorporation in annealed samples, in particular giving an explication for the origin of the blue shift observed upon annealing. This blue shift of the band gap is a concern for applications since it hinders access to the longest emission wavelengths. Our results suggest that it is not due to a removal upon annealing of N-related defects (for example interstitials, as proposed by other groups) present on large scale in the as grown material; in fact angle-dependent N-K edge XANES and Nuclear Reaction Analysis show how N is substitutional to As, both in as grown and annealed samples. The improvement of the PL efficiency upon annealing can be due to the removal of heterogeneous impurities or defects present in the as grown samples on a concentration scale of two orders of magnitude smaller than the N concentration. We think that, beside the scientific importance, this information is of interest for growing materials with improved characteristics.

By XAS performed on $GaAs_{1-y}N_y$ epilayers at the Ga K-edge, we studied the behavior of the Ga-As bond length at the N-dilute limit and compared these results to the predictions of different Valence Force Field models and first principles calculations. We found that the models which employ two couples of force constants (two bond bending and two bond stretching terms), related to the Ga-As and Ga-N bonds respectively,

well reproduce the experimental data. On the contrary, a model which exploits an unique rigidity parameter (depending on one couple of force constants only) does not predict the bond lengths behavior satisfactory. In our opinion the failure of the unique-rigidity parameter model, which very well reproduce bond lengths for a large variety of semiconductors, is due to the very different force constants which characterize the constituent compounds GaAs and GaN, i.e. to the very different physical characteristics of the two anions. The experimental distribution of the Ga-As distances broadens for increasing N concentration, due to local structural disorder induced by the tetragonal distortion; this broadening is well reproduced by one of the VFF models which employ two force constants couples and by first-principles total energy calculations performed in the frame of the Density Functional Theory (DFT).

By means of X-Ray Diffraction measurements, we have characterized the effects of hydrogenation on the unit cell of $GaAs_{1-y}N_y$ and $In_xGa_{1-x}As_{1-y}N_y$ alloys. We have found that hydrogenation induces a dramatic relaxation of the lattice which leads the unit cell to recover the values of the N-free alloys. We showed how this large structural variation is completely reversible upon a thermal annealing. The effect can be explained assuming the formation of N-H complexes and in particular of the $H_2^*(N)$ complex, which involves the presence of two H atoms, one binding to the N and the other to the Ga atom whose direct bond is broken by hydrogenation. The same complex accounts for the effects observed on the optical properties of these materials and in particular for the reopening of the band gap, red shifted by the N incorporation; the breaking of these complexes upon annealing explains the full reversibility of the effect. A similar relaxation of the lattice upon hydrogenation, associated to the formation of B-H complexes, has been previously observed in boron-doped silicon. Nevertheless the present work reports the first observation of such a phenomenon in the case of a semiconductor characterized by the presence of isovalent substitutional impurities.

By exploiting XAS, performed at the In and Ga K-edges on hydrogenated $In_xGa_{1-x}As_{1-y}N_y$ quantum wells and $GaAs_{1-y}N_y$ epilayers respectively, and DAFS, performed at the Ga K-edge on hydrogenated $In_xGa_{1-x}As_{1-y}N_y$ quantum wells, we extended our considerations about the effects of hydrogenation on the local scale. We showed how the likely formation of $H_2^*(N)$ complexes leads also to a stretching of the In-As and Ga-As bond lengths (which are not directly involved in the breaking of the Ga-N bond) with respect to the prediction of VFF models.

The results achieved on the structural effects of hydrogenation are also important from the technological applications standpoint; in fact hydrogen is a common contaminant of growth techniques used for large scale semiconductors production (MOCVD). The knowledge of the remarkable structural effects of H incorporation in the lattice is important because they deeply affect the emission properties. On the other hand, an improved control of the hydrogenation process could be exploited for a post-growth tailoring of the band gap of $In_xGa_{1-x}As_{1-y}N_y$, thanks also to the reversibility of the treatment. In order to use hydrogenated alloys for lasing, the problem of the formation of non-radiative defects upon hydrogen irradiation, which reduce the optical efficiency of the material, has to be overcome.

Appendix A

Dead time corrections for *FLY* XAFS

A.1 Introduction

As discussed in section 2.2, Extended X-ray Absorption Fine structure Spectroscopy (EXAFS) is a powerful tool for local structural determination. The aim of any EXAFS measurement is the determination, in the first few coordination shells, of local structural parameters around the excited atom: coordination numbers (N), interatomic distances (R) and Debye-Waller factors (σ^2). These parameters enter the expression for the EXAFS modulation of the absorption cross section described in section 2.2.2, which, in the single scattering and plane wave approximation, is:

$$\chi(k) = \sum_i N_i A_i(k) sin\left[2kR_i + \varphi_i(k)\right] e^{-2k^2\sigma^2} \tag{A.1}$$

In this expression $A_i(k)$ and $\varphi_i(k)$ are the amplitude and phase shift of the backscattering function from atoms in the *i-th* coordination shell (we have included many-body multiplicative terms in $A_i(k)$), k is the photoelectron wave vector and the sum is over all coordination shells. When fluorescence yield (FLY) detection is employed [107] the technique is able to probe the structure of atoms present in rather high dilutions or in thin films. The physical origin of this is that fluorescence detection isolates the signal of the excited atom from the total absorption of the matrix. Fluorescence detection is popular on EXAFS beamlines world-wide and has developed into a flexible experimental tool. Solid-state energy-resolving detectors [184] are often used in fluorescence EXAFS measurements. They allow, within the moderate energy resolution they posses (typically 200 eV at 5.9 keV), to select the desired fluorescence line rejecting scattered photons and fluorescence lines coming from other absorbers. The limitation of this kind of detectors is the relatively high dead time of the electronics used, which needs several microseconds in order to sample the voltage signal with a sufficiently low statistical noise thus causing pulse pile-up.

The aim of this work is to investigate the possibility of obtaining correct structural information when performing fluorescence EXAFS measurements with a high input

count rate; the particular case of a high-purity Ge detector coupled to digital electronics is addressed. There are at least two reasons why this study is relevant, both relating to the high brilliance beams provided by state-of-the-art beamlines on third generation synchrotron radiation sources. If the spectrum of photons scattered from the sample is dominated by the fluorescence line of interest, recording data at high-count rate allows to reduce the total acquisition time per spectrum. Fluorescence yield detection has been successfully extended even to the case of concentrated samples, providing to self absorption is either minimized by an appropriate low exit angle-geometry or accounted for using appropriate corrections [109, 110, 111, 112]. If, on the other hand, the fluorescence line of interest represents only a minor fraction of photons scattered from the sample, it might be inevitable to perform the experiment with a high number of total photons impinging on the detector in order to have sufficient count rate in the region of interest. It has been generally recognized that when high-count rates are used dead time effects can be important, the most well known effect being an artificial decrease of the amplitude of the EXAFS signal. It is possible to recover such errors, by using suitable corrections, as already observed by different groups [185, 186, 187, 188].

Even if the problem is in general well known, a quantitative and systematic study of the effect of dead time losses on the structural parameters extracted from EXAFS data and of the reliability of dead time corrections in recovering the correct structural information is at the present missing in the literature. In this appendix three different approaches to the data correction problem are presented. For each approach we estimate the maximum count rate up to which the particular kind of correction can be used, by considering the deviation of the evaluated structural parameters with respect to the known values in a model sample. In this work we assume that the fluorescence intensity is directly proportional to the absorption coefficient of the excited atom, that is that self-absorption effects are negligible or can be corrected subsequently.

A.2 Data correction methods

There are two models of dead time behaviour for pulse counting systems: the paralyzable and the nonparalyzable response [184]. It is recognized that solid-state detectors used for x-ray spectroscopy and the associated electronics have a paralyzable response function, so we will focus on this model here. For a paralyzable response function a dead time τ is assumed to follow each true event that occurs during the live period of the detector. True events that occur during the dead period, although not recorded as counts, extend the dead time by another period τ following the last lost event. If we call n the true count rate (i.e. the real rate of photons impinging on the detector), m the apparent count rate (i.e. the rate measured by the pulse counting electronics) and τ the system dead time, statistical considerations [184] lead to the following relation for the system throughput:

$$m = ne^{-n\tau} \tag{A.2}$$

This relation is, strictly speaking, valid for the total i.e. for the energy integrated count rates. In discussing possible data correction strategies we assume that the system dead time τ has been measured (in our experiment we determined it in the way which will be explained in section A.4) and that it is possible to measure, for every energy point E in the EXAFS scan, the ratio between the true energy integrated count rate (using an amplifier channel with negligible dead time) and the corresponding apparent energy integrated count rate (measured with an amplifier dead time τ). We will call these two count rates $n_T(E)$ and $m_T(E)$, and distinguish them from $n_F(E)$ and $m_F(E)$ which refer to the count rates in the region of interest of the selected fluorescence line. The amplifier channel with low deadtime will be referred to as the "fast" channel and the amplifier channel with non-negligible dead time as the "slow" channel. The ratio between $n_T(E)$ and $m_T(E)$ is automatically recorded in our acquisition output file, together with $m_F(E)$, for each detector element. We will discuss three methods to correct the data taken at high-count rates.

A.2.1 Numerical inversion (method I)

The system throughput relation, equation A.2, can be numerically inverted to extract the true count rate $n(E)$ from $m(E)$, providing the dead time τ is known. As the raw signal to be treated is given by the fluorescence count rate $m_F(E)$ whereas equation A.2 is rigorously valid for total count rates $m_T(E)$, first we have to modify $m_F(E)$ in order to obtain a variable (that we will call simply $m(E)$) which mimics the magnitude of $m_T(E)$. This is necessary in order to perform the inversion on the correct point of non-linearity curve and can be done by multiplying $m_F(E)$ by a constant (namely to consider the presence of the $K\beta$ line when measuring the $K\alpha$) and/or by adding a constant to account for the scattered radiation (elastic and inelastic) plus possible fluorescence from lighter elements. A method to carry out the conversion of $m_F(E)$ into $m(E)$ is described below. Then the numerical inversion is undertaken on the variable $m(E)$ by means of a Fortran code developed by the authors [189].

The inversion routine first assigns, for each energy point, the value $m(E)$ to the variable $n(E)$; then it calculates a new value of $m(E)$ by using equation A.2. If the calculated $m(E)$ (that we will call $m_c(E)$) is smaller than the measured $m(E)$ and if the absolute value of the difference between the two is greater than $\frac{m(E)}{e1}$, where $e1$ is a fixed parameter, $n(E)$ is incremented by $\frac{n(E)}{e2}$ and another $m_c(E)$ is calculated through the equation starting from the new $n(E)$. The process is iterated until $m_c(E)$ approaches the measured one within a tolerance parameter $\frac{m(E)}{e1}$, the value of $n(E)$ which generates the last value of $m_c(E)$ is kept as definitive true value. e1 and e2 are respectively the tolerance and the step parameter of the iteration which yields, at the end, the "true" count rate $n(E)$ for each energy point; they determine the systematic error on the extracted value of $n(E)$ and they can be easily assigned different values according to users' requests; for our purpose the values of $e1 = 2000$ and $e2 = 500$ were found to give excellent results. The choice of these values depends on the signal count rate; the systematic error is in fact, at most, equal to the step $\frac{n(E)}{e2}$ and must

be kept below the statistical one. If $n(E)$ follows Poisson's statistics, the error on it is given by its square root, so in our case the systematic error is surely under the statistics level when $\frac{n(E)}{500} \leq \sqrt{n(E)}$ i.e. when $n(E) \leq 250000$ cps. In our experiment the energy integrated count rate on the fast channel is at the most 132000 cps; $n(E)$ is, of course, even smaller and always ≤ 90000 above the edge for each channel and for each spectrum; for the last point we claim to be able to correct, $n(E)$ is ≤ 70000 for each channel above the edge. It follows that the correction procedure is always applicable, with the chosen values for the parameters. Output obtained by increasing both the parameters by a factor ten was checked to be virtually identical.

The program checks if the input value of $m(E)$ is compatible with the selected peaking time of the system; also it ends iteration when $m_c(E)$ starts decreasing as the number of iteration increases, keeping the last positive-derivative value, in case numerical approximations lead to a point above the peak of the non-linearity (NL) function.

A.2.2 Correcting by the measured system livetime (method II)

Starting from equation A.2, the system throughput $e^{-n\tau}$ can be experimentally determined by measuring at each energy point the energy integrated count rates $n_T(E)$ and $m_T(E)$ exploiting the two amplifier channels:

$$e^{-n\tau} = \frac{m_T(E)}{n_T(E)} = \frac{1}{C(E)}$$

If we assume that the fast channel dead time in measuring the energy integrated count rate is negligible and that the correction factor $C(E)$, obtained from the energy-integrated count rates, is applicable to any subset of photons (i.e. dead time losses are energy independent) the true count rate in the region of interest is obtained at each energy as :

$$n_F(E) = m_F(E) \times C(E) \tag{A.3}$$

A.2.3 Linearization (method III)

Since the EXAFS effect is a normalized weak modulation of the absorption coefficient $m(k)$, it is reasonable to propose a linearization of the system throughput function equation A.2. The EXAFS signal $\chi(k)$ is given by:

$$\chi(k) = \frac{\mu(k) - \mu_0(k)}{\mu_0(k)} \approx \frac{n(k) - J}{J} \tag{A.4}$$

which implies

$$n(k) \approx J\{\chi(k) + 1\}$$

Here $\mu_0(k)$ is the atomic absorption coefficient, $n(k)$ is the true fluorescence count rate in the region of interest and J is the true fluorescence "Jump", that is the discontinuity

in the absorption coefficient at the absorption edge. We have approximated the atomic background function $\mu_0(k)$ with the constant edge jump, which is reasonable for samples with a well defined and ordered structure as in our case (in the inset of Fig. A.1 we report a raw fluorescence spectrum).

In a real experiment, because of pulse pile-up, we measure neither $n(k)$ nor J but a function R of these quantities, which is the same as equation A.2:

$$R(y) = ye^{-\tau y}$$

In making this choice we do a significant approximation because we extend equation A.2, which is rigorously valid for the energy integrated counts, to a subset of photons corresponding to the fluorescence line of interest. The pulse-counting electronics actually responds to the total count rate, so by using this approximation we are not working on the correct point of the NL curve, but on a less critical one at lower count rates. On the other hand, as far as the fast total count rate does not get too close to the NL curve maximum, it is reasonable to perform corrections both on the different EXAFS scan points $m_F(E)$ and on the measured jump in the same point of the NL curve. Due to the definition of EXAFS in Eq. A.4 the two terms compensate and variations in the amplitude of $\chi(k)$ are not too severe moving through the NL curve, keeping sufficiently far away from the maximum (see section A.5). Therefore, the measured EXAFS signal $\chi_m(k)$ is :

$$\chi_m(k) = \frac{R[n(k)] - R[J]}{R[J]}$$

which, with the approximation $\tau J \ll 1$ (moderate pile up) becomes:

$$\chi_m(k) = \frac{n(k)[1-\tau n(k)] - J[1-\tau J]}{J[1-\tau J]} = \chi(k)\left[1 - \frac{\tau n(k)}{1-\tau J}\right]$$

Straightforward manipulations lead to:

$$\begin{aligned} \chi_m(k) &= \chi(k)[1 - B(k)] \\ B(k) &= \frac{\tau J}{1-\tau J}[1+\chi(k)] \approx \tau J \\ \chi(k) &\approx \chi_m(k)\left[\frac{1}{1-\tau J}\right] \end{aligned} \tag{A.5}$$

According to this expression the dead time correction on $\chi_m(k)$ is an overall amplitude factor and depends only on the product between dead time and true value of the fluorescence jump, the latter can be obtained by using one of the two previous methods. The appearance of only an overall amplitude reduction implies that the only effect predicted on the structural parameters is a reduction of the estimated coordination numbers, without any effect on interatomic distances or Debye-Waller factors. Equation A.5 gives us the simplest way to correct data for dead time losses: we can perform a conventional quantitative analysis starting from the extracted $\chi_m(k)$ and correct *a posteriori* the obtained coordination numbers by the term $(1-\tau J)^{-1}$.

A.3 Experimental

In order to check the applicability of the correction methods presented above we have performed test experiments at the GILDA CRG beam line of the European Synchrotron Radiation Facility in Grenoble, France. The monochromator was equipped with a pair of Si(311) crystals and run in the so called dynamical focusing mode [126]. The sample analyzed was an $InAs_{0.36}P_{0.64}$ polycrystalline alloy grown on Al substrate [190]. In this context the advantage of using this sample is the well-defined local structure around As (4 In atoms at equal distance in the first coordination shell). Moreover, the thickness of the epilayer was 30 mm and this guaranteed intense As Kα and Kβ fluorescence lines; in fact, the spectrum of photons emitted from the sample is dominated by these fluorescence lines with negligible contribution from elastic or Compton scattering, as shown in Fig. A.1. The detector was placed at 90° to the impinging beam in the

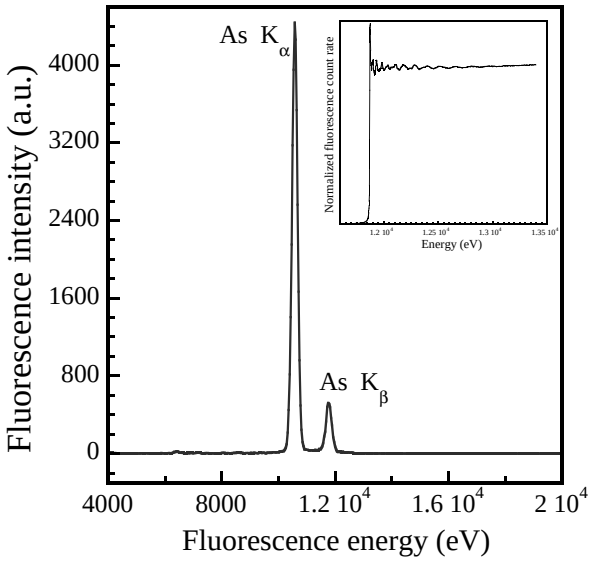

Figure A.1: Spectrum of photons emitted from the InAsP sample, dominated by As Kα and As Kβ fluorescence lines. In the inset a typical raw absorption spectrum.

horizontal plane and the sample surface formed an angle of 45° with the incident and fluorescence beams. Since the filling mode of the storage ring was uniform, the dead time of our acquisition system was by far bigger than the time interval between electrons bunches; furthermore at any used count rate there was very much less than one detectable event per bunch. In this condition, the arrival of events on the detector can be considered random in time and the experiment was not sensitive to the beam time structure, which allowed us to use the standard equation A.2 as an expression of the system throughput. Different formulations need to be employed in case of few bunches or single bunch mode, when the time separation between two bunches (corresponding to the circuit of the ring in the latter case) is comparable with the electronics dead

time [191].

The detector used was a thirteen element high purity Germanium model by EG&G ORTEG, model IGLET-11150X7-S, the preamplifier model is 239R, the active diameter is 11.3 mm, average energy resolution (FWHM) for the thirteen elements with a Fe^{55} source and 1000 cps is about 290 eV with a 1 μs peaking time constant and about 265 eV with a 4 μs peaking time constant. The detector elements are arranged symmetrically on two circles centered on the central element. The pulse processing electronics is a Digital X-ray Processor (DXP) manufactured by XIA (model 4C/4T, Revision C)[192]; this electronics has trapezoidal fast and a slow amplifier channels which run at the same time, thus allowing data correction according to method II outlined above. Each detector element is coupled to an independent pulse processing electronics channel. The fast amplifier channel has a dead time equal to 0.8 μs, and can be used to count almost all the photons that arrive on the detector. The peaking time for the slow amplifier channel was set for the series of measurements reported here to 4 μs, which corresponds to a nominal dead time of 8.2 μs; this rather high value was chosen to highlight the system non-linearity.

A.4 Results

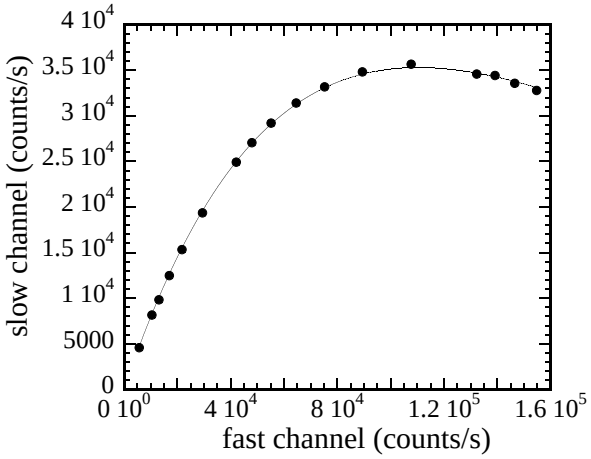

Figure A.2: Response of the slow channel of the counting electronics as a function of the total count rate, measured by the fast channel. Dots: experiment; continuous line: fit with equation A.6.

As a first step, the system throughput was determined at fixed incoming photon energy (12500 eV) by measuring the fluorescence count rate in the slow amplifier channel as a function of the energy integrated count rate recorded in the fast channel. This was achieved by varying the intensity of the beam impinging on the sample using filters, different relative alignment of the monochromator crystals and different sample-detector

distances. The system throughput was fitted with equation A.6 and the result is shown in Fig. A.2. The fit gave $\tau = 9.1$ μs in reasonable agreement with the expected value.

$$m_F = a n_T e^{-n_T \tau} \tag{A.6}$$

Equation A.6 is similar to equation A.2, where the constant a was introduced to take into account that the fluorescence count rate measured on the slow channel substitutes the total count rate in the formulation; the best fit gives a value of 0.87 for this constant. The inverse of a provides us with a factor to convert the Kα fluorescence count rate into energy integrated count rate and it was exploited while correcting by method I, as described above. Since the total count rate, excluding Kα counts, is in this case essentially given by the Kβ line and being the intensity ratio between the two fluorescence lines energy independent, the value determined for a at about 600 eV above the As edge is valid all over the EXAFS scan, otherwise the knowledge of the entire function $m_T(E)$ could be necessary.

The function in equation A.6 increases monotonically until $n_T = \frac{1}{\tau}$, where it has a maximum, after which it decreases and goes to zero as n_T increases further; the true count rate corresponding to the maximum of the NL curve ($n_T = \frac{1}{\tau}$) can be considered a characteristic frequency of the acquisition system. EXAFS spectra at the Arsenic K-edge were collected at various fast energy-integrated count rates (6 - 132 K c/s i.e. 5%-120% of the characteristic frequency) taking care to adjust the integration times in order to keep the number of counts per energy point as constant as possible. The count rates refer, here and in the following, to each detector element. The spectra will be labelled with the fast energy-integrated count rates measured on the central detector element.

For correction methods I and II the signal from each detector element was first corrected, in order to take into account the different count rates, and then the average of these spectra was calculated and quantitatively analyzed as described below. For method III an average spectrum was calculated, then analyzed and the corrected coordination number subsequently calculated according to equation A.5. EXAFS spectra (in the energy range 11650 - 13400 eV) were recorded by monitoring the intensity of the Kα fluorescence line with the slow amplifier channel; at the same time, the ratio $C(E)$ (equation A.3) between the energy integrated count rates measured with the fast and the slow channels was recorded. This procedure was carried out for each of the 13 detector elements. Quantitative data analysis was done with the experimental standard method using the package by A. Michailowitz [193]. EXAFS oscillations were extracted by fitting the pre-edge background using a linear function and by using a fifth order polynomial to model the atomic background.

Fig. A.3 reports the uncorrected, background subtracted EXAFS spectra: the progressive distortion of the signal with increasing count rate is apparent; when the total count rate reaches 107 K c/s (97 % of $1/\tau$) the EXAFS oscillations are nearly completely smoothed out. The data were corrected by the methods I and II and the corresponding EXAFS spectra are shown in Fig. A.4 and A.5. For the uncorrected spectra and for each data correction method the spectrum taken at the lowest count

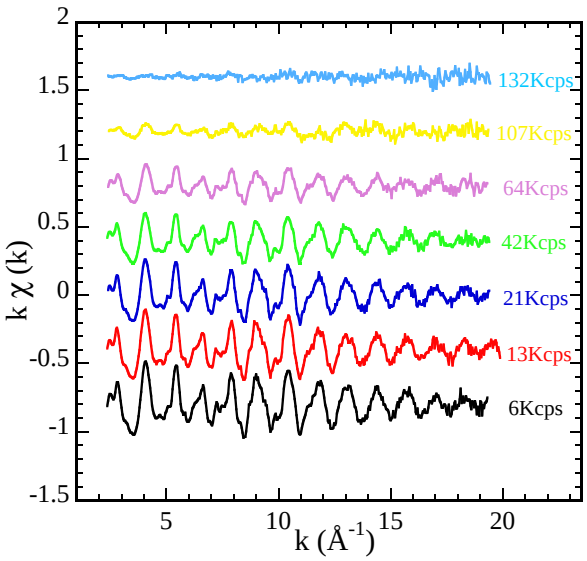

Figure A.3: Uncorrected EXAFS data obtained at different total count rates.

rate (6 K c/s) was used as a reference to extract experimental amplitudes and phases, the first shell structural parameters were determined using a non-linear fitting routine in which these parameters, along with an energy origin shift, were varied until a best fit was found. The following structural values were taken as a reference, based on the known structure of the sample: N = 4, R = 2.582 Å, $\sigma^2 = 2.5{*}10^{-3}$ Å^2.

The values obtained from the fitting procedure are reported in table A.1 as a function of the energy integrated count rate measured in the fast channel. We point out that the strongest effect of the distortions induced by the high-count rates is on the coordination numbers while the other structural parameters are practically unaffected within the error bars. For method III, the correction to the coordination numbers was applied *a posteriori* to the values obtained from the analysis of the uncorrected data. The As coordination numbers obtained by using the three methods as a function of the total counting rate are shown in Fig. A.6.

A.5 Discussion

The progressive distortion of the EXAFS signal with increasing count rate (Fig. A.3) makes it impossible to evaluate correctly the As coordination number if corrections are not applied. With a true total count rate of 42 K c/s (38% of $1/\tau$) the coordination number obtained from the uncorrected data corresponds to 70% of the true value (see Fig. A.6), a deviation which is well above the statistical error bar and is thus unacceptable. Correction method I permits to evaluate reasonable As coordination numbers (96% of the true value) up to 64 Kc/s (58% of $1/\tau$), the as-determined values are well within the statistical error bar. Above 60% of the characteristic frequency, method I

Table A.1: Structural parameters obtained from the uncorrected spectra and from the ones corrected by methods I and II: coordination number (N), interatomic distance (R) and Debye-Waller factor (σ^2). Error bars are calculated from a χ^2 analysis at 90 % confidence level.

Total Count Rate (Kcps)	N (atoms)	R (Å)	σ^2 (10^{-3} Å^2)
Uncorrected data			
13	3.75 ± 0.54	2.584 ± 0.004	2.6 ± 0.6
21	3.42 ± 0.45	2.583 ± 0.004	2.6 ± 0.6
42	2.76 ± 0.32	2.584 ± 0.003	2.5 ± 0.5
64	2.04 ± 0.36	2.580 ± 0.009	2.5 ± 0.1
107	0.70 ± 0.35	2.582 ± 0.029	2.5 ± 2.0
132	0.30 ± 0.60	2.586 ± 0.142	4.9 ± 9.2
Method I			
13	3.99 ± 0.46	2.584 ± 0.006	2.5 ± 0.5
21	4.06 ± 0.57	2.582 ± 0.004	2.5 ± 0.6
42	4.04 ± 0.51	2.583 ± 0.004	2.4 ± 0.7
64	3.84 ± 0.59	2.581 ± 0.005	2.5 ± 0.5
107	1.92 ± 0.79	2.580 ± 0.012	2.0 ± 1.6
Method II			
13	4.00 ± 0.32	2.585 ± 0.004	2.6 ± 0.4
21	3.93 ± 0.28	2.583 ± 0.004	2.6 ± 0.3
42	3.84 ± 0.20	2.585 ± 0.003	2.6 ± 0.2
64	3.71 ± 0.49	2.583 ± 0.004	2.5 ± 0.6
107	3.50 ± 0.20	2.582 ± 0.002	2.6 ± 0.3
132	3.47 ± 0.23	2.581 ± 0.004	2.8 ± 0.3

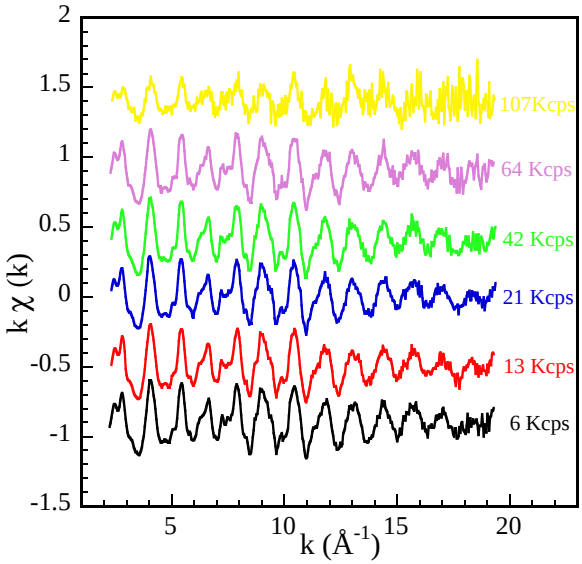

Figure A.4: EXAFS data corrected by numerical inversion of the non-linear system response (method I).

is unreliable and evaluated coordination numbers exhibit very large deviation from the known values. Here m_T begins to saturate and oscillations in m_F become comparable with statistical noise; the numerical inversion, performed in a region in which the NL curve has a low slope, expands both the signal and the noise providing a very noisy $n_F(E)$ from which it is impossible to recover correct structural information; finally method I cannot be applied to the last point at 132 Kc/s in Fig. A.6, beyond the NL maximum, because it cannot treat multi-values functions, since the numerical iteration stops as the non-linearity curve peak is reached.

It is worth remarking that the possibility of working at 60% of $1/\tau$ might appear surprising because it is rarely exploited by experimentalists, most probably due to a lack of quantitative information on the recovering power of dead time corrections: if a peaking time of 1 μs was employed (this is the more common choice for most experiments) this correction method is expected to be adequate up to 260 Kc/s. Correction with method II appears to be a little worse than method I until 60% of $1/\tau$ (93% of the true values), on the other hand it becomes more powerful than method I at very high count rate, near and beyond the characteristic frequency where it is able to recover a signal of good quality (Fig. A.5) and quite reasonable values for the coordination numbers (87% of the true value at 132 Kc/s). It must be noted, however, that this remarkable effect is due to the presence of an EXAFS signal in the correction factor $C(E)$ itself. In fact, since $C(E)$ is the ratio between the total counts recorded by the fast channel and those recorded by the slow one, at very high count rates the denominator is practically constant because of pile up while the numerator continues to oscillate. The corrected spectrum is the product between the apparent count rate of the selected fluorescence

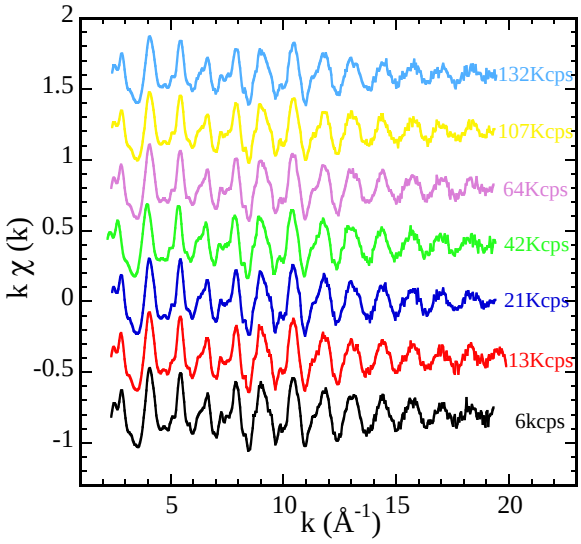

Figure A.5: EXAFS data corrected by multiplying the fluorescence rate by the ratio of the total count recorded in the fast amplifier channel to those in the amplifier slow (method II).

signal, which is virtually constant and the oscillating correction factor. The correction works very well in this case because the spectrum of photons reaching the detector is dominated by the As Kα fluorescence line; if the selected line represented only a small fraction of the total counts, the oscillations present in $C(E)$ would be much weaker compared to the baseline and the resulting $n_F(E)$ near NL maximum would be as noisy as for method I, or even worse in case of high dilution for the element of interest. Actually, when applying method II at very high count rates in the present case we are not exploiting the energy resolution of the detector. The peculiarity of method II is that it exploits the energy resolution of the acquisition when it is possible, otherwise it automatically uses the fast channel.

Correction with method III provides a very simple way to correct data, applying an overall factor directly on coordination numbers extracted from uncorrected data. On the other hand it should not be surprising, considering the strong approximation involved in this procedure, the lower recovering power of this kind of approach. As it is shown in Fig. A.5, methods III allows to evaluate reliable coordination numbers (95 % of the true value) up to 42 Kc/s (38% of $1/\tau$). At a count rate of 64 Kc/s (58% of $1/\tau$), however, the coordination numbers obtained using this method III are $\sim$ 80% of the correct value, a deviation which is unacceptably large compared to the statistical error bar. Corrections applied to data taken at even higher count rates (107 and 132 Kcounts/s) dramatically fail: this method relies on the assumption that $J\tau \ll 1$, which here is clearly not valid. By choosing this simplification we "lose" the range 40% - 60 % of $1/\tau$ because as long as we remount the NL curve and the local derivative

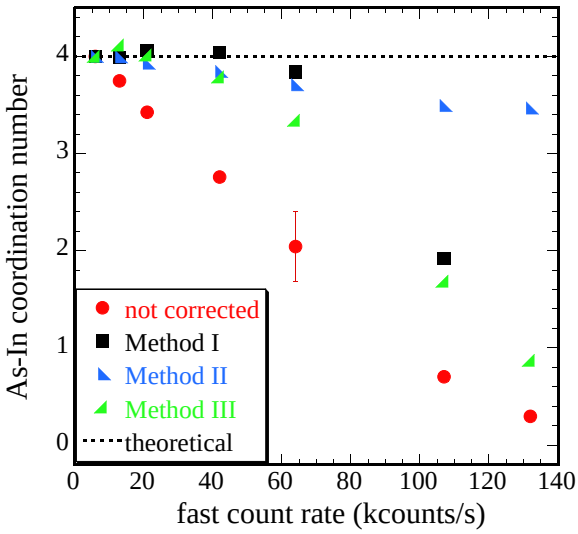

Figure A.6: Arsenic coordination numbers evaluated from uncorrected data and from data corrected with methods I, II and III as a function of the total count rates. For clarity only one, typical, error bar is reported.

becomes flatter and flatter, the approximation for which it is possible to correct all the energy points of the EXAFS scan on the same point of the NL curve doesn't work any more, and the correction on the jump doesn't normalize the correction on m_F. Even if method III is less powerful than the others, it permits to evaluate reliable structural information up to 160 Kc/s if a peaking time of 1 μs is chosen, well above the fast count rates commonly used in fluorescence EXAFS experiments. On the other hand it does not require the point to point knowledge of $n_T(E)$ and $m_T(E)$, nor the numerical inversion of $m_F(E)$: the knowledge of the two parameters in equation A.6 is in fact sufficient and they can be determined by measuring a few points and performing a simple fit, as we did in this paper.

A.6 Conclusions

The aim of the study presented in this appendix was to investigate the possibility of extracting correct structural parameters from fluorescence EXAFS data taken at high count rates with an energy-resolving detector. This situation is often encountered on third generation synchrotron radiation sources, which provide a high flux on the sample. We have quantified in a real experiment the errors caused by pulse pile-up in the extraction of structural information and have elaborated different approaches (three) to the problem of data correction. If no corrections are performed pulse pile-up results in a severe decrease of the estimated coordination numbers, while interatomic distances and Debye-Waller factors are not affected.

We have discussed the different approaches by comparing the ability of each kind of correction to recover the correct structural parameters. The result of our analysis is that it is possible to work in non-linear conditions and correct the data, providing the response function of the acquisition system is known. Reliable structural information can be obtained with data acquired up to a count rate equal to approximately 60% of the inverse of the dead time [194]. In particular, a method based on the numerical inversion of the throughput of the pulse counting electronics allows to recover the correct value of the coordination number within a 4% deviation up to count rates corresponding to $\sim$ 60% of the inverse dead time. Beyond 60% this method fails and another one, which exploits the measured system livetime, has to be considered the most efficient.

In the analysis of the $(In_x)Ga_{1-x}As_{1-y}N_y$ samples performed in this thesis work we didn't need to correct data for dead time losses, since total fast count rate during the acquisition with 1μs peaking time was 40 Kc/s at most, corresponding to about only 8 % of the inverse dead time. Table A.1 and Fig. A.6 show how pile up distortions on the uncorrected coordination numbers are well within the experimental error bars already at a 13 Kc/s count rate, which corresponds to 12 % of the inverse dead time with the peaking time selected for the measurements discussed in this appendix. Although not directly exploited for the main subject of this thesis, we reported this technical investigation in the appendix of the work for two reasons. First, because it helps in better understanding the physics and the electronics of the acquisition system employed in fluorescence measurements performed on $(In_x)Ga_{1-x}As_{1-y}N_y$ alloys. Second, because working at very high count rates, and correcting data accordantly to the procedure described here, could open a quite novel working route for the part of XAFS community devoted to the fluorescence detection mode (included that of semiconductors and dilute nitrides in particular), interested in saving beam-time in future measurement runs on bending magnet and insertion device X-Ray sources.

Conclusion

Le but de ce travail de thèse a été celui de fournir une caractérisation structurale pour les nitrures d'éléments III-V, en particulier des alliages $(In_x)Ga_{1-x}As_{1-y}N_y$, semiconducteurs d'importance stratégique pour la fabrication de nouveaux composants optoélectroniques et cellules solaires.

En exploitant la spectroscopie d'absorption de rayons X au seuil K de l'In en détection de fluorescence X, réalisée sur la ligne de lumière Gilda CRG de l'installation européenne de rayonnement synchrotron (ESRF), nous avons étudié les phénomènes d'ordre local autour des atomes d'indium. Nous avons trouvé que le nombre de coordination relatif In-N franchit la valeur stœchiométrique dans les échantillons $In_xGa_{1-x}As_{1-y}N_y$ recuits; au contraire, il correspond à celui attendu dans la condition de distribution aléatoire de liaisons dans les échantillons non recuits. Cela fournit l'indication que dans les échantillons recuits la liaison In-N est énergiquement privilégiée par rapport à celle In-As, comme récemment prévu par des calculs Monte Carlo. Par contre d'un point de vue quantitatif, les paramètres d'ordre mesurés sont inférieurs (un ordre de grandeur) par rapport à ceux prévus. Cela peut être dû soit au fait que le recuit entraîne les échantillons vers la condition d'équilibre (à laquelle les simulations se rapportent), mais que le processus n'est pas complet, soit aux possibles erreurs dans la modélisation théorique. Les résultats XAS au seuil de l'In sont qualitativement supportés par expériences XANES au seuil du N, réalisées sur le synchrotron de Elettra (ligne Aloisa), et par simulation en analyse de diffusion multiple (FMS, full multiple scattering). Le paramètre d'ordre mesuré par le XAS justifie quantitativement les changements au niveau de la bande interdite des échantillons recuits et, en particulier, donne une explication de l'origine du décalage vers le bleu de la bande interdite conséquent au recuit. Ce décalage, qui est une contrainte car il empêche l'accès aux longueurs d'onde plus élevées, n'est pas dû apparemment à l'enlèvement des défauts non radiatifs liés à l'azote présents sur large échelle dans les échantillons non recuits, contrairement à ce que des autres groupes ont proposé. En effet, des expériences XANES au seuil de l'azote en fonction de l'angle d'incidence, réalisées sur le synchrotron de Bessy II (ligne Cottbus), et expériences NRA montrent que l'azote est substitutif sur le site de l'arsenic dans une erreur correspondant à une fraction de quelque pourcentage de la concentration d'azote, que les échantillons soient recuits ou pas. L'augmentation du rendement de photoluminescence avec le recuit, nécessaire pour l'utilisation des ces nitrures pour l'optoélectronique, peut être due à l'enlèvement de défauts non radiatifs ou d'impuretés hétérogènes grâce au recuit, mais sur une échelle de concentrations de

deux ordres de grandeur inférieurs à celle de l'azote. Nous pensons que, au-delà de l'importance scientifique, toutes ces informations peuvent être utiles pour la croissance de matériaux et dispositifs aux caractéristiques améliorés.

En exploitant la spectroscopie d'absorption de rayons X au seuil K du Ga en détection d'électrons, aussi réalisée sur la ligne de lumière Gilda CRG nous avons étudié la structure locale autour des atomes de gallium dans couches épaisses de $GaAs_{1-y}N_y$/GaAs et en particulier le comportement de la distance Ga-As à la limite de dilution de l'azote; nous avons comparé ces résultats avec prédictions théoriques VFF et simulations DFT. Nous avons découvert que les modèles qui utilisent deux couples de constantes de force dans l'expression du potentiel élastique VFF sont plus adaptés à reproduire les distances inter-atomiques par rapport à un modèle qui exploite un paramètre de rigidité unique dépendant d'une seule paire de constantes de force. L'erreur faite par la modélisation avec paramètre de rigidité unique n'est pas dans la simulation de l'effet d'extension des distances, dû au fait que les échantillons sont épitaxiés sur un substrat (GaAs) de paramètre de maille plus large. Par contre, elle est due à la modélisation de la longueur de liaison relaxée. Dès que la même modélisation avec paramètre de rigidité unique reproduit proprement les distances de liaisons pour la majorité des semi-conducteurs III-V, nos croyons que l'échec dans le cas du $GaAs_{1-y}N_y$ est lié à la grande différence entre les constantes de force pour les deux alliages binaires constituants GaAs et GaN et, à l'origine, aux caractéristiques très différentes des deux anions arsenic et azote. La distribution des distances Ga-As élargit en augmentant la concentration d'azote à cause du désordre lié à la progressive distorsion de la maille de la couche épaisse épitaxiée sur GaAs. Cet élargissement est bien pris en compte par une des modélisations VFF qui exploitent deux couples de constantes de force et par les simulations DFT.

En utilisant la diffraction de rayons X, réalisée par des sources de lumières conventionnelles aux laboratoires de cristallographie du CNRS Grenoble et sur la ligne de lumière D2AM de l'ESRF, nous avons étudié les effets de l'hydrogénation sur le paramètre de maille des alliages $GaAs_{1-y}N_y$ et $In_xGa_{1-x}As_{1-y}N_y$. Nous avons trouvé que l'hydrogénation produit une relaxation du paramètre de la maille qui revient aux valeurs des alliages non nitrurés. Nous avons montré que ces changements structuraux sont complètement réversibles, grâce à un traitement particulier de recuit. Ces effets peuvent être expliqués par la formation des complexes $H_2^*(N)$, dans lesquels deux atomes d'hydrogène sont impliqués dans le processus de passivation. L'hydrogénation cause la rupture de la liaison Ga-N due à l'electronégativité élevée de l'atome d'azote et à la réactivité de l'hydrogène. Dans le complexe $H_2^*(N)$, le premier des deux atomes d'hydrogène se lie à l'atome de gallium et le deuxième à l'atome d'azote entre lesquels la liaison vient d'être cassée. Le même complexe explique la passivation des propriétés optiques, et sa rupture après le recuit justifie la pleine réversibilité du processus de passivation. Un effet de relaxation similaire sur la maille d'un semi-conducteur dû à l'hydrogénation a été observé dans les cas du silicium dopé avec bore, cependant nos résultats constituent la première observation du phénomène dans le cas d'une impureté isoélectronique comme l'azote.

En exploitant le XAS au seuil K de l'In en détection de fluorescence X et au seuil K du Ga en détection d'électron, réalisé sur la ligne GILDA, et aussi le DAFS au seuil K du Ga réalisé sur la ligne D2AM de l'ESRF, nous avons étudié les effets de l'hydrogénation sur la structure locale de couches épaisses $GaAs_{1-y}N_y$ et de puits quantiques $In_xGa_{1-x}As_{1-y}N_y$. Nous avons montré que la probable formation de complexes $H_2^*(N)$ cause un allongement des distances de liaison In-As et Ga-As, qui ne sont pas impliquées dans la rupture de la liaison Ga-N, par rapport aux prédictions VFF et parfois aussi aux distances dans les alliages non nitrurés.

Les résultats obtenus sur les effets structuraux de l'hydrogénation sont importants au point de vue de la technologie, car l'hydrogène est un contaminant très commun dans les techniques de croissance utilisées pour la production de semi-conducteurs sur une large échelle, comme le dépôt en phase vapeur par organométalliques (MOCVD). La connaissance des remarquables effets structuraux présentés dans cette thèse est par conséquent nécessaire, dû au fait qu'ils influencent profondément les propriétés d'émission.

D'un autre côté, un meilleur contrôle du processus d'hydrogénation pourrait être utilisé pour régler la longueur d'onde d'émission de ces semi-conducteurs après la croissance, grâce à la réversibilité de ce phénomène. Du fait que les échantillons hydrogènes ne sont pas encore utilisables pour la construction de lasers à cause de la diminution du rendement de fluorescence lié la formation des défauts non radiatifs, beaucoup de pas doivent encore être faits dans cette direction.

En parallèle à l'étude de la structure des nitrures d'éléments III-V, nous avons aussi conduit une étude instrumentale du régime non-linéaire des détecteurs à l'état solide pour le XAS en détection de fluorescence X. Nous avons étudié la possibilité d'extraire des paramètres structuraux corrects à partir d'expériences XAS dans lesquelles le flux sur l'échantillon est très intense et le nombre de coups sur le détecteur très élevé. Nous avons quantifié les erreurs dues au temps mort sur les paramètres extraites et élaborées différentes stratégies de correction des données. Le résultat de notre analyse est que, en connaissant la réponse du système d'acquisition, il est parfaitement possible de travailler en régime non-linéaire. En effet, avec l'utilisation de corrections opportunes on peut obtenir des informations structurales plausibles jusqu'à un nombre de coups/s équivalent à 60 % de l'inverse de la constante de temps mort.

Bibliography

[1] M. Kondow, K. Uomi, A. Niwa, T. Kitatani, S. Watahiki, and Y. Yazawa. *Jpn. J. Appl. Phys.*, 35(1-2B):1273, 1996.

[2] S. Sato, Y. Osawa, and T. Saitoh. *Jpn. J. Appl. Phys.*, 36(1-5A):2671–2675, 1997.

[3] J. F. Geisz and D. J. Friedman. *Semicond. Sci. Technol.*, 17:769–777, 2002.

[4] W. Shan, W. Walukiewicz, J. W. Ager III, E. E. Haller, J. F. Geisz, D. J. Friedman, J. M. Olson, and S. R. Kurtz. *Phys. Rev. Lett.*, 82(6):1221, 1999.

[5] P. R. C. Kent and A. Zunger. *Phys. Rev. B*, 64:115208, 2001.

[6] A. Amore Bonapasta, F. Filippone, P. Giannozzi, M. Capizzi, and A. Polimeni. *Phys. Rev. Lett.*, 89(21):216401, 2002.

[7] A. Janotti, S. B. Zhang, Su-Huai Wei, and C. G. Van de Walle. *Phys. Rev. Lett.*, 89(8):086403, 2002.

[8] L. Bellaiche and A. Zunger. *Phys. Rev. B*, 57(8):4425, 1998.

[9] K. Kim and A. Zunger. *Phys. Rev. Lett.*, 86(12):2609–2612, 2001.

[10] T. Wipiejewski. High-tech lasers for the information superhighway. Components, March 1999. http://www.infineon.com/fiberoptics.

[11] L. Grenouillet. *Spectroscopie optique de nouveaux matériaux a base de (Ga,In)(N,As) pour la réalisation de composants a cavité verticale émettant a* $1.3\mu m$ *sur substrat GaAs.* PhD thesis, Institut National des Science Appliquees de Lyon, 2001.

[12] T. Takamoto, E. Ikeda, H. Kurita, and M. Ohmori. *Appl. Phys. Lett*, 70(3):381, 1997.

[13] H. Mariette. *Physica B*, 146B:286, 1987.

[14] X. Liu, M. E. Pistol, L. Samuelson, S. Schwetlick, and W. Seifert. *Appl. Phys. Lett*, 56:1451, 1990.

[15] D. J. Wolford, J. A. Bradley, K. Fry, and J. Thompson. *Physics of Semiconductors*. Springer, New York, 1984. p. 627.

[16] J. N. Baillargeon, K. Y. Cheng, G. E. Hofler, P. J. Pearah, and K. C. Hsieh. *Appl. Phys. Lett.*, 60:2540, 1992.

[17] M. Weyers, M. Sato, and H. Ando. *Jpn. J. Appl. Phys.*, 31:L853–L855, 1992.

[18] Landolt-Bornstein. *Numerical Data and Functional Relationships in Science and Technology*, volume 17. Springer-Verlag, Berlin, 1982.

[19] J. E. Bernard and A. Zunger. *Phys. Rev. B*, 36:3199, 1987.

[20] R. Magri, S. Froyen, and A. Zunger. *Phys. Rev. B*, 44:7947, 1991.

[21] S-. H. Wei and A. Zunger. *Phys. Rev. Lett.*, 76(4):664, 1996.

[22] M. Kondow, K. Uomi, K. Hosomi, and T. Mosume. *Jpn. J. Appl. Phys.*, 33:L1056, 1992.

[23] A. Rubio and M. L. Cohen. *Phys. Rev. B*, 51:4343, 1995.

[24] J. Neugebauer and C. G. Van de Walle. *Phys. Rev. B*, 51:10568, 1995.

[25] T. Mattila, S-. H. Wei, and A. Zunger. *Phys. Rev. B*, 60(16):11245, 1999.

[26] Y. Zhang, B. Fluegel, A. Mascarenhas, H. P. Xin, and C. W. Tu. *Phys. Rev. B*, 62:4493, 2000.

[27] Y. Zhang, A. Mascarenhas, J. F. Geisz, H. P. Xin, and C. W. Tu. *Phys. Rev. B*, 63:085205, 2001.

[28] P. N. Keating. *Phys. Rev.*, 145(2):637, 1966.

[29] J. Martins and A. Zunger. *Phys. Rev. B*, 30:6217, 1984.

[30] L. Wang and A. Zunger. *J. Chem. Phys.*, 100:2394, 1994.

[31] B. Gil and H. Mariette. *Phys. Rev. B*, 35:7999, 1987.

[32] H. A. McKay, R. M. Feenstra, T. Schmidtling, and U. W. Pohl. *Appl. Phys. Lett.*, 78:82, 2001.

[33] T. Makimoto, H. Saito, T. Nishida, and N. Kobayashi. *Appl. Phys. Lett*, 70:2984, 1997.

[34] S. Francoeur, S. A. Nikishin, C. Jin, Y. Qiu, and H. Temkin.

[35] H. P. Xin, K. L. Kavanagh, Z. Q. Zhu, and C. W. Tu. *Appl. Phys. Lett.*, 74:2337, 1999.

[36] R. K. Ahrenkiel, S. W. Johnston, B. M. Keyes, and D. J. Friedman. *Appl. Phys. Lett*, 77:3794, 2000.

[37] P. R. C. Kent and A. Zunger. *Phys. Rev. Lett.*, 86(12):2613, 2001.

[38] L. Bellaiche. *Appl. Phys. Lett.*, 75:2578, 1999.

[39] S. Kurtz, J. Webb, L. Gedvilas, D. Friedman, J. Geisz, J. Olson, R. King, D. Joslin, and N. Karam. *Appl. Phys. Lett.*, 78(6):748, 2001.

[40] H. P. Xin, C. W. Tu, and M. Geva. *Appl. Phys. Lett*, 75:1416, 1999.

[41] H. P. Xin, C. W. Tu, and M. Geva. *J. Vac. Sci. Technol. B*, 18:1476, 2000.

[42] J. I. Pankove and N. M. Johnson, editors. *Hydrogen in Semiconductors and Semimetals*, volume 34. Academic, New York, 1991.

[43] A. Amore Bonapasta. *Phys. Rev. B*, 42(12):8771, 1993.

[44] G. Baldassarri, M. Bissiri, A. Polimeni, M. Capizzi, M. Fischer, M. Reinhardt, and A. Forchel. *Appl. Phys. Lett*, 78(22):3472, 2001.

[45] Yong-Sung Kim and K. J. Chang. *Phys. Rev. B*, 66:073313, 2002.

[46] P. Hohenberg and W. Kohn. *Phys. Rev.*, 136(3B):864, 1964.

[47] W. Kohn and L. J. Sham. *Phys. Rev.*, 140(4A):1133, 1965.

[48] D. M. Ceperley and B. J. Alder. *Phys. Rev. Lett*, 45(7):566, 1980.

[49] J. P. Pedrew and A. Zunger. *Phys. Rev. B*, 23(10):5048, 1981.

[50] J. Neugebauer and C. G. Van de Walle. *Phys. Rev. Lett.*, 75:4452, 1995.

[51] L. Pavesi and P. Giannozzi. *Phys. Rev. B*, 46:4621, 1992.

[52] A. Polimeni et al. *Phys. Rev. B*, 63:201304(R), 2001.

[53] K. J. Chang and D. J. Chadi. *Phys. Rev. Lett.*, 62(8):937, 1989.

[54] K. J. Chang and D. J. Chad. *Phys. Rev. B*, 42(12):7651, 1990.

[55] T. Suzuki. *MRS Bull.*, 22(7):33, 1997.

[56] A. M. Saitta, S. de Gironcoli, and S. Baroni. *Phys. Rev. Lett.*, 80:4939, 1998.

[57] R. S. Goldman, R. M. Feenstra, B. G. Briner, M. L. O'Steen, and R. J. Hauenstein. *Appl. Phys. Lett*, 69(24):3698, 1996.

[58] Y. Narukawa, Y. Kawakami, M. Funato, S. Fujita, S. Fujita, and S. Nakamura. *Appl. Phys. Lett*, 70(8):981, 1997.

[59] M. Ichimura and A. Sasaki. *Phys. Rev. B*, 36:9694, 1987.

[60] W. A. Harrison. *Electronic Structure and the Properties of Solids*. Dover, New York, 1989. p. 176.

[61] K. Kim et. al. *Phys. Rev. B*, 53:16310, 1996.

[62] G. Ciatto, F. d'Acapito, L. Grenouillet, H. Mariette, D. de Salvador, G. Bisognin, R. Carboni, L. Floreano, R. Gotter, S. Mobilio, and F. Boscherini. *Phys. Rev. B*, 68:161201(R), 2003.

[63] G. S. Cargill and F. Spaepen. *J. Non-Cryst. Solids*, 43:91, 1981.

[64] S. G. Spruytte, C. W. Coldren, J. S. Harris, W. Wampler, P. Krispin, K. Ploog, and M. C. Larson. *J. Appl. Phys.*, 89(8):4401, 2001.

[65] W. Li, M. Pessa, and J. Likonen. *Appl. Phys. Lett.*, 78(19):2864, 2001.

[66] W. J. Fan, S. F. Yoon, T. K. Ng, S. Z. Wang, W. K. Loke, R. Liu, and A. Wee. *Appl. Phys. Lett*, 80:4136, 2002.

[67] L. Grenouillet, C. Bru-Chevallier, G. Guillot, P. Gilet, P. Ballet, P. Duvaut, G. Rolland, and A. Million. *J. Appl. Phys.*, 91(9):5902, 2002.

[68] M. Stutzmann, J. Harsanyi, A. Breitschwerdt, and C. P. Herrero. *Appl. Phys. Lett.*, 52(20):1667, 1988.

[69] Y. L. Soo, S. Huang, Y. H. Kao, J. G. Chen, S. L. Hulbert, J. F. Geisz, S. Kurtz, J. M. Olson, S. R. Kurtz, E. D. Jones, and A. A. Allerman. *Phys. Rev. B*, 60(19):13605, 1999.

[70] L. Bellaiche, S. H. Wei, and A. Zunger. *Phys. Rev. B*, 54(24):17568, 1996.

[71] L. Vegard. *Z. Phys.*, 5:17, 1921.

[72] J. C. Mikkelsen and J. B. Boyce. *Phys. Rev. B*, 31:6903, 1985.

[73] L. Pauling. *The Nature of the Chemical Bond*. Cornell University Press, Ithaca, 1967.

[74] J. G. Kirkwood. *J. Chem. Phys.*, 7:506, 1939.

[75] Y. Cai and M. F. Thorpe. *Phys. Rev. B*, 46(24):15872, 1992.

[76] T. Sasaki, T. Onda, R. Ito, and N. Ogasawara. *Jpn. J. Appl. Phys., Part 1*, 25:231, 1985.

[77] A. Balzarotti. *Tenary and Multinary Compounds*, volume 9. Materials Research Society, Pittsburgh, 1987.

[78] A. Balzarotti, N. Motta, A. Kisiel, M. Zimnal-Starnawska, M. T. Czyzyk, and M. Podgorny. *Phys. Rev. B*, 31(12):7526, 1985.

[79] J. C. Woicik. *Phys. Rev. B*, 57:6266, 1998.

[80] J. C. Aubry, T. Tyliszczak, A. P. Hitchcock, J. M. Baribeau, and T. E. Jackman. *Phys. Rev. B*, 59:12872, 1999.

[81] M. C. Ridgway, K. M. Yu, C. J. Glover, G. J. Foran, C. Clerc, J. L. Hansen, and A. N. Larsen. *Phys. Rev. B*, 60(15):10831, 1999.

[82] Y. Cai and M. F. Thorpe. *Phys. Rev. B*, 46(24):15879, 1992.

[83] M. Tormen, D. De Salvador, M. Natali, A. Drigo, F. Romanato, G. Rossetto, F. Boscherini, and S. Mobilio. *J. Appl. Phys.*, 86:2533, 1999.

[84] F. D'Acapito, S. Colonna, F. Arciprete, A. Balzarotti, I. Davoli, F. Patella, and S. Mobilio. *Nucl. Instr. and Meth. in Phys. Res. B*, 200:85, 2003.

[85] M. J. Paisley and R. F. Davis. *Journal of Crystal Growth*, 127:136, 1993.

[86] R. Kudrawiec, G. Sek, J. Misiewicz, D. Gollub, and A. Forchel. *Appl. Phys. Lett.*, 83(14):2772, 2003.

[87] R. de Kronig. *Z. Phys.*, 70:317, 1931.

[88] L. V. Azaroff. *Rev. Mod. Phys.*, 35:1012, 1963.

[89] C. Maurizio. *binary alloy nanocluster formation by ion implantation in dielectrics : a study based on EXAFS spectroscopy.* PhD thesis, Università degli studi di Padova, December 2001.

[90] E. A. Stern. *Phys. Rev. B*, 10:3027, 1974.

[91] D. E. Sayers, E. A. Stern, and F. W. Lytle. *Phys. Rev. Lett.*, 27:1204, 1971.

[92] B. M. Kincaid and P. Eisemberger. *Phys. Rev. Lett*, 34:1361, 1975.

[93] L. G. Parratt. *Rev. Mod. Phys.*, 31:616, 1959.

[94] P. A. Lee, P. H. Citrin, P. Eisenberger, and B. M. Kincaid. *Rev. Mod. Phys.*, 53(4):769, 1981. part I.

[95] J. J. Rehr and R. C. Albers. *Rev. Mod. Phys.*, 72:621, 2000.

[96] E. Sevillano, H. Menth, and J.J. Rehr. *Phys. Rev. B*, 20:4908, 1979.

[97] J. M. Tranquada and R. I. Ingalls. *Phys. Rev. B*, 28:3520, 1983.

[98] E. A. Stern. *X-Ray absorption : principles and application techniques of EXAFS, SEXAFS and XANES.* J. Wiley, 1988. chapter I, p.34.

[99] A. Filipponi, A. Di Cicco, and C. R. Natoli. *Phys. Rev. B*, 52:15122, 1995.

[100] B. L. Gyoffry. *Phys. Rev. B*, 5:2382, 1972.

[101] C. R. Natoli and M. Benfatto. *J. de Phys.*, C8:11, 1986.

[102] P. J. Durham. *X-Ray absorption : principles and application techniques of EXAFS, SEXAFS and XANES*. J. Wiley, 1988. chapter II.

[103] A. L. Ankudinov, B. Ravel, J. J. Rehr, and S. D. Conradson. *Phys. Rev. B*, 58:7565, 1998.

[104] J. E. Muller, O. Jepsen, and J. W. Wilkins. *Solid State Commun.*, 42:365, 1982.

[105] R. C. Albers, A. K. McMahan, and J. E. Muller. *Phys. Rev. B*, 31:3435, 1985.

[106] J. E. Muller, O. Jepsen, O. K. Andersen, and J. W. Wilkins. *Phys. Rev. Lett*, 40(11):720, 1978.

[107] J. Jaklevic, J. A. Kirby, M. P. Klein, A. S. Robertson, G. S. Brown, and P. Eisenberger. *Solid St. Comm.*, 23:679, 1977.

[108] P. Fornasini. Introduzione alla spettroscopia di assorbimento di raggi x. SILS - V Scuola Nazionale di LdS, S. Margherita di Pula (Ca), September 1999.

[109] T. M. Hayes and J. B. Boyce. *Solid State Physics*. New York: Academic, 1983. pp. 256 - 351.

[110] L. Troger, D. Arvanitis, K. Baberschke, H. Michaelis, U. Grimm, and E. Zschech. *Phys. Rev. B*, 46:3283, 1992.

[111] S. Eisebitt, T. Boske, J.-E. Rubensson, and W. Eberhardt. *Phys. Rev. B*, 47:14103, 1993.

[112] P. Pfalzer, J.-P. Urbach, M. Klemm, S. Horn, M. L. den Boer, A. I. Frenkel, and J. P. Kirkland. *Phys. Rev. B*, 60:9335, 1999.

[113] M. Newville, P. Livins, Y. Yacoby, J. J. Rehr, and E. A. Stern. *Phys. Rev. B*, 47:14126, 1993.

[114] L. Brillouin. *Science and Information Theory*. Academic, New York, 1962.

[115] B. Ravel. *J. Synchrotron Rad.*, 8:314–316, 2001.

[116] A. L. Ankudinov and J. J. Rehr. *Phys. Rev. B*, 56:R1712, 1997.

[117] S. I. Zabinsky, J. J. Rehr, A. Ankudinov, R. C. Albers, and M. J. Eller. *Phys. Rev. B*, 52:2995, 1995.

[118] L. Mattheiss. *Phys. Rev.*, 133:A1399, 1964.

[119] U. von Barth and L. Hedin. *J. Phys. C*, 5:1629, 1972.

[120] L. Hedin and S. Lundqvist. *Solid State Phys.*, 23:1, 1969.

[121] D. D. Koelling and B. N. Harmon. *J. Phys. C*, 10:3107, 1977.

[122] M. Newville. *Feffit*. http://cars9.uchicago.edu/ newville/feffit/, v 2.32 edition.

[123] M. Newville, B. Ravel, D. Haskel, J. J. Rehr, E. A. Stern, and Y. Yacoby. *Physica B*, 208&209:154, 1995.

[124] P. R. Bevington. *Data reduction and Error Analysis for the Physical Science*. McGraw-Hill Book Company, 1969.

[125] F. D'Acapito. *Etude structurale de verres silicates dopés au cuivre et á l'argent*. PhD thesis, Université Joseph Fourier - Grenoble I, July 1997.

[126] S. Pascarelli, F. Boscherini, F. D'Acapito, J. Hrdy, C. Meneghini, and S. Mobilio. *J. Synchrotron Radiat.*, 3(3):147, 1996.

[127] L.Floreano, G.Naletto, D.Cvetko, R.Gotter, M.Malvezzi, L.Marassi, A.Morgante, A.Santaniello, A.Verdini, and F.Tommasini. *Rev. Sci. Instrum.*, 70:3855, 1999.

[128] K. J. Sawhney, F. Senf, M. Scheer, F. Schafers, J. Bahrdt, A. Gaupp, and W. Gudat. *Nucl. Instr. Meth. A*, 390:395–402, 1997.

[129] W. Friedrich, P. Knipping, and M. Von Laue. Sitzungsberichte der (kgl.) bayerische akademie der wissenschaften. volume 303, 1912.

[130] W. H. Bragg and W. L. Bragg. In *Proc. R. Soc. A*, volume 88, page 428, 1913.

[131] N. W. Ashcroft and N. D. Mermin. *Solid state physics*. Saunders College / Harcourt Brace College Publishers, 1976.

[132] B. E. Warren. *X-ray Diffraction*. Dover Publication, New York, 1990.

[133] Z. G. Pinsker. *Dynamical theory of X-rays in crystals*. Springer, 1978.

[134] R. M. Moon and C. G. Shull. *Acta Cryst.*, 17:597, 1964.

[135] Y. Cauchois. Distribution spectrale observe dans une rgion d'absorption propre de divers cristaux. In *Compte Rendus de l'Acadmie des Sciences (Paris)*, volume 242, pages 100–102, 1956.

[136] C. Cohen-Tannoudji, B. Diu, and F. Laloe. *Mécanique quantique*, volume II. Hermann, 1973.

[137] M. Benfatto and R. Felici. *Phys. Rev. B*, 64:115410, 2001.

[138] J. J. Sakurai. *Advanced Quantum Mechanics*. Benjamin Cummings Publishing Company, 1967.

[139] I. J. Pickering, M. Sansone, J. Marsch, and G. N. George. *J. Am. Chem. Soc.*, 115:6302, 1993.

[140] H. Stragier, J. O. Cross, J. J. Rehr, L. B. Sorensen, C. E. Bouldin, and J. C. Woicik. *Phys. Rev. Lett.*, 69:3064, 1992.

[141] M. G. Proietti, H. Renevier, J. L. Hodeau, J. Garcia, J. F. Berar, and P. Wolfers. *Phys. Rev. B*, 59(8):5479, 1999.

[142] A. Wilson and E. Prince. *Interational Tables for Cristallography*, volume C. Kluver Academic Publishers, Dordrecht, 1999.

[143] S. Grenier. *Spectroscopie de Diffraction résonante. Etudes de nanostructures de semiconducteur III-V et de l'ordre de charge dans α'-NaV_2 O_5.* PhD thesis, Université Joseph Fourier - Grenoble, 2001.

[144] W. K. Chu. *Backscattering Spectroscopy.* Academic Press, 1977.

[145] M. Berti, D. de Salvador, A. V. Drigo, F. Romanato, A. Sambo, S. Zerlauth, J. Stangl, F. Schaffler, and G. Bauer. *Nucl. Instr. and Meth. in Phys. Res. B*, 143:357, 1998.

[146] J. W. Mayer. *Ion Beam Handbook for Material Analysis.* Rimini.

[147] G. Amsel and D. Davies. *Rev. Phys. Appl.*, 4:383, 1969.

[148] G. Bisognin, D. de Salvador, C. Mattevi, M. Berti, A.V. Drigo, G. Ciatto, L. Grenouillet, P. Duvaut, P. Gilet, and H. Mariette. *J. Appl. Phys.*, 94(1):48, 2004.

[149] D. M. Ceperley and B. J. Alder. The code is available on the web site URL http://www.pwscf.org.

[150] D. Vanderbilt. *Phys. Rev. B*, 41:7892, 1990.

[151] A. Polimeni, G. Ciatto, L. Ortega, F. Jiang, F. Boscherini, F. Filippone, A. Amore Bonapasta, M. Stavola, and M. Capizzi. *Phys. Rev. B*, 68:085204, 2003.

[152] D. Murnaghan. In *Proc. Acad. Sci. U.S.A.*, volume 30, page 224, 1944.

[153] P. E. Blochl. *Phys. Rev. B*, 50:17953, 1994.

[154] G. Kresse and D. Joubert. *Phys. Rev. B*, 59:1758, 1999.

[155] G. Kresse and J. Furthmüller. *Comput. Mat. Sci.*, 6:15, 1996.

[156] G. Kresse and J. Furthmüller. *Phys. Rev. B*, 54:11169, 1996.

[157] G. Makov, R. Shah, and M. C. Payne. *Phys. Rev. B*, 53:15513, 1996.

[158] G. Ciatto, F. Boscherini, F. D'Acapito, S. Mobilio, G. Baldassarri, A. Polimeni, M. Capizzi, D. Gollub, and A. Forchel. *Nucl. Instr. and Meth. in Phys. Res. B*, 200:34–39, 2003.

[159] J. Y. Duboz, J. A. Gupta, Z. R. Wasilewski, J. Ramsey, R. L. Williams, G. C. Aers, B. J. Riel, and G. I. Sproule. *Phys. Rev. B*, 66:085313, 2002.

[160] P. J. Klar, H. Gruning, J. Koch, S. Schafer, K. Volz, W. Stolz, W. Heimbrodt, A. M. Karnal Saadi, A. Lindsay, and E. P. O'Reilly. *Phys. Rev. B*, 64:121203, 2001.

[161] J. Hornstra and W. J. Bartels. *J. Cryst. Growth*, 44:513, 1978.

[162] J. Stohr. *NEXAFS Spectroscopy*, volume 25 of *Springer Series in Surface Science*. Springer-Verlag, Berlin, 1992.

[163] W. Orellana and A. C. Ferraz. *Appl. Phys. Lett.*, 78:1231, 2001.

[164] V. Lordi, V. Gambin, S. Friedrich, T. Funk, T. Takizawa, K. Uno, and J. S. Harris. *Phys. Rev. Lett.*, 90(14):145505, 2003.

[165] G. Ozolins, G. K. Averkieva, A. Ievins, and N. A. Goryunova. *Kristallografiya 7*, 7:850, 1962.

[166] P. F. Fewster and N. L. Andrew. *J. Appl. Cryst.*, 28:451, 1995.

[167] A. F. Wright and J. S. Nelson. *Phys. Rev B*, 51(12):7866, 1994.

[168] A. F. Wright and J. S. Nelson. *Phys. Rev B*, 50(4):2159, 1994.

[169] R. M. Martin. *Phys. Rev. B*, 1(10):4005, 1970.

[170] A. F. Wright. *J. Appl. Phys.*, 82(6):2833, 1997.

[171] P. J. Klar, H. Gruning, W. Heimrodt, J. Koch, H. Hohnsdorf, W. Stolz, P. M. Vicente, and J. Camassel. *Appl. Phys. Lett.*, 76:3439, 2000.

[172] B. Gil. *Solid State Commun.*, 114:623, 2000.

[173] *Properties of Lattice-Matched and Strained Indium Gallium Arsenide*. 8. Pallab Battachatya Datareviews.

[174] G. Ciatto, F. d'Acapito, S. Sanna, V. Fiorentini, A. Polimeni, M. Capizzi, S. Mobilio, and F. Boscherini. 2004. submitted to Phys. Rev. B.

[175] A. Erbil, R. Frahm G. S. Cargill III, and R. F. Boehme. *Phys. Rev. B*, 37(5):2450, 1988.

[176] L. Reimer. *Scanning Electron Microsc.*, II:111, 1979.

[177] D. Liljequist, T. Ekdahl, and U. Baverstam. *Nucl. Intrum. Methods*, 155:529, 1978.

[178] A. Neukermans and W. Saperstein. *J. Vac. Sci. Technol.*, 16:1847, 1979.

[179] H. Seiler. *Z. Angew. Phys.*, 22:249, 1967.

[180] F. d'Acapito. unpublished, 2003.

[181] W. H. Press, S. A. Teukolsky, W. T. Vetterling, and B. P. Flannery. *Numerical Recipes*. Cambridge University Press, 2002.

[182] A. Amore Bonapasta and F. Filippone. *Phys. Rev. B*, 68:073202, 2003.

[183] M. Capizzi, A. Polimeni, G. Baldassarri, M. Bissiri, A. Amore Bonapasta, F. Jiang, M. Stavola, M. Fischer, A. Forchel, I. K. Sou, and W. K. Ge. Photoluminescence and infrared absorption study of isoelectronic impurity passivation by hydrogen. In S. Ashok, J. Chevallier, N. M. Johnson, B. L. Sopori, and H. Okushi, editors, *MRS Symposia Proceedings*, volume 719, page 251. Material Research Society, Warrendale, PA, 2003.

[184] G. F. Knoll. *Radiation Detection and Measurement*. Wiley, New York, 1989. chapter 4.

[185] S. P. Cramer, O. Tench, M. Yocum, and G. N. George. *Nuclear Instr. and Meth. in Phys. Res. A*, 266:586, 1988.

[186] A. J. Dent, G. E. Derbyshire, G. Derst, and R. C. Farrow. *Rev. Sci .Instrum.*, 66(2):2306, 1995.

[187] R. C. Farrow, J. Headspith, A. J. Dent, B. R. Dobson, R. L. Bilsborrow, C. A. Ramsdale, P. C. Stephenson, S. Brierley, G. E. Derbyshire, P. Sangsingkeow, and K. Buxton. *J. Synchrotron Rad.*, 5:845, 1998.

[188] M. Nomura. *J. Synchrotron Rad.*, 5:851, 1998.

[189] G. Ciatto. Invert 3b; fortran 77 program. The code is available, on request, from the author: ciatto@esrf.fr, 2003.

[190] S. Pascarelli, F. Boscherini, C. Lamberti, and S. Mobilio. *Phys. Rev. B*, 56:1936, 1997.

[191] J. E. Bateman. *J. Synchrotron Rad.*, 7(5):307, 2000.

[192] XIA. *Model 4C/4T,Revision C*. for a description see http://www.xia.com.

[193] A. Michalowicz. *J.Phys. IV, France*, 7(C2):235, 1997.

[194] G. Ciatto, F. d'Acapito, F. Boscherini, and S. Mobilio. Treatment of exafs data taken in the fluorescence mode in non-linear conditions. accepted on J. Synchrotron Rad., 2004.